UNIVERSITÀ DEL SALENTO

DEPARTMENT OF MATHEMATICS AND PHYSICS “E. DE GIORGI”
PhD in Physics and Nanoscience

Searching for the dark photon with PADME and measurement of the $e^+e^- \to \gamma\gamma$ cross section at $\sqrt{s} = 21$ MeV

Candidate:
Isabella Oceano

Advisors:
Prof.ssa Stefania Spagnolo
Dott. Gabriele Chiodini

Academic year 2020-2021

Contents

Introduction

The Standard Model (SM) of particle physics is a quantum field theory that describes with extreme accuracy the behaviour of fundamental particles interacting through the strong, electromagnetic and weak forces. Although the SM has an extraordinary record of successes, the most recent of them established with the discovery of the Higgs Boson in 2012, it is unable to explain some of the more prominent observed physical phenomena in the Universe. An ever-increasing amount of evidence suggests that most of the universe content is composed of some non-luminous, and hitherto unknown, "Dark Matter" (DM). Physicists have been working on and trying to solve the DM problem for decades. The first evidence that much more than the visible matter should fill the Universe dates back to 1933 when F. Zwicky measured the dispersion velocity of galaxies in the Coma cluster. In the following years, other observations confirmed the gravitational evidence for the dominance of the dark with respect to the visible component of the universe. In Chapter 1 the astronomical and cosmological indication for this new kind of matter was summarised. The properties of dark matter are described along with the proposed particle candidates, with a focus on the dark photon hypothesis. This model foresees a new abelian symmetry $U_D(1)$ in addition to the SM symmetry $SU_C(3) \times SU_{EW}(2) \times SU_Y(1)$ and as a consequence a new massive Gauge Boson A' called dark photon. The A' production mechanisms and decay channels are presented along with the techniques that have been proposed to verify the existence of the dark photon. They are summarised in Chapter 1, together with specific experiments that are looking for the A'.

This dissertation discusses the search for A' at the Laboratori Nazionali di Frascati (LNF) of INFN with the PADME (Positron Annihilation into Dark Matter Experiment) experiment. A positron beam is used to search for the production of the dark photon in the annihilation with an an atomic electron of a Diamond target: $e^+e^- \to \gamma A'$. The technique used to search for the dark photon is based on the missing mass $M^2_{miss} = (P_{e^-} + P_{e^+} - P_\gamma)^2$, a quantity that corresponds to the A' mass but can be computed as a function of kinetic properties of the visible photon produced along with the A'. The SM photon is recorded by the main calorimeter (ECAL) of the experiment. If A' exists, a peak in the missing mass spectrum will emerge at its mass. A detailed description of PADME and all the sub-detectors is reported in Chapter 2, together with the PADME simulation and reconstruction software, to which I largely contributed. Once the PADME detectors and software are described, the A' search strategy is discussed. As will become clear from the work described in the thesis, the main problem is the background rejection. Therefore, in Chapter 2 the SM processes observed in PADME are described with particular attention to those representing a significant physics background to A'. If no evidence for the A' will emerge from data, the experiment will set limits in the parameter space $(M_{A'}, \epsilon)$, where ϵ is the effective coupling of the A' to the photon. At the end of Chapter 2, the design PADME sensitivity is discussed.

PADME was approved by INFN in 2016, it was built in the summer of 2018 and took data continuously from October 2018 up to March 2019 (RunI). During this first data taking period, a huge background level was observed. MC simulations helped to understand the sources leading to a change of the beam line configuration. A reduction of the beam related background was obtained reaching the lowest level in RunII, which took place in Autumn 2020 after a beam commissioning run. I contributed in person at LNF to all these phases of the life of PADME, starting with the assembly of the main calorimeter, participating actively in data taking periods, and studying the quality of the data, with particular attention to the level of beam background and pileup in the ECAL detector. The description of the different beam configurations is given in Chapter 3, where some MC studies done to understand the beam background and how to reduce it are also reported.

ECAL is the main calorimeter of PADME composed of 616 BGO crystals with an inner hole of 5×5 cm^2 and an outer radius of 30 cm. The central hole is designed to prevent the high rate of forward Bremsstrahlung photons from swamping the BGO calorimeter. These photons reach the small-angle colorimeter located behind the ECAL hole. In the design phase, the probability to have two photons hitting the same ECAL crystal was deemed very small. Therefore, the photon reconstruction was developed to reconstruct only one signal per channel per event. The first data taking showed the limitation of this assumption and I made an effort to develop a multi-hit reconstruction for ECAL. In this thesis work, this novel reconstruction algorithm, based on a template for a single BGO pulse, is presented, describing in detail all the problems observed and how they were fixed. Chapter 4 contains the description of the original single-hit signal reconstruction followed by the hit clusterization algorithm, then the multi-hit template fitting is introduced, and compared to the single hit reconstruction. The multi-hit ECAL reconstruction is currently the default ECAL signal reconstruction adopted by the experiment. To have the same reconstruction also for MC, I developed the software to simulate the ECAL waveforms in PADME MC, with all features observed in data. The waveform simulation process is described in the same Chapter.

A crucial goal for the experiment is to reach a good understanding of the Standard Model process of electron-positron annihilation in two photons $e^+e^- \to \gamma\gamma$ observed in the main calorimeter ECAL. This theoretically well known QED process allows to calibrate the experimental apparatus and to obtain a physics monitor for the beam intensity. The main topic of this thesis where the first measurement of the cross section for this process at the PADME energy scale $\sqrt{s} = 21$ MeV is reported. For the determination of the annihilation yield, the acceptance and the photon reconstruction and identification efficiency deep studies were done with MC and data and summarised in Chapter 5. The most crucial step of the analysis is represented by the measurement of the efficiency for identifying photons from the annihilation process. This measurement needs to be done in data, to properly take into account the features of the PADME calorimeter, beam, and background conditions. On the other hand, the experimental apparatus has no redundancy for the detection of photons, therefore an ad-hoc data-driven method is developed to measure the photon efficiency. It is an original variation of the usual "Tag-and-Probe" technique which exploits only the ECAL detector and the constrained annihilation kinematics. The method was validated using special MC samples, which allowed to verify the correctness of the measured efficiency. Finally, the analysis was performed on seven selected runs from the RunII data taking for a total of 4×10^{11} POT of good quality data deriving the photon efficiency and selecting a sample of annihilation events. From these results, the measurement of the annihilation cross section was obtained along with a careful assessment of the systematic errors. The final chapter is devoted to a quantitative and critical discussion of the sensitivity to the dark photon signal of the current PADME data, in comparison with the design goal anticipated in the proposal, where no beam background was considered.

1

Dark Matter and Dark Photon

The existence of Dark Matter (DM) is a well established fact since many decades, thanks to the observation of several effects that can be interpreted as effects of gravitational interaction of dark matter with ordinary matter in the Universe. However, our knowledge of the nature of Dark Matter is still rather incomplete. For this reason today the investigation of Dark Matter, from its origin to its composition, and the way it interacts with the ordinary matter, apart from gravity, play a crucial role in fundamental science. Huge and ambitious efforts have been devoted in the last years to its identification, concentrating especially on the search of the so called Weakly Interacting Massive Particles at the electroweak scale. However, no positive results have been achieved so far. Therefore, it appears necessary to introduce new ideas and models. An intriguing hypothesis is that the Dark Matter constituents are neutral with respect to Standard Model interactions, but they interact through a new, still unknown, force due to an "hidden" charge. This new symmetry would be mediated by a massive abelian gauge boson, the dark photon, which is expected to couple to the Standard Model particles via a kinetic mixing with the photon. The search for such a massive mediator has been pursued with large enthusiasm in the latest years, since many experiments can re-interpreted their data to probe this model.

1.1 Origin of the universe

The formulation of the Big-Bang model dates back to 1940 with the work of George Gamow and his collaborators, Ralph Alpher and Robert Herman. In order to account for the possibility that the relative abundances of the elements had a cosmological origin, they proposed that the early Universe was very hot and dense (enough to allow the nucleosynthesis of light elements), and has subsequently expanded and cooled to its present state [1], [2]. In 1948, Alpher and Herman predicted that a direct consequence of this model is the presence of a relic background radiation with a temperature of the order of a few K [3],[4]. This radiation was observed 16 years later and it is known as the Cosmic Microwave Background (CMB) [5]. Indeed, this observation determined the big success of the Big-Bang model as candidate description of the early Universe.

The cosmological equations of motion are:

$$H^2 \equiv \left(\frac{\dot{R}}{R}\right) = \frac{8\pi G_N \rho}{3} - \frac{k}{R^2} + \frac{\Lambda}{3} \tag{1.1}$$

and

$$\frac{\ddot{R}}{R} = -\frac{4\pi G_N}{3}(\rho + 3p) \tag{1.2}$$

where H is the time dependent Hubble parameter, Λ is the cosmological constant interpreted as a vacuum energy density, p is the isotropic pressure, ρ is the energy density, k is the curvature constant, $R(t)$ is the expansion parameter and G_N is the gravitational constant. Assuming energy conservation, a third equation can be written:

$$\dot{\rho} = -3H(\rho + p). \tag{1.3}$$

By interpreting $-\frac{k}{R^2}$ Newtonianly as a "total energy", then we see that the evolution of the Universe is governed by a competition between the potential energy, $\frac{8\pi G_n \rho}{3}$, and the kinetic term $\frac{\dot{R}}{R}$. It can be shown that for $\Lambda = 0$ the Universe must be expanding or contracting. The ultimate fate of the Universe is determined by the curvature constant k. For $k = +1$, the Universe will recollapse in a finite time, whereas for $k = 0$ and $k = -1$, the Universe will expand indefinitely. These simple conclusions can be altered if $\Lambda \neq 0$ or if some component of the universe leads to $(\rho + 3p) < 0$.

The Friedmann Equation 1.1 can be used to define a critical density such that $k = 0$ when $\Lambda = 0$

$$\rho_c \equiv \frac{3H^2}{8\pi G_N} = 1.88 \times 10^{-26}\ \mathrm{h^2 kgm^{-3}} = 1.05 \times 10^{-5}\mathrm{h^2 GeVcm^{-3}} \tag{1.4}$$

where the Hubble parameter is defined as $H = 100\ \mathrm{hkms^{-1}Mpc^{-1}}$. The ratio between the energy density and the critical density is defined as $\Omega_t = \frac{\rho}{\rho_c} = \frac{8\pi G_N \rho^2(t)}{3H(t)^3}$. Since ρ and H depend on time, Ω will have different values for each Universe epoch. The Friedmann equation becomes:

$$\frac{k}{R^2} = H^2(\Omega_t - 1). \tag{1.5}$$

From equation 1.5 several interesting considerations can be derived: when $\Omega_t > 1$, $k = +1$ and the Universe is closed, when $\Omega_t < 1$, $k = -1$ and the Universe is open, if $\Omega_t = 1$, $k = 0$, and the Universe is spatially flat. It is often necessary to distinguish different contributions to the density. It is therefore convenient to define present-day density parameters for pressureless matter (Ω_m) and relativistic particles (Ω_r), plus the quantity $\Omega_\Lambda = \frac{\Lambda}{3H^2}$ that represent the vacuum energy density. The Friedmann equation, for present-day values, can be written as

$$\frac{k}{R_0^2} = H_0^2(\Omega_m + \Omega_r + \Omega_\Lambda - 1) \tag{1.6}$$

thus, it is the sum densities of matter, relativistic particles, and vacuum that determines the overall sign of the curvature.

Most recent measurements indicate that vacuum energy is indeed the largest contributor to the cosmological density budget, with $\Omega_\Lambda = 0.685 \pm 0.007$ and $\Omega_m = 0.315 \pm 0.007$, assuming $k = 0$ [6]. The vacuum energy is better known as dark energy. Observations with telescopes and measurements from astronomical experiments provide information regarding luminous and non-luminous matter: from these observations, the density of baryonic matter (visible and invisible) can account for about 5% of the total matter.

1.2 Origin of the dark matter

Several anomalous effects have been observed over the years in many astronomical and cosmological measurements.

1.2.1 Astronomical anomalies

Coma cluster

In 1933, F. Zwicky used, for the first time, the viral theorem to infer the existence of unseen matter. He measured the radial velocities of member galaxies in the Coma cluster (that contains about 1000 galaxies) and the cluster radius from the volume they occupy. With these data he could compare the total mass, deduced from the viral theorem, and the visible mass, which was much less abundant [7]. The investigation of the rotation velocity of spiral galaxies, made by Vera Rubin and Kent Ford (1970) [8], confirmed Zwicky results.

Taking into exam the Andromeda Galaxy, Rubin focused her attention on star motion inside the galaxy. Starting from kinematic considerations

$$m\frac{v^2}{r} = \frac{mM(r)G_N}{r^2} \tag{1.7}$$

where m is the mass of a star, v its rotation velocity, r its distance from the galactic center and $M(r)$ the mass inside the sphere of radius r. The equation predicts that $v \propto \sqrt{r}$. What Rubin observed was not in agreement with the theory: the velocity was indeed constant, independently of the galactic center distance. Similar results have been found also for other galaxies; for example in Figure 1.1 fit to the rotation galaxy curves of NGC 2903 e NGC 3198 are presented. Each non solid-line curve represents a different contribution to the radial velocity (dark matter halo, galactic disk and gas) [9].

Small galaxy groups emitting X-rays

There are examples of groups formed by a small number of galaxies which are enveloped in a large cloud of hot gas Intra Cluster Medium (ICM),which is visible through its X-ray emission. If it is assumed that the electron density distribution associated with the X-ray brightness is in hydrostatic equilibrium, it is possible to estimate the ICM radial density profiles. The amount of matter in the form of hot gas can be deduced from the intensity of this radiation. Adding

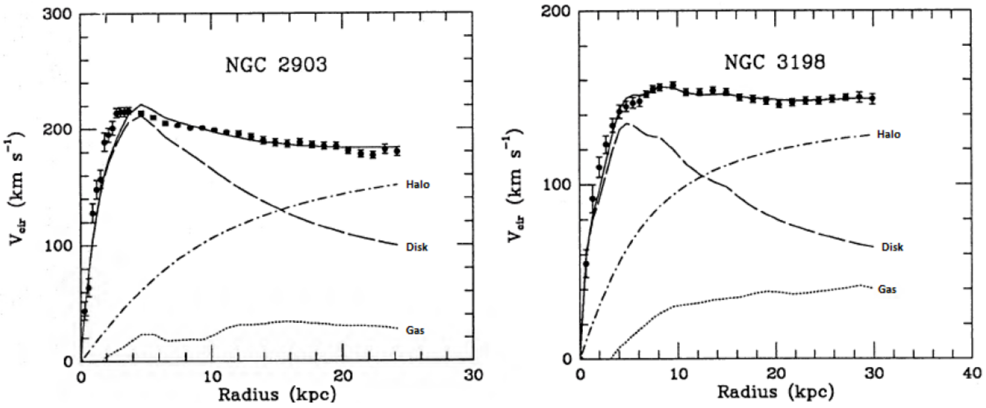

Figure 1.1: *Rotation curves of NGC 2903 e NGC 3198. Curves not represented with solid lines are different contribution to the velocity (dark matter halo, galactic disk and gas) [9].*

the gas mass to the observed luminous matter, the total amount of baryonic matter, M_b, can be estimated [10]. The temperature of the gas depends on the strength of the gravitational field, from which the total amount of gravitating matter, M_{grav}, in the system can be deduced. In many such small galaxy groups one finds $M_{grav}/M_b \geq 3$, thus a dark halo must be present. In the M_{grav} estimation there are several uncertainties due to the presence of the dark energy, thus the velocity can be overestimated. On the scale of large clusters of galaxies like the Coma, it is generally observed that dark matter represents about 85% of the total mass and that the visible matter is mostly in the form of a hot ICM.

Strong and weak lensing

A consequence of the Strong Equivalence Principle (SEP) is that a photon in a gravitational field moves as if it was massive, and therefore light rays bend around system of large mass. Thus celestial bodies can serve as gravitational lenses probing the gravitational field, produced either by baryonic or non barionic dark matter. If the mass of the lensing object is very small, one will merely observe a magnification of the brightness of the lensed object, an effect called microlensing.

Weak Lensing refers to deflection through a small angle when the light ray can be treated as a straight line and the deflection occurs discontinuously at the point of closest approach (the analog of thin-lens approximation in optics). In Strong Lensing the photons move along geodesics in a strong gravitational potential which distorts space as well as time, causing larger deflection angles and requiring the full theory of General Relativity GR. The images in the observer plane can then become quite complicated because there may be more than one geodesic connecting source and observer; it may not even be possible to find a unique mapping onto the source plane. A scheme of the two lensing image kinds are represented in Figure 1.2 (a): on the left the light source star, in the middle the non-luminous matter and on the right the observer at different positions with the relative star image after the light deflection. Figure 1.2

(b) shows a strong lensing image recorded by Hubble Space Telescope [11].

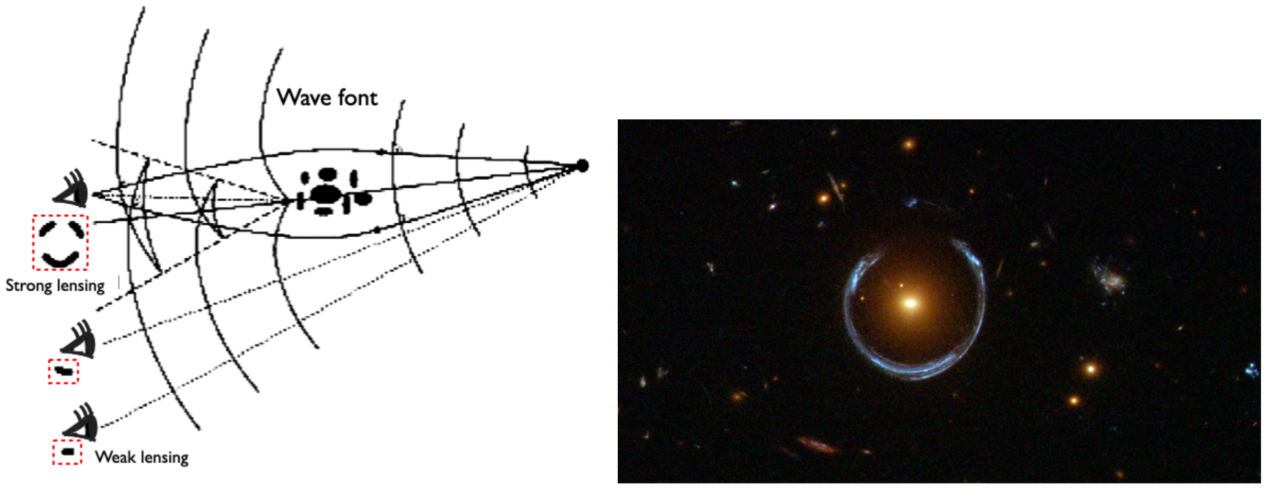

(a) (b)

Figure 1.2: *On the left: strong lensing effect (top pattern), and two weak lensing effect (middle and bottom patterns). On the right: a Hubble Space Telescope image recording a strong lensing effect [11].*

Merging galaxy clusters

A direct empirical proof of the existence of dark matter is furnished by the observations of the 1E0657-558 cluster merger [12]. After the collision of two large galaxy clusters, the dissipationless stellar component and the fluid-like X-ray emitting plasma appear spatially separated because the dense plasma blobs are slowed down by the electromagnetic interactions taking place in the crossing, while the sparse galaxy distributions are almost unaffected in the collision. The gravitational potential inferred by weak and strong lensing effects does not match the plasma distribution, which is the dominant baryonic mass component, but rather approximately traces the distribution of galaxies, Figure 1.3. The center of the total mass is offset from the center of the baryonic mass peaks, proving that the majority of the matter in the system is unseen and feebly self-interacting.

1.2.2 Cosmological anomalies

Cosmic Microwave Background (CMB)

Cosmic Microwave Background (CMB), discovered in 1965 by Arno Penzias and Robert Wilson, is the residual of the thermal and isotropic Big Bang radiation [4]. Observations show that the CMB contains temperature scalar anisotropies at the 10^{-5} level and polarisation anisotropies at 10^{-6} level [13], over a wide range of angular scales. These anisotropies are usually expressed

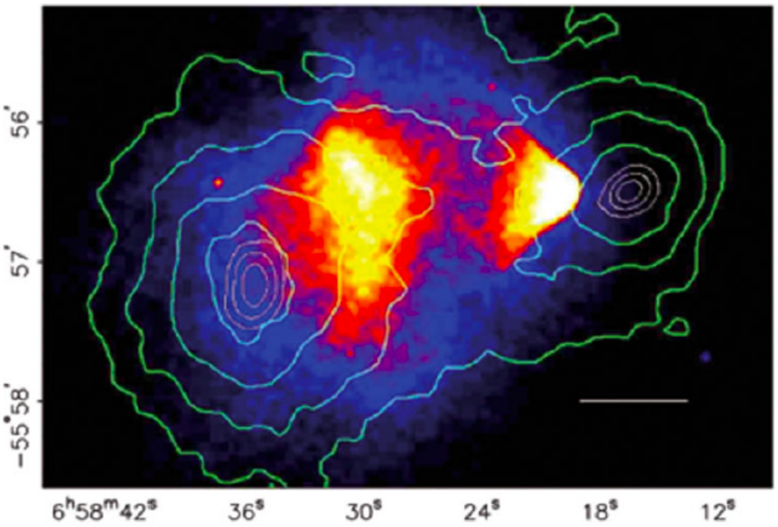

Figure 1.3: *The merging cluster 1E0657-558. On the right is the smaller "bullet" cluster which has traversed the larger cluster. The colors indicate the X-ray temperature of the plasma: blue is the coolest and the white is the hottest. The green contours are the weak lensing reconstruction of the gravitational potential of the clusters [12].*

using a spherical harmonic expansion of the CMB sky:

$$T(\theta, \phi) = \sum_{lm} a_{lm} Y_{lm}(\theta, \phi). \tag{1.8}$$

The variations in the CMB temperature map at higher multipoles ($l \geq 2$) are interpreted as being mostly the result of perturbations in the density of the early Universe, manifesting themselves at the epoch of the last scattering of the CMB photons. Therefore, by measuring a_{lm}, we are learning directly about physical conditions in the early Universe. There has been a steady improvement in the quality of CMB data that has led to the development of the present-day cosmological model. The most robust constraints currently available come from the Planck satellite [14] [6], although data at smaller-scale from the ACT (Atacama Cosmology Telescope) [15] and SPT (South Pole Telescope) [16] experiments are beginning to add useful constrain power. Figure 1.4 displays the power spectrum estimates from these experiments, along with WMAP (NASA's Wilkinson Microwave Anisotropy Probe) data [17]. The spectrum is in good agreement with the Lambda-Cold Dark Matter (ΛCDM) model. The position of the first peak determines $\Omega_m h^2$. Combining the 5-year WMAP measurements of the temperature power spectrum with determinations of the Hubble constant h, the WMAP team found a total mass density parameter $\Omega_m \sim 0.26$ [18]. The ratio of amplitudes of the second-to-first peaks determines a baryonic density parameter $\Omega_b \sim 0.04$, which implies that the dark matter component is $\Omega_{DM} \sim 0.22$. These results bring relevant insight on the universe content: since $\Omega_{Tot} = 1$, a large component $\Omega_\Lambda \sim 0.74$ is missing and it is of unknown nature (*dark energy*); the ordinary barionic matter is only a small fraction of the universe matter, the rest in unknown.

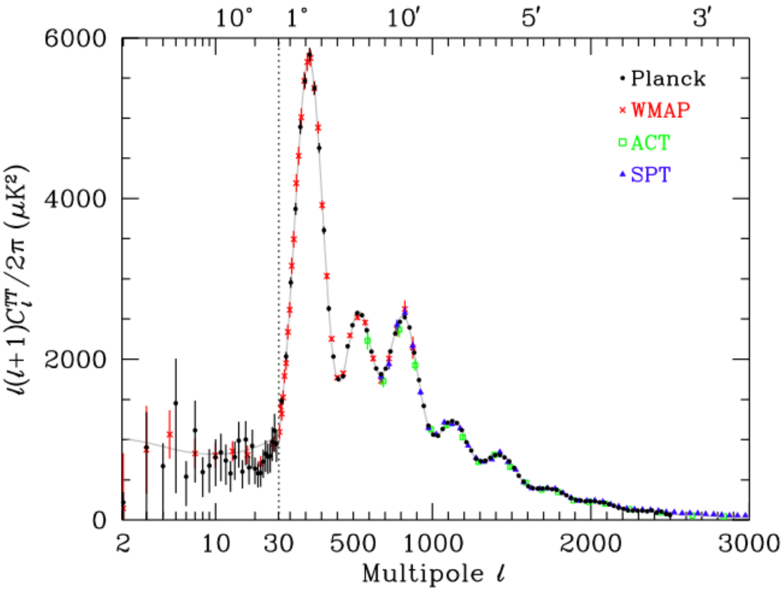

Figure 1.4: *CMB temperature anisotropy band-power estimates from the Planck, WMAP, ACT, and SPT experiments, the curve plotted is the best-fit Planck ΛCDM model [13].*

Baryonic acoustic oscillations

On smaller, with respect to the CMB fluctuations scale, we observe in the Universe inhomogeneities in the forms of galaxies, galaxy groups, and galaxies clusters. The common approach to describe this situation is to use the non-relativistic hydrodynamics and treat matter in the Universe as an adiabatic, viscous, non-static fluid, where random fluctuations around the mean density, manifest themselves as compressions in some regions and rarefactions in other (Baryonic acoustic oscillations BAO). The origin of these density fluctuations lies on the tight coupling existing before decoupling between radiation and charged matter, causing them to oscillate in phase. Inflationary models predict that the primordial mass density fluctuations should be adiabatic, Gaussian, and should exhibit the same scale invariance as the CMB fluctuations. The BAO can be treated similarly to CMB, they are defined in terms of the dimensionless mass autocorrelation function, which is the Fourier transform of the power spectrum of a spherical harmonic expansion. The power spectrum is shown in Figure 1.5 [19]. As the Universe approached decoupling, the photon mean free path increased and radiation diffused from overdense regions into underdense ones, thereby smoothing out any inhomogeneities in the plasma. The situation changed dramatically at recombination, 380000 yr after Big Bang, when all the free electrons suddenly disappeared, captured into atomic Bohr orbits, and the radiation pressure almost vanished. From that point the BAO and the CMB continued to oscillate independently, but adiabatically, and the density perturbations, which have entered the Hubble radius, reflect today into baryonic structures.

Since the scale of BAO depends on Ω_m and on the Hubble constant h, one can extract from the oscillation amplitudes $\Omega_m \sim 0.25$, thus $\Omega_\Lambda \sim 0.75$ [19] in agreement with the indications

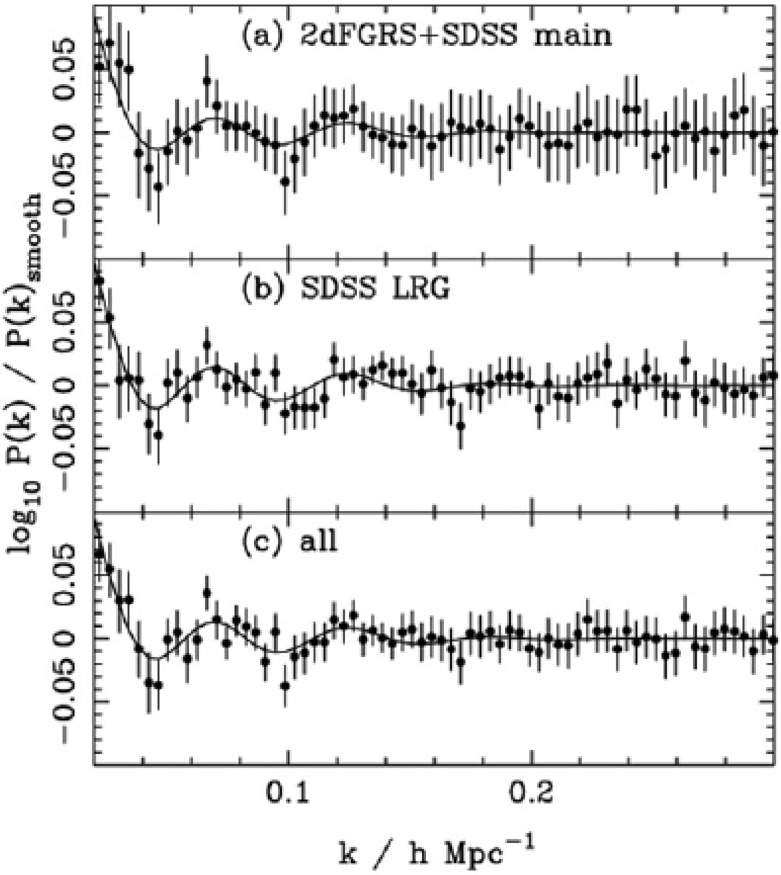

Figure 1.5: *BAO power spectra calculated from (a) the combined SDSS and 2dFGRS main galaxies, (b) the SDSS DR5 LRG sample, and (c) the combination of these two samples [19].*

coming from the CMB temperature anysotropy.

Big Bang nucleosynthesis

The study of the production of light nuclei during the early phases of the Big Bang can provide information regarding the composition of the Universe [20]. Predictions of the abundances of the light elements, D, ^3He, ^4He and ^7Li synthesized at the end of the first three minutes, are in good overall agreement with the primordial abundances inferred from observational data, thus validating the standard hot Big-Bang cosmology. The synthesis of the light elements is sensitive to physical conditions in the early, radiation dominated, era at a temperature $kT \sim 1$ MeV ($t \sim 1$ s). At higher temperatures, weak interactions were in thermal equilibrium, thus fixing the ratio of the neutron and proton number densities to be $n/p = e^{-Q/T}$, where $Q = 1.293$ MeV is the mass difference of neutron and proton. This ratio has been close to unity until neutrinos weak processes were in thermal equilibrium. As soon as the temperature dropped to $kT \sim 3$ MeV, neutrinos went out of the equilibrium, and nucleosynthesis began with the formation of deuteron $p(n,\gamma)D$. The nucleosynthesis chain begins with the formation of deuterium in the process. After deuteron, the formation of ^3He, ^4He, ^7Li and ^7Be took place. At this stage, while the Universe was expanding and cooling, most of neutrons were bound in atom nuclei. The most relevant fraction of the elements produced during Big Bang nucleosynthesis did not change with time: the contribution given by nuclear reaction in stars is negligible.

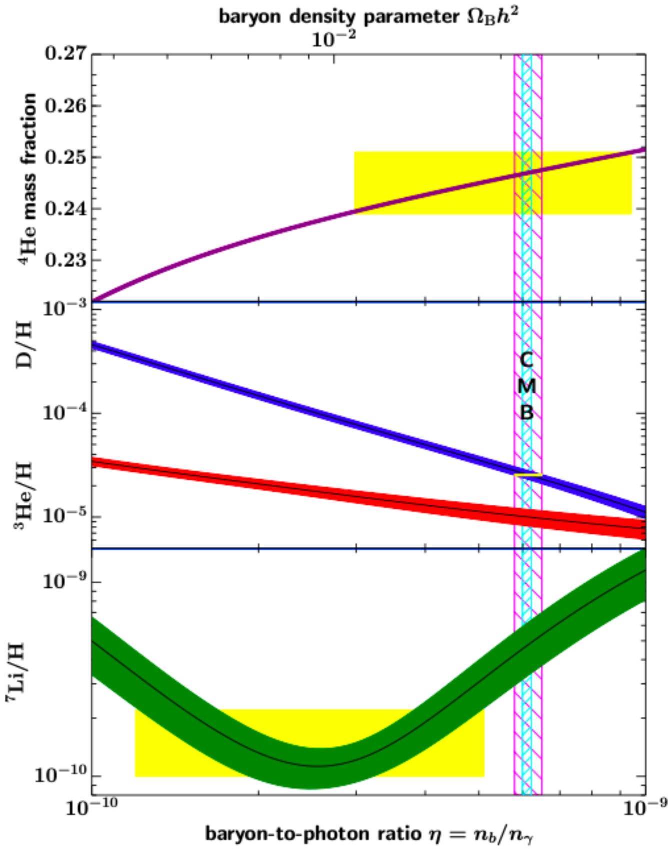

Figure 1.6: *The primordial abundances of D, ^3He, ^4He and ^7Li as predicted by the standard model of Big-Bang Nucleosynthesis (BBN) — the bands show the 95% CL range [21]. Boxes indicate the observed light element abundances. The narrow vertical band indicates the CMB measure of the cosmic baryon density, while the wider band indicates the D+^4He of BBN concordance range (both at 95% CL) [13].*

Figure 1.6 shows the predicted elements abundances as a function of n_b/n_γ, where n_b is the density of baryon and n_γ is the relic black-body photon density. With n_γ fixed by the present CMB temperature of 2.7255 K, the baryon mass density today can be extracted $n_b = (3.9 - 4.6) \times 10^{-31}$ gcm^{-3}, or interpreted as a baryonic fraction of the critical density, $\Omega_b = \rho_b/\rho_c \simeq \eta_{10} h^{-2}/274 = (0.021 - 0.024)h^{-2}$. The measurements of D and ^3He abundance are in agreement with the CMB measurements of Ω_b. This is a major success for the standard cosmology, and inspires confidence in extrapolation back to such early times. The inconsistency on ^7Li is known as *Lithium problem*, and could arise from systematic errors in the observed abundances, and/or uncertainties in stellar astrophysics or nuclear inputs, whether there might be new physics [22].

Large Scale Structures simulation

In the ΛCDM paradigm, the non-linear growth of dark matter structures is a well-posed problem where both, the initial conditions and the evolution equations, are known. The Aquarius Project [23] is a Virgo Consortium programme carrying out high-resolution dark matter simulations of Milky-Way-sized halos in the ΛCDM cosmology. This project seeks clues to the formation of galaxies and to the nature of the dark matter by designing strategies for exploring the formation of our Galaxy and its luminous and dark satellites. The galaxy population on scales from 50 kpc to the size of the observable Universe has been predicted by hierarchical ΛCDM scenarios, and compared directly with a wide array of observations. So far, the ΛCDM paradigm has passed these tests successfully, specifically those that consider the large-scale matter distribution and has led to the discovery of a universal internal structure for dark matter halos. Given this success, it is important to test ΛCDM predictions also on smaller scales, because these are sensitive to the nature of the dark matter. Indeed, a number of serious challenges to the paradigm have emerged on the scale of individual galaxies and their central structure. In particular, the abundance of small dark matter subhalos predicted within CDM halos is much larger than the number of known satellite galaxies surrounding the Milky Way.

1.2.3 Nuclear anomalies

Muon anomalous magnetic moment

The magnetic moments of the electron and muon predicted by the free Dirac equation are

$$\mu_l = g_l \left(\frac{q}{2m_l} \right) \vec{s} \tag{1.9}$$

where $g_l = 2$ is the gyromagnetic ratio for $l = e, \mu$. From quantum electrodynamics, a small deviation of g_μ is predicted, arising from quantum loops. This deviation is named the anomalous magnetic moment and can be written as:

$$a_\mu = \frac{g_\mu - 2}{2}. \tag{1.10}$$

The SM prediction for a_μ can be calculated as the sum of three terms:

$$a_\mu^{SM} = a_\mu^{QED} + a_\mu^{EW} + a_\mu^{HAD} \tag{1.11}$$

where a_μ^{QED} includes photonic and leptonic loops, a_μ^{EW} is the contribution from $W^\pm, Z$ and Higgs particles, and a_μ^{HAD} contains quark and gluon loops corrections. The g-2 muon Experiment at Fermilab measures the muon magnetic moment [24] founding a difference between experiment and Standard Model prediction equal to: [24]:

$$\Delta a_\mu(FNAL) = 116592040(54) \times 10^{-11} (0.46 \text{ ppm}) \tag{1.12}$$

with a significance of 3.3σ. Adding the results for μ^+ and μ^- from other experiments seems to increase the tension between experiment and theory to 4.2 standard deviations. The existence of new particles contributing to new quantum corrections might justify this discrepancy. However, a long standing scrutiny of the SM predictions, and in particular of the hadronic virtual corrections to the muon anomalous magnetic moment, is still ongoing and may eventually cure the discrepancy.

Beryllium-8 and Helium-4 anomaly

Two excited states (17.64 MeV and 18.15 MeV) of the ^8Be nucleus can be obtained by proton irradiation of a ^7Li nucleus. These states will de-excite with the emission of a e^+e^- pair (Internal Pair Production). The angular correlation of the charged particles produced have been studied by the Institute for Nuclear Research, Hungarian Academy of Sciences (ATOMKI) [25]. A 5 MeV proton beam, accelerated by Van de Graaff accelerator in Debrecen, was used. The pairs were detected by plastic detector telescopes, in combination with multiwire proportional counters, in order to detect both energy and position of the emitted e^+e^-. A slight deviation on the number of pairs was observed at around 140° for the resonant capture of proton, see Figure 1.7 (a). A second measurement has been published by the ATOMKI group [26] based on the studies made with ^4He exited states. Also in this case, a small peak has been observed in the angular correlation of e^+e^- pair production, see Figure 1.7 (b). The excess observed cannot be explained in terms of nuclear interactions. A possible explanation relies in the hypothesis of a new interaction: in a small fraction of the decays a new particle of about 17 MeV mass decaying to e^+e^- pairs is produced, the kinematics of the e^+e^- pair is consistent with the observations.

1.2.4 Properties of dark matter candidates

Electric charge

The "darkness" of DM can be quantified based on constraints from the CMB and large-scale structures: if DM were charged, or "milli-charged", it would impact the baryon-photon plasma during recombination; in particular, DM density fluctuations can be suppressed by radiation pressure and photon diffusion, additionally altering the baryon acoustic peak structure. The most stringent constraints, on dark matter charge q', derived by the requirement that the DM is completely decoupled from the baryon-photon plasma at recombination, are [27]:

- if $m_{DM} > 1$ GeV, then $q' < 3.5 \times 10^{-7}(m_{DM}/1\ \mathrm{GeV})^{0.58}\mathrm{q_e}$;
- if $m_{DM} < 1$ GeV, then $q' < 4.0 \times 10^{-7}(m_{DM}/1\ \mathrm{GeV})^{0.35}\mathrm{q_e}$,

where q_e is the electron electrical charge.

Self interaction

Observations of merging clusters [28] and of the ellipticity of certain galaxies as inferred from X-rays [29] constrain the level of DM-DM self interactions. The Figure of merit is the ratio

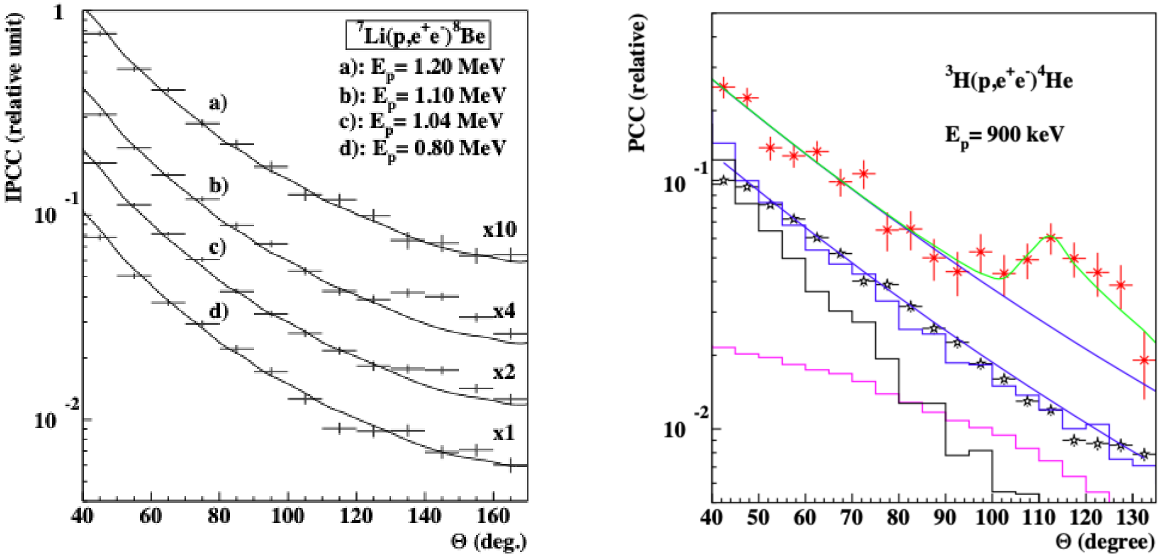

(a) (b)

Figure 1.7: *Left: Measured angular correlations of the* e^+e^- *pairs produced in the* ${}^7Li(p,\gamma)^8Be$ *reaction (dots with error bars) compared with the theoretical nuclear predictions (full curves) [25]. Right: Angular correlations for the* e^+e^- *pairs produced in the* ${}^3H(p,\gamma)^4He$ *reaction. Red dots are data in the signal region (sum of positron and electron energies between* 19.5 *and* 22 MeV*), and black dots are data in the orthogonal region (sum of energies between* 5 *and* 19 MeV*). The smooth blue curve is a fit to the orthogonal region data, which is then re-scaled to to be used as background estimation in the signal region. The blue, black, and magenta histograms are Monte Carlo simulations of expected backgrounds. The green curve is a fit to the data with the hypothesis of a new "*X_{17}*" particle [26].*

of the DM-DM cross section and the DM mass [30], $\sigma(DM - DM)/m_{DM} < 0.47\ \text{cm}^2/\text{g} \simeq 0.84$ barn/GeV at 95% C.L..

Mass: Lower Limits

Observations of the velocity dispersion (or, equivalently, measurements of the enclosed mass) and physical density in dwarf galaxies, lead to a lower limit on *fermionic* DM masses, sometimes known as the Tremaine-Gunn limit [31]. Using the Fornax dwarf [32] can be extracted that $m_f > 70$ eV. In the case of *bosonic* DM, the Compton wavelength of an ultra-light species might erase small-scale structure, in conflict with CMB and large-scale structures [33]. Lyman-α lines observations [34] [35], measurements of high-redshift galaxy luminosity functions and the Milky Way satellite luminosity function [36] [37] indicate that $m_b \geq 10^{-22}$ eV.

Mass: Upper Limits

General upper limits exist on the mass of the DM constituents from the stability against disruption of structures immersed in DM halos, such as galactic disks and globular clusters, and of individual small galaxies. The most stringent limits can be derived using halo wide binary stars [38] and the stability of the star clusters within Eridanus II [39]. Such limits constrain an individual, point-like DM constituent, assuming it makes up 100% of the DM, to be lighter than around $5 \times M_{\odot}$.

Stability

An indication on the DM lifetime was done assuming decays into relativistic particles. The model tested was compared with cosmological data from Planck, WMAP, WiggleZ and Baryon Acoustic Oscillations. The DM lifetime was found be long compared to cosmological timescales at 95% confidence level [40].

1.2.5 Dark matter models

According to the observations, many hypotheses have been made regarding the nature of DM. The first distinction can be made between baryonic DM and non-baryonic DM. The first one can be responsible for large structures, called Massive Astrophysical Compact Halo Objects (MACHOs) [41]. Nevertheless, gravitational observations show that their contribution on total DM mass is not enough to reach the predictions. From CMB and Big Bang nucleosynthesis studies, most DM particles seem to be non-baryonic, produced during the first phases of the Universe and subject at least to gravitational interaction. A second distinction can be operated on the basis of DM velocity at the time of decoupling between matter and radiation ($T_{dec} = 3000K$). Hot Dark Matter (HDM) particles are the ones that were relativistic at decoupling era, while Cold Dark Matter (CDM) particles are the ones that were not. Neutrino is one of the most prominent candidate for HDM, nevertheless CMB studies show that CDM is the largest fraction of DM in the Universe.

The best motivated DM candidates are the WIMP (Weak Interacting Massive Particles), massive particles ($\sim 10^2$ GeV), interacting weakly and gravitationally with the known matter. Despite the enthusiasm in these new particles hypothesis, severe constraints were put on these models [42]. This scenario motivates the investigation of other dark matter hypothesis. A possible model is the introduction of a new hidden sector with new interactions. This could justify the dynamics of the galactic structure formation, the dark matter abundance and it could also represent the solution for some of the known unsolved discrepancies between experiments and SM predictions, like the anomalous magnetic moment of the muon. The connection between the ordinary and the dark sector can be possible through a neutral portal, a particle that possesses the quantum numbers of the dark sector and is weakly coupled to a neutral particle of the ordinary sector. Depending on the theory that predicts this new mediator, one can have different Lagrangian terms, consequently mediators with different characteristics:

- Scalar mediator ϕ: dark Higgs, interact with the SM Higgs boson [43]. The best way to search this particle is studying the decays and the properties of the ordinary Higgs boson. The interaction between the dark and SM Higgs happens via the Lagrangian term:

$$L_{int} = (\mu\phi + \lambda\phi^2)H^{\dagger}H; \tag{1.13}$$

- Axion (pseudo-scalar) portal a: a particle with properties comparable to the Goldstone boson related to the broken symmetry of Peccei-Quinn $U_{PQ}(1)$ [44]. This symmetry was introduced to explain the CP violation problem [45]. The interaction between the axion and the SM photon is given by:

$$L_{int} = \frac{a}{f_a} F_{\mu\nu}^{QED}; \tag{1.14}$$

- Fermionic mediator N with sterile neutrinos properties [46]. The neutrino mass origin puzzle opens the possibility to have neutrino as dark matter. The possible existence of the sterile neutrino could add a Yukawa term to the Lagrangian:

$$L_{int} \sim Y_N LHN \tag{1.15}$$

  where Y_N is the Yukawa constant, L is a lepton, H the Higgs boson and N is the sterile neutrino;

- Vector mediator A': including the dark photon case, that will be discussed in detail.

1.3 The dark photon hypothesis

The neutral portal vector is a representative case of a class of more general models in which a dark vector could couple with SM fermions in a different way, e.g. only with leptons and not with quarks or vice versa. These models predict the existence of an additional force field due to the existence of a new abelian gauge symmetry $U(1)$ and a corresponding gauge boson A', the dark photon. In the theory of Quantum Electrodynamics (QED), this can generate current-vector interactions

$$L \sim g' q_f \bar{\psi}_f \gamma^\mu \psi_f A' \tag{1.16}$$

where g' is the universal coupling constant of the new interaction and q_f is the dark charge of the interacting fermion. Not all particles of the standard model must be charged under this new $U(1)$ group, thus having in general a different (and sometimes non-existent) interaction for quarks or leptons. In fact, in case only the quarks have dark charge, the new gauge boson can be directly produced in hadronic collisions but not in leptonic collisions. The coupling constant g' and the charge q_f can be originated from direct interaction between the SM fermions and the new gauge field, or by the mechanism of "kinetic mixing". In this latest case the charge q_f of equation 1.16 is proportional to the fermion electric charge and to the kinetic mixing coefficient defined by the kinetic mixing Lagrangian term:

$$L_{int} = \frac{\epsilon}{2} F_{QED}^{\mu\nu} F_{\mu\nu}^{Dark}. \tag{1.17}$$

The associated coupling constant, ϵ, may be so small ($\sim 10^{-3}$) to preclude the discovery dark photon in many of the experiments.

Another possible mechanism is the mass mixing with the heavy Z boson, in which case the particle could have properties like those of Z and the appropriate place for its search is at high energy colliders such as the LHC.

1.3.1 Dark photon decays

The simple kinetic mixing structure of Equation 1.17 leads to a highly predictive theory. For example, under the assumption that the dark sector has no dark particle lighter than half the A' boson mass, the branching ratios of A' in particles of the Standard Model shown in Figure 1.8 are predicted by the model. Furthermore, if the mass of A' is smaller than that of a muon pair, A' can only decay into the e^+e^- pair. In this case, A' is expected to decay as a very narrow resonance with a total decay width equal to :

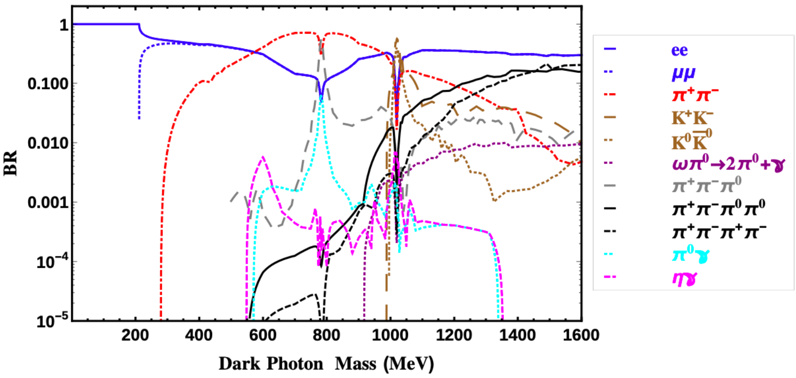

Figure 1.8: *Dark photon visible decay branching ratios [47].*

$$\Gamma_{A'} = \Gamma_{A'\to e^+e^-} = \frac{1}{3}\alpha\epsilon^2 m_{A'}\sqrt{1-\frac{4m_e^2}{m_{A'}^2}}\left(1-\frac{2m_e^2}{m_{A'}^2}\right) \tag{1.18}$$

with a decay time proportional to $\tau_{A'} \propto 1/(\epsilon^2 m_{A'})$. If instead the A' mass is large enough, it would decay in mesons with a width:

$$\Gamma_{A'\to had} = \frac{1}{3}\alpha\epsilon^2 m_{A'}\sqrt{1-\frac{4m_\mu^2}{m_{A'}^2}}\left(1-\frac{2m_\mu^2}{m_{A'}^2}\right)\cdot R_{had} \tag{1.19}$$

where R_{had} is the ratio of the hadron production cross section and $\mu^+\mu^-$ production cross section in e^+e^- annihilation evaluated at an energy equal to the dark boson A' mass.

If $m_{A'} > 2m_\chi$, where χ is a dark particle, A' will decay dominantly in dark particles since the coupling to standard model matter is suppressed by the square of epsilon parameter, thus the final state can not be visible in the detectors and indirect experimental techniques like those based on the missing energy or missing momentum analysis, need to be deployed.

If the dark sector has a single particle χ with mass $m_{A'} > 2m_\chi$ and coupling with A' thorough α_D, the decay width is:

$$\Gamma_{A'\to\chi\chi} = \frac{1}{3}\alpha_D m_{A'}\sqrt{1-\frac{4m_\chi}{m_{A'}^2}}\left(1-\frac{2m_\chi^2}{m_{A'}^2}\right). \tag{1.20}$$

This implies that, according to the mass hierarchy of the dark sector, the phenomenology can be distinguished in three scenarios. If $m_\chi > m_{A'}$, the dark photon will decay in SM particles with a $\Gamma \propto \epsilon^2$ and if $m_{A'} < 2m_\mu$ the only final state accessible is $A' \to e^+e^-$; if $m_{A'} > 2m_\chi$ the main decay mode will be $A' \to \chi\chi$ since it is not suppressed by the ϵ factor. A schematic representation of these scenarios are reported in Figure 1.9 .

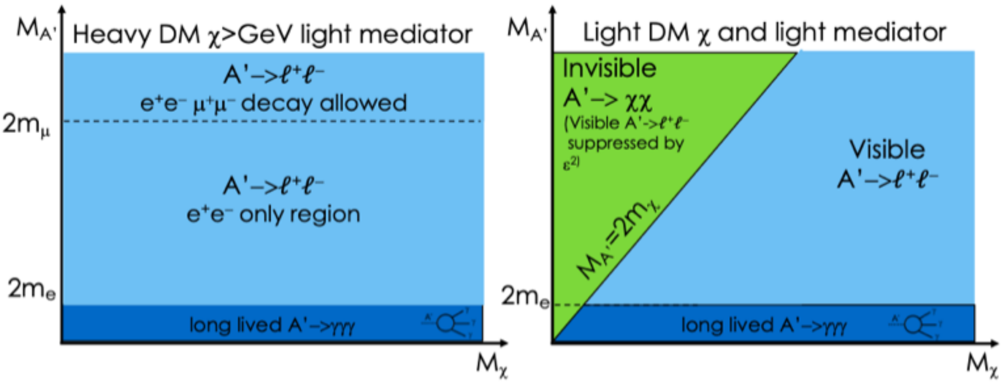

Figure 1.9: *Schematic representation of the dark photon decays as a function of the mass hierarchy.*

1.3.2 Dark photon mass

The mass term of the dark photon breaks the gauge invariance of the dark interactions and can be generated through different mechanisms [48]:

- The Higgs mechanism in the dark sector: the $U_D(1)$ symmetry might be spontaneously broken by the vacuum expectation value of an additional scalar field, "dark Higgs". The masses of dark Higgs and the dark photon would be of similar order. Then the additional terms to the "dark" Lagrangian after spontaneous symmetry breaking would be:

$$L_{mass} \sim \frac{1}{2} m_{A'}^2 A'_\mu A'^\mu + g' m_{A'} h' A'_\mu A'^\mu + \frac{1}{2} g'^2 h'^2 A'^2 \tag{1.21}$$

  where h' is the dark Higgs field and g' is the $U_D(1)$ coupling constant. Thus the interactions and the parameters of the dark photon could also be probed through searches for the hidden Higgs boson;

- The Stückelberg mechanism: The mass term of the gauge vector field A' could be introduced through an interaction term of A' with a scalar of the form:

$$L_{mass} \sim \frac{1}{2} (\partial^\mu \alpha + m A'^\mu)(\partial_\mu \alpha + m A'_\mu). \tag{1.22}$$

  In unitary gauge, this leads exactly to the well-known mass term for spin-1 field. The Stückelberg mechanism could also be viewed as a special case of the Higgs mechanism when the Higgs field mass (or more precisely the vacuum expectation value) goes to infinity. In this case there are no extra particles needed to have massive dark photon and the phenomenology of the processes does not change with respect to the simplest effective model;

- Interactions of the dark photon with the Standard Model Higgs: In principle it is theoretically possible to consider interactions of the Standard Model Higgs with the dark photon [49].

1.4 Dark photon search

1.4.1 Dark photon production

A variety of dark photon production mechanisms have been exploited in dark photon searches, which can be categorized as follows [34]:

- Bremsstrahlung, or A'-strahlung on nuclei, $e^{\pm}N \to e^{\pm}NA'$: dark photon production in lepton-on-target processes;
- Annihilation process, with positron beam, $e^+e^- \to \gamma A'$ in collider or in fixed target experiments;
- Neutral meson decays like π^0, η, ϕ e Υ. Mesons may be produced in fixed target experiments, e^+e^- colliders or jets in hadron colliders;
- Drell-Yan (DY), $q\bar{q} \to A' \to l^+l^-, h^+h^-$ at hadron colliders and at fixed target experiments with a proton beam.

1.4.2 Dark photon search strategy

A main distinction is made according to the A' decay, implying two main A' search groups. If the A' is the lightest dark matter particle, i.e., a DM particle with mass $m_{A'} > 2m_\chi$ does not exist, A' can only decay into SM particles. In this case, experiments are searching for A' through visible search technique. If DM particles with mass $m_{A'} > 2m_\chi$ exist, A' will mainly decay into DM particles, and SM particles decays are strongly suppressed. In the latter scenario, A' is commonly searched through the invisible channel.

1.4.3 Visible search techniques

The experimental methods used to search for dark photon decay in the visible channel are the following:

- beam dump experiments;
- fixed target experiments with bump-hunting;

- fixed target experiments with detached vertexing;
- colliders.

Visible search techniques exploit two characteristics of dark photon that distinguish it from SM photon: mass and decay time.

Beam dump experiments

The dump experiment technique exploits the fact that in the low-coupling region of the parameter space $(m_{A'}, \epsilon)$, A' is a long-lived particle. High energy beams are favoured due to relativistic enhancement of the A' lifetime in the laboratory frame. A beam-dump experiment consists in smashing a high intensity beam on a thick fixed target: the high current provides enough luminosity to probe very weak A' couplings. An electron/proton beam with energy E_0 impinges on the dump, producing A' mainly by A'-strahlung. A' can be identified by its decay products, l^+l^-, detected behind a massive shield. SM particles are absorbed by the dump and the shield, while neutral long-living particles do not interact: the detection of a pair of leptons with opposite charge behind the dump and the shield can be identified as the evidence of a new particle, if the rate is not compatible with the estimated background. The three parameters characterizing this kind of experiment are the beam energy, the length of the shield and the distance between the target and the detector.

Beam dump experiments can be classified into lepton beam and proton beam experiments. Lepton beam experiments cannot constraints leptophobic dark photon models (where the A' is barely coupled to leptons), while proton beam experiments cannot constrain leptophilic dark photon models (where the new boson have only tree-level couplings to leptons but not to gauge bosons or quarks). For this reason, these two techniques are complementary.

Electron beam dump experiments

- KEK: an experiment looking for neutral penetrating particles at the National Laboratory for High Energy Physics (KEK) in Japan (1986). A 2.5 GeV electron beam (1.69×10^{17} e$^-$) hits a tungsten target: after a 220 cm long decay region, a lead and plastic shield was placed. Multi-wire proportional chambers, scintillation counters and a lead glass Cherenkov counter were used as detectors. The experiment did not observe any signal [50];
- E141: an experiment designed to search for short lived axions at SLAC (1987). A 9 GeV electron beam (2×10^{15} e$^-$) hits a 12 cm tungsten target: a spectrometer was placed 35 m downstream of the dump, looking for positrons with energy $70\% - 90\%$ E_0. The shield was provided by lead and concrete, surrounding the beam pipe. The number of positrons subtracted from background and observed at different energies was obtained, on the basis of 3419 background events. No evidences for axions have been found with 95% C.L. [51];
- E137: an experiment searching for neutral metastable penetrating particles at SLAC (1988), using a 20 GeV electron beam (1.86×10^{20} e$^-$) on an aluminum target. The shield

was provided by a 179 m thick hill, followed by a 204 m long decay valley. An electromagnetic shower counter, perpendicular to the beam axis and with different dimensions depending on the phase of the beam, was used as detector. No candidates for axion-like events with energy above 3 GeV were observed [52];

- E774: an experiment searching for short-lived neutral bosons decaying into e^+e^- at Fermilab (1991). A 275 GeV electron beam (5.2×10^9 e$^-$) hit a 30 cm long tungsten calorimeter. The decay region was 2 m long, and four scintillation counters were placed behind the shield. A second electromagnetic calorimeter was used as trigger for the data taking, and it was placed 7.25 m downstream the dump. No eligible e^+e^- pair was found [53];
- Orsay: an experiment searching for light Higgs bosons at the Orsay linear accelerator (1989). A 1.6 GeV electron beam (2×10^{16} e$^-$) hit a 1 m long tungsten target, surrounded by lead shielding. Behind a 2 m long decay region, the detectors of the experiment (scintillation and lead-glass Cherenkov counters) were placed. No evidence of electrons/positrons with energy larger than 0.75 GeV were found [54].

Among the proton beam experiments, that could in the future contribute to the dark photon search, there are multi-purpose experiments such as: SeaQuest at FermiLab, SHIP, NA62 and FASER at CERN.

Bump-hunt experiments

The bump-hunt technique is relying on having A' as a massive particle. This technique exploits the reconstruction of the four-momentum of the A' decay products, e^+e^-, $\mu^+\mu^-$, to compute the final state invariant mass. Invariant mass of pairs originating from SM QED background, has a smooth distribution, while in the dark photon case it is equal to the A' mass. Contrary of dump experiments, where the background is normally negligible, but the lifetime limits the sensitivity to large couplings, bump-hunt experiment have good sensitivity to high couplings, but are limited by background. For this reason, the two techniques are complementary, and allow exploring very different region in the parameter space. Dark photon with masses in the GeV range can be produced efficiently by fixed-target and collider experiments. The production processes depend on the beam type. In electron-beam based experiments, the main production processes are A'-strahlung (fixed target) and annihilation (colliders). In proton-beam based experiments, the production is mainly obtained through meson decays, for example $\pi^0 \rightarrow A'\gamma$.

Electron-beam fixed target experiments

- A1: this experiment performed dark photon searches at the Mainz Microtron (2015). A variable energy (180 MeV to 885 MeV) electron beam hit an optimized target of tantalum foils. The couple e^+e^- produced after the decay of A' is detected by two spectrometers, equipped with different kind of detectors for particles identification. No significant signals for dark photon decay was observed [55];

- APEX: this experiment looked for the dark photon at the Jefferson Laboratories (2010). The experiment consisted in an electron beam hitting a thin tantalum target: two magnets with opposite polarity deflected charged particles into high resolution spectrometers, containing different kind of detectors measuring momentum and direction of the particles. The precise reconstruction of the e^+e^- invariant mass distribution heavily affects the sensitivity of the experiment. APEX data did not show any signal in the interval $(175 - 250)$ MeV, but an upper limit on ϵ has been set. A second run on a more sophisticated experimental setup has been performed in 2019, for which reconstruction of data is ongoing [56];

- HPS: it searches for the dark photon using a 1.056 GeV electron beam (50 nA) provided by the CEBAF accelerator at the Thomas Jefferson National Accelerator Facility (2015). The dark photon signal would appear as a resonance in the e^+e^- invariant mass distribution above the large QED background and as a displaced vertex search for long-lived dark photons. Engineering runs have been completed, and a physics run has been performed in 2019 [57];

Electron/positron colliders experiments

- KLOE and KLOE-2: KLOE was an experiment studying K_L^0 mesons decay at the Laboratori Nazionali di Frascati, by means of the e^+e^- collider of the laboratories DAϕNE (center of mass energy ~ 1.019 GeV). KLOE-2 was an upgraded version of the experiment. Dark photon physics have been performed on three different processes: $\phi \to \eta A'$, $e^+e^- \to A'$ and $e^+e^- \to A'h'$, where h' is a Higgs-like particle. For each of these processes, A' evidences can be found as a peak in the leptons invariant mass. No peaks were found in such distribution [59].

Proton/ions-beam based on fixed target

- NA48/2: it is a high intensity kaon experiment at CERN that explored the dark photon production in the reaction $\pi^0 \to A'\gamma \to e^+e^-\gamma$, assuming that A' only decays into SM fermions. A dark photon signal was searched in the interval $9 < m_{A'} < 120$ MeV . No evidences were found [61];

- HADES: an experiment searching for the dark photon at GSI (1994) using the beam from the heavy-ion synchrotron SIS18. A 3.5 GeV proton beam on a liquid hydrogen target or a solid niobium target to study hadron modifications in nuclear matter. The e^+e^- invariant mass distribution is the result of many different decays (π^0 , η , Δ). Dark photon searches did not provide evidences [62];

- PHENIX and ALICE: Mesons like π^0 , η ,ω can be produced in large amount from heavy ion collisions. Dark photon studies in heavy ion collisions have been performed by the PHENIX and ALICE collaborations. The PHENIX experiment, performed at the Brookhaven National Laboratories, searched for dark photon in $\pi^0 \to A'\gamma \to e^+e^-\gamma$ and $\eta \to A'\gamma \to e^+e^-\gamma$. An upper limit on ϵ^2 was obtained for dark photon masses up to

90 MeV [63]. The ALICE experiment at LHC searched for A' looking for e^+e^- pairs in data collected from RUN1. Upper limits from ALICE fall in the same region examined by PHENIX, and already populated by NA48/2 experiment [61].

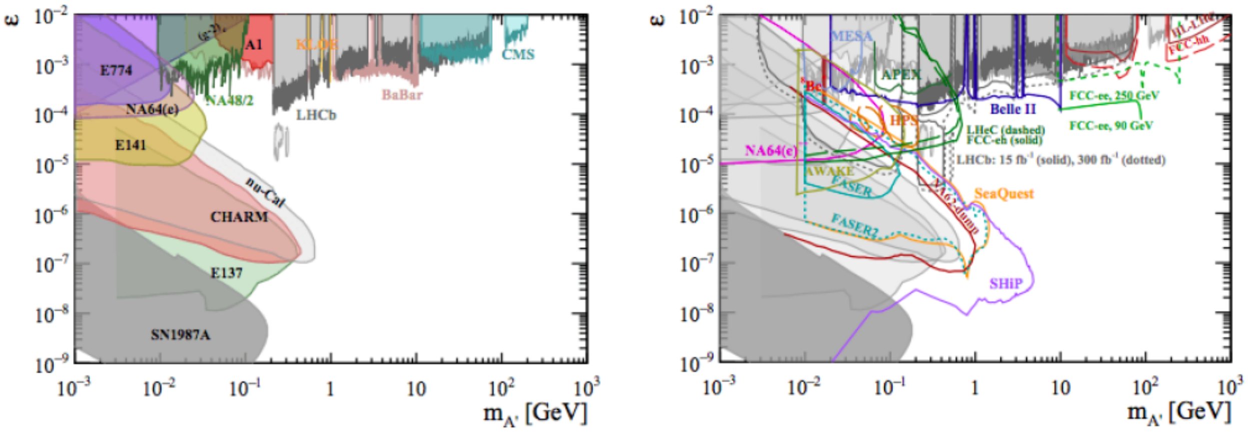

(a)

(b)

Figure 1.10: *On the left: Regions of the parameter space* $(M_{A'}, \epsilon)$ *excluded by different experiments looking for visible decay of the dark photon [64]. On the right: Perspectives in terms of exclusion regions of the parameter space* $(M_{A'}, \epsilon)$ *for visible decay of the dark photon from different future experiments [65].*

Limits from all visible search techniques are summarized in Figure 1.10 [64] [65]: the exclusion plots in the parameter space of dark photon mass $M_{A'}$ and coupling ϵ^2 are shown also for some of the described experiments. The features of the excluded area are connected to the experiment characteristic: if A' decays before the dump region, no information about dark photon can be obtained. Similarly, if A' lifetime is too long, the decay happens after the detector region. Concerning fixed target experiment, the main limit is given by the low center of mass energy. Colliders experiment, on the other hand, cannot explore low A' masses. The not excluded white region on the right bottom side of the plot is affected by a relevant background: one of the possibility to explore this region could be using the displaced vertex signature of e^+ and e^- [66].

1.4.4 Invisible search techniques

Under the assumption of $m_{A'} > 2m_\chi$ a large region of the parameter space is still unexplored. In this case, the branching ratio for the visible decays of A' are strongly suppressed with respect to invisible decays since the coupling between SM particles and A' is very weak with respect the coupling between A' and DM particles. Therefore, search techniques based on escaped particles will be used to detect the decay of A' in invisible particles. The experimental methods for the search of the invisible decay modes are based on inconsistencies with respect the SM prediction in the distributions of:

- missing mass;
- missing momentum;
- missing energy;

indeed a bump in the invisible mass spectrum will be a model independent evidence for a new dark particle existence.

Missing mass searches

Missing mass searches of particles can be performed only when a process is kinematically constrained: no assumptions on A' decays are needed. The accessible mass range is limited by the center of mass energy of the annihilation or by the meson mass $m_{A'} \leq \sqrt{2m_e E_{beam}}$.

- E787/E949: experiments searching for the very rare decay $K^+ \to \bar{\nu}\nu\pi^+$ at Brookhaven National Laboratory (1998/2001)[67]. The missing mass, from the neutrinos, in this process may be reinterpreted as due to a dark photon thus allowing to set upper limits on the measurement of the branching ratio of the process $K^\pm \to \pi^\pm A'$;
- BaBar: searching for a single photon at PEPII (2000) [60]. The analysis was done reinterpreting, in terms of the dark photon, the data set (integrated luminosity of 53 fb^{-1} e^+e^- annihilation) used to search for a light scalar particle from the decay of the $\Upsilon(3S)$ resonance [68]. The searched process is $\Upsilon(3S) \to A'\gamma$, with a single photon in the final state. In addition, BaBar searched for A' also in the reaction $e^+e^- \to A'\gamma$, $A' \to l^+l^-$, using data collected at the $\Upsilon(4S)$, $\Upsilon(3S)$ and $\Upsilon(2S)$ resonances. Also in this case, no signal was observed by the collaboration [60].

Missing energy and momentum searches

The missing momentum and missing energy techniques are based essentially on missing energy detection in A'-strahlung processes like $e^-Z \to e^-ZA'$ with $A' \to \chi\chi$. In these kind of experiments a positron or an electron can interact with a target, and produce a shower in an electromagnetic calorimeter (missing energy), where its energy is measured, or be deflected in a spectrometer (missing momentum), where its momentum is measured.

- Na64: this experiment was designed to search for the dark photon at CERN (2016) using an electron beam of 100 GeV energy. A total number of electrons on target equal to 2.84×10^{11} was collected in 2016, 2017 and 2018. Behind the target, the electrons interact with an electromagnetic calorimeter acting as active beam dump. The Na64 data helped to exclude the regions for dark photon mass below 200 MeV using the missing energy techniques. The experiment can search for A' also in the visible decay channel. The occurrence of $A' \to e^+e^-$ decays would appear as an excess of events with two electromagnetic-like showers in the detector, with the total energy equal to the beam energy, above those expected from the background sources [58].

Future searches

- VEPP3: In 2012 a collaboration at BINP proposed to perform the search for the dark photon using the missing mass technique, covering the DP mass range $5 - 20$ MeV, using a 500 MeV positron beam on a hydrogen target [69]. The foreseen luminosity was 10^{33} cm^{-2}s^{-1} [70]. However, the experiment has not yet been run;

- MMAPS: It is a fixed target experiment that will be located in Cornell which will use the 5.3 GeV beam extracted from the synchrotron [71]. In the e^+e^- annihilation inside a Beryllium target the isolated photon, emitted in association with the dark photon, can be detected using a CsI calorimeter;

- LDMX at SLAC or CERN [72] will use a primary electron beam to produce dark matter in fixed-target collisions, applying the missing momentum technique. The limits on the dark photon are referred to a integrated luminosity of 10^{14} electrons-on-target for a beam energy of 4 GeV at SLAC or, alternatively, 10^{16} electrons-on-target and a beam energy of 16 GeV at CERN;

- BelleII: it is looking for A' produced in the $e^+e^- \to A'\gamma$ annihilation at the KEK collider [73]. A mono-photon trigger, sensitive to low energies, allows the reconstruction of the isolated photon emitted in association with a dark photon;

- POKER: an experiment searching for the dark photon at CERN (approved 2020). It is a missing-energy search exploiting an active thick-target with high-energy positrons that will collect 10^{13} POT for $E_{beam} = 100$ GeV.

Figure 1.11 shows the limits on the parameters for the invisible search. In this panorama the PADME experiment has been approved in 2015 with the goal of searching for the invisible decay of A' in the mass region below 23.7 MeV for $\epsilon > 10^{-3}$ with a positron beam in a fixed target setup. This region of the parameter space was marginally explored at the time of the PADME proposal, while currently several constraints have been set. The project stems from the opportunity offered by the Beam Test Facility at the Laboratori Nazionali of INFN in Frascati with its high intensity pulsed positron beam of energy < 550 MeV. In spite of the limited reach compared to the present scenario of searches, PADME allows to assess the potential of a peculiar experimental technique. Indeed, it is so far the only experiment using a pulsed positron beam and implementing the missing mass technique in fixed target collisions. The search strategy envisaged in the PADME proposal is discussed in Chapter 2 and a first study with the data collected so far in presented in Chapter 6.

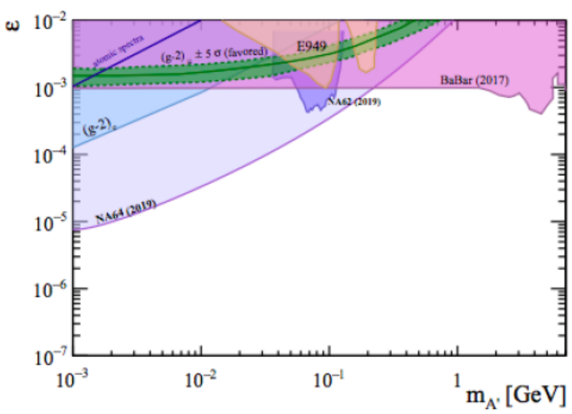

(a)

(b)

Figure 1.11: *On the left: Regions of the parameter space* $(M_{A'}, \epsilon)$ *excluded by different experiments looking for invisible decay of the dark photon [64]. On the right: Perspectives in terms of exclusion regions of the parameter space* $(M_{A'}, \epsilon)$ *for invisible decay of the dark photon from different future experiments, the grey regions have been already investigated [65].*

2 PADME

In 2015 a new experiment was approved by INFN to search for the dark photon A' in the invisible decay: PADME (Positron Annihilation into Dark Matter Experiment). The experiment is at the Laboratori Nazionali di Frascati (LNF) and would search the dark photon produced in the annihilation of the positron of the LINAC beam, on a thin Diamond Target. According to the PADME proposal, the experiment will collect 4×10^{13} Positron On Target (POT) to reach a sensitivity on ϵ parameter of 10^{-3} for masses $M_{A'} \leq 23.7$ MeV.

2.1 BTF positron beam at LNF

The BTF (Beam Test Facility) of Laboratori Nazionali di Frascati [74] can provide a beam of electrons or positrons to the users, to test or calibrate their detectors. These beams are produced by the LINAC of DAϕNE and can be delivered with several energies, multiplicity and time duration of pulses.

Electrons are produced by a gridded electron gun, while positrons are produced from the interaction of the electrons with converters of high Z. The position of the converters along the beam line set the beam and its features:

- a Tungsten- Rhenium (T-Re) target (2 X_0) after the first five accelerating sections produce the so-called “primary positron beam”;
- a Copper (Cu) target (1.7 X_0) before the entrance of BTF hall produce the so-called “secondary positron beam”.

A scheme of the beam line is shown in Figure 2.1 and the features of the beams are reported in Table 2.1.

PADME is hosted in BTF-Line1 and used a positron beam with a maximum energy of 550 MeV, a bunch length of $\sim$ 250 ns and a repetition rate of 50 Hz. One of the bunches out of 50 is sent to a hodoscope for energy measurement. PADME used both positron beams, observing a huge background level for the secondary positron beam. In order to reduce the beam induced background, the configurations of the beam line was also changed. During the RunI a Beryllium window was used to separate the LINAC vacuum with the PADME, see Figure

Table 2.1: *BTF beams parameters.*

Fearures	e^-	**primary** e^+	**secondary** e^+
Maximum beam energy (MeV)	800	490	550
RF frequency (MHz)	2856	2856	2856
Beam pulse length (ns)	$1 - 300$	$1 - 300$	$1 - 300$
RMS energy spread	0.56	< 0.96	0.96
LINAC repetition rate (Hz)	$1 - 50$	$1 - 50$	$1 - 50$
Emittance (mm mrad)	1	~ 1	~ 1
Divergence (mrad)	$1 - 1.5$	$1 - 1.5$	$1 - 1.5$

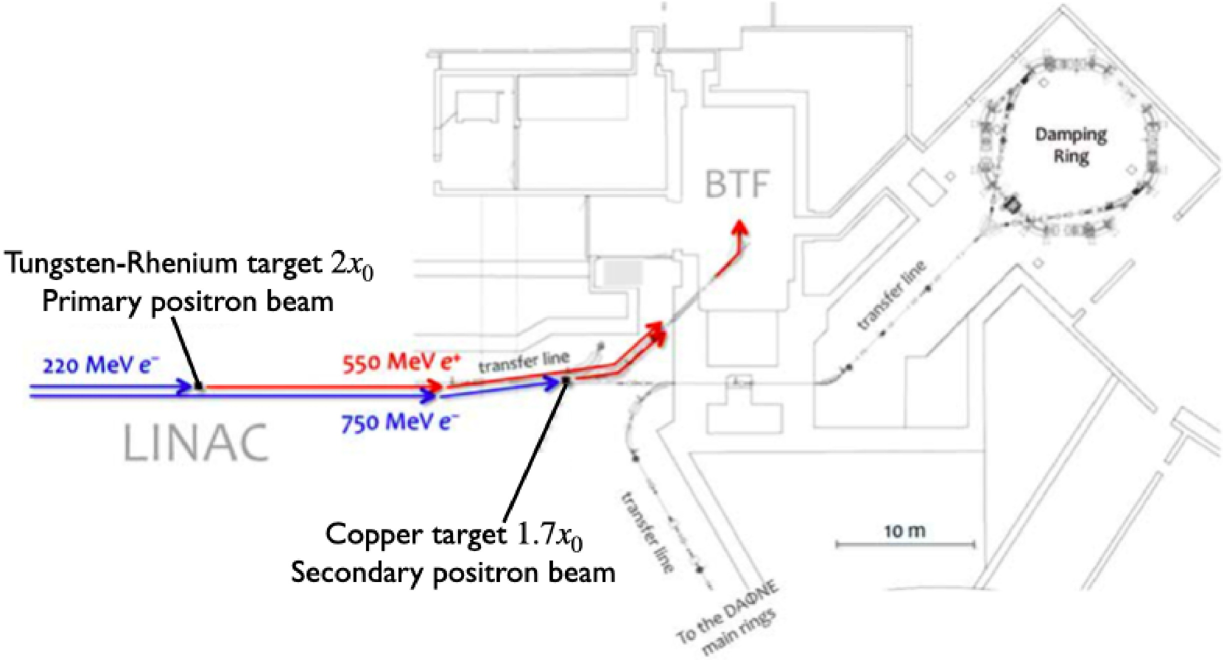

Figure 2.1: *The BTF transfer line and the two positron beam configurations: LINAC primary positrons from the converter or secondary positrons from the BTF target.*

2.2 (a). In order to understand the background observed, a Monte-Carlo (MC) simulation was done including all the beam components. The results showed that this is an important source of background and it was tried to move it after the last bending magnet, just before PADME, to improve the situation. Unfortunately, during the vacuum restoration, the Beryllium window broke. This accident required a long and expensive cleaning and refurbishing of the last part of the beam line. In addition to that, more adjustments were done to provide a better beam: the beam pipe was replaced with a new one of larger cross section, new collimators were introduced, and a 125μm thick Mylar vacuum separation window was placed more upstream and behind the BTF concrete wall. Figure 2.2 (b) shows the new configuration.

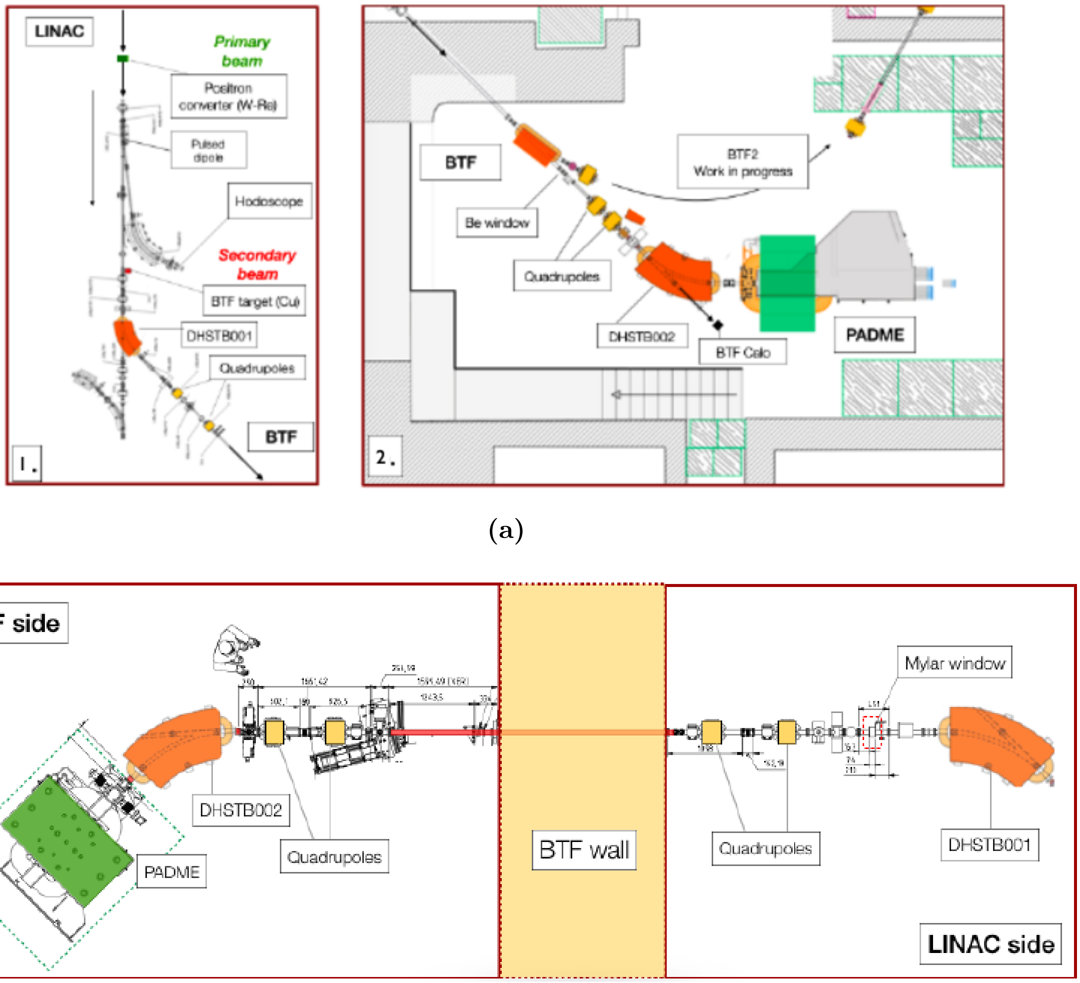

(a)

(b)

Figure 2.2: *(a1): Drawing of the beam transfer line from the LINAC to the BTF entrance with the location of the production points of the primary and secondary positron beams. (a2): Drawing of the BTF experimental hall. (b): The secondary beam line from the LINAC to the PADME hall.*

2.2 The PADME experiment

2.2.1 A' production in PADME

The A' boson production mechanisms accessible in positron-on-target collision are two: the annihilation of the positron, with the electron of the target, $e^+e^- \to A'\gamma$ and the so called A-strahlung, with the nucleus of the target, $e^+N \to Ne^+A'$. Figure 2.3 shows the Feynman diagrams of the processes. Both processes are similar to the ones needed to produce the SM photons, but with a cross section which scales as ϵ^2. With a positron beam of 550 MeV energy, PADME can produce a dark photon with mass $M_{A'} \leq 27.3$ MeV [75]. Figure 2.4 (a) shows the A' production cross section, while Figure 2.4 (b) shows the ratio between the $e^+e^- \to A'\gamma$ and

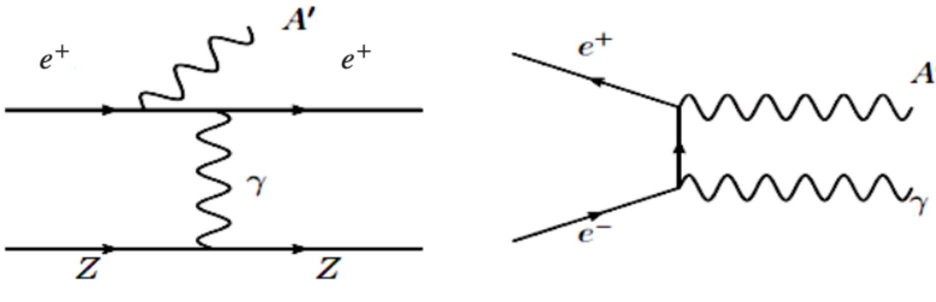

(a) (b)

Figure 2.3: *Feynman diagrams of the A' production in PADME : A-strahlung (a) and annihilation (b) productions.*

$e^+e^- \to \gamma\gamma$ process cross sections. An enhancement of the A' production cross section, with respect to the SM annihilation, happens when the center of mass energy is close to the mass of the dark photon, as Figure 2.4 (b) shows.

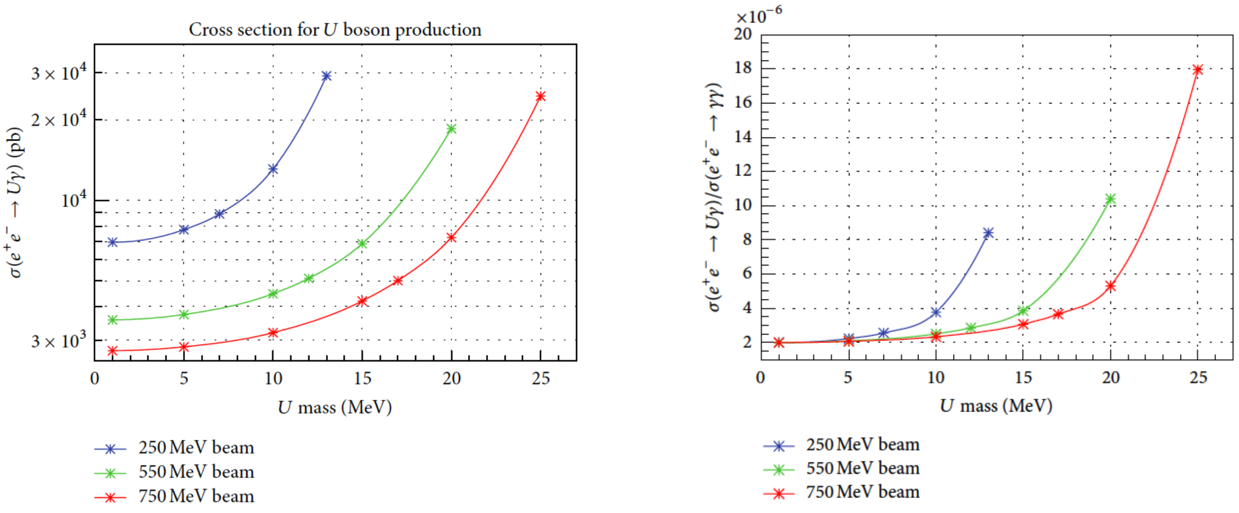

(a) (b)

Figure 2.4: *(a) A' (U) boson production cross section (for $\epsilon = 10^{-3}$) as a function of mass for different beam energies in positron annihilation [75]. (b) Ratio of (a) cross sections and the corresponding two-photon annihilation cross section [75].*

2.2.2 Experimental technique for the dark photon search in PADME

The goal of the experiment [76] is to search for the A' produced through the annihilation $e^+e^- \to A'\gamma$, in which the e^+ is the positron of the beam and e^- is the electron of the target. From the photon produced, is possible to extract the mass of the A' independently from its decay channel. Indeed, thanks to the close kinematic of the event, the missing mass:

$$M^2_{miss} = (P_{e^+} + P_{e^-} - P_\gamma)^2 \tag{2.1}$$

can be calculated from the momentum of the visible particles and its distribution will have a peak in correspondence to the A' mass value. This method can be applied for the case of the invisible decay and for the visible decay. In the latter case, the A' decay products can not be detected in the calorimeter because outside its acceptance.

The detector is divided in sub-detectors and main parts:

- active target: target of the experiment and used to estimate the multiplicity and position of the beam, then the luminosity and the interaction point;
- dipole magnet: bend not interacting beam positrons out of the calorimeters acceptance and interacting ones in the veto system acceptance;
- charged particle veto system: detect charged particles with good segmentation along z;
- vacuum vessel: minimise the interaction of primary and secondary particles with air molecules;
- electromagnetic calorimeter: needed to measure the momentum of the photon in the final state;
- small angle calorimeter: needed to detect photons with a small angle and allows to reject the Bremsstrahlung background.

Figure 2.5 shows a scheme of the experiment with its components. Arriving from left and going to right, a positron beam impinges on the Active Diamond Target. Due to the small thickness of the target, most of the positrons don't interact with it. The beam particles that do not interact are bent out of the experiment acceptance, while the others that interact, losing at least 50 MeV, are bent in the veto for positrons. Then, downstream and symmetric to the beam axis, the electromagnetic calorimeter system is located to detect the photons produced in the interaction.

2.2.3 PADME subdetectors

The Active Diamond Target

The active target of PADME is a full carbon detector, made of a polycrystalline Diamond film, grown by Chemical Vapor Deposition (CVD) technique, 100 μm thick and with an area of

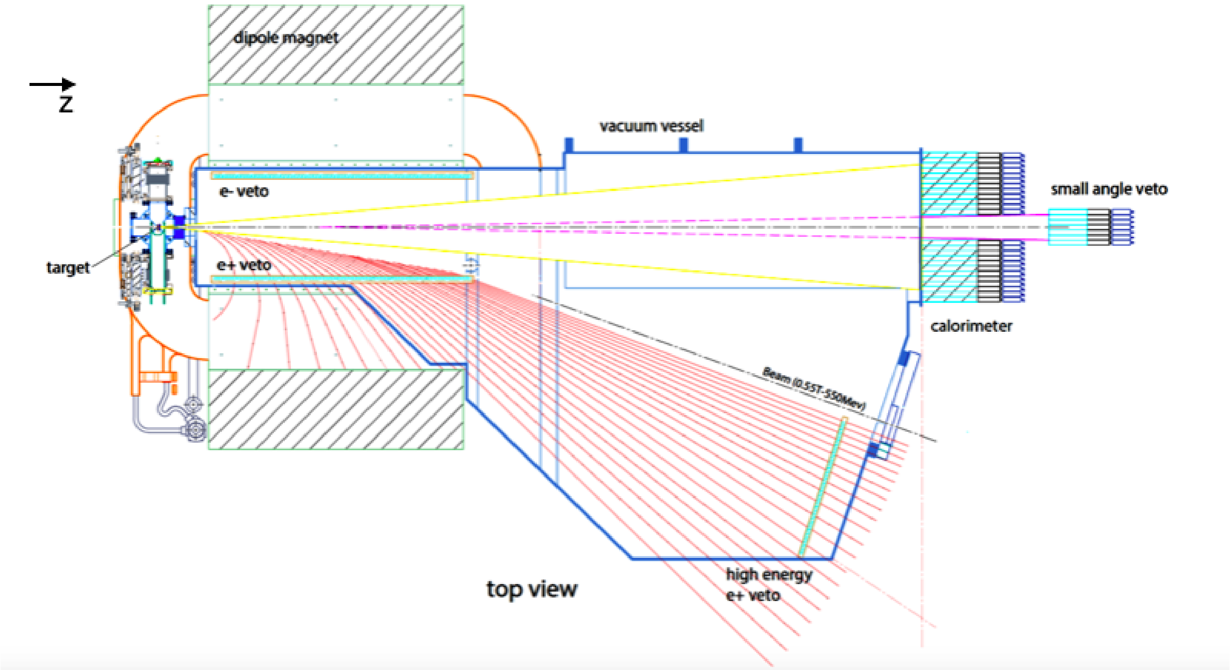

Figure 2.5: *Schematic layout of the PADME experiment.*

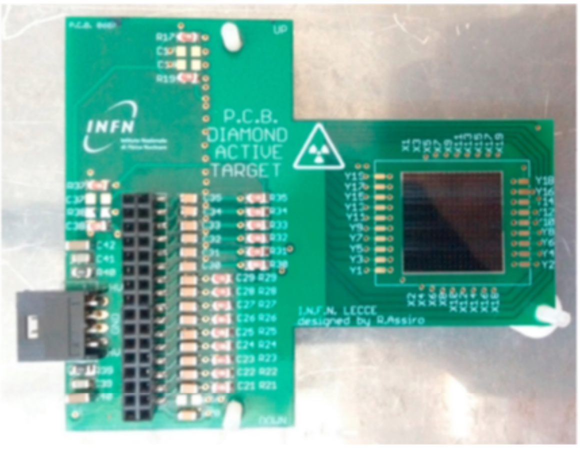

Figure 2.6: *A picture of the PADME Active Diamond Target.*

2×2 cm^2 (see Figure 2.6). It has been realised in the laboratory of the Università del Salento in collaboration with INFN. The selection of the target material was made to minimise the Bremsstrahlung background that is the main physics background of the experiment for the dark photon search. Indeed, its cross section is proportional to Z^2, the square of the atomic number of the target material, but the dark photon production cross section is $\propto Z$ and the signal-to-noise ratio scales as $1/Z$. In addition, the target should be thin enough to reduce the number of pile-up events to a level manageable by the electromagnetic calorimeter. The denomination

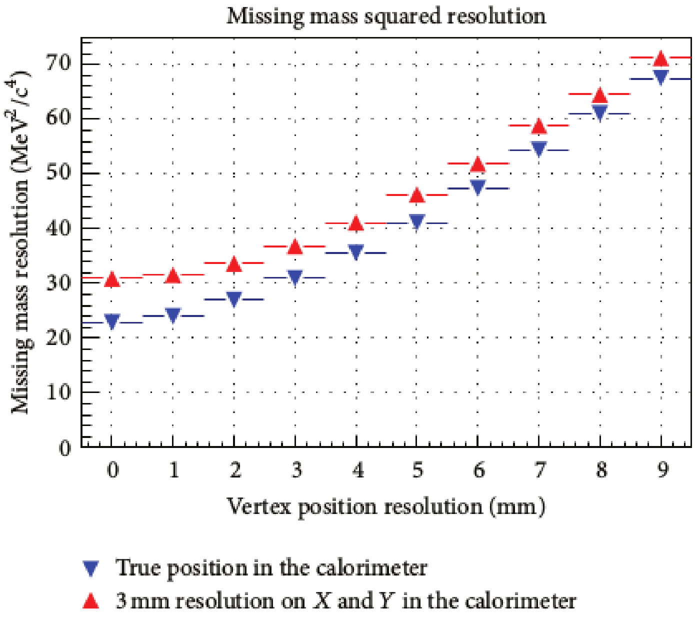

Figure 2.7: *Resolution of the square of the missing mass as a function of the resolution of the interaction point* $e^+e^- \to \gamma A'$ *for a dark photon with* $M_{A'} = 15$ MeV.

active is due to the fact that it must measure the position of the interaction point, and the beam profile. The knowledge of these values improves the resolution of the missing mass, as Figure 2.7 shows. Furthermore, it is used as a bunch by bunch beam multiplicity monitor. To measure these quantities, on both the target surfaces, there are 19 strip electrodes realized by means of an ArF laser. The strips of the two sides are oriented in orthogonal directions with a pitch of 1 mm, a length of 1.9 cm and 0.85 mm wide. Two front-end electronics boards provide the readout of 16 strips from each side out of 19, enough to detect the beam and measure the needed parameters. Electrical contacts between the boards and the strips are made in two different ways: for the x beam coordinates reconstruction (vertical) strips, by a 2-component conductive glue (EPOXY E-solder 3025); for the y beam coordinates reconstruction (horizontal) strips, by wire-bonding. The target is placed in vacuum and a remotely controlled step-motor allows moving it in and out of the beam axis.

During the data takings, the Active Diamond Target showed a stable response in time and a spatial resolution lower than the proposal requests of 1 mm (see Figure 2.8 (a)). The absolute response of the Active Diamond Target was calibrated by a lead-glass Cherenkov calorimeter working in full containment mode using a beam of 545 MeV positrons. The calorimeter was used as a bunch multiplicity reference. Figure 2.8 (b) shows the good linearity obtained for RunI data, when the beam profile was spread on more than two strips and no one electronic channel saturated (positrons per strip less than about 5000). In RunII data, more relevant for this thesis work, the beam was focused to about one strip and ad-hoc non-linear calibration was necessary [77].

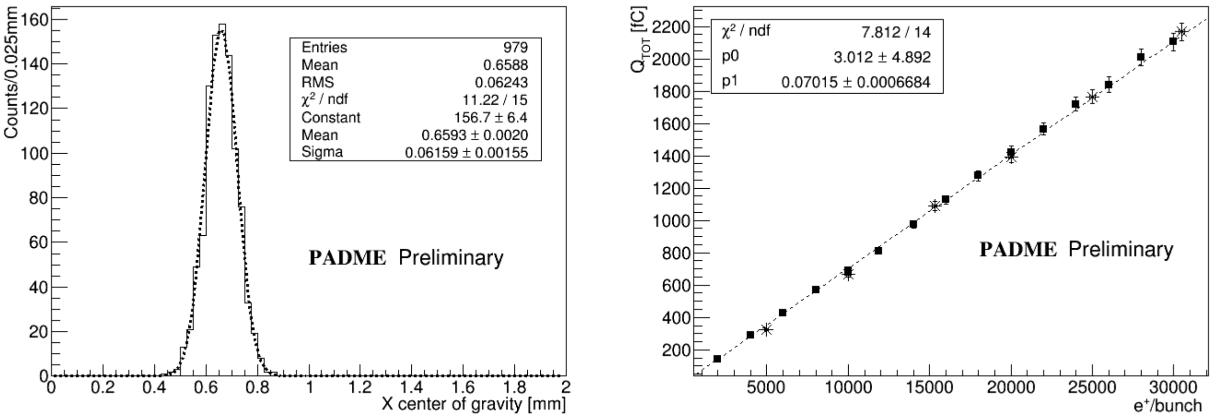

(a) **(b)**

Figure 2.8: *(a) Distribution of the average positron bunch position as obtained by the charge center of gravity method in the X measuring view. A Gaussian fit is superimposed. The positron bunch multiplicity was about* 2×10^4 *POT. (b) The average total charge collected by the Active Diamond Target as a function of detector horizontal displacement. The detector bias voltage was* 250 V *and the beam energy* 545 MeV. *Plots are from [78].*

The dipole magnet

After the crossing with the target, the charged particles are bent horizontally by a dipole magnet. Due to the very thin target, most of the beam positrons do not interact with the Diamond entering the dipole with an energy more or less equal to the initial one and leave the dipole along a fixed direction. The presence of the magnetic field allows to bring these positrons out the PADME acceptance and avoid to overwhelm the calorimeters. The dipole magnet is the sweeping magnet 984 used for the SPS transfer line at CERN. It has a H shape, a length of 1 m and a gap of 52 cm (see Figure 2.9). A mapping of the magnetic field was done before the magnet installation in the PADME hall. The relation between the current I and the magnetic field central value B was extracted and it is:

$$B \text{ [Gauss]} = 19.44 \text{ I [Ampere]} + 32.801. \tag{2.2}$$

Charged particle veto system

The vetoes have a fundamental role in the background rejection. Since the most abundant background is the Bremsstrahlung, the veto for the positrons is designed to identify this kind of background. The veto detectors are made of plastic scintillator bars of 184 mm length and 10×10 mm^2 transversal area. They are made of polystyrene-based material with 1.5% concentration of POPOP and they are produced by UNIPLAST. The bars have a wavelength

(a) (b)

Figure 2.9: *Pictures of the PADME dipole magnet lateral (a) and front (b) views.*

shifter (WLS) fiber inserted into a groove and connected to a Hamamatsu 13360 SiPM (on both sides of the bar for the HEPVeto). The WLS fiber selected for the veto bars are BCF-92 (1.2 mm diameter). The scintillating bars are placed vertically with respect to the beam line. The emitted light is collected by a lateral clear fibre and detected by silicon photomultipliers (SiPM). The veto system is located inside the vacuum vessel and is composed by three sections: the positron veto (PVeto), the electron veto (EVeto) and the high energy positron (HEPVeto). The PVeto and EVeto are located inside the magnet and placed along the beam direction, the first on the positron bending side, and the second in front of it, on the opposite side (see Figure 2.10 (a)). The HEPVeto (see Figure 2.10 (b)) is placed transversely to the bent positron beam, between the PVeto and the beam dump. The total number of vetoes bars are different:

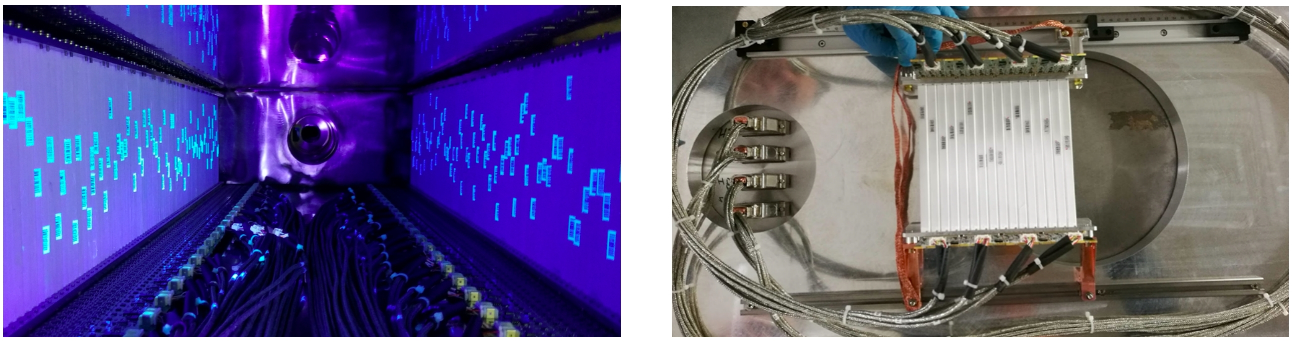

(a) (b)

Figure 2.10: *Pictures of the PADME veto system composed by the positron and electron veto (a) and the high energy positron veto (b).*

- PVeto: array of 90 scintillating units;

- EVeto: array of 96 scintillating units;
- HEPVeto: array of 16 scintillating units with double readout.

To obtain the maximum of the acceptance in the charged particle detection, the bars are placed on a aluminium support and rotated with an angle of 0.1 rad.

The vetoes time resolution is required to be better than 1 ns to resolve interactions occurring in the same bunch crossing. This was reached with an optimisation of the light collection done in test beams [79]. The best configuration was found for a WLS fiber glued inside a groove and light collected from scintillator and fiber. Figure 2.11 shows the time resolution of the prototype, that was estimated to be 0.67 ns.

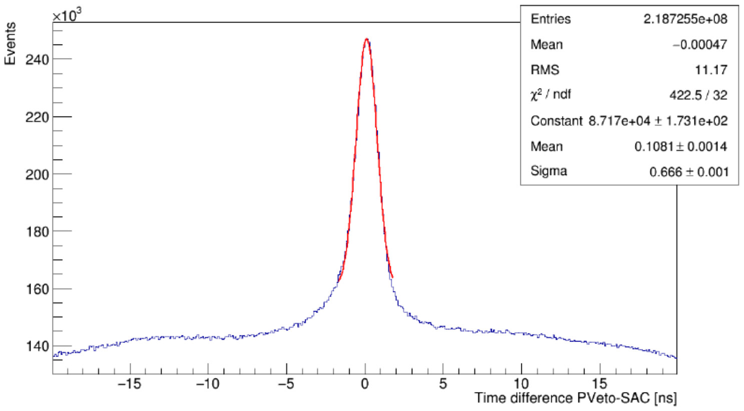

Figure 2.11: *Time resolution measured in test beam for the veto charged particle prototype.*

Momentum calibration of PVeto

The positrons at the exit of the PADME target travel in a uniform magnetic field of 0.5 T pointing in the negative vertical direction. The magnetic field bends their trajectories and if the energy lost in the target is negligible ($\sim$ few MeV), the positrons will be deflected on the beam dump; if the energy lost is more than < 50 MeV they will be bent toward the HEPVeto and the PVeto. The z coordinate of the particle hit depends on its momentum and this correlation is exploited to evaluate the charged particles momenta. Single positrons with fixed energy were simulated to determine the momentum vs z position correlation function. Figure 2.12 shows the calibration curve obtained with this simulation [77]. The magnetic field in the simulation was described in detail with the map of the fringe field which includes the weak dependence of the intensity on the lateral coordinate x.

Vacuum vessel

Positrons interactions in air can produce a significant contribution to the background due to the high intensity of the beam. Since the radiation length X_0 of air at a pressure of 1013 mbar is 285 m and the distance calorimeter-target is 3.5 m, the atmospheric air thickness is $1.2\% X_0$, much larger than the thickness of the target itself ($0.04\% X_0$). The vacuum is needed to reduce

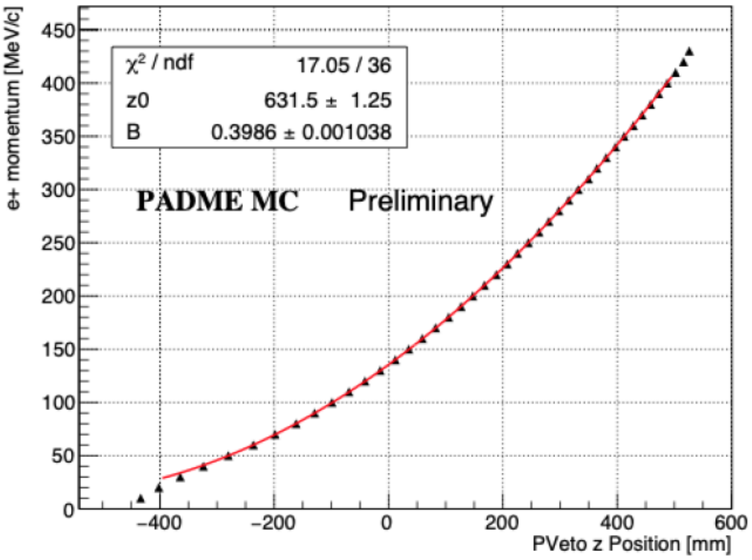

Figure 2.12: *Momentum calibration of the PVeto obtained by simulation for RunI [77]. The points are fitted with the function* $P[\mathrm{MeV/c}] = 0.3\mathrm{B}[(\mathrm{z[mm]} + \mathrm{z_0})^2 + \mathrm{x_0^2}]/(2\mathrm{x_0})$*, where* $x_0 = 192.5$ mm *is the PVeto x position and B and* z_0 *the parameters of the fit. For RunII the fit parameters were* $B = 0.389$ T *and* $z_0 = 608.3$ mm *since the B field value was different with respect to RunI due to a different beam energy.*

the background due to interaction in air of beam positrons and from all particles coming from the interactions in the target. PADME has a vacuum vessel pressure of 10^{-2} mbar, separated from the LINAC vacuum (10^{-4} mbar) by a thin window. Until July 2019 the window separating the two vacuum was made of Beryllium. In July 2020 the window material was replaced with Mylar and moved upstream.

The electromagnetic calorimeter ECAL

The main detector of the PADME experiment is the electromagnetic calorimeter ECAL, illustrated in Figure 2.13. An energy resolution of better than $\sim 5\%$ for photons with energies lower than 100 MeV and a cluster position resolution of 3 mm are needed in order to achieve squared missing mass resolution of 30 MeV^2. It is a segmented calorimeter, made of 616 BGO crystals, with a density $\rho = 7.13$ g/cm^3, a radiation length $X_0 = 7.97$ g/cm^2 and a Moliere radius $R_M = 16.10$ g/cm^2. Each crystal has dimension $2.1 \times 2.1 \times 23$ cm^3, as a consequence the electromagnetic shower is fully contained along the longitudinally direction, but due to the fact that the radius of the crystals is less than the R_M, only $\sim 70\%$ is contained along the transversal plane. The crystals are arranged in a cylindrical shape whit a central squared hole of 5×5 cm^2 area and an external radius of ~ 30 cm.

The presence of the central square hole is needed to not overwhelm the central crystals with Bremsstrahlung photons, mainly produced in the forward direction. Those photons are detected using the Small Angle Calorimeter placed behind the ECAL and covering its hole. To

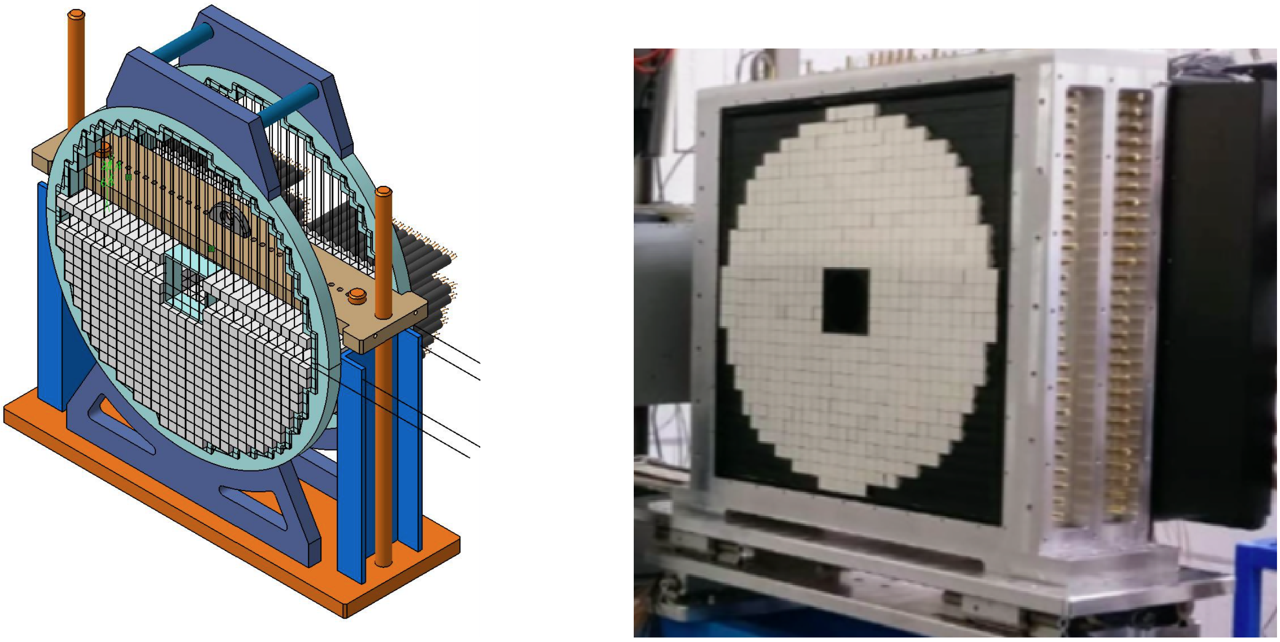

Figure 2.13: *(Schematic layout of PADME ECAL on its mechanical support (a) and its photograph after crystals mounting (b).*

reduce the light crosstalk each crystal was covered by a reflective white paint, and a 50 μm thick sheet of black Tedlar was placed between each crystals (vertically and horizontally) when the ECAL was built. To convert the light in an electrical signal, a HZC XP1911 type B PMT [80] is used, which has a diameter of 19 mm and a quantum efficiency of 21% at 480 nm (the BGO maximum emittance wavelength). Another important feature of the BGO material is that the amount of light collected changes with the temperature of $-0.9\%/^\circ$C. To monitor the temperature of the detector 40 thermometers were attached to the scintillating units. In particular 16 sensors were placed along the lateral side of the crystals and 24 were placed on the back side, as Figure 2.14 shows. The scintillating units were calibrated in energy using a ^{22}Na source before mounting the calorimeter [81]. At each scintillating unit was applied a variable voltage in the range $[1100, 1550]$ V to extract a gain calibration curve. In PADME, the final voltages applied equalized the gain of the readout to 15.3 pC/MeV. During the data taking the calorimeter gain equalisation is checked by studying the charge distributions obtained from cosmic rays in the various scintillating units. The ECAL cosmic trigger was made with four plastic scintillators: two on the top and two immediately below. The information of the cosmic trigger were recorded in the regular data stream and were used also to extract the efficiency of each crystal. The average efficiency of each crystal was found be about 99.6% [81]. The energy resolution for the BGO crystals was extracted in a test beam [82] using a prototype of 5×5

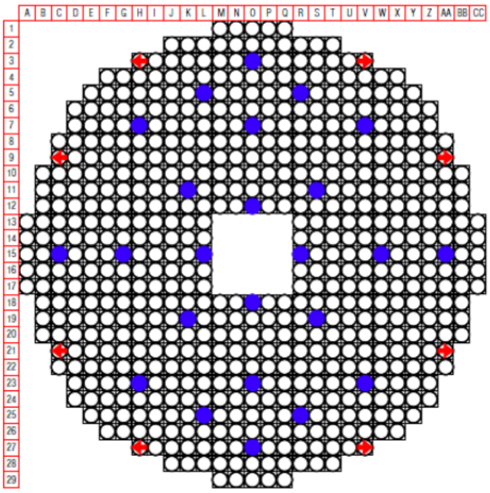

Figure 2.14: *Schematic representation of the thermometers position attached to ECAL crystals. In blue the 24 probes positioned on the back sides; in red the 8 probes pairs positioned along the left and the right lateral sides of the external BGO crystals.*

crystals matrix. The measurements are shown in Figure 2.15 and interpolated with the curve

$$\frac{\sigma(E)}{E} = \frac{2.0\%}{\sqrt{E[\mathrm{GeV}]}} \oplus \frac{0.003\%}{E[GeV]} \oplus 1.1\%. \tag{2.3}$$

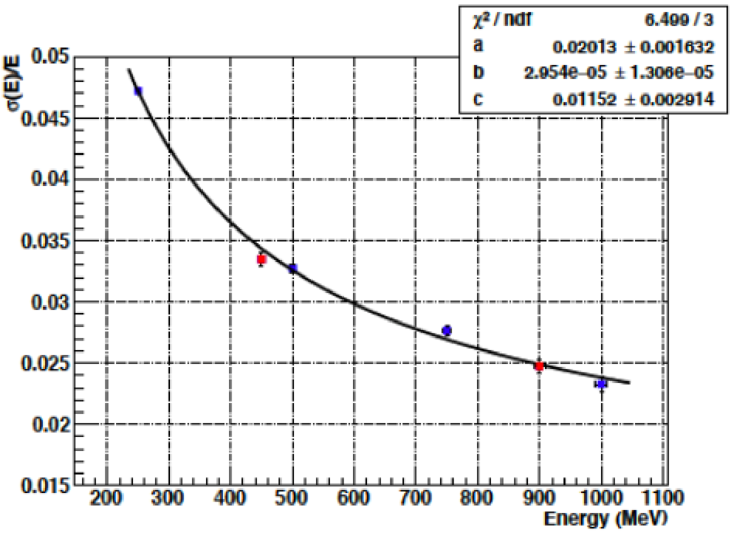

Figure 2.15: *Energy resolution of the PADME calorimeter prototype measured in the test beam as a function of the deposited energy (*250 MeV e^- *data blue points and* 450 MeV e^- *data red points) fitted by the resolution function of Equation 2.3 [82].*

The Small Angle electromagnetic Calorimeter (SAC)

As mentioned before, a huge amount of background is produced in the forward direction. To detect it, a fast small angle calorimeter SAC (see Figure 2.16) was placed behind the central hole of ECAL. It is a 5×5 PbF_2 crystals matrix, each with a length of 140 mm and an area of 30×30 mm^2. To reduce the light crosstalk, a 50 μm thick sheet of Tedlar cover the surface of each crystal. To readout the light the back surfaces are coupled to Hamamatsu R13478UV PMTs via UV transparent optical grease. The PbF_2 has a time decay constant $\sim$ 10 ns,this very fast signal allows to be more efficient in background rejection at high rate. A prototype of the SAC was used to characterize the detector performance in a test beam obtaining: light yield of 2.05 p.e./MeV, energy resolution of 10% at 550 MeV, time resolution of 81 ps, and a double-peak separation capability of 1.8 ns [83].

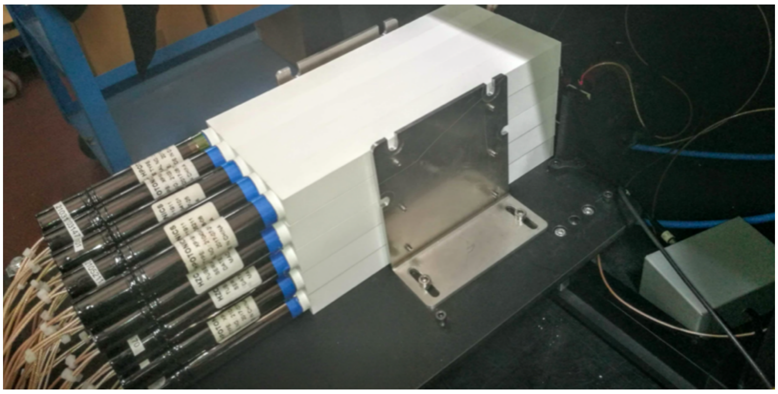

Figure 2.16: *Picture of the Small Angle Calorimeter (SAC) of PADME.*

Pixel detectors as monitor of the beam

PADME has two Silicon pixel detector to monitor the beam: MIMOSA and TimePix3. The first one is a monolithic detector consisting of 928×960 pixels of 20.7 μm pitch (1.921×1.987 cm^2) [84]. The MIMOSA detector is placed inside the target vacuum cross on the opposite side. The MIMOSA detector works at low bunch multiplicity saturating when about 500 particles hit it between two readout frames. The second one, a hybrid Silicon pixel detector [85], is placed outside the vacuum vessel to monitor the outgoing not interacting positrons of the beam. The detector consists of 12 sensors, each made of a 256×256 pixels matrix with an area of 14×14 mm^2 (see Figure 2.17).

Trigger and data acquisition

The PADME detectors are readout by 879 channels, divided, as described in Table 2.2, by 29 CAEN V1742 32 + 2 channels Switched Capacitor ADC boards. Each channel consists of a 1024 cells with a adjustable sampling rate. Two channels are dedicated to sample the trigger signal for the two groups of 16 channels. Signal is continuously stored in consecutive sampling cells;

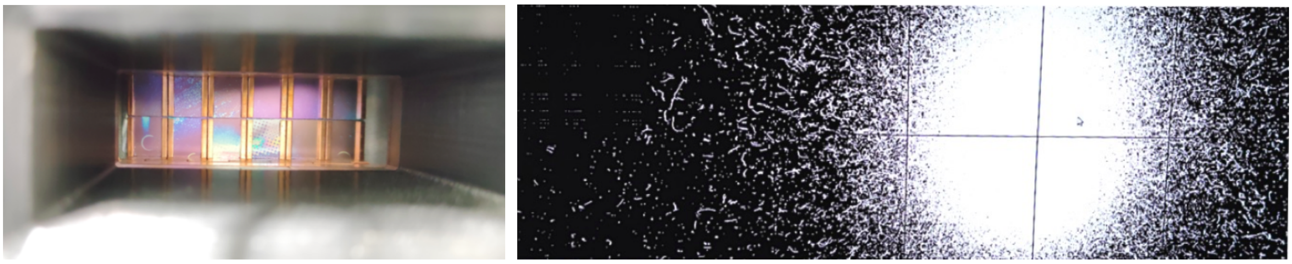
(a) (b)

Figure 2.17: *Picture of TimePix3 silicon pixel detector (a) and an example of a 2D beam reconstruction with it (b).*

Table 2.2: *Number of channels and signal sampling rate for each detector.*

Detector	**# Channels**	**Sampling rate**
Target	32	1 GS/s
ECAL	616	1 GS/s
Vetoes	224	2.5 GS/s
SAC	25	2.5 GS/s

the trigger signal stops this process and starts the digitization process of the cells content with a 12 bit ADC. In Table 2.2 the data sampling rate selected for each detector is also reported. For the slower detectors a sampling rate of 1 GS/s is adopted, while the faster detectors are digitized at 2.5 GS/s. All ADC boards receive from the PADME Trigger and Timing Systems the global external trigger and the phase-aligned clock for synchronisation. The global trigger signals is the logical OR of different signal triggers:

- BTF trigger (machine clock);
- ECAL cosmic ray trigger system;
- ECAL radioactive source calibration system;
- test signals with a rate of 50 Hz;
- delayed trigger (900 ns after the BTF trigger) to study the background.

The data acquisition consists of two main processes: the zero level trigger (L0), which collected the data from all ADC boards, and the first level trigger (L1) which merged the data of the same event in a single file. A fraction of these files are reconstructed immediately to give the main information to the shifter on the online monitor.

2.2.4 PADME software

The data format and data persistency mechanism are based on Root [86] and Geant4 [87] libraries. The data to be processed are composed by the full digitised waveforms recorded for each detector channel and each board trigger signal. From this information the reconstruction software extracts a collection of reconstructed hits, applying decoding procedures based on configuration files to map the electronic channels into the physical elements of the PADME detector. The information that will be saved are the time, after a time alignment calibration, the position, in the PADME coordinate reference system, and the energy, corrected for the relative scale factors.

To reconstruct the physics objects, all the hits are processed by detector specific clusterization algorithm. The selected hits are merged in time and in space using different parameters for each detector (the clusterization algorithm and parameters optimisation for the ECAL calorimeter is explained in Section 4.3). The Active Diamond Target is the only detector for which the hits are not clustered. In fact, from the digitised waveform, the charge collected from each strip is calculated in order to provide the main features of the beam bunch, as multiplicity and, for the X and Y views, profile, centroid and width.

The Monte Carlo simulations produce for each detector the GEANT4 hits with true position, energy and time information. These hits are elaborated, including a simulation of the readout electronic, and saved in digi4, in order to match the detectors resolution observed in data. An additional tool convert the digi4 into collections of reconstructed hits with the same format of the data. Then the information is passed to the same reconstruction software of the data files.

Analysis software is designed in such a way that the reconstructed data, real or simulated, are analysed by the PADME Analysis software. The users can build easily its own analysis, or run prearranged tools to validate data and check the data quality.

During my PhD I strongly contribute to the development of all these three PADME software frameworks.

2.2.5 Simulation of detector and physics processes

The simulation of the experiment is done in the GEANT4 environment. All detectors are described with their active parts and inert supports, the vacuum chamber with a realistic shape, the magnetic field mapped in space and the beam line downstream to the vacuum separating window, which is also included. The beam is generated in the vacuum separating window and it is transported to the target. Each beam positron can interact with the materials according to the GEANT4 electromagnetic libraries.

The generation of the dark photon in association with a photon is done internally in the simulation. A positron of the beam impinging on the Active Diamond Target is stopped and removed. At the same time, the photon generated in the $e^+e^- \to A'\gamma$ process is introduced in the list of GEANT4 particles with a production vertex in the target corresponding to the point where the positron was stopped. The propagation of such photon is simulated by GEANT4 along with all other particles born in the electromagnetic interactions of the beam with the target. Similarly, the physical process $e^+e^- \to \gamma\gamma(\gamma)$ is generated with CalcHEP [88], since

GEANT4 libraries does not include the three photons annihilation. The generation of the two-photon annihilation process is described in detail in Chapter 5.

2.3 Dark photon search and SM processes

The interesting physics processes in PADME are produced in the interaction of a beam positron with a target electron. PADME can measure the cross section of SM processes in an energy range where no many measurements exist (see Appendix A). ThePADME primary goal is to look for Beyond SM process such as the production of a dark photon from the annihilation $e^+e^- \to A'\gamma$.

2.3.1 A' search strategy

The dark photon production in PADME comes from the annihilation of a beam positron with a target electron according to the process:

$$e^+e^- \to A'\gamma \tag{2.4}$$

where in the final state there is only a SM photon, a dark photon and nothing else. The dark photon, in case of invisible decay, can not be detected, while the ordinary photon will be detected in the main electromagnetic calorimeter ECAL, if it is inside the acceptance. The signature of the event is very simple, a single photon in the experiment, but can be overwhelmed by background processes (see next section).

To better discriminate the A' event with respect to background events, a series of selection cuts are applied [89]:

- no other photons in time coincidence in the calorimeter to reject events with more than one photon in the final state and pile-up events;
- set an energy threshold on photons;
- define a radial fiducial region to reject bad reconstructed photons;
- reject the main background Bremsstrahlung vetoing events in time coincidence between positron veto and calorimeter with total energy compatible with beam energy.

The analysis was performed on MC samples, simulated assuming a mass for the dark photon. Figure 2.18 (a) shows the distribution of the squared missing mass for each sample. Due to the close kinematic, the range of the energy spectrum of the photon coupled with A' is fixed once the mass is fixed (see Figure 2.18 (b)).

The squared missing mass is calculated assuming that the momentum of the target electron is $\vec{P_{e^-}} = 0$ and the momentum of the positrons along the beam axis z is $P_{beam} = P_z \simeq E_{beam}$. A peak in this distribution can be associated, without ambiguity, to the existence of a massive dark photon A' having the same squared mass. Once the peak is observed, the coupling constant

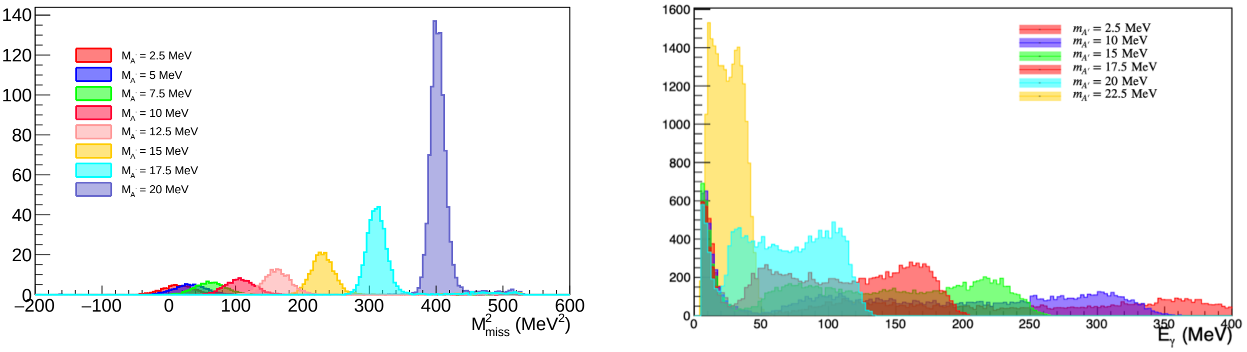

(a) **(b)**

Figure 2.18: *(a): Missing mass squared distribution for different dark photon mass hypothesis* ($M_{A'}$) *extracted using PADME MC [89]; (b) energy spectrum of the photon produced along with the dark photon for different* $M_{A'}$ *[89]. The distributions correspond to* 4×10^{13} POT, $\epsilon = 10^{-3}$ *and positron energy of* $E_{beam} = 550$ MeV.

can be estimated using a simple relationship linking the two-photon annihilation cross section and the signal cross section. Indeed, the ratio of the two cross sections depends only on the effective coupling ϵ and on a kinematic factor $\delta(M_{A'})$ which is an increasing function of the A' mass once the energy of the beam is fixed. Therefore, one has:

$$\frac{\sigma(e^+e^- \to A'\gamma)}{\sigma(e^+e^- \to \gamma\gamma)} = \frac{N(A'\gamma)}{N(\gamma\gamma)}\frac{Acc(\gamma\gamma)}{Acc(A'\gamma)} = \epsilon^2 \cdot \delta(M_{A'}) \tag{2.5}$$

where $N(A'\gamma) = N(A'\gamma)_{obs} - N(A'\gamma)_{bkg}$ is the yield of the A' obtained subtracting from the candidate events the background, $N(\gamma\gamma)$ is the background subtracted annihilation yield and $Acc(A'\gamma)$ are, respectively the two-photon annihilation and the dark photon acceptances. With this strategy, the ϵ parameter can be extracted without knowing the number of positrons that hit the target. In fact, the yield and the efficiencies for the two processes will be extracted from data, the acceptances through the simulations and $\delta(M_{A'})$ calculated.

2.3.2 SM processes

The SM processes produced in the e^+e^- annihilation can be divided in two groups, processes that are background to the A' search and processes that are not.

Backgrounds for A' search

The most dangerous background is the positron Bremsstrahlung, due to the high cross section and the presence of a single photon in the final state that mimic the signal. The positron Bremsstrahlung cross section at leading order was extracted using GEANT4 and turned out to be of the order of $\sigma(e^+N \to e^+N\gamma) \simeq 4$ b for positron energy of 550 MeV and a photon energy above 1 MeV. Bremsstrahlung photons are produced mainly in the forward direction

Table 2.3: *Ratio δ between the cross section of $\sigma(e^+e^- \to \gamma\gamma)$ and of $\sigma(e^+e^- \to A'\gamma)$ (for $\epsilon = 1$) for $\epsilon = 10^{-3}$ at different dark photon masses M'_A.*

$M_{A'}(MeV)$	δ	$\sigma(e^+e^- \to A'\gamma)$ nb ($\epsilon = 10^{-3}$)
2.5	2.0	31
5.0	2.0	31
7.5	2.0	34
10.0	2.3	37
12.5	3.0	47
15.0	3.8	62
17.5	6.5	91
20.0	10.5	160

with a geometrical acceptance very close to 1. The same is true for the radiative Bhabha $e^+e^- \to e^+e^-\gamma$. Its cross section is extracted at leading order using CalcHEP and it is $\simeq$ 180 mb for $E_\gamma > 1$ MeV. In PADME, these events can be identified with good efficiency using the Veto detectors for the charged particles, and the two electromagnetic calorimeters, mainly the SAC, for the photons.

This kind of background is particularly relevant at low photon energy and, therefore, at high values of the squared missing mass, as Figure 2.19 shows.

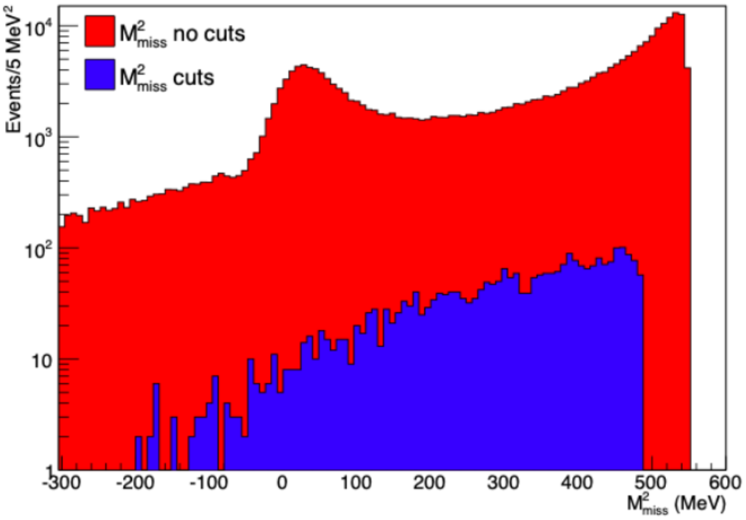

Figure 2.19: *M^2_{miss} distribution for background events before selection cuts applied (red) and after selection cuts applied (blue) [75].*

Another SM process that can mimic the signal is the annihilation to two or three photons $e^+e^- \to \gamma\gamma(\gamma)$. The leading order cross section of the annihilation $e^+e^- \to \gamma\gamma$ is given by the

Heitler formula:

$$\sigma(E,Z) = \frac{Z\pi r_e^2}{\gamma+1} \times \left[\frac{\gamma^2+4\gamma+1}{\gamma^2-1} ln(\gamma+\sqrt{\gamma^2-1}) - \frac{\gamma+3}{\sqrt{\gamma^2-1}}\right] \tag{2.6}$$

where E is the positron energy, r_e is the classical electron radius and γ is the Lorentz factor of the positron.

The leading order cross section for a beam energy of $E_{beam} = 550$ MeV obtained with Equation 2.6 is in agreement with CalcHEP calculation: $\sigma(e^+e^- \to \gamma\gamma) = 1.55$ mb. In PADME, two photons in the ECAL angular acceptance are required for the full reconstruction of these events. Using CalcHEP generated events and the MC simulation of the experiment, the geometrical acceptance α and the efficiency ϵ of the event reconstruction have been estimated to be of the order of $\alpha \times \epsilon \simeq 0.08$. A photon inefficiency gives entries at values of squared missing mass peaked to zero, as Figure 2.19 shows.

The three-photon final state process can have the same signature of the dark photon if two photons don't fall in the acceptance of the calorimeter or in case of two-photon inefficiency. The cross section is calculated using CalcHEP and it is about 170 μb for $E_\gamma > 1$ MeV. A reliable value of detector acceptance is not easy to obtain without a proper generator, thus the yield of three-photon annihilation process is not yet precisely determined in PADME. An estimation of the order of magnitude obtained with CalcHEP calculation using $E_\gamma > 50$ MeV gives ~ 10 μb. Table 2.4 reports the number of events expected in ECAL , for a standard day of data taking, together with total cross section and the acceptance corrected cross section.

Other SM processes in PADME

The other SM processes in PADME foresee only leptons in the final state. The Bhabha scattering process is well known considering that it has been used as a luminosity monitor at e^+e^- colliders for decades. On the other hand, a few measurements of the QED process are based on positron interaction with an electron bound to a nucleus of a fixed target, which is expected to be relevant if the impinging particle has low energy. The Bhabha cross section, calculated at leading order, is $\sigma(e^+e^- \to e^+e^-) \simeq 0.5$ b for a minimum electron energy of 1 MeV. The process in visible using only the vetoes and requiring signals in time coincidence in the positron veto and in the electron veto. The PADME veto system is designed to detect positrons and electrons, emerging orthogonally from the target, with an energy higher than an energy threshold of 50 MeV, reducing the visible cross section to $\simeq 3.3 \times 10^{-3}$ b.

Other processes that can be identified by PADME foresee more than one pair of leptons in the final state, like four and six leptons, originating from gamma-gamma scattering:

$$e^+e^- \to e^+e^-X \qquad X \to e^+e^- \quad or \quad X \to e^+e^-e^+e^-. \tag{2.7}$$

These processes are hard to be calculated in the SM, even at tree level, due to the large number of processes. A semi analytical calculation was obtained in [90] and checked, when possible, with a numerical calculation and eventually using CalcHEP. The interest in these processes is due to the fact that no cross section measurements exist, and PADME could be the first experiment to check the theoretical predictions.

Table 2.4: *Simulated total cross sections (σ) and daily production rates (N) of SM processes in PADME in standard run conditions ($\simeq 28 \times 10^3$ POT/bunch corresponds to $N_{POT} = 1.11 \times 10^{11}$/day,). Acceptance corrected cross sections $\sigma*$ and daily production rates (N*). The MC generators used are also reported.*

Process	σ [pb]	**N/10^{11}POT**	$\sigma*$ [pb]	**N*/10^{11}POT**	**Generator**	E_{beam} [MeV]
$e^+e^- \to \gamma\gamma$	$1.55E9$	$1.8E6$	$0.12E9$	$1.3E5$	CalcHEP	550
$e^+e^- \to \gamma\gamma\gamma$	$0.170E9$	$1.9E5$	$0.01E9$	$1.2E4$	CalcHEP	550
$e^+N \to e^+N\gamma$	$4E12$	$4.7E9$	$4E12$	$\simeq 1E9$	GEANT4	500
$e^+e^- \to e^+e^-\gamma$	$0.18E12$	$2.1E8$	$0.131E9$	$1.5E5$	CalcHEP	550
$e^+e^- \to e^+e^-$	$0.5E12$	$5.8E8$	$3.3E9$	$3.4E6$	CalcHEP	500
$e^+e^- \to 2(e^+e^-)$	$1.2E8$	1.4×10^5	$< 1.2E6$	$< 1.4E3$	CalcHEP	500
$e^+e^- \to 3(e^+e^-)$	$1.5E3$	2	not known	not known	/	500

In Table 2.4 all these processes are also reported with the total cross section, the acceptance corrected cross section and the number of events produced in a standard day of data taking of PADME .

2.4 PADME sensitivity

In absence of peaks in the squared missing mass spectrum, PADME can extract the limit on the ϵ parameter as a function of the mass $M_{A'}$. The sensitivity of PADME experiment was extracted from simulation and assuming a total luminosity of 4×10^{13} Positron On Target (POT). The maximum density of the beam that gives a good rejection of pileup events, is $N_{e^+}/\Delta t \simeq 100$ e$^+$/ns. Assuming a bunch multiplicity of 30000 e$^+$/bunch, the experiment needs one year of running to reach the above luminosity. The number of events can be estimated as follows:

$$N(A'\gamma) = N_{\gamma\gamma}^{tot}\epsilon^2\delta(M_{A'})Acc(A'\gamma) = \epsilon^2\delta Acc(A'\gamma)N_{POT}\sigma(e^+e^- \to \gamma\gamma)N_{e^-}/S_{target} \simeq 10^8\epsilon^2\delta \tag{2.8}$$

for $\sigma(e^+e^- \to \gamma\gamma) = 1.55$ mb, which corresponds to a beam energy of $E_{beam} = 550$ MeV, and $Acc(A'\gamma) \sim 20\%$ from MC simulation. As it is shown in Table 2.3, the δ factor can be considered ~ 2 for masses of A' below $M_{A'} < 15$ MeV and the number of electron on target surface N_{e^-}/S_{target} is equal to 0.0105 b^{-1} for 100 μm thick Diamond. Under the assumption that $N_{signal} < N_{bkg}$, the limit on ϵ^2 at 68% of confidence level is $\sim 10^{-6}$, as Figure 1.11 (b) shows. The maximum value of the A' mass for the experiment is fixed by the energy of the beam. Since the maximum E_{beam} that the LINAC can accesses is 550 MeV, the maximum A' mass that PADME can investigate is $M_{A'} = 23.7$ MeV.

2.5 Other physics models beyond the SM

The PADME experiment can search for other dark particles in addition to the dark photon, like the dark Higgs. It can also probe a different theoretical scenario, looking for axion like particles. Furthermore, the PADME collaboration is investigating the possibly to confirm or exclude the existence of the X_{17} [91] boson observed nowadays only in nuclear experiment, as described in 1.2.3.

2.5.1 Dark Higgs

The dark Higgs [90] h' is introduced in theoretical models where the mass of the A' boson is generated through the spontaneous symmetry breaking mechanism. The dark Higgs can be produced in PADME via Higgs-strahlung $e^+e^- \to A'h'$. If $m_{h'} \geq 2M_{A'}$ the dark Higgs will decay in two dark photons. If A' decays in visible particles, $A' \to e^+e^-$, the dark Higgs can be discovered using the veto system with a multi-lepton time coincidence request. For a center of mass energy of $\sqrt{2m_eE_{beam}} \sim 22$ MeV, the dark Higgs production has a cross section not negligible with respect to the SM process $e^+e^- \to e^+e^-e^+e^-e^+e^-$ (which scale as $\epsilon^2 \times \alpha \times \alpha_{dark}$). More precisely:

- the cross section of the dark Higgs production is of the order of $\sigma(e^+e^- \to h'A' \to 3(e^+e^-)) \sim 1000$ pb;
- the cross section of the SM process that produce six leptons in the final state is $\sigma(e^+e^- \to 3(e^+e^-)) \sim 1500$ pb.

In this kind of search, a factor to consider is the acceptance of the experiment to observe six leptons. The studies on the sensitivity are ongoing.

2.5.2 ALP particle

The experiment can be also used to test other models, like the one that, to solve the strong CP problem, introduces the axion, a pseudoscalar particle generated by the spontaneously broken $U(1)$ Peccei-Queen symmetry. PADME can look for a Axion Like Particle (ALP) α with masses of the order of MeV-GeV. ALPs can be produced in accelerator-based experiments and they can be a portal between the SM and the dark sector. The communication between the visible and invisible sector is allowed by an effective interaction with photons and fermions. In the first case, the ALP can decay in two ordinary photons $\alpha \to \gamma\gamma$ thorough the coupling $g_{\alpha\gamma\gamma}$, in the second one the ALP can decay in two leptons $\alpha \to e^+e^-$ thorough the coupling $g_{\alpha ee}$.

The production of the ALPs in PADME could occur via annihilation $e^+e^- \to \gamma\alpha$, then its decay depends on the two coupling factors [92].

3 PADME data taking and beam studies

The installation of the PADME detector began in July 2018, and already on September 15th, the experiment started taking data. PADME tested several beam configurations with the aim of understanding the sources of beam induced background and reducing to a minimum the occupancy of the PADME detectors. The effort of minimising the beam related background was particularly addressed to ECAL, used to detect the SM photon produced along with the dark photon in signal events and for the identification of the $e^+e^- \to \gamma\gamma$ process and to the positron veto detector, responsible for the identification of forward Bremsstrahlung photons. After RunI, calibration runs were taken during summer 2019 both to study the beam related background and to commission and calibrate the detectors. During RunII, from September to

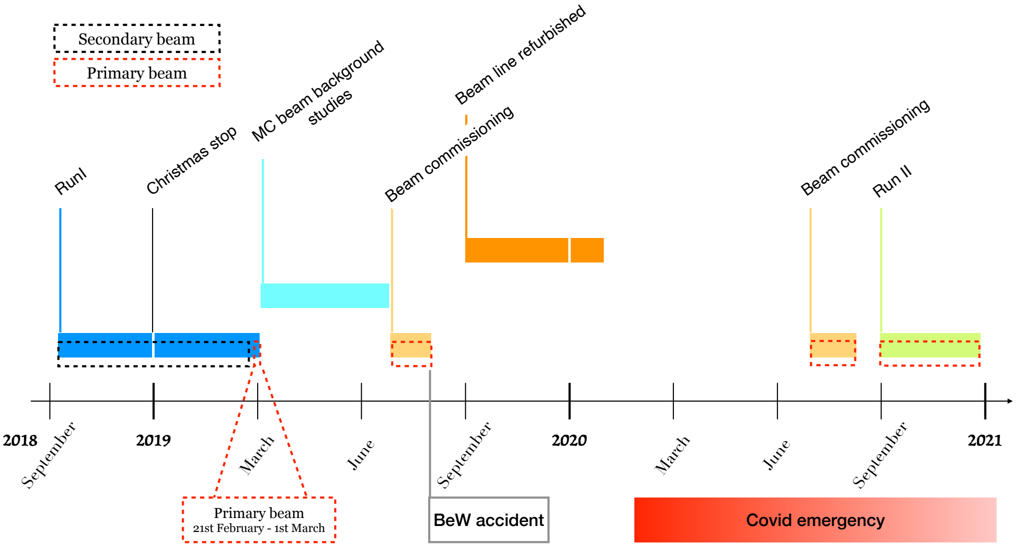

Figure 3.1: *Timeline of the PADME data taking.*

December 2020, PADME collected data in the best background conditions. Figure 3.1 shows a plot of the evolution of the data taking. In this chapter the understanding of the main sources of the beam background and the solution adopted to reduce it are summarised. Then the quality of data collected in RunII is presented.

3.1 RunI

At the time of RunI the old beam line, sketched in Figure 2.2 (a), was in place. The first few weeks of data taking (from 15th September to 31st October) were devoted to beam and detector commissioning; from 1st November 2018 to 21st February 2019, with a small interruption in December 2018, PADME took data in the following default configuration:

- beam energy of 545 MeV;
- $\sim 20 \times 10^3$ POT/event, where the event corresponds to a beam bunch;
- bunch length of ~ 250 ns.

Later, dedicated studies of the background in data were performed and PADME took data until the 1st of March with a primary beam of energy equal to 490 MeV and a bunch length of 150 ns. Figure 3.2 shows the trend of the integrated luminosity collected by PADME from the 1st of November until the beginning of March. The total luminosity acquired by PADME during RunI is $L_{RunI} = (6.37 \pm 0.32_{sys}) \times 10^{12}$ POT.

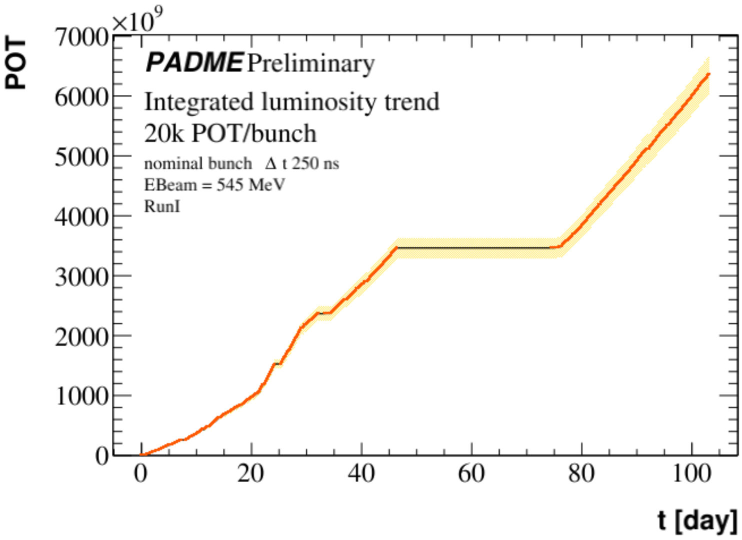

Figure 3.2: *Integrated luminosity collected by PADME in RunI: the orange dots represent the cumulative measurement of the POT (Positron On Target) as a function of the data taking day; the yellow band shows the systematic error (5%).*

Table 3.1: *Main parameters of the runs used to compare data collected with secondary and primary beams during RunI.*

	Secondary beam sample	**Primary beam sample**
Run number	0000000_20181217_203029	0000000_20190724_152634
Beam energy	545 MeV	490 MeV
POT/bunch	17000	23000
POT_{tot}	1.87×10^9	9.06×10^9
Bunch length	250 ns	150 ns

During the beam commissioning data taking of July 2019, some of the runs were recorded in the same conditions as in the latest phase of RunI. In particular, run 0000000_20190724_152634, hereafter indicated as "golden run", represents a data set with primary beam and the old beam line. Therefore, in this chapter the golden run is used as a benchmark for the data quality in RunI with the primary positron beam.

3.2 Comparison of the background in PADME with two different beam setups

The features of two runs used for the comparison of data collected with the secondary and primary beams in RunI are summarised in Table 3.1. The background level of the two samples is estimated using the main calorimeter. Figure 3.3 (a) shows the distributions of the total energy in ECAL, overlayed in different colors for data collected with the secondary (red) and

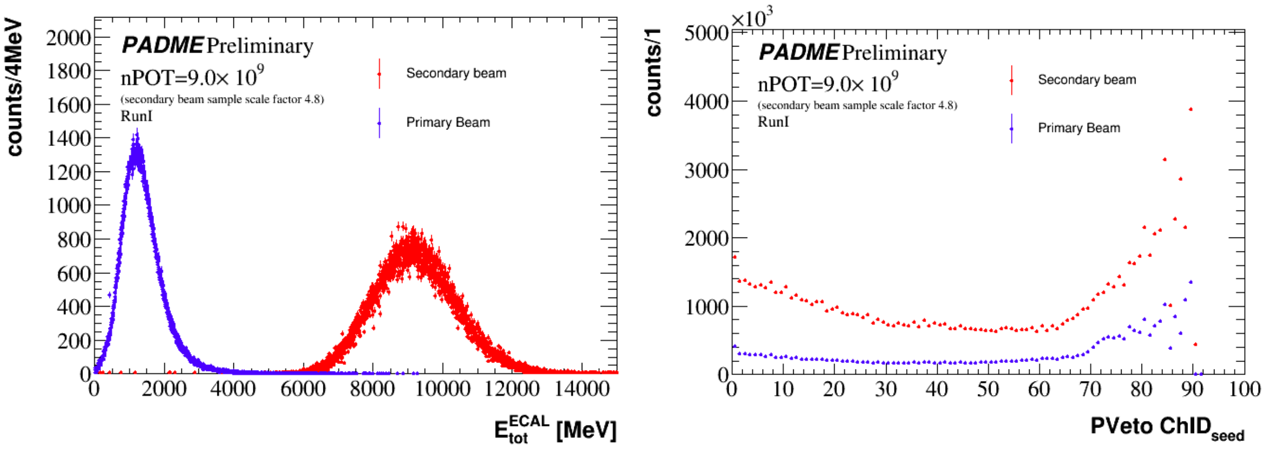

(a) (b)

Figure 3.3: *Comparison between the RunI data collected with secondary (red dots) and primary beam (blue dots). (a) Total energy distribution in ECAL; (b) profile of the positron cluster seed channel ID.*

primary (blue) beam, while Figure 3.3 (b) shows, for the same runs, the number of hits observed in each channel of the positron veto detector. Plot (a) shows that the energy deposited in PADME for each bunch of the secondary beam is much higher than in the run recorded with the primary beam. In more details:

- Secondary beam: the total energy in ECAL is $E_{tot}^{ECAL} = 9220 \pm 1200$ MeV, where the error is represented by the sigma of the gaussian distribution. For the same run the multiplicity is $N = 16770 \pm 730$ POT/bunch (mean and sigma of the distribution). Thus the background per positron is given by $< E_{tot} > / < N >= 0.551 \pm 0.073$ MeV/e$^+$;

- Primary beam: the total energy in ECAL is $E_{tot}^{ECAL} = 861 \pm 433$ MeV and the number of POT per bunch is $N = 23420 \pm 933$ POT/bunch, thus the background level is $< E_{tot} > / < N >= 0.037 \pm 0.019$ MeV/e$^+$.

These numbers clearly tell that the use of the primary beam, leading to a background reduction by more than one order of magnitude, is mandatory. Also in the PVeto the occupancy is lower in the primary beam configuration. Indeed, Figure 3.3 (b) shows that with the secondary beam the total occupancy of 21 central scintillators (from channel ID 40 to 60) normalised to the bunch luminosity is ~ 775. This is reduces by a factor of ~ 4.6 in the primary beam run.

3.3 MC simulation

The initial MC was missing the simulation of the beam line. Later the main components shown in Figure 2.2 (a) were added. Among them the DHSTB002 magnet, with its inner chamber and pipes, sketched in Figure 3.4 (c). This magnet is used to bend the positron beam into the PADME hall. The simulation of the inner chamber was developed using the real measurements provided by the corresponding CAD project, shown in Figure 3.4 (a); also the complete pipe structure inside the magnet was simulated, as shown in Figure 3.4 (b).

The simulation was used to identify the main beam background sources. Photons produced in the interaction of the beam with the walls of DHSTB002 and by positrons off momentum grazing the inner part of the magnet and the vacuum pipe are identified as the main responsible for the beam induced background. However, the simulation of the DHSTB002 magnet is not enough to reproduce the amount of background observed in data. As a second upgrade of the simulation the Beryllium window was added, separating the vacuum of the PADME beam line from the more stringent atmosphere of the LINAC beam line. The resulting simulation of the experiment and of the beam line is shown in Figure 3.5.

Using this more detailed simulation, a sample was generated with the following features:

- $E_{beam} = 490$ MeV with an initial energy spread of 1.55 MeV and a Gaussian spot of width $\sigma = 0.01$ mm in both directions;

- N_{POT}/bunch = 23000 before the Beryllium window; after propagation in the beam line 22680 N_{POT}/bunch reach the target with a spot of $\sigma_x \times \sigma_y = 3.2 \times 2.4$ mm;

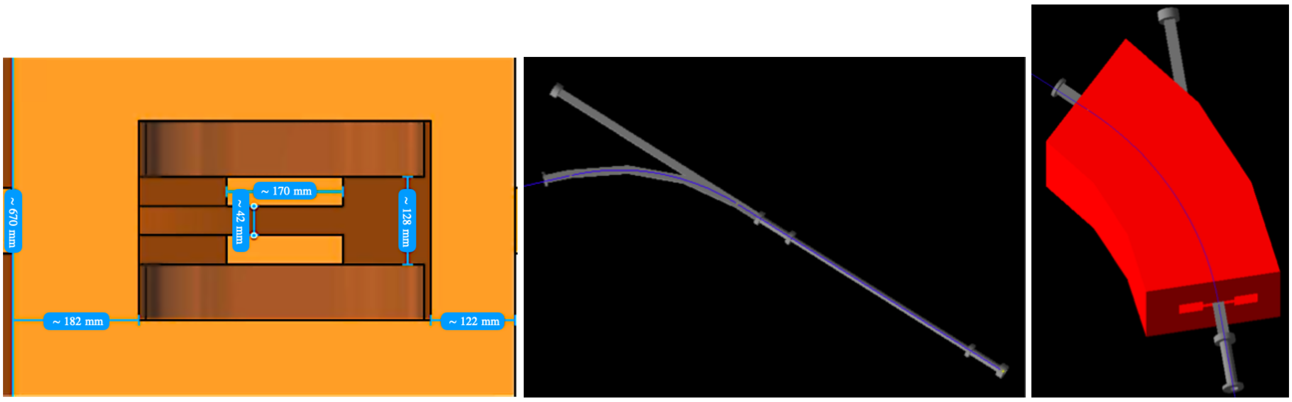

(a) (b) (c)

Figure 3.4: *(a) Top view of the inner chamber of DHSTB002; (b) pipe line inside the magnet simulation from GEANT4; (c) simulation of the magnet with all the components from GEANT4.*

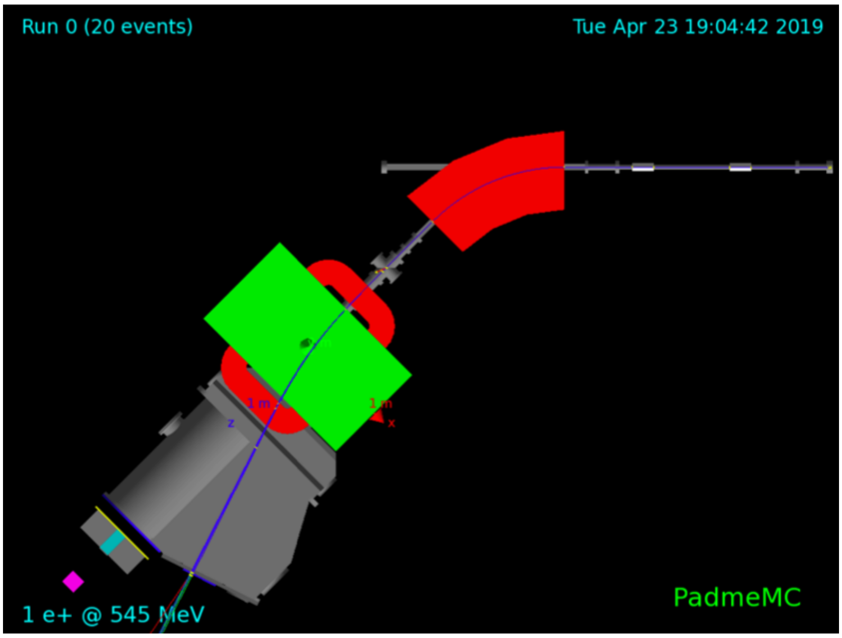

Figure 3.5: *Simulation of the PADME experiment with the main components of the beam line.*

- bunch length of 150 ns.

These parameters defining the beam at the entrance of the Beryllium window, allow to reproduce the information collected by the Active Diamond Target observed in data

The simulation was reconstructed using the same software used for the reconstruction of the PADME data. In particular, the energy released in ECAL crystals according to GEANT4, was converted in waveforms and processed with the same reconstruction code developed for data (a detailed description of the algorithm is given in Chapter 4). The total energy recorded in ECAL,

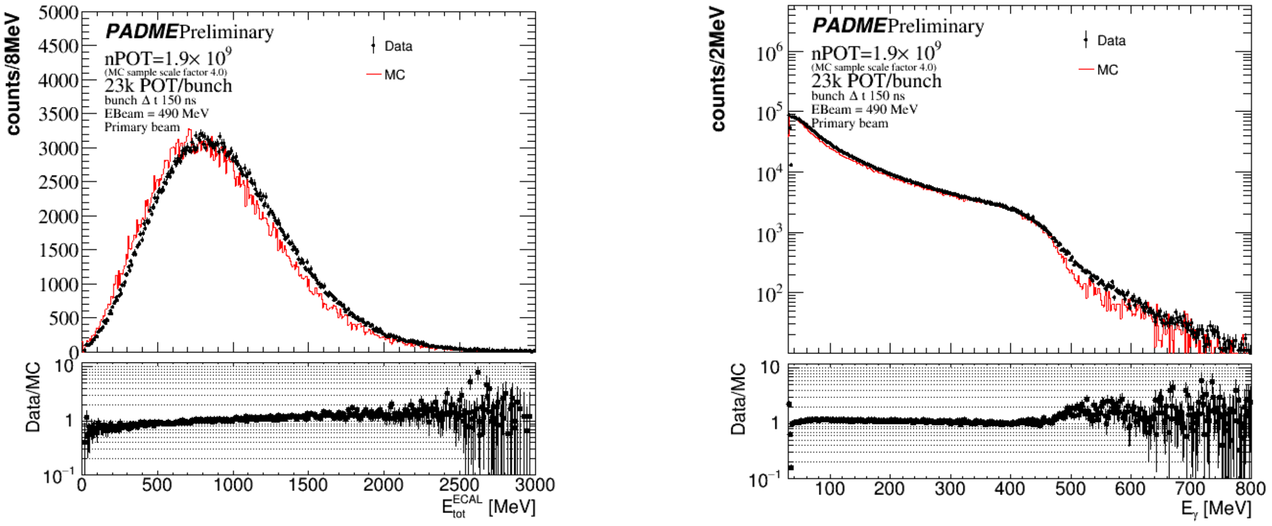

(a) **(b)**

Figure 3.6: *Comparison between data collected with the primary beam (black dots) and MC simulation with the beam line included (red solid line). (a) ECAL total energy distribution; (b) ECAL cluster energy distribution.*

red solid line of the Figure 3.6 (a), is in average $E_{tot}^{ECAL} = 813$ MeV with a width of 445 MeV and the number of POT per bunch reaching the target is $N = 22680 \pm 213$ POT/bunch, thus the background level is $< E_{tot} > / < N >= 0.036 \pm 0.019$ MeV/e$^+$. The distributions of the same quantities obtained with the MC simulation show a slight difference with respect the same distributions represented in data $([< E_{tot} > / < N >]_{Data} - [< E_{tot} > / < N >]_{MC} = 1$ keV) . However the simulation is able to reproduce the main features of the background, as Figure 3.7 shows, where the ECAL cluster maps for (a) the data and (b) MC samples are reported. It is easy to observe that the direction $y \sim 0$ mm at $x < 0$ mm has a slightly higher occupancy than the others. In addition, two separate regions at $y = 0$ mm and $x > 0$ mm appear particularly hot, one at the edge of the central hole and the second, separated by a less noisy region, at around $x \sim 250$ mm. The MC simulation allowed to understand that the two spots appear as a consequence of the window that separate the vacuum of PADME with the vacuum of the LINAC (in this phase Beryllium). In Figure 3.8 the three maps of the clusters recorded in ECAL are shown for the following configurations: (left) beam generated in front of the target, (middle) beam generated at the beginning of the PADME beam line after the Beryllium window and (right) a beam generated in front of Beryllium window. From the comparison, it appears clear that the critical element is the window, where the positrons are subject to multiple coulomb scattering with the nuclei and to Bremsstrahlung much more than it happens in the low density atmosphere inside the beam pipe (which anyway is responsible for the widening of the beam halo in ECAL in Figure 3.8 (b)). In case of multiple scattering, the beam develops a halo that can shower hitting the pipe during transportation. In case of Bremsstrahlung, the emitted

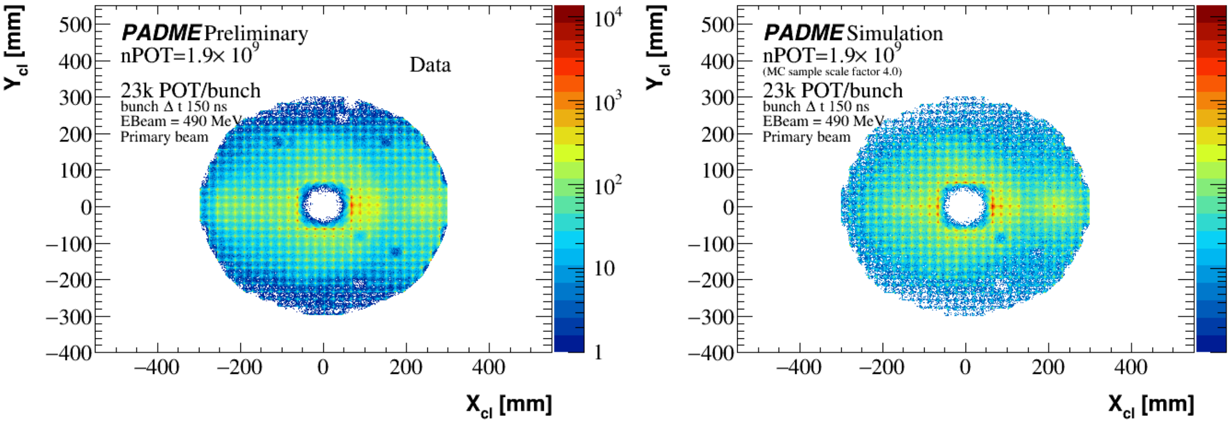

(a) (b)

Figure 3.7: *Map of the clusters recorded in ECAL for (a) data and (b) MC simulation with the beam line included.*

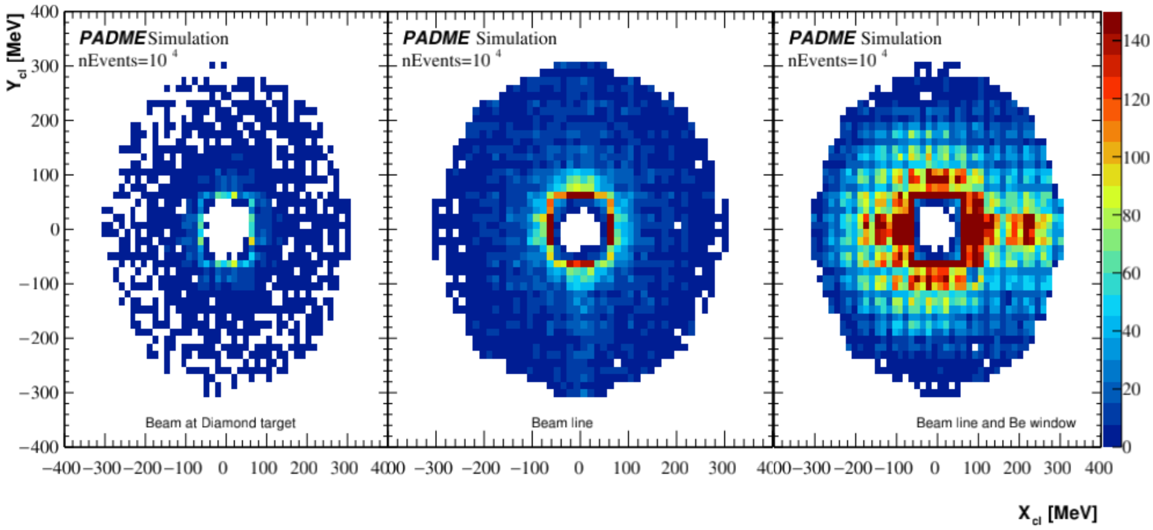

Figure 3.8: *ECAL cluster map for MC simulation with the beam line included: (left) beam generated in front of the target, (middle) beam generated after the Beryllium window at the beginning of the beam line and (right) beam generated in front of the Beryllium window.*

photons travel unaffected by the magnetic fields and may produce secondary charged or neutral particles, that can reach the PADME detector in regions far from the main spot of the positron beam.

3.3.1 Effects of the Beryllium and Mylar windows in MC

The simulation of various components of the beam line allows reproducing in simulation the background level observed in data. In particular, the most important element is represented by the Beryllium window, which separates the PADME and LINAC lines. Beryllium is a light material with $Z = 4$ and $X_0 = 65.19$ gcm^{-}2 [13] and the thickness of the window was equal to 250 μm, corresponding to $7.1 \times 10^{-4} X_0$. An alternative material is Mylar with average atomic number $Z = 3$ [87] and $X_0 = 39.95$ gcm^{-2} [13] . A special simulation was implemented replacing the Beryllium window with a Mylar window 125 μm thick separating the beam lines in a position much further away from the PADME target then the Beryllium window. The material budget of the Mylar window corresponds to only $4.4 \times 10^{-4} X_0$ and the increased distance from the PADME hall is also contributing to reduce the background reaching the detectors. Indeed, the comparison shows as the background level in the main calorimeter is lower when the Mylar separator is used, as suggested by Figure 3.9 (a). The distribution of the photons in ECAL exhibits the same features with respect to the sample simulated with the Beryllium window, see Figure 3.9 (b), but the overall rate is considerably reduced.

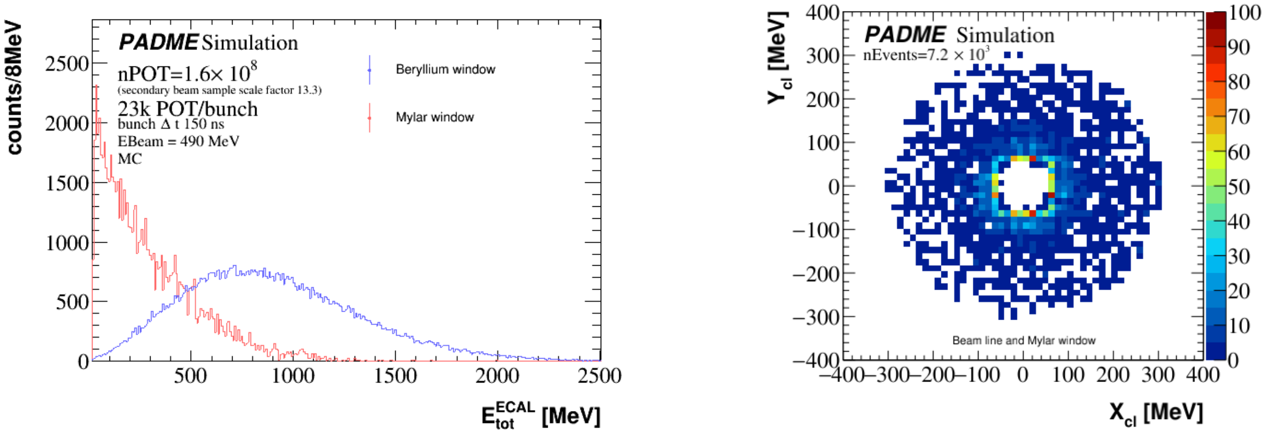

(a)

(b)

Figure 3.9: *(a) Total energy in ECAL for the MC samples simulated with the Beryllium window vacuum separation (red) and Mylar one (blue). (b) Map of the ECAL clusters for the MC sample simulated with the vacuum separation window made of Mylar.*

At the end of the beam commissioning campaign of July 2019 it was decided to move the Beryllium window just in front of the Active Diamond Target. In this configuration, the positrons losing energy in the vacuum separator would not have any path before the target and, therefore, they would not have the chance of showering in the materials of the beam line and producing a diffuse background in the experiment. The relocation of the Beryllium window took place, but unfortunately, while restoring the vacuum an accidental overpressure broke the window and the beam line was polluted by the Beryllium fragments. This required the refurbishing of a long section of the beam line. The stop caused by the accident was exploited

Table 3.2: *Main parameters of the run used for the commissioning of RunII beam.*

	Primary beam sample
Run number	0030563_20201026_121402
Beam energy	430 MeV
POT/bunch	27000
POT_{tot}	1.2×10^{10}
Bunch length	~ 280 ns

to improve the beam transport line and replace the Beryllium vacuum separator window with a new one made of Maylar located further away from the PADME hall.

3.4 Beam commissioning for RunII

In July 2020 a new beam was commissioned with the main aims to improve the beam stability and reduce the beam background replacing with the following interventions on the beam transportation line:

- substitution of the Beryllium window with a Mylar one;
- replacement of the beam pipe with a new one with a wider cross section;
- installation of additional beam collimators and other quadrupole magnets.

Before the nominal data taking on RunII, several runs were taken in order to understand the quality of data and of the background level in the experiment.

The features of the run used to compare the performance of the new beam line with the previous one are summarised in Table 3.2. The amount of beam related background in the experiment is improved with respect the old beam line. This is clearly shown in Figure 3.10 where a direct comparison between background levels in RunI with primary beam (golden run and blue distributions) and of RunII (green distributions) are reported. Both data samples were collected with a beam of primary positrons of similar features, therefore, the only difference lies in the beam line structure. From Figure 3.10 (a) the average total energy in ECAL is found to be $E_{tot}^{ECAL} = 71 \pm 350$ MeV in RunII. Since the number of POT per bunch is $N = 26796 \pm 1131$ POT/bunch, the background level is $< E_{tot} > / < N >= 0.0027 \pm 0.0130$ MeV/e^{+} corresponding to a fraction of the background per positron in RunI as low as 7%. an improvement of $\sim 93\%$ with respect to RunI. The clusters profiles in the PVeto are reported in Figure 3.10 (b). The reduction of the beam background is clearly visible at low channel ID. Instead, at high channel ID, where the rate is dominated by Bremsstrahlung positrons, the cluster rate is apparently higher in RunII. However this is due to saturation in RunI due to the large beam background. Indeed, if the occupancy is normalised to the bunch luminosity of the run, one finds that the PVeto occupancy in RunII for channel ID in the range [40,60] is 14% lower than RunI.

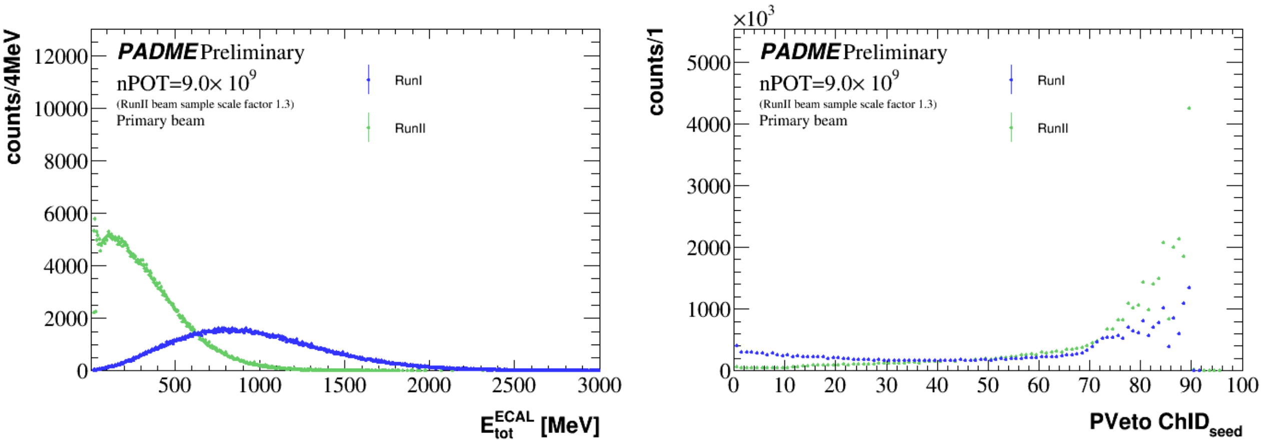

(a) (b)

Figure 3.10: *(a)Total energy distribution in ECAL and (b) profile of the cluster seed channel ID of PVeto. Data collected during beam commissioning of RunII (green dots) and during the so called "golden run" of RunI (blue dots).*

3.4.1 Event pileup studies using the annihilation process

In order to choose the better configuration for data taking, a study of event pileup in ECAL was done during the beam commissioning for the RunII. For this purpose, runs with different bunch multiplicity were collected in two configurations: standard data taking and a few special runs with the Active Diamond Target, and its mechanical support, out of the beamline. These latter runs allowed to estimate the beam related background not overlapped with beam interactions in the target. A summary of all these runs is reported in Table 3.3, all corresponding to a beam energy of $E_{beam} = 450$ MeV and a bunch length of ~ 150 ns.

Time and spatial distribution of the beam

Figure 3.11 shows the time structure of the bunch as observed by the ECAL detector for all runs taken with the target in the nominal position. This is given by the time distribution of all ECAL clusters. The distribution have two abroad peaks in the initial and final parts of the bunch and a very broad peak in the middle. This structure is due to the formation and acceleration of the bunch. The electron gun emits a flat bunch with a fixed length whose value is defined by the user. However, later the frequencies and phases of the RF cavities needs to be carefully modulated in order to keep the time structure of the bunch as uniform as possible by providing accelerated micro bunches of similar intensity. This tuning is not trivial and not very successful at low intensity of the beam, such as the case of 5×10^3 POT/event where three peaks clearly emerge. A good beam feature observed with the new beam line was a tight beam spatial distribution at the target. Figure 3.12 shows the beam profile in the X (a) and Y (b) views measured for all runs with the target located regularly in the beamline. While the average positions of the beam along the Y axis were the same for all runs, along the X

Table 3.3: *Summary of the runs used to study the pileup effect in ECAL .*

Run number	Target in the beam	Target out of the beam	$(N_{POT}/\text{event})\ /10^3$	$N_{POT}/10^9$
0030211_20200722_191822	✓		5	3.7
0030220_20200723_054920		✓	5	\
0030205_20200722_081640	✓		10	2.4
0030207_20200722_115800		✓	10	\
0030201_20200721_224335	✓		15	5.6
0030202_20200722_010224		✓	15	\
0030203_20200722_031723	✓		20	7.7
0030204_20200722_054045		✓	20	\
0030209_20200722_143634	✓		25	9.12
0030210_20200722_173655		✓	25	\

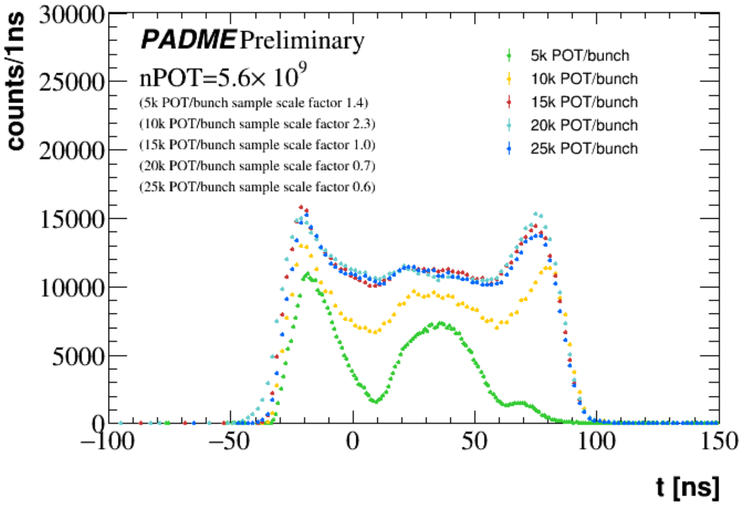

Figure 3.11: *ECAL time cluster distribution for runs with different bunch multiplicity in RunII commissioning and beam energy of* 450 MeV*.*

axis a shift towards the center of the target (strip 8) for increasing multiplicity was visible. A consequence of the well focused beam on the target was the saturation of the front-end of the Active Diamond Target and then a biased reconstruction of the number of positrons per event for $N_{POT/bunch} > 15 \times 10^3$. Figure 3.13 (a) shows the distributions of the number of positrons per event, reconstructed assuming a linear response. The N_{POT} reconstruction fails at high bunch multiplicity due to the target saturation. Therefore, the reconstruction was updated in order to match the average target response to the nominal number of positrons per bunch provided by the LINAC diagnostic equipment based on BGO calorimeter (often referred as BTF calorimeter), that is assumed as a reference measurements. Figure 3.13 (b) shows the

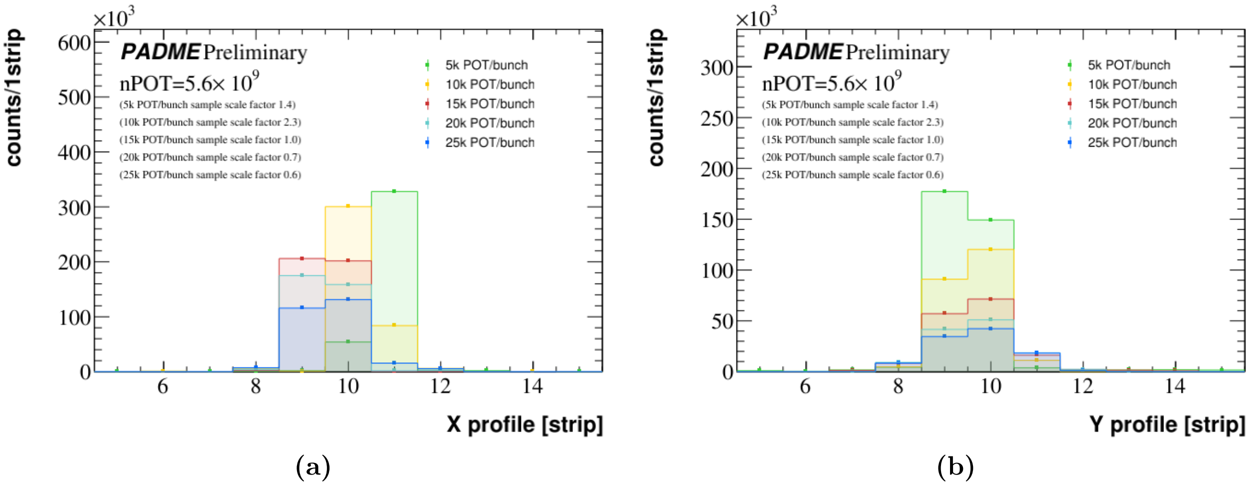

(a) (b)

Figure 3.12: *X (a) and Y (b) beam profiles reconstructed by the Active Diamond Target for different bunch multiplicity during RunII commissioning and beam energy of* 450 MeV*.*

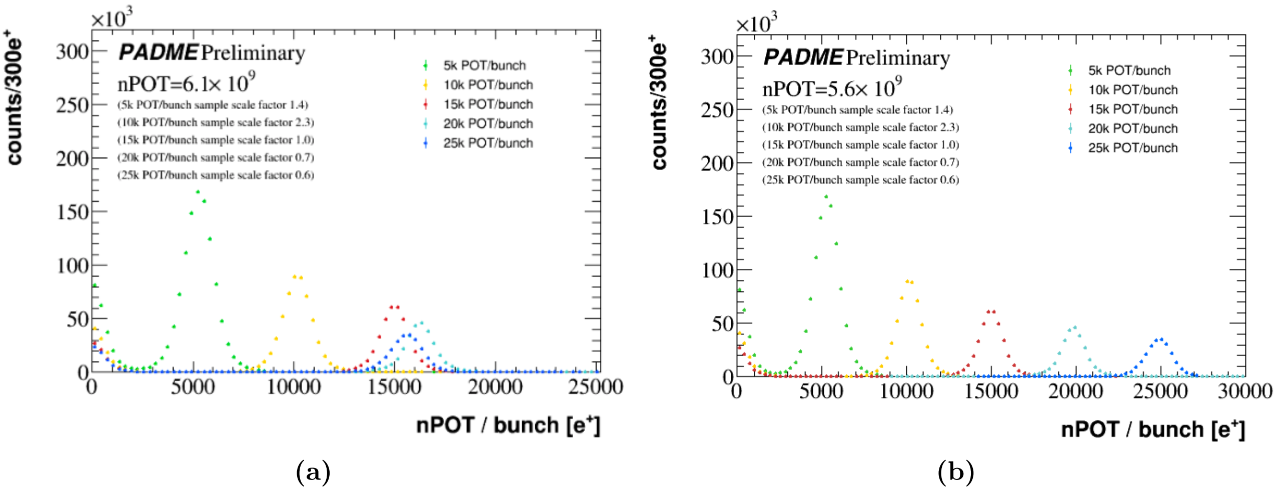

(a) (b)

Figure 3.13: *Number of positrons reconstructed with the Active Diamond Target in RunII commissioning and beam energy of* 450 MeV*. (a) assuming RunI calibration with unfocused beam; (b) after applying a correction factor to compensate the Active Diamond Target front-end saturation, due to RunII focused beam, and to match the BTF calorimeter multiplicity measurements.*

positron multiplicity per bunch obtained in several runs after this recalibration.

$e^+e^- \to \gamma\gamma$ selection

The physics channel $e^+e^- \to \gamma\gamma$ was used to assess the effects of the pileup on the ability to identify physics processes over the combinatorial background and to measure correctly their rate.

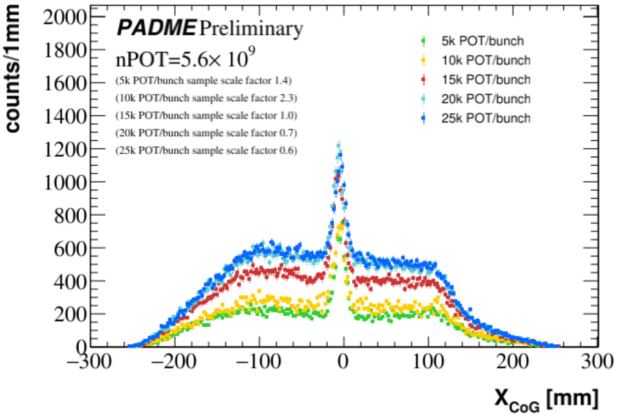

(a) **(b)**

Figure 3.14: *Two-photon center of gravity for the X (a) and Y (b) coordinates for runs of different bunch multiplicity before any two-photon annihilation cuts.*

A simple selection was applied on non empty events (i.e. events with a measured number of $N_{POT} > 5000$ events in all runs except for run $0030211_20200722_191822$, where $N_{POT} > 1800$) was requested) by applying the following requirements:

1. at least two clusters. i.e. photon candidates, reconstructed in ECAL;
2. time coincidence between two photons $|\Delta t| = |t_{\gamma_1} - t_{\gamma_2}| < 10$ ns;
3. both photons in the region (hereafter indicated as fiducial region, FR): $R_\gamma \in [92\,\text{mm}, 258\,\text{mm}]$ to avoid badly reconstructed photons at the border of the calorimeter;
4. x and y coordinates of the two-photon Center Of Gravity (COG) $x(y)_{CoG} = \frac{x(y)_{\gamma1}E_{\gamma1}+x(y)_{\gamma2}E_{\gamma2}}{E_{\gamma1}+E_{\gamma2}}$ within 50 mm from the origin;
5. energy of the photons $E_\gamma > 90$ MeV.

At the energy of PADME and within the acceptance of ECAL, the latter two requirements would be fully satisfied by annihilation events if the energy and position measurements were very precise, due to stringent kinematic constraints. Figure 3.14 shows the distribution of X_{CoG} and Y_{CoG}, where the narrow peaks at zero correspond to annihilation events. Figure 3.15 shows the sum of the energy of the two photons that pass all selection cuts for the runs with $N_{pot/bunch} = 15 \times 10^3$ (red dots) and the one without the target in the beam (pink dots). As the plot shows, the data collected without the target predict most of the background due to electromagnetic showers produced in the interaction of the beam with the beam line.

The background distribution for that variable was almost flat and a normalisation factor was obtained comparing the integrals of the two distributions in the range $\Delta t \in [-10\text{ ns}, -7\text{ ns}]$.

Form the distribution of Figure 3.15, the annihilation yield was estimated by subtracting the distribution from the run with the target out of the beam line and integrating in the range

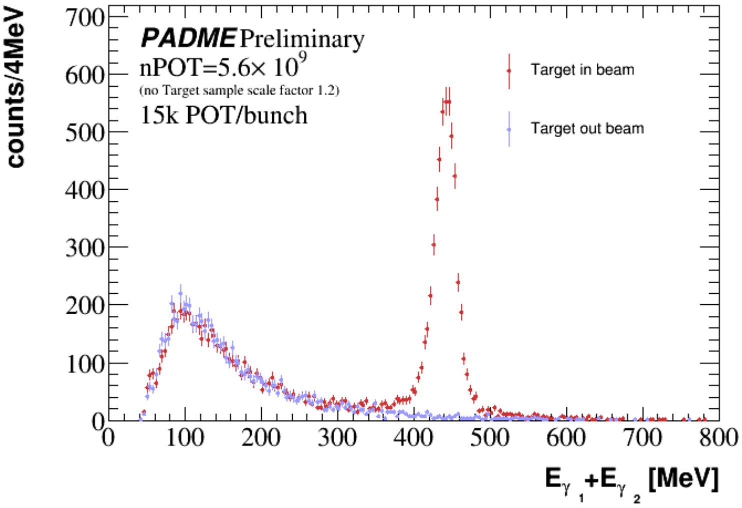

Figure 3.15: *Sum of the photon energies that pass the selection cuts 1,2 and 3 for bunch multiplicity* $N_{pot/bunch} = 15 \times 10^3$ *with the target in the beam line (red dots) and without the target in the beam line (pink dots).*

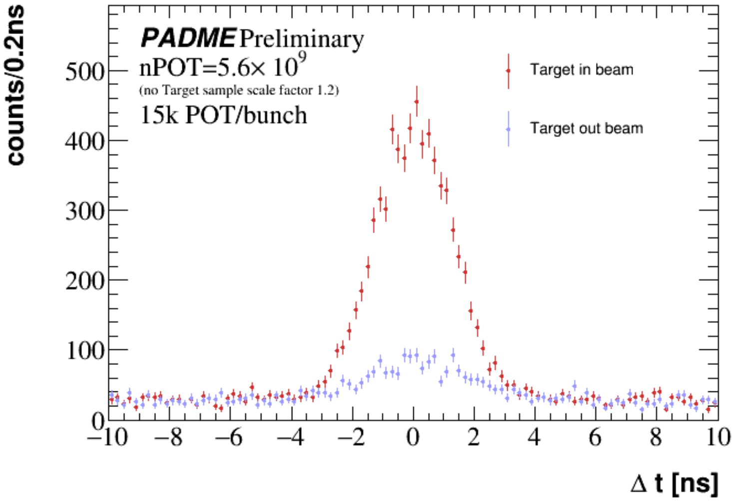

Figure 3.16: *Two-photon time difference for bunch multiplicity* $N_{pot/bunch} = 15 \times 10^3$ *with the target in the beam line (red dots) and without the target in the beam line (pink dots) after selection cuts 1, 2 and 3.*

$[300, 700]$ MeV. Since the run without target has no N_{POT} measurement, the two data samples were normalised using the distribution of $\Delta t = t_{\gamma_1} - t_{\gamma_2}$ reported in Figure 3.16. The yield of annihilation events obtained in the different data samples, normalised to 5.6×10^9 POT, are reported in Table 3.4. In Figure 3.18 the ratio between these measurements and the theoretical prediction is shown as a function of the density of positrons in the bunch. Detection and reconstruction efficiencies are responsible for a factor common to all measurements and the

Table 3.4: *Number of annihilation event candidates, with their statistical error, observed in different conditions of* N_{POT}*/bunch. Results are normalised to the total number of POT of* 5.6×10^9 *using the scale factors* Sf*. The ratio of each measurement to the yield observed at* 15000 POT/bunch *is also reported.*

$(N_{POT}/\text{bunch})\ /10^3$	Sf	$e^+e^- \to \gamma\gamma$ **yield**	N_{gg}/N_{gg}^{15k}
5	1.49	4231 ± 79	0.76
10	2.38	5797 ± 117	1.04
15	1.	5568 ± 75	1.
20	0.74	5891 ± 66	1.06
25	0.62	5257 ± 57	0.94

ratio should be constant. A trend in the ratio might be indicative, for example, of a loss of efficiency at increasing pileup. The predicted yield is estimated as follows:

$$N_{\gamma\gamma} = N_{POT} \times A \times N_{e^-/S} \times \sigma(e^+e^- \to \gamma\gamma) \tag{3.1}$$

where $A = 0.0681$ is the acceptance estimated with CalcHEP generator, $N_{e^-/S} = 0.0105$ b^{-1} corresponds to the number of electrons per unitary surface in the Active Diamond Target and $\sigma(e^+e^- \to \gamma\gamma) = 1.81$ mb is the tree level cross section for a positron with energy $E = 450$ MeV and an electron at rest, according to CalcHEP. In order to study possible biases coming from the measurement of the number of positrons in the bunch, the total N_{POT} in each sample was evaluated using three different methods:

- $N_{BTFtrigger} \times N_{POT/event}^{BTF}$, where $N_{BTFtrigger}$ is the number of BTF triggers and $N_{POT/event}^{BTF}$ is the nominal measurement of the beam multiplicity performed with the BTF calorimeter by the BTF staff at the beginning of the run;
- N_{POT}/event from the target, using the linear algorithm corrected by an empirical factor to match the BTF calorimeter measurement;
- $N_{SACtrigger} \times N_{POT/event}^{BTF}$, where $N_{SACtrigger}$ is the number of events that pass the requirements of a minimum number of SAC clusters. In fact, the SAC detector is quite sensitive to the number of POT, since most of the Bremsstrahlung photons fall in its acceptance. As shown in Figure 3.17, the SAC calorimeter response provide a clear way to identify the events with no interactions in the target. Therefore, a cut of $N_{cl}^{SAC} > 1$ was applied to the run with 5000 POT/event, $N_{cl}^{SAC} > 6$ for 10000 POT/event and $N_{cl}^{SAC} > 10$ for all other runs.

In Figure 3.18 empty dots correspond to annihilation events that pass the time coincidence, FR and CoG requests. solid markers correspond to the same selection with the additional request of the energy threshold. The different colours indicate the technique used to estimate the total number of POT: orange for the measurement by the target, pink for the measurement based on

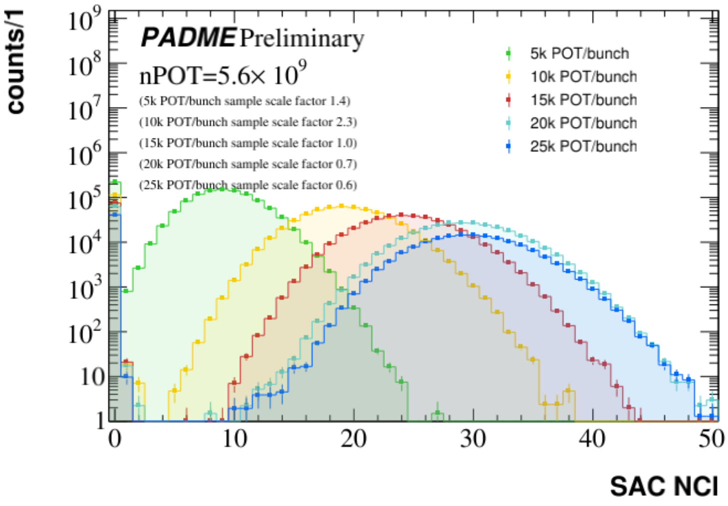

Figure 3.17: *Distribution of the number of clusters in the SAC for runs of different beam multiplicity.*

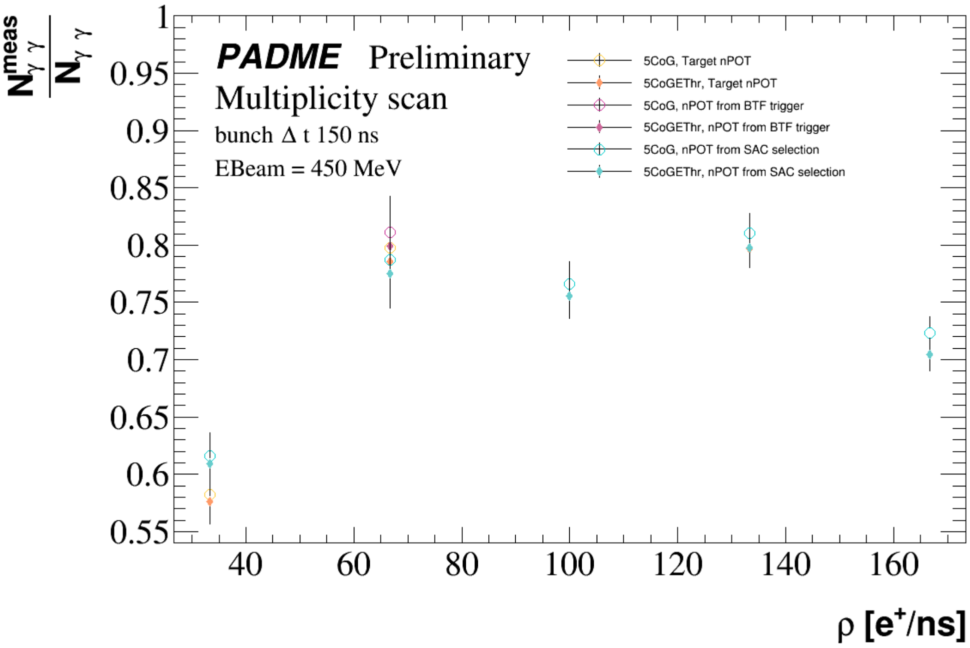

Figure 3.18: *Ratio between measured and predicted annihilation yield as a function of the bunch density. The empty dots correspond to the annihilation events that pass the time coincidence, the FR and the CoG requests. The full dots correspond to the annihilation events that pass the same selection with the additional request of the energy threshold. The different colours indicate the technique used to estimate the total number of POT.*

the BTF trigger and azure for the measurement based on the number of clusters in the SAC. A pathologically low value of the ratio is observed for $\rho =\sim 35$ e$^+$/ns ($N_{POT/bunch} = 5 \times 10^3$ and bunch length of 150 ns), in spite of the low occupancy, this run exhibits a strongly distorted time structure of the bunch (see Figure 3.11) implying the occurrence of very high density of overlapping events, likely leading to very low efficiency. A constant trend in the range $[60, 140]$ e$^+$/ns was observed, while at higher densities the efficiency starts decreasing. Based on this study the working point for RunII was set to ~ 100 e$^+$/ns. In order to collect as many N_{POT} as possible in a reasonable run time, the bunch multiplicity must be increased, i.e. to 27000 POT/bunch, therefore, the bunch length is increased to ~ 280 ns, keeping the particle density below 100 e$^+$/ns.

3.5 RunII

The data in RunII were collected with the new beam line, sketched in Figure 2.2 (b) under stable beam conditions. The data taking started on September 15th and ended on December 2nd 2020. The default beam configuration was:

- primary beam;
- beam energy of 430 MeV;
- $\sim 27 \times 10^3$ POT/event;
- bunch length of ~ 280 ns;

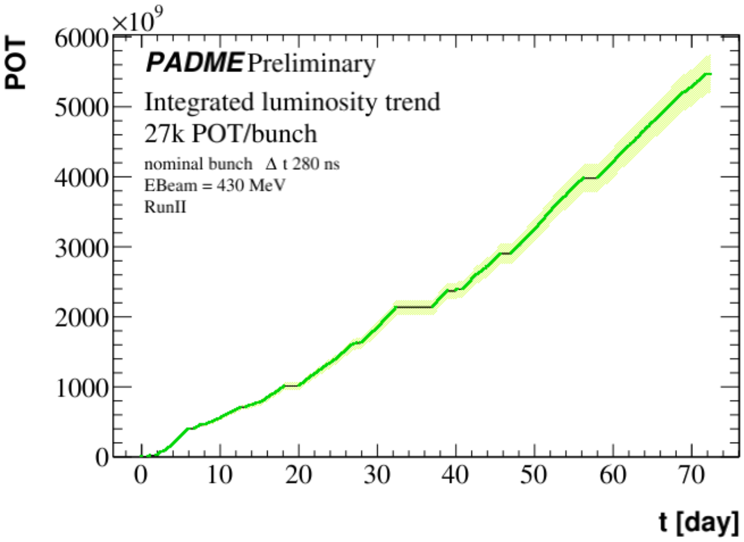

Figure 3.19: *Integrated luminosity for the PADME RunII: the green dots represent the cumulative measurement of the POT as a function of the data taking day; the green band is given by the systematic error (5%).*

Figure 3.19 shows the integrated luminosity trend of PADME for RunII. The total integrated luminosity acquired by PADME is $L_{RunII} = (5.47 \pm 0.27(sys)) \times 10^{12}$ POT.

3.6 Electromagnetic processes

The main physics channels studied with the PADME data were the Bremsstrahlung and the annihilation in two photons, which are also the main backgrounds for the dark photon search. In this section the Bremsstrahlung and annihilation signals as emerging in RunII data are presented along with the resolution on the missing mass. The comparison with RunI is also discussed. I general, an improvement on the physics signals and resolution from RunI to RunII is clearly visible.

3.6.1 Bremsstrahlung

The Bremsstrahlung process $e^+N \to e^+N\gamma$ is detected through a positron recorded in the PVeto and a photon recorded mainly in the SAC, this is due to the fact that most of the photons are emitted in the forward direction. Once the two detectors are aligned in time[1], the following cuts must be applied:

a. time coincidence $|\Delta t| = |t_{e^+} - t_{SAC}| < 1$ ns. The choice of the time coincidence window was done after the assessment of the resolution of the two detectors: $\sigma(t_{PVeto}) \sim 700$ ps and $\sigma(t_{sac}) \sim 80$ ps;

b. fiducial region cut along z: $40 < \mathrm{ChID_{PVeto}} < 70$, in this region the detector was not affected by high pileup or crystals saturation;

c. an energy threshold for the photons detected by SAC detector $E^{SAC}_{thr} \geq 150$ MeV. This threshold corresponds to Bremsstrahlung positrons hitting the veto in $\mathrm{ChID_{PVeto}} < 70$.

The signature of the Bremsstrahlung process is an anti-correlation between the energy of the photon in the SAC and the position where the positron hits the PVeto, expressed as channel ID of the cluster seed.

A comparison of the Bremsstrahlung signature for different beam conditions shows the improvements in the data taking. But before doing this, it is necessary to introduce an energy scale factor for the SAC in data collected with secondary beam.

SAC energy scale for RunI with secondary beam

To determine the SAC energy scale, events, after the application of the Bremsstrahlung time coincidence cut, are considered.

Figure 3.20 (a) shows the correlation between the SAC photon energy and the PVeto channel ID. The expected photon energy reconstructed in SAC has an upper limit given by the energy of the positron beam (this condition is approached when the positron looses almost entirely its energy in a Bremsstrahlung interaction). For PVeto channel ID ≤ 50 the peak in the SAC energy distribution is found at value higher with respect the energy of the beam (545 MeV)

---

[1] The time alignment was done using the central crystal of SAC, the detector with the best time resolution $\sigma(t_{sac}) \sim 80$ ps.

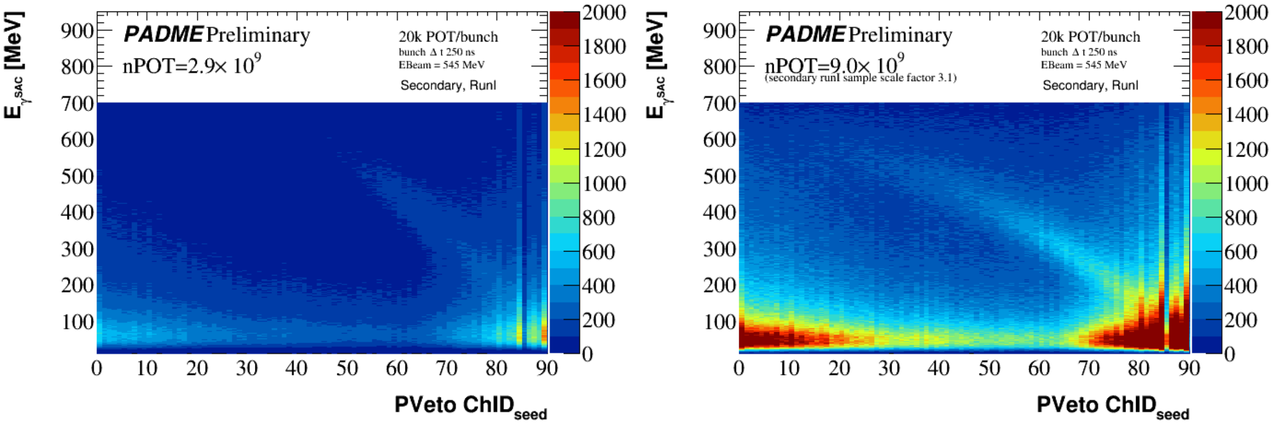

(a) (b)

Figure 3.20: *Correlation between SAC photon energy and PVeto positron cluster seed channel ID in time coincidence* $|\Delta t| < 1$ ns. *(a) Before SAC photon energy calibration. (b) After SAC photon energy calibration.*

indicating the need to introduce an absolute energy scale factor. This was extracted using Bremsstrahlung events with a positron detected in the channel ID range $[43, 69]$. For each of these PVeto channel a Gaussian fit was done to the photon energy distribution, extracting the mean energy of Bremsstrahlung photons as a function of the channel ID. These values were compared with values obtained with the same procedure for data collected with RunI and the 490 MeV primary beam, since in this case the SAC calorimeter was well calibrated. Because of the different beam energy, an additional energy shift was applied to clusters in the SAC. The final energy scale factor, $f_{SAC} = 0.76$, to be applied to the SAC clusters is given by the average ratio between the energies of Bremsstrahlung photons in the two runs. Figure 3.20 (b) shows the correlation obtained after the recalibration of SAC photons. The correction of the energy improved significantly the Bremsstrahlung signature in RunI with secondary beam despite the huge beam background.

Bremsstrahlung signature comparison

The comparison of the Bremsstrahlung signatures for the main data taking periods is shown in Figure 3.21. The scatter plots represents the correlation between the SAC photon energy and the PVeto positron channel ID for events that pass the time coincidence cut. From the comparison of the Bremsstrahlung signatures the reduction of the background level and the improvement in the reconstruction can be appreciated.

PVeto as spectrometer

A charged particle emerging from the target enters in a region with a uniform magnetic field, to be deflected. Therefore, a positron with a given momentum, hits the PVeto in a well defined z

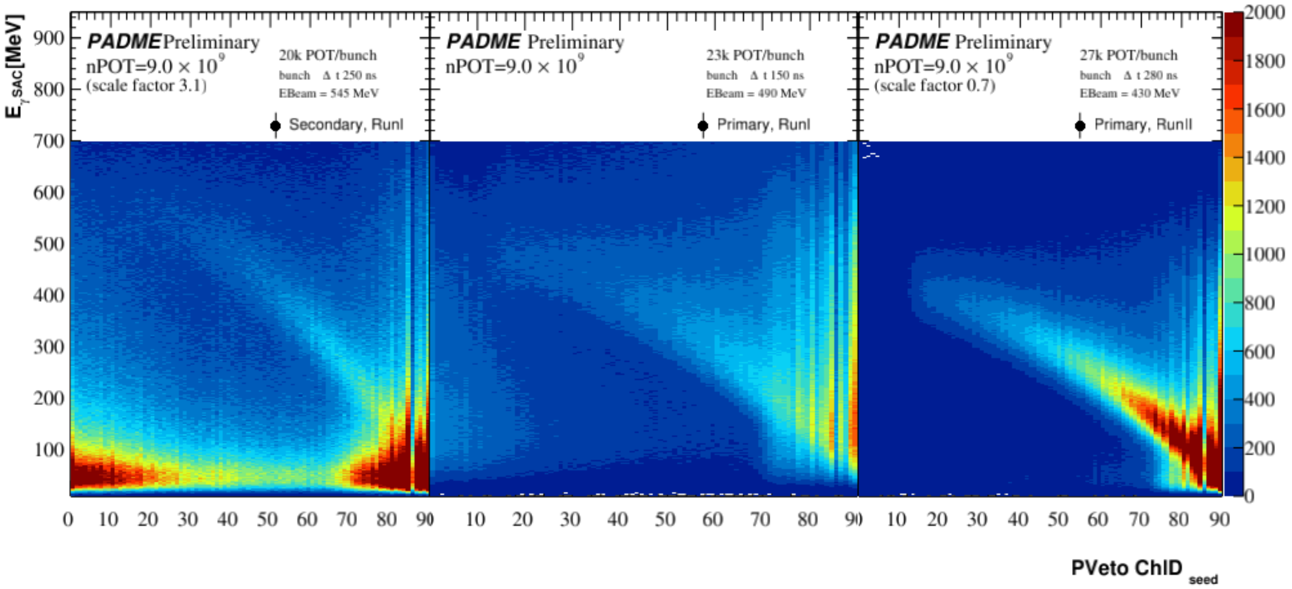

Figure 3.21: *Correlation between the energy of the photon in the SAC and the PVeto channel ID of the cluster seed corresponding to the positron for events passing the time coincidence selection for three different beam configurations: (left) RunI secondary beam, (middle) RunI primary beam, (right) RunII primary beam.*

position. For this reason, a calibration in momentum can be performed, as explained in Section 2.2.3. In the PADME reference frame the correlation between the momentum p and the z coordinate can be written as follows:

$$p(z) = \frac{0.3B[(z - z_c)^2 + x^2]}{2x} \tag{3.2}$$

where z_c is the z coordinate in millimetres of the center of the circular trajectory and it is also the location where the magnetic field sets on, x is the PVeto x coordinate in millimetres and B is the effective value of the magnetic field in Tesla. The parameters obtained by a calibration based on simulation were $B = 0.399 \pm 0.001$ T and $z_c = 631.5 \pm 1.3$ mm [77]. This calibration has been used to compute the sum of the energies of candidate Bremsstrahlung photons and positrons. This is shown in Figure 3.22. The positron energy is approximated with the momentum perpendicular to the magnetic field, relying on the direction of the positrons almost perpendicular to the target and thanks to the negligible mass of the positron. Three different data taking conditions are considered: (left) RunI secondary beam, (middle) RunI primary beam, (right) RunII primary beam. In RunI with the secondary beam, a significant Bremsstrahlung peak appears over a large background at the energy of the beam.

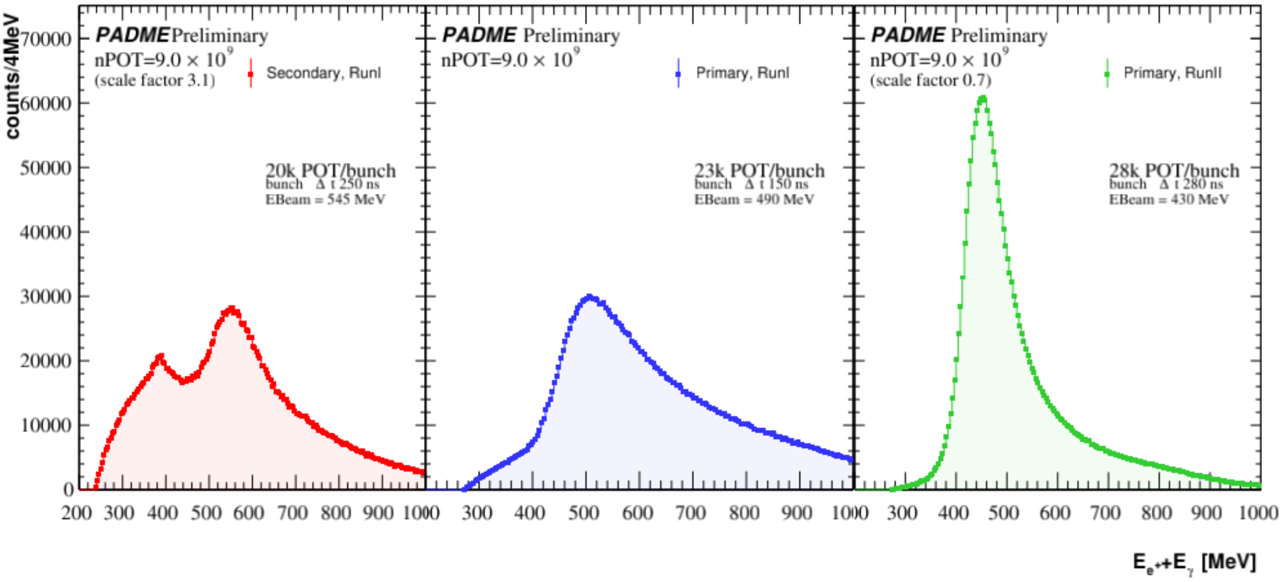

Figure 3.22: *Distribution of the sum of the energies of pairs of photons and positrons passing all selection cuts a., b. and c. for three different beam configurations: (left) RunI secondary beam, (middle) RunI primary beam, (right) RunII primary beam.*

3.6.2 Annihilation in two photons

The annihilation selection described in section 3.4.1 leads to the distribution of the sum of the two leading photons in ECAL shown in Figure 3.23. In contrast to Bremsstrahlung, the annihilation process is not visible in RunI with secondary beam (see Figure 3.23 red distribution). In this case, the huge amount of background photons reaching ECAL invalidates the cluster reconstruction. Using the primary positron beam the annihilation peak appears on the $E_{\gamma_1} + E_{\gamma_2}$ distribution, as shown by the blue distribution. In RunII the background for the annihilation process become negligible (green distribution). The ECAL resolution can be expressed by the sum of the stochastic, noise and constant error terms:

$$\frac{\sigma(E)}{E} = \frac{a}{\sqrt{E}} \oplus \frac{b}{E} \oplus c. \tag{3.3}$$

The noise term b and the constant term c were extracted using the ECAL prototype [82] and were equal to $b = 0.003\%$, $c = 1.2\%$. Assuming that only the stochastic term a depends on the data taking conditions, it is possible to extract its value from beam data:

$$a = \sqrt{E\left[\left(\frac{\sigma(E)}{E}\right)^2 - \left(\frac{b}{E}\right)^2 - c^2\right]} \tag{3.4}$$

Using the parameters reported in Table 3.5. For the data collected in RunI with primary beam the stochastic term correspond to $a = 3.412 \times 10^{-2}$, while for RunII it is $a = 2.065 \times 10^{-2}$, showing an improvement of 40%.

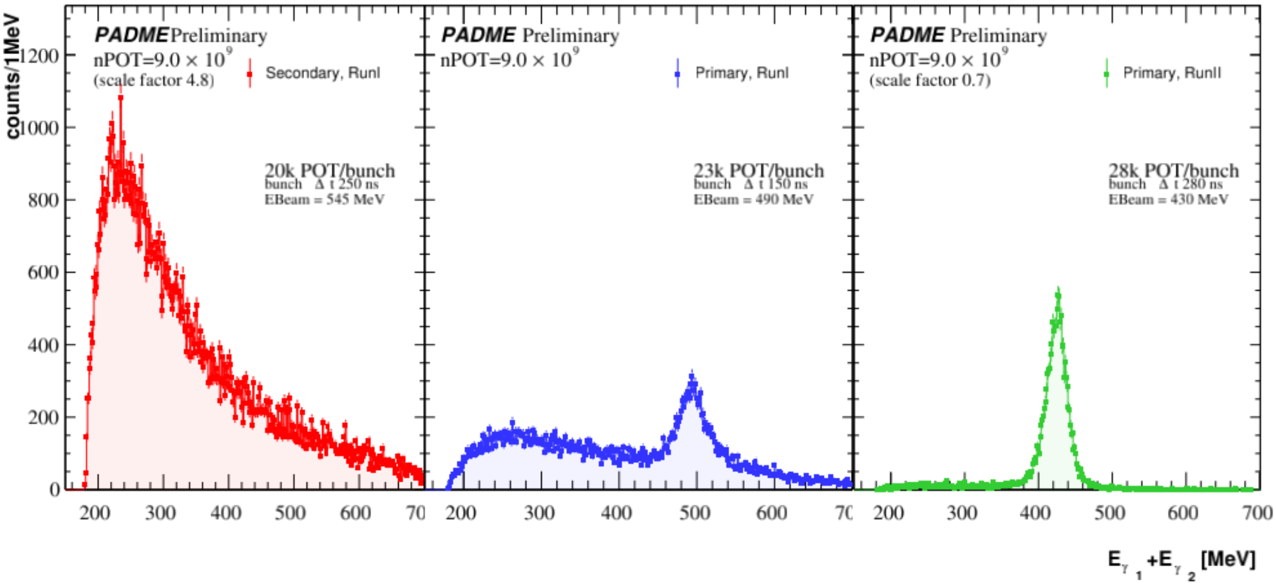

Figure 3.23: *Sum of the two-photon energies that pass the selection described in section 3.4.1 for three beam configurations: (left) RunI secondary beam, (middle) RunI primary beam, (right) RunII primary beam.*

Table 3.5: *Mean and sigma parameters of a Gaussian fit to the energy sum of two photons tagged as coming from an annihilation and their ratio.*

Data	E [MeV]	$\sigma(E)$ [MeV]	$\frac{\sigma(E)}{E}$
RunI primary beam	493.15	24.75	0.0502
RunII primary beam	424.67	14.31	0.0337

3.6.3 Missing mass resolution

To extract the squared missing mass resolution, the two ECAL photons that pass the annihilation selection were used. Figure 3.24 shows distributions of the variable:

$$M^2_{mass} = 2m_e \left[E_{e^+} - E_\gamma \left(1 + \frac{E_{e^+}}{2m_e} \theta^2 \right) \right] \tag{3.5}$$

where E_{e^+} is the energy of the beam, E_γ the photon energy and θ is the angle between the beam and the photon direction. As for the annihilation case, the squared missing mass distribution for RunI with secondary beam does not show any peak (red distribution). In the other cases the peak at zero is visible and con be fit with a Gaussian function.

In Table 3.6 the parameters of the Gaussian fits are reported showing a clear improvement in the quality of data in RunII.

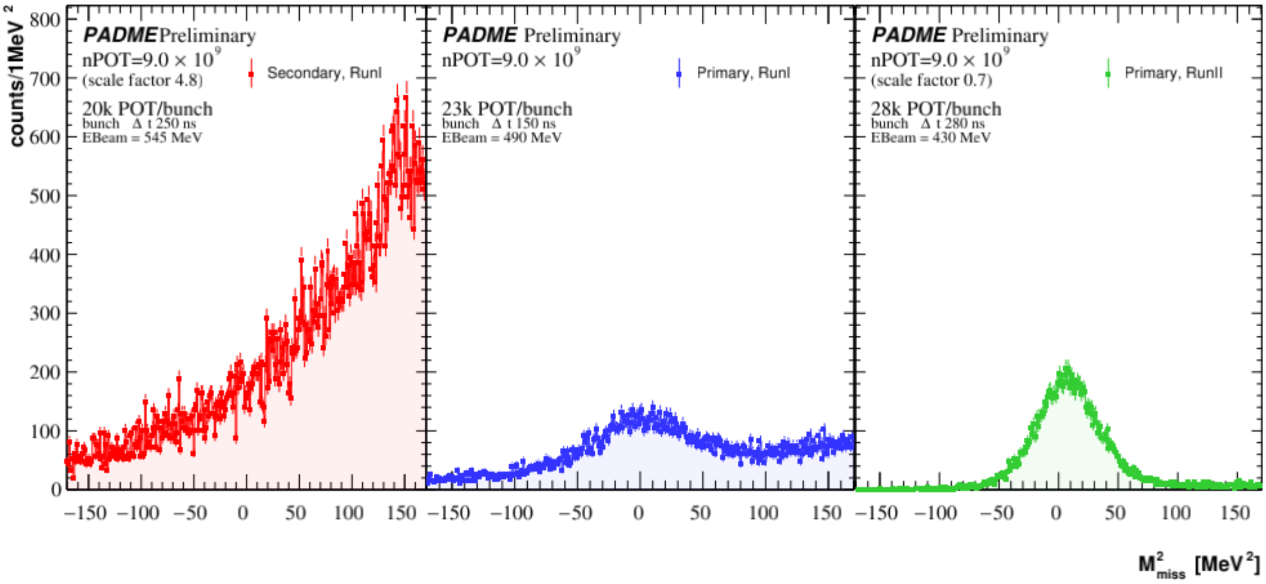

Figure 3.24: *Missing mass squared distribution for the events that pass the annihilation selection cuts for three different beam configurations: (left) RunI secondary beam, (middle) RunI primary beam, (right) RunII primary beam.*

Table 3.6: *Mean and sigma of a Gaussian fit to the squared missing mass distribution of photons tagged as coming from an annihilation process.*

Data	M^2_{mass} [MeV^2]	$\sigma(M^2_{mass})$ [MeV^2]
RunI primary beam	9.52	57.04
RunII primary beam	7.91	26.54

4 ECAL reconstruction

The ECAL calorimeter is the main detector of the experiment because it aims to detect the isolated photon produced with the dark photon A' with good energy and angular resolution. The detector is described in Section 2.2.3 and it is made of 616 BGO crystals coupled to Photo Multipliers and readout by as many digitiser channels. The digitiser sampling frequency was set to 1 GHz, enough to follow the relatively slow signal produced by the BGO crystals scintillation light ($\tau_{decay} \sim 300$ ns [13]). All these raw data are written in Root [86] format and they will be read by the reconstruction software and converted in hits and clusters by specific algorithms as explained in this chapter. In the original proposal the beam background of the experiment has been considered negligible, consequently the probability that a crystal collects light coming from two nearby photons was very low. For this reason, the reconstruction of the hit in the ECAL detector was implemented as a single-hit reconstruction, thus, for each channel, only one hit per event was considered. Unfortunately, in the real experiment, the presence of a high beam background made necessary the use of a multi-hit reconstruction technique which has been developed in this thesis work.

A multi-hit algorithm for the ECAL was not easy to implement, because the long BGO scintillation light decay time is comparable with the beam bunch length. For this reason two hits occurring in the same bunch have signals overlapping in the digitised waveform. The technique developed to disentangle the hits is based on a comparison between the waveform and a template for a single pulse. A strong effort was devoted to handle the few signals with tails and amplitudes truncated due to the limited digitization window (1024 ns) and voltage range (from -1 V to -0 V). The good performance of the multi-hit template technique is proved using a single positron run, where up to seven hits are reconstructed with good energy resolution and high efficiency. The chapter concludes with the implementation in MC of the simulated ECAL waveforms, with the important goal to apply to MC samples the same multi-hit reconstruction technique as data.

4.1 BGO light emission

As already said, the PADME calorimeter is built with inorganic crystals made of Bismuth Germanate ($B_4Ge_3O_{12}$). Its advantage is the high stopping power, due to the high density, which results in a good energy resolution. Its main features are reported in Table 4.1. Using

Table 4.1: *Main parameters of BGO crystal [13], [93].*

Density $[g\ cm^{-3}]$	Rad. Len. X_0 $[g\ cm^{-2}]$	Z/A	E_c $[MeV]$	R_M $[g\ cm^{-2}]$	τ_{fast} $[ns]$	τ_{slow} $[ns]$
7.130	7.97	0.42	10.50	16.10	60	300

the Rossi approximation [94] for the critical energy E_c, it is possible to estimate the depth of maximum shower development in the crystal:

$$x_{max} = 1.4 \times \ln\left(\frac{\mathrm{E_0}}{\mathrm{E_c}}\right) \times \mathrm{X_0} = 5\mathrm{X_0} = 6.06 \text{ cm}. \tag{4.1}$$

Since the length of a single crystal is 23 cm $\sim$ $20\mathrm{X_0}$, the shower is fully contained in the longitudinal direction. By comparing the length side of a crystal cross section ($\sim$ 2.1 cm) with the Moliere radius in BGO $R_M = 2.26$ cm, it appears clear that the crystal contains less than the 90% of the energy, thus the photon reconstruction algorithm must use more than one crystal. The emission spectrum of BGO has a maximum at a wavelength of 480 nm. The time evolution of the light emission process in the BGO has two components: a fast component, relative to fluorescence phenomena, and the slow component, due to phosphorescence phenomena. The time evolution of the light emission can be described as:

$$N = Ae^{-\frac{t}{\tau_f}} + Be^{-\frac{t}{\tau_s}} \tag{4.2}$$

where τ_f is the fast component and τ_s is the slow one. The two decay times are reported in Table 4.1. In Figure 4.1 the time profile of BGO light emission is shown (red line) with the two components, the faster (green line) and the slower (blue line). The scintillation light intensity of BGO crystal is strongly dependent on the temperature, the light yield changes by $-0.9\%/\mathrm{C}$ [13]. To cope with this problem, the calibration constants, derived using cosmic rays collected during the data taking [81], are corrected for the temperature.

4.2 Hit reconstruction

The simulation of the experiment shows a negligible probability to have two photons releasing energy in a single crystal when interactions of the positrons with the beam line are neglected. From this consideration, the reconstruction software for the ECAL detector was developed to recognise a single light emission decay curve from the 1024 ADC values sampled at 1 ns (the waveform). The information saved for each hit are the channel identification number, the signal start time and the signal charge. From them, it is possible to measure the position, in the PADME reference system, the arrival time and the energy, after a proper calibration is applied.

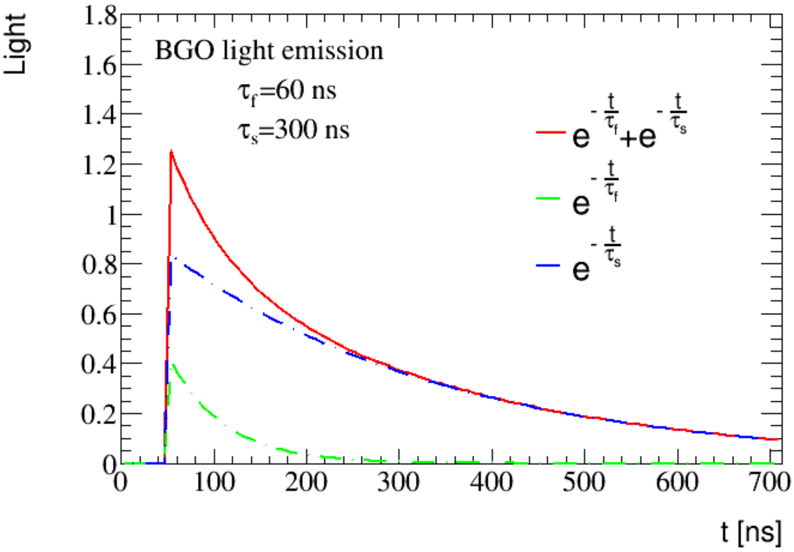

Figure 4.1: *Shape of the total emission light curve from BGO in red. In blue and in green the components corresponding to fast and slow decay times quoted in literature [13], [93] are shown separately.*

Most of the 616 ECAL waveforms do not record a light signal from the corresponding scintillation units, then a huge data size suppression is possible if they are identified and not saved on disk. The rejection of the empty waveforms was done by studying the deviation of the signal with respect to its baseline, by evaluating the RMS of the first 1000 samples (equivalently a time window of 1000 ns after the LINAC trigger). If the waveform has an RMS lower that 5 ADC, it will be identified as empty signal and rejected. This corresponds to reject all energy deposit less than ∼ 1 MeV. The suppression of ECAL data was made at two levels: software and hardware. The hardware suppression was made automatically by the digitiser, while the software one during the raw data reconstruction. The two procedures give identical results and have been used at the same time or as alternative approaches during data taking or processing.

The ECAL waveforms of the raw data, which survived the data suppression algorithm, were saved with the ADC board and channel identifiers, which were converted into a geometry based numbering of the corresponding crystal in the software.

The arrival time of the hit is estimated by the time of the sample where the derivative is maximum.

The energy is measured from the charge evaluated after pedestal subtraction by the formula:

$$Q = \sum_{i=100}^{1000} \frac{W_i \times T_{bin}}{Z} \text{ [pC]} \tag{4.3}$$

where $W_i = \frac{N_{ADC}}{4096 \times 1000}$ [mV] [95] is the ADC counts N_{ADC} converted in voltage, t_{bin} is the sampling time and Z is the impedance equal to 50 Ω. Then the energy is calculated with a nominal conversion factor E [MeV] $= \frac{\text{Q [pC]}}{\text{15 MeV/pC}}$ [81].

Due to the long tail of the BGO scintillation light pulse and to the limited window time acquisition, the energy may be underestimated by the fraction of signal falling outside the digitisation time interval. For this reason a time dependent correction is used

$$R\ [\mathrm{t}] = 1 - \mathrm{e}^{\frac{1000\ [\mathrm{ns}] - \mathrm{t_{hit}}\ [\mathrm{ns}]}{\tau_\mathrm{s}\ [\mathrm{ns}]}} \tag{4.4}$$

where τ_s is the BGO decay time and the energy is redefined as $E \rightarrow E'/R$.

In case of large energy deposits, the waveform can reach the ADC maximum value leading to saturation. A waveform is tagged as saturated if its value stays equal to the saturation threshold V_{sat} for a time $\Delta t_{sat} > 4$ ns (four consecutive sampling). When this happens the real maximum V_{MAX} of the saturated waveform is

$$V_{MAX} = \frac{V_{sat}}{e^{-\frac{\Delta t_{sat}}{\tau_f}}} \tag{4.5}$$

The missing charge of a saturated waveform is estimated to be:

$$\Delta Q^{sat} = \frac{1}{Z}(V_{MAX} - V_{sat}) \times \tau \times (1 - e^{\frac{{}^{t}\Delta t_{sat}}{\tau}}). \tag{4.6}$$

Where $\tau = 150$ ns. This charge will be added to the one extracted from the integration of the waveform and converted into hit energy.

4.3 Cluster reconstruction

Photons hitting the calorimeter deposit energy in more than one crystal, thus hits need to be clustered to reconstruct the original particle. The clusterization algorithm groups hits close in time and space. The hit association process starts searching for a hit acting as a cluster seed. This is the most energetic hit in ECAL not yet associated to any previously built clusters. In the seed search an energy threshold $E_{seed} > E_{seed}^{thr}$ is applied in order to avoid to build cluster for very low energy particles. The other hits will be clustered to the seed if:

- its energy is higher than a hit energy threshold $E_{hit} > E_{hit}^{thr}$;
- its time is close to the seed hit time $|t_{hit} - t_{seed}| < t_{max}^{thr}$;
- its crystal is at a distance from the seed crystal $\Delta Cell = \Delta N_{hit}^{row/column} < \Delta Cell_{hit}^{thr}$.

To optimise the parameters of the clusters reconstruction special MC samples was used simulating a photon that hit ECAL in the radial position $(x, y) = (14\text{ cm}, 14\text{ cm})$. The maximum allowed distance between the seed and the hits $\Delta Cell$ is set to 3 in order to avoid merging hits from other photons. The choice of the cluster seed energy threshold was done studying the parameter $\alpha = 1 - N_{ev}^{N_{cl}>1}/N_{ev}$, where $N_{ev}^{N_{cl}>1}$ is the number of single photon events with more than one reconstructed cluster. Alpha quantifies the capability to reconstruct a single photon as a single cluster. The parameter was studied for different seed energy threshold and the

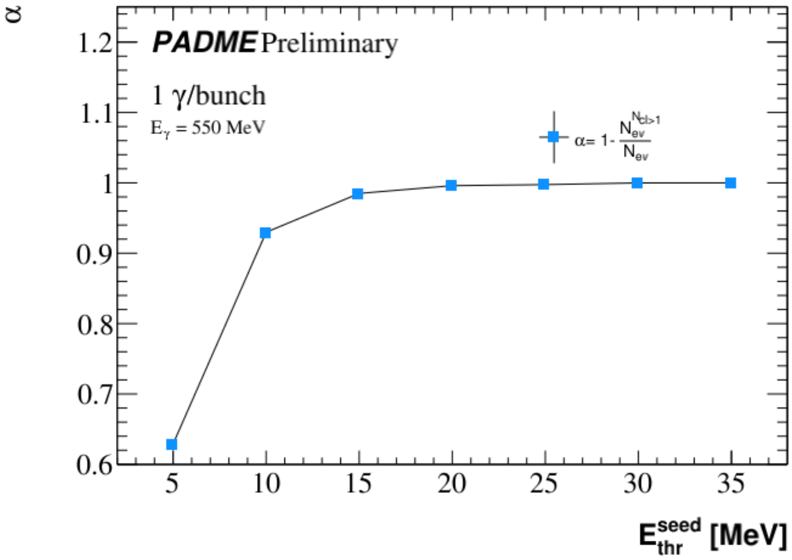

Figure 4.2: *The probability α to reconstruct a photon of energy* 550 MeV *as a single cluster as a function of the cluster seed energy threshold.*

behaviour is plotted in Figure 4.2. The value of E_{seed}^{thr} chosen was 20 MeV which corresponds to the beginning of the region where alpha reaches the maximum value 1.

The next parameter to set is the time clusterization window. To set this parameter, the relative energy resolution $\sigma(E)/E$ was studied and shown in Figure 4.3. The value chosen is $\Delta t = 6$ ns that is a good compromise leading to $\sigma(E)/E$ close to the minimum and it is small enough to prevent the association of spurious hits.

The last parameter to set is the hit energy threshold. This parameter has a relevant impact on the cluster energy determination. The impact on the relative resolution was studied with several MC samples where photons with energy E_γ in the range $[0, 1000]$ MeV were simulated. The relative energy resolution $\sigma(E)/E$ as a function of the photon energy is shown in Figure 4.4 (a) for several hit energy thresholds. The plots show a high dependence on the relative energy resolution of the hit energy threshold at low values of the photon energy. The lower is the hit energy threshold the better is the energy resolution. The same is true for another quantity: the ratio E_{tot}/E_γ between the mean of a gaussian fit to the total cluster energy and the photon energy as shown in Figure 4.4 (b). Eventually, this parameter is set to 1 MeV, the value setting the noise threshold.

In summary, based on MC studies the clusterization parameters optimized in this thesis work were set to the following values:

- $E_{seed}^{thr} = 20$ MeV;
- $E_{hit}^{thr} = 1$ MeV;
- $t_{hit}^{thr} = 6$ ns;

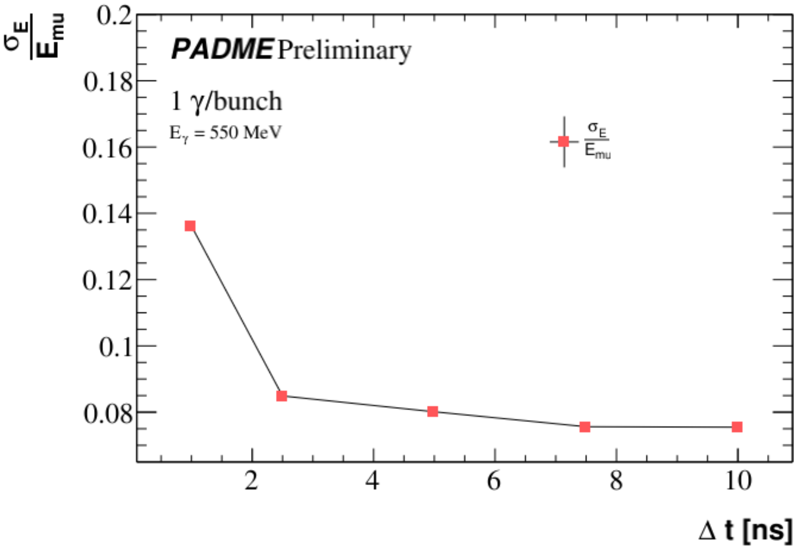

Figure 4.3: *The relative energy resolution* $\sigma(E)/E$ *of a* 550 MeV *photon as a function of the time clusterization window.*

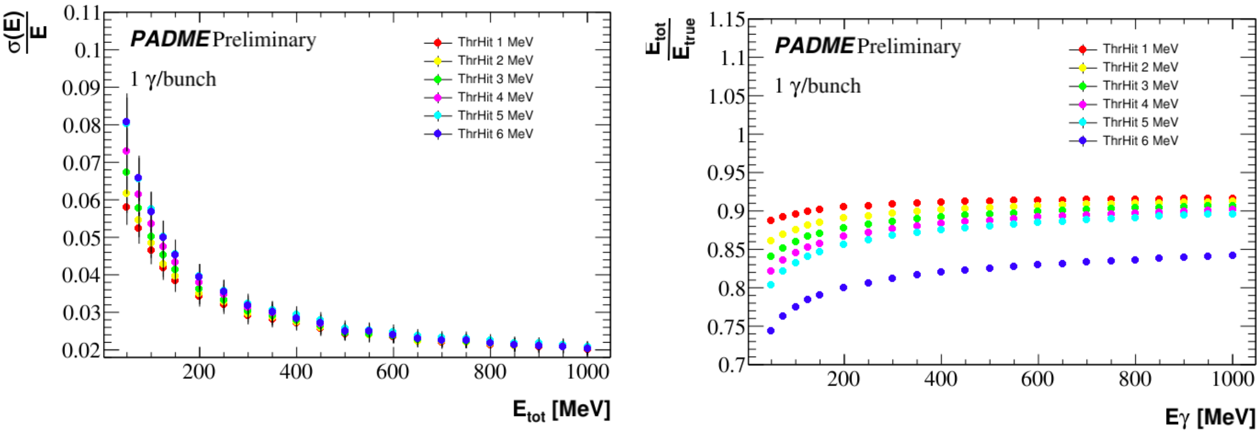

(a) **(b)**

Figure 4.4: *(a) The relative energy resolution as a function of the photon energy for different values of the hit energy threshold. (b) The ratio of the total cluster energy and photon energy as a function of the photon energy for different values of the hit energy threshold.*

- $\Delta Cell_{thr} = 3$.

4.4 Multi-hit reconstruction

The single-hit reconstruction was found to be adequate for ECAL by the default PADME simulation, where the beam was generated just in front of the Active Diamond Target with a bunch multiplicity of 25000 positrons and a bunch length of 250 ns. In real data the photon background appeared much higher than expected from pileup photons generated in the target. Clear evidence of a large background in data comes from the high amount of total energy in the detector exceeding expectations and the presence of more than one peak in the BGO light emission signals. Indeed, this dominant background was due to the beam scraping the beam line or radiating in the vacuum separation window. This was confirmed by MC simulations where the beam was generated in front of the vacuum separation window and was propagated through the beam line was simulated. All these considerations point to the inadequacy of the single-hit reconstruction and the need of a multi-hit reconstruction. As a consequence, I developed a novel multi-hit reconstruction algorithm which became the default reconstruction of the PADME ECAL detector. Usually, a multi-hit reconstruction algorithm is based on a peak search algorithm, making use of general purpose libraries. Considering the slow BGO light decay and the noise in the waveform, an alternative technique was applied, based on a signal template built from data. The method developed can deal also with other exception like the overlap in time of the signals, the long tail and the waveform saturation. In practice, the procedure is similar to a fit of the waveform with the sum of up to three templates, each with free normalization and starting time. However, the implementation is not based on fits thus avoiding time consuming procedures. In order to develop and optimize this new multi-hit reconstruction algorithm, a run with a single positron per bunch was used, in Table 4.2 the main parameters of the run are reported.

Table 4.2: *Main parameters of the single positron run used to develop and validate the ECAL multi-hit algorithm.*

Feature	value
Run number	0000000_20190301_071513
N_{e^+}/bunch	1
E_{beam}	490 MeV
N_{events}	213079

4.4.1 Single-hit template

The template is a histogram representing the waveform of a typical signal from the ECAL scintillating unit. It is built from data averaging on real waveforms of the single positron run. In order to exclude noisy and saturated waveforms, only signal with energy in the range $[1\ \text{MeV}, 400\ \text{MeV}]$were considered. This selection allows also to have only a single pulse in the signal. The waveforms were normalised to have integral equal to one, shifted in time, to have the same arrival time, and then averaged, to reduce fluctuations. The average template is shown in Figure 4.5 (a). The tail of the template is distorted due to the limited acquisition time window, which cuts the tail of the signal differently for different signal arrival times. For this reason the template is corrected using the extrapolation of an exponential fit applied between

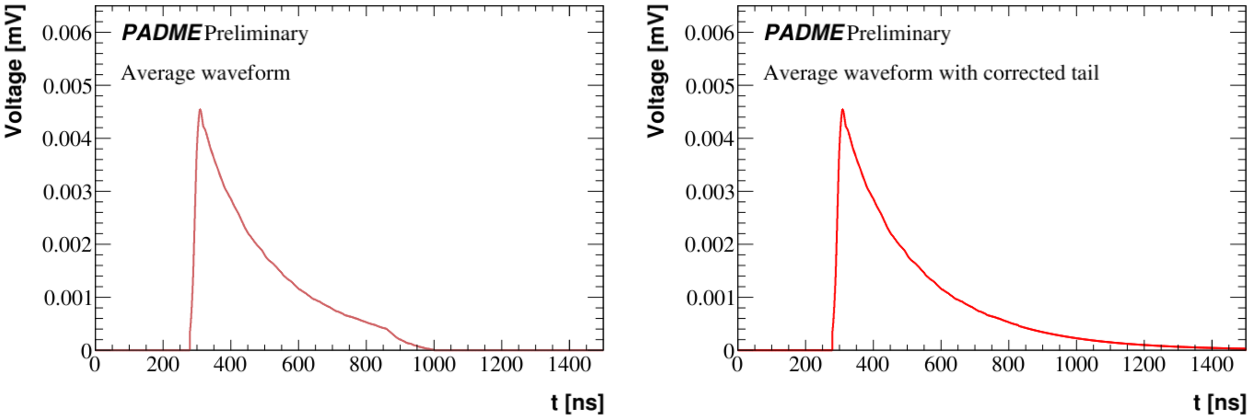

(a)

(b)

Figure 4.5: *Average of all waveforms with single-hit energy in the range* $[1, 400]$ MeV *(a) and after truncated tail correction by an exponential tail (b).*

600 ns and 800 ns giving a decay time of $\tau = 240 \pm 92$ ns. The final template is shown in Figure 4.5 (b).

4.4.2 Multi-hit search

The multi-hit search starts by computing the derivative of the waveform. The time t_{hit} of the maximum derivative is adopted as the arrival time of the first hit and the maximum V_{max} of the waveform closest to t_{hit} is identified as the amplitude of the pulse. The template is scaled by the amplitude V_{max} and it is shifted in time until the bin with maximum height of template and waveform overlap. In Figure 4.6 an example of single-hit waveforms with a template scaled and shifted according to the procedure is shown. The search for a second hit is done by applying the same procedure to the difference between the waveform and the template adapted in position and amplitude to the first hit. This means that the arrival time and the amplitude of the second hit candidate are estimated using the position of the derivative maximum and the maximum of the subtracted waveform. The amplitude of the second hit candidate is required to be higher than 5 mV and the time distance with respect to the first hit is requested to be at least 25 ns. If a second hit is identified, the second hit template can be subtracted from the previously subtracted waveform and a search for a third hit can starts with the same procedure and requirements on the amplitude and the distance from previous hits. No more than three hits are searched within a waveform. In Figure 4.7 some examples of waveforms with two and three reconstructed hits are shown.

Once the hits are identified, the energy is estimated as the charge integral in the range $[80 \text{ ns}, 5000 \text{ ns}]$ of properly scaled template. This allows to overcome the problem of the energy bias due to the fraction of the signal tail falling outside the digitization time window. Since the peak search procedure does not imply that hits are ordered in time, some correction must

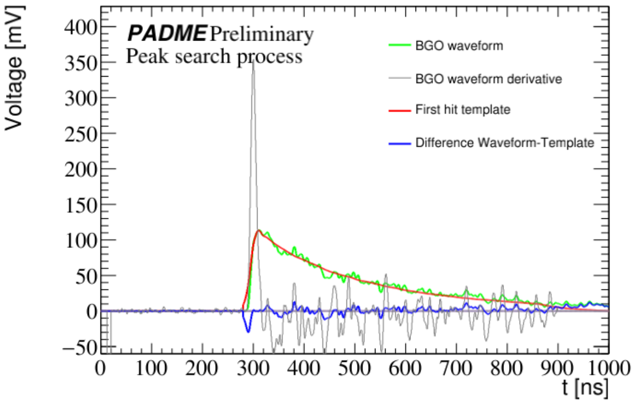

Figure 4.6: *Example of single-hit waveforms (green) with their derivatives (grey), scaled and shifted templates (red) and the difference between waveforms and templates (blue).*

be applied if a second or third hit is found with an earlier time with respect to a previously identified hit. Indeed, in this case the amplitude of the first hit identified by the algorithm is overestimated, because the pulse is developing on top of the tail of a previous pulse. This is cured by subtracting from the energy of the late hit the integral of any previous hit in the time domain of the late hit.

For the sake of clarity, Figure 4.7 (c) shows an example where the arrival time of the reconstructed first hit is higher than the third one $t_{hit_1} > t_{hit_3}$. In this specific example the energy of hit 1 is corrected for the tail of the hit 3 that come earlier in time by subtracting the energy obtained from the integration of the third hit template over an interval with lower edge equal to t_{hit_1} and upper edge equal to the usual boundary of 5 ms.

Hits reconstructed with this procedure are accepted only if their energy is > 2 MeV.

If only one hit is found, its energy and time are computed as in the single-hit reconstruction algorithm.

4.4.3 The case of saturated waveforms

When there is a large energy deposit, the waveform can saturate and the signal appears truncated, i.e. for several consecutive bins the amplitude stays constant to a value V_{sat} in the range [700 mV, 1000 mV], depending on the channel pedestal. A toy MC was used to extract the correlation between the real value of V_{max} and the length in time of the saturated part of the signal for different values of V_{sat} (see Figure 4.8 (a)). Second order polynomial fits of the correlation plots for different values of V_{sat} are used to estimate the maximum amplitude of waveforms tagged as saturated. In Figure 4.8 (b) a saturated waveform and its corrected version is reported.

A waveform is tagged as saturated if the number of bins, Δt_{sat}, where the amplitude differs from the saturation value less than 20 mV, exceeds 4 ns. In this case, the template is shifted to the value of V_{max} computed as a function of Δt_{sat} and the position of the template is

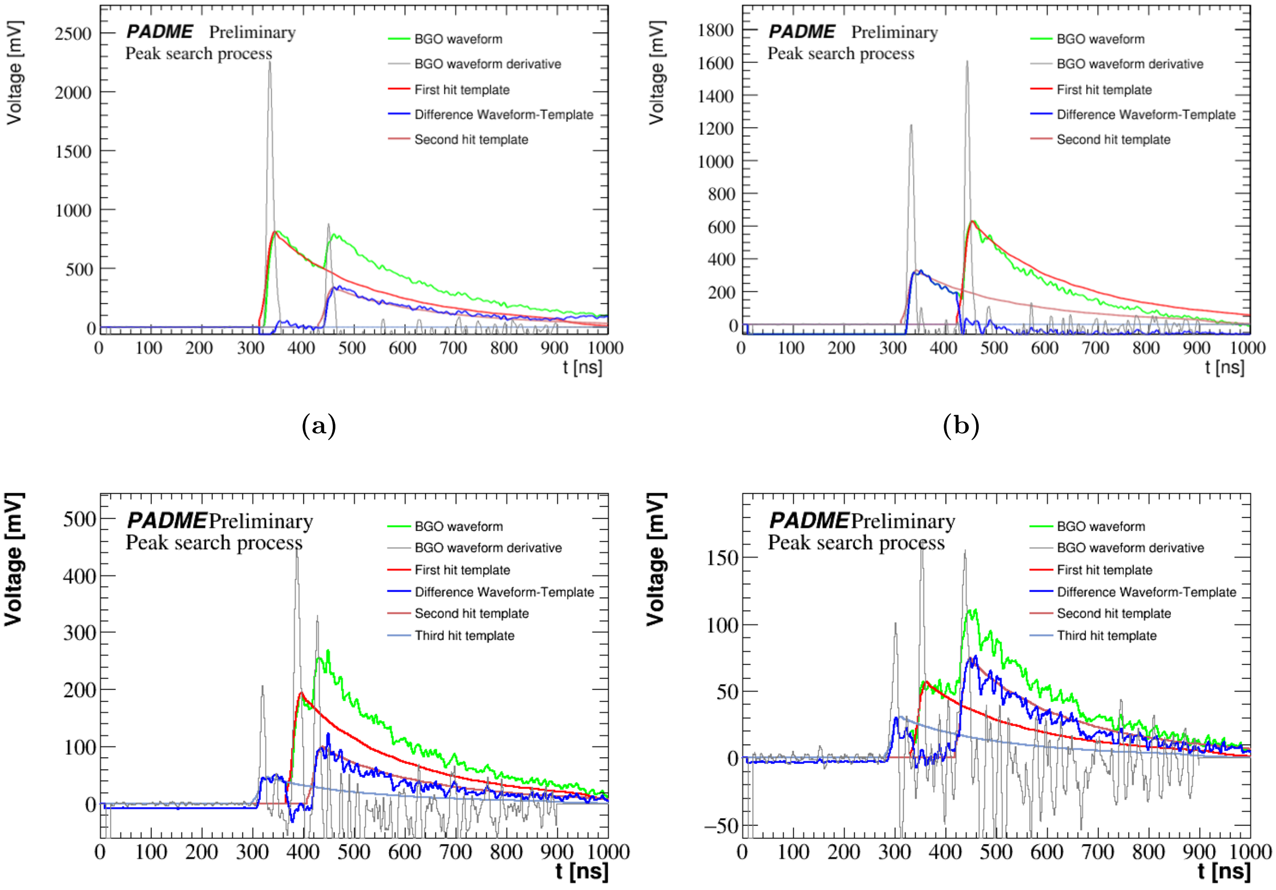

(a)

(b)

(c)

(d)

Figure 4.7: *Two examples of waveforms with double hits (upper plots) and triple hits (bottom plots). The colors are as in Figure 4.6 with the addition of the second (pink) and third (violet) hit template where present.*

defined matching the height of the waveform before and after the saturation region. Figure 4.9 shows examples of saturated waveform overlapped with the corresponding hit template. The arrival time of the saturated hit is defined by the position of the maximum derivative of the template and the energy is computed by integrating the hit template from 80 ns up to 5 ms. Also in presence of a saturated hit the multi-hit search is applied starting with the difference between the waveform and the hit template. The same energy correction is applied if the second reconstructed hit is found at an earlier time with respect to the first. Examples are shown in Figure 4.9 (b), (c) and (d).

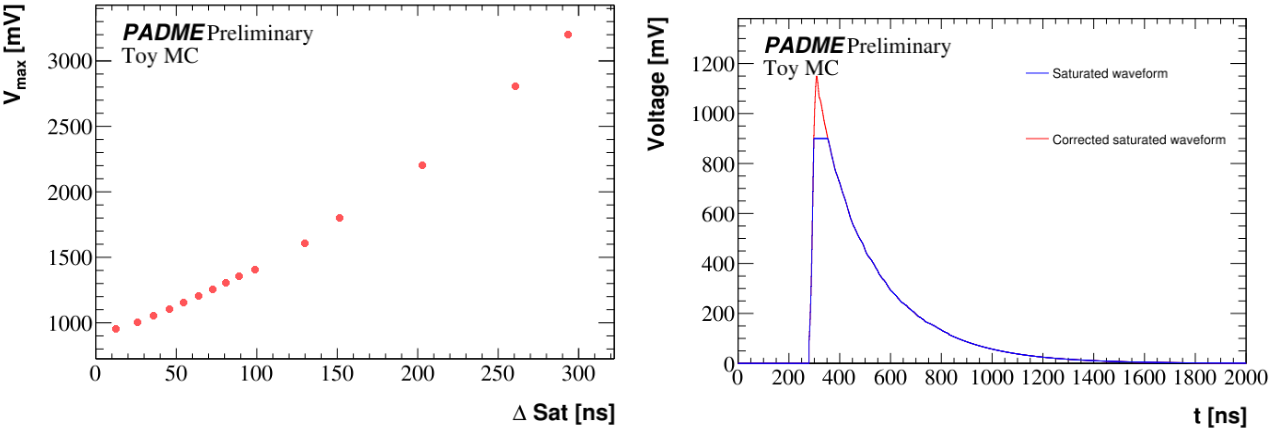

(a) **(b)**

Figure 4.8: *(a) Correlation between the maximum amplitude of a BGO light pulse truncated at* $V_{sat} = 900$ mV *and the number of samples* ΔSat *at* $V = V_{sat}$ *from a toy MC. (b) In blue a simulated saturated waveform with* $V_{sat} = 900$ mV *and* $\Delta Sat = 30$ ns *and in red the corrected version with maximum amplitude inferred by the polynomial fit to the correlation plot shown in (a).*

4.4.4 Multi-hit search with two saturated hits

Some waveforms present two saturated hits with different saturation regions separated and of different time length. On the other hand, in real data the occurrence of three saturated hits in the same channel appears very rare. This justifies the choice of allowing in the multi-hit search with at most two saturated hits and eventually a third not saturated hit.

Double saturated waveform

The condition of double saturation is defined when the distance between two saturation regions is higher than 6 ns. Thus two templates are scaled and shifted according to the first and second Δt_{sat}. The arrival time of the two hits is the time of the hit template maximum derivatives and the energy is defined with the usual integration procedure. Of course, the energy of the second hit in the pair is subtracted of the contribution of the tail of the first hit. Some examples of double saturated hits identification are shown in Figure 4.10.

In some rare cases, large saturated signals appear compatible with a double pulse structure even if the separation of the saturation regions is less than 6 ns. In cases like the example shown in Figure 4.11, the procedure just described fails. For these cases a check is done to see if the gap is consistent with a local minimum and inconsistent with a random downward fluctuation. The $m_i = \frac{W(t_{i+1})-W(t_i)}{\Delta t}$ of the waveform $W(t_i)$ is computed at any time t_i in the region of interest with $\Delta t = 1$ ns and a pattern of a few negative values of the derivative followed by a few positive values is searched. From the measurements of derivatives of a large set of saturation regions, the width of the distribution is obtained ($RMS = 0.79$). Then the sequence of criteria applied to identify a double pulse is the following:

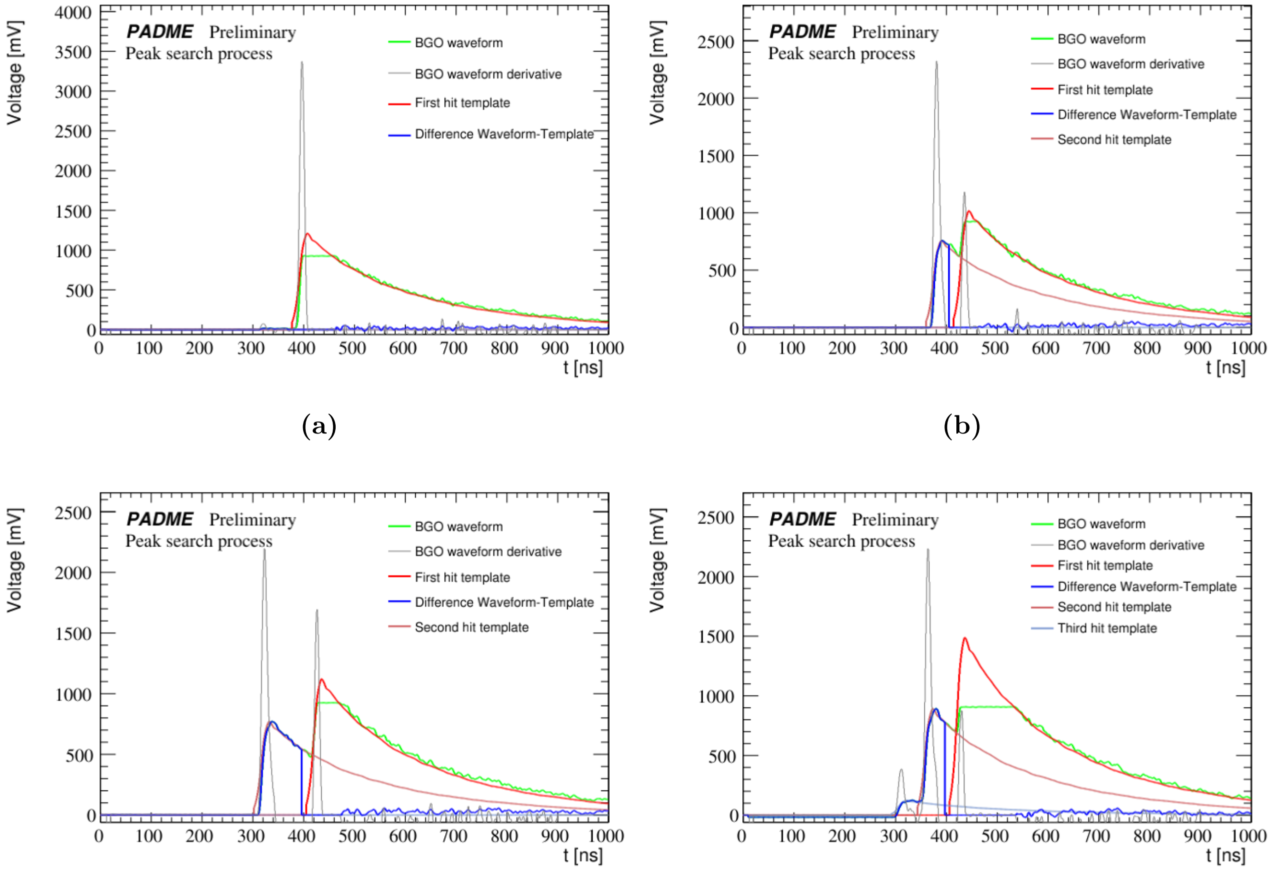

(a) **(b)**

(c) **(d)**

Figure 4.9: *Examples of multi-hit search with hit template for saturated waveforms. Only one saturated hit found (a), one not saturated hit found after the saturated hit (b,c) and two not saturated hits found after the saturated one (d). The saturated hit energy is corrected from not saturated hit tail because its late arrival time.*

- all bins, t_i, in the saturation region, with $|m_i| > 3 \times RMS_m$ are used;
- consecutive points t_i, $t_i + 1$ close in time $|t_{i+1} - t_i| < 5$ ns and with opposite derivative $m_i \times m_j < 0$ are considered if bin i is not the first of the saturation region;
- at least one bin on the left of i-th point has derivative with the same sign of m_i and $|t_{i+1} - t_{i-1}| < 3$ ns;
- at least one bin on the right of bin i+1 has derivative with the same sign of $m_j = m_i + 1$ and $|t_{i+1} - t_{i+2}| < 3$ ns.
- in the set of bins with large absolute value of the derivative

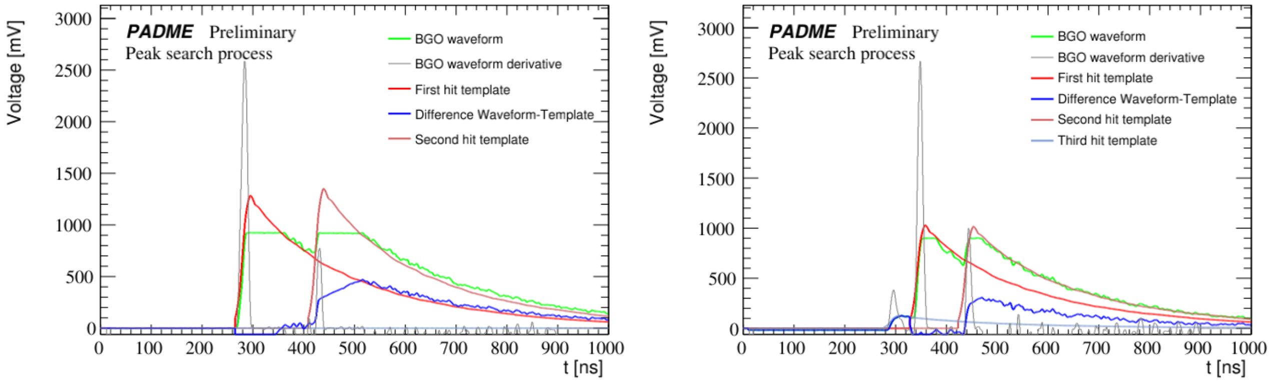

(a) **(b)**

Figure 4.10: *Examples of double saturated waveforms with two identified hits.*

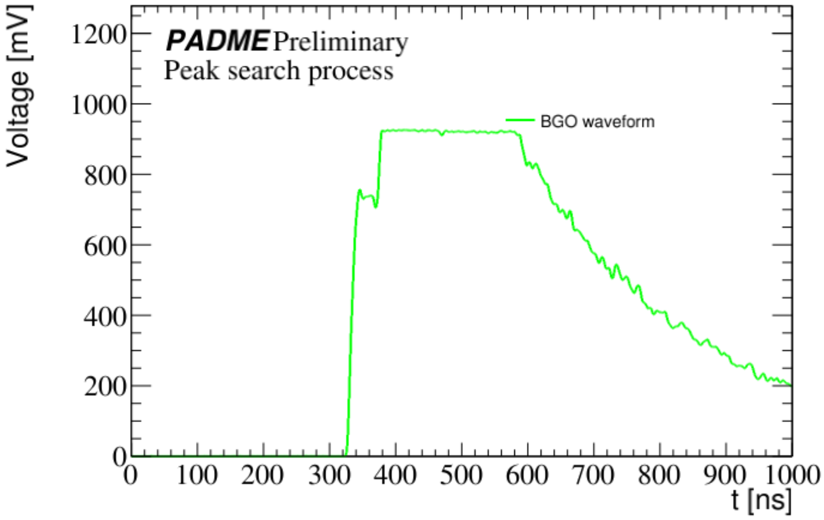

Figure 4.11: *Example of a waveform with two saturated hits with almost overlapping saturation and a small distance between the two regions.*

  - at least two must be found in the 8 ns before t_i, separated with each other by less than 2 ns and with m of the same sign as t_i;
  - similarly, at least two bins must be found in the 8 ns after t_{i+1}, separated with each other by less than 2 ns and with m of the same sign as t_{i+1};
- the end of the dip must be at a distance greater than $\sim$ 25 ns from the end of the saturation region, where fluctuations are usually large.

If the waveform satisfies all these criteria, the usual procedure to reconstruct two saturated hits is applied.

As an example, the algorithm applied to the waveform showed in Figure 4.11 return the points of large derivatives m reported in Table 4.3. The first change of sign of m happens between $t_i = 379$ and $t_{i+1} = 342$, but there are no other points t_k with $t_k < t_i$ having the same m sign of t_i, thus these points are not considered. The next change of sign happens between $t_i = 447$ and $t_{i+1} = 466$, but they are not considered for the same reason and because $t_{i+1} - t_i > 5$ ns. Then there are $t_i = 468$ and $t_{i+1} = 471$ and for both there are other two points on the left and on the right respectively, closer less than 8 ns and with the same m sign. This condition allows to tag the waveform as having a pair of saturated hits. The other consecutive bins with opposite derivative $t_i = 473$ and $t_{i+1} = 582$ can not be considered, because the difference in time is higher than 5 ns.

Table 4.3: *Time t_i and m_i derivative values of the waveform of Figure 4.11 with large derivative in the saturation region.*

Time [ns] ($\|m_i\| > 3 \times RMS_m$)	m
379	5.6
442	-2.6
447	2.6
466	-3.0
467	-2.5
468	-3.7
471	3.4
472	4.1
473	3.0
582	-3.7
588	-4.1
589	-9.8

In Figure 4.12 the result of the template algorithm for this example is reported. Also in this case, the arrival times and energies are defined by the maximum derivatives and the integration of the templates corrected for the tail of the previous hit. Other examples of this correction are reported in Figure 4.13.

4.4.5 Limits of the saturated waveform multi-hit reconstruction

The reconstruction of overlapping saturated hits with fully merged saturation regions are impossible to distinguish. From Figure 4.8 it is possible to extract V_{max} as a function of Δt_{sat}:

$$V_{max}\ [\mathrm{mV}] = 904.438\ [\mathrm{mV}] + 3.639 \times \Delta \mathrm{t_{sat}}\ [\mathrm{ns}] + 0.014 \times \Delta \mathrm{t_{sat}^2}\ [\mathrm{ns}] \tag{4.7}$$

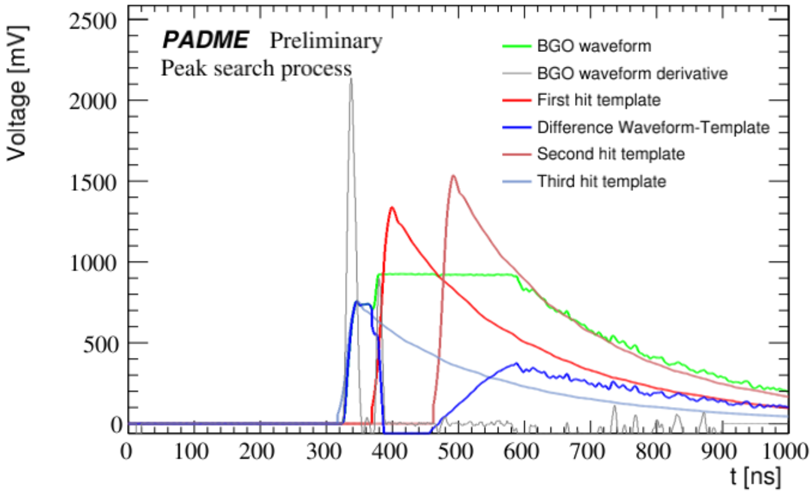

Figure 4.12: *Example of a waveform with a double hit saturation and a small distance between the two regions overlapped with the adjusted templates.*

for $V_{sat} = 900$ mV. Using the scaled hit template it is also possible to extract the correlation between V_{max} and the saturated hit energy by integration:

$$V_{max} = 3.21 \times E_{hit} \tag{4.8}$$

and extract the correlation between the saturated hit energy and Δt_{Sat}, reported in Figure 4.14. Since the maximum energy of a photon can be the beam energy, the Δt_{sat} maximum should be ~ 130 ns. This implies that all waveforms having a saturation region larger than that limit correspond to at least two saturated hits, for an energy release of 490 MeV, corresponding to a single positron energy special run. One example is shown in Figure 4.15. These events represent a limit in the multi-hit reconstruction of saturated waveforms.

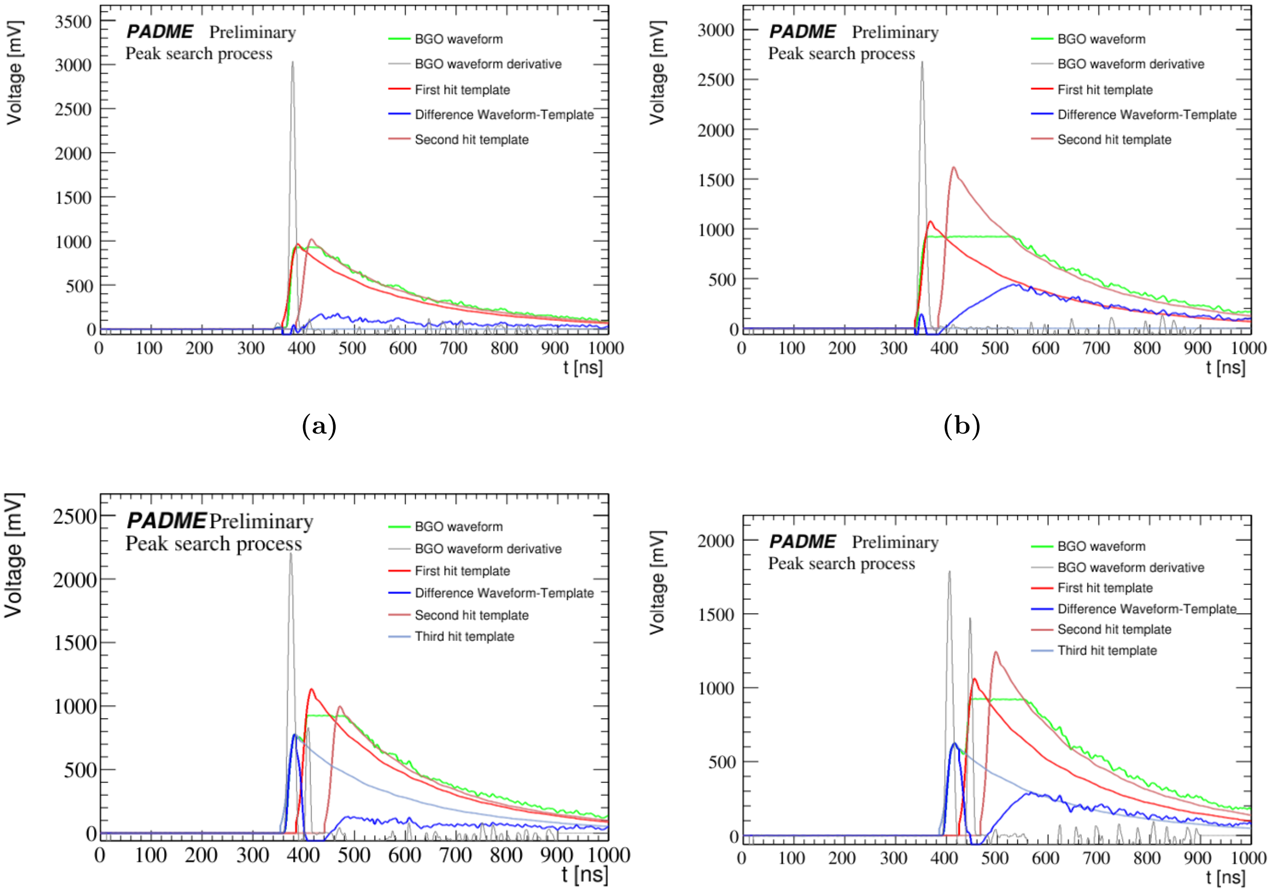

(a) (b)

(c) (d)

Figure 4.13: *Examples of template algorithm results on single-hit saturated waveform with additional hits.*

4.5 Comparison between single-hit and multi-hit reconstruction

In this section the gain in performance from the multi-hit reconstruction, in the presence of pileup, will be discussed by comparing event features estimated with the single-hit and with the multi-hit reconstruction. The single positron run, where events with more than one positron per bunch are detected always in the same area of the calorimeter, offers a very useful test bench. Figure 4.16 (a) shows the number of hits reconstructed for each event. In the distribution three regions can be identified. The first corresponds to empty events where hits are reconstructed because of instrumental noise or very low energy background photons. The second region with number of hits between 6 and 20, corresponds to single positron events. Then the third region corresponds to events with more than one positron. Here a big difference between the two

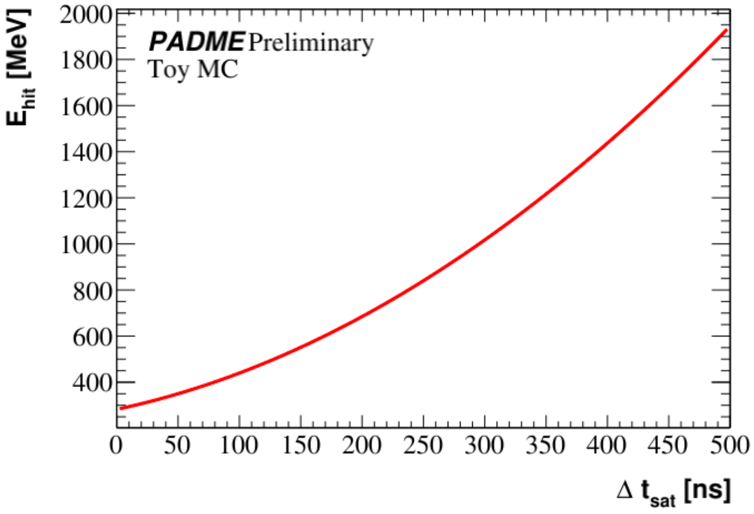

Figure 4.14: *Correlation between the hit energy* E_{hit} *and saturation region length* Δt_{Sat} *for* $V_{Sat} = 900$ mV.

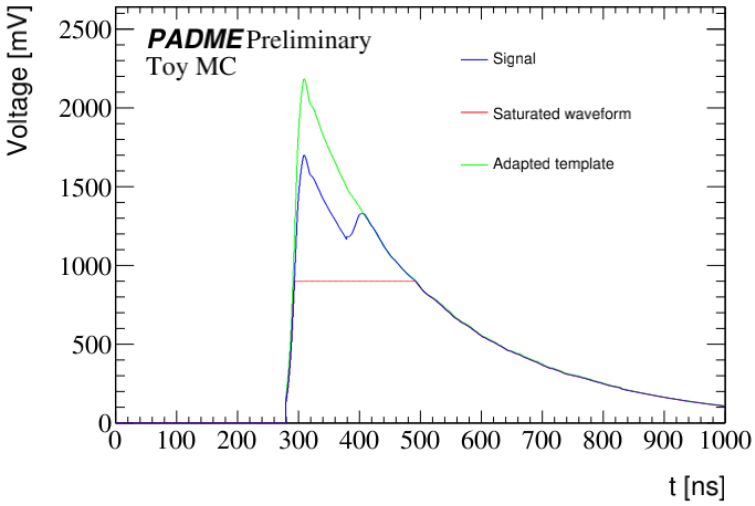

Figure 4.15: *The blue curve is the signal sum of saturated hit with amplitude* 1700 mV *and arrival time of* 300 ns *and a hit with amplitude of* 300 mV *and arrival time* 400 ns*, resulting in a merged saturation region. The red curve is the saturated waveform and the green curve the reconstructed hit from hit template method.*

algorithms can be observed, proving the capability of the multi-hit to resolve hits overlapping in the same crystal. In Figure 4.16 (b) there are the distributions of the number of clusters and again the differences between the two algorithms are visible at high multiplicity, where more than one positron per bunch hits the calorimeter. In Figure 4.16 (c) the distribution of the cluster size is shown. The plots indicate that the multi-hit algorithm not only reconstructs more than one hits per event, but also that the average cluster size is slightly higher than in the single-hit reconstruction. It is interesting to study these distributions as a function of the total energy reconstructed in ECAL. Figure 4.17 (a) ahows the number of hits as a function of the sum of the energies of all hits for the single-hit reconstruction. The scatter plots shows that the number of hits begins to saturate for a total energy of ~ 1.5 GeV, corresponding to three positrons of the event. In Figure 4.18 (b) the same distribution for the multi-hit reconstruction is shown. A clear improvement in the energy resolution and in the linearity between number of hits and total hit energy can be easily observed.

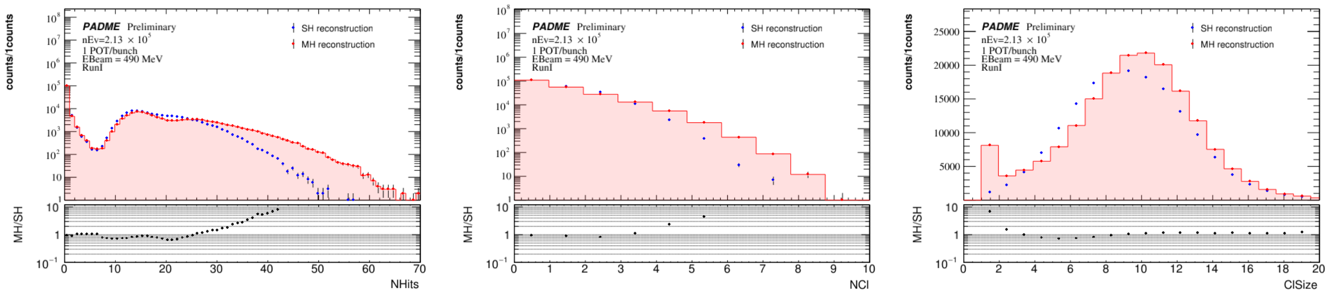

(a) (b) (c)

Figure 4.16: *Comparison between single-hit (blue) and multi hit (red) reconstruction for the single positron run. (a) Distribution of number of hits per event. (b) Distribution of number of cluster per event. (c) Distribution of the cluster size.*

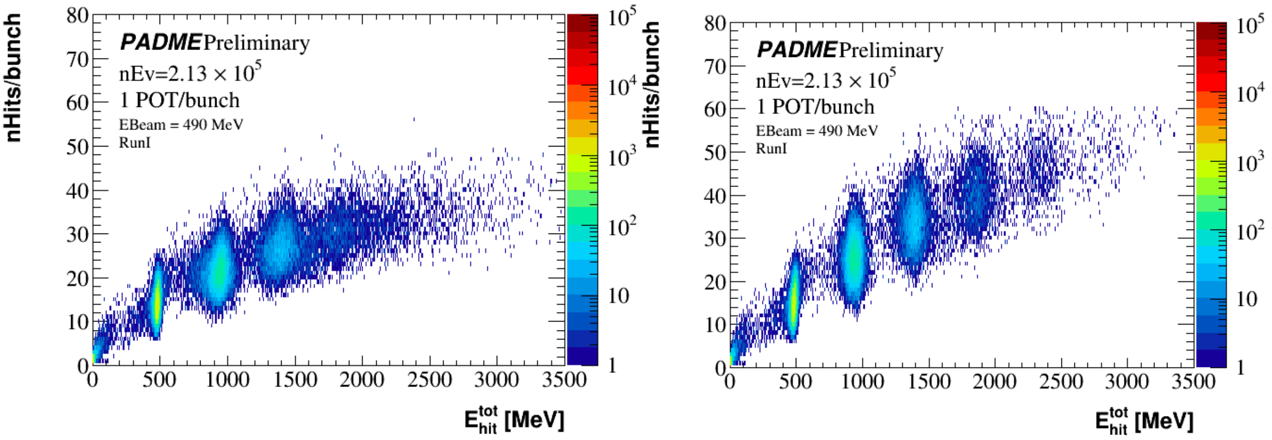

(a) (b)

Figure 4.17: *Number of hits as a function of the sum of the energy of all hits in ECAL in the single positron run. On the left the distribution for the single-hit reconstruction; on the right the same distribution for the multi-hit reconstruction.*

The same improvement can be appreciated in Figure 4.18 where the number of clusters is shown as a function of the sum of the energy of all clusters in the event.

Figure 4.19 shows the sum of the cluster energy in the event, again for the two reconstruction procedures. At the bottom, the ratio of the two distributions exhibits a very good agreement until the energy is consistent with the beam energy; later the peaks corresponding to twice or several times the beam energy are narrower in the case of the multi-hit reconstruction and the better resolution achieved allows to observe the occurrence of up to 7 positrons in the same bunch. Figure 4.20 shows the distribution of the hit energy for the two reconstruction

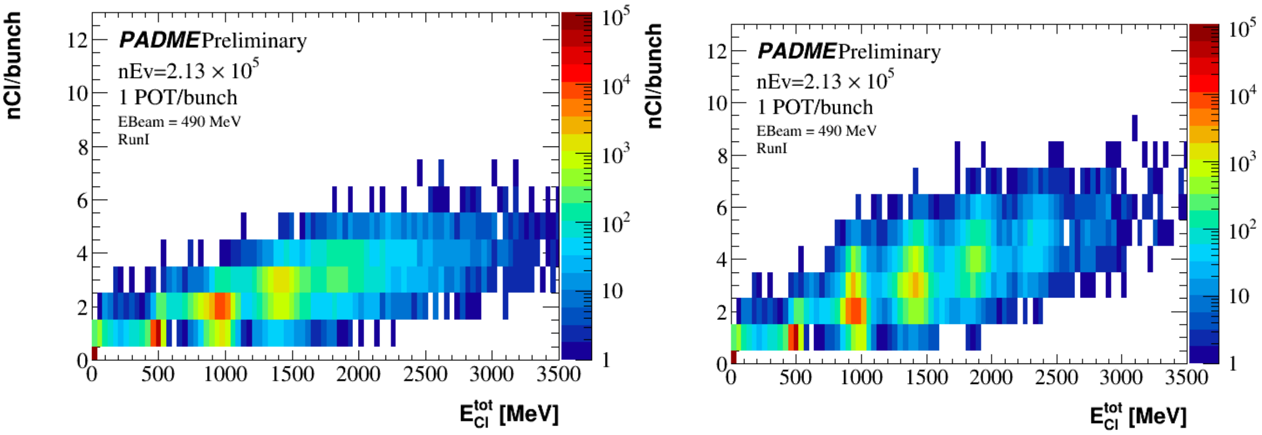

(a)

(b)

Figure 4.18: *Number of clusters as a function of the sum of the energy of all clusters in ECAL in the single positron run. On the left the distribution for the single-hit reconstruction; on the right the same distribution for the multi-hit reconstruction.*

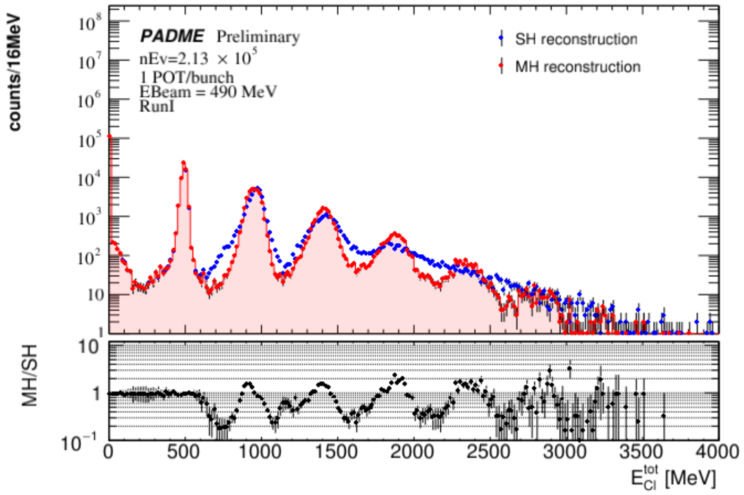

Figure 4.19: *Distribution of the total cluster energy in ECAL for the single positron run with the single-hit (blue dots) and multi-hit (red dots) reconstructions (upper plot) and ratio of the two (lower plot).*

procedures. The multi-hit algorithm finds more hits in the energy range between 200 and

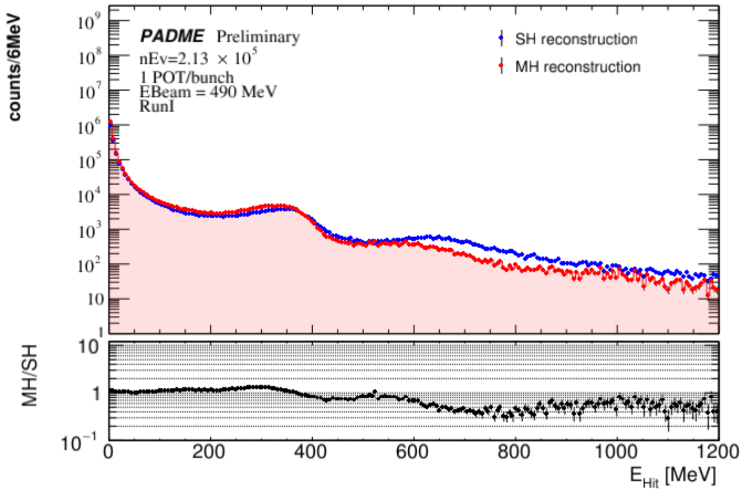

Figure 4.20: *Hit energy distribution reconstructed in ECAL for the single positron run with the single-hit (blue dots) and multi-hit (red dots) reconstruction (upper plot) and ratio of the two (lower plot).*

400 MeV and less above this interval, indicating the ability of the multi-hit reconstruction to resolve overlapping signals that are assigned an-physical energy values by the single-hit reconstruction. In Figure 4.21 the cluster energy distributions for events with a given number of clusters N, from 1 to 8, are shown. Figure (a) shows similar performance when only one positron hit the calorimeter. However, for the single-hit is visible a fraction of hits of about two times the beam energy which is not present in the multi-hit reconstruction meaning that events with two positrons are recognised like one by the single-hit reconstruction. The performance improves on the main peak with the multi-hit when the number of positrons hitting the calorimeter is more than one. In Figure 4.21 (b) is reported the case $N = 2$ where the single-hit have satellite secondary peaks around the main peak due to three merged positrons and unclusterized hits. These secondary peaks are not present for the multi-hit which have also a much better energy resolution. In Figure 4.21 (c-h) are reported the case $N = 3, .., 8$ which show how the multi-hit is capable to reconstruct up to 8 positrons with good efficiency and energy resolution. This is not true for the single-hit which can not reconstruct more than 3 positrons in the event.

For events with more than two clusters the multi-hit have a fraction of unclusterized hits at low energy. These hits can be merged in the leading cluster of the event, improving the energy resolution, changing some parameters of the clusterization algorithm, such as the hit merging time length. This change can lead to obtain the maximum of the performance in this special single positron run but not in the standard runs with $\sim 25 \times 10^3$ POT/bunch.

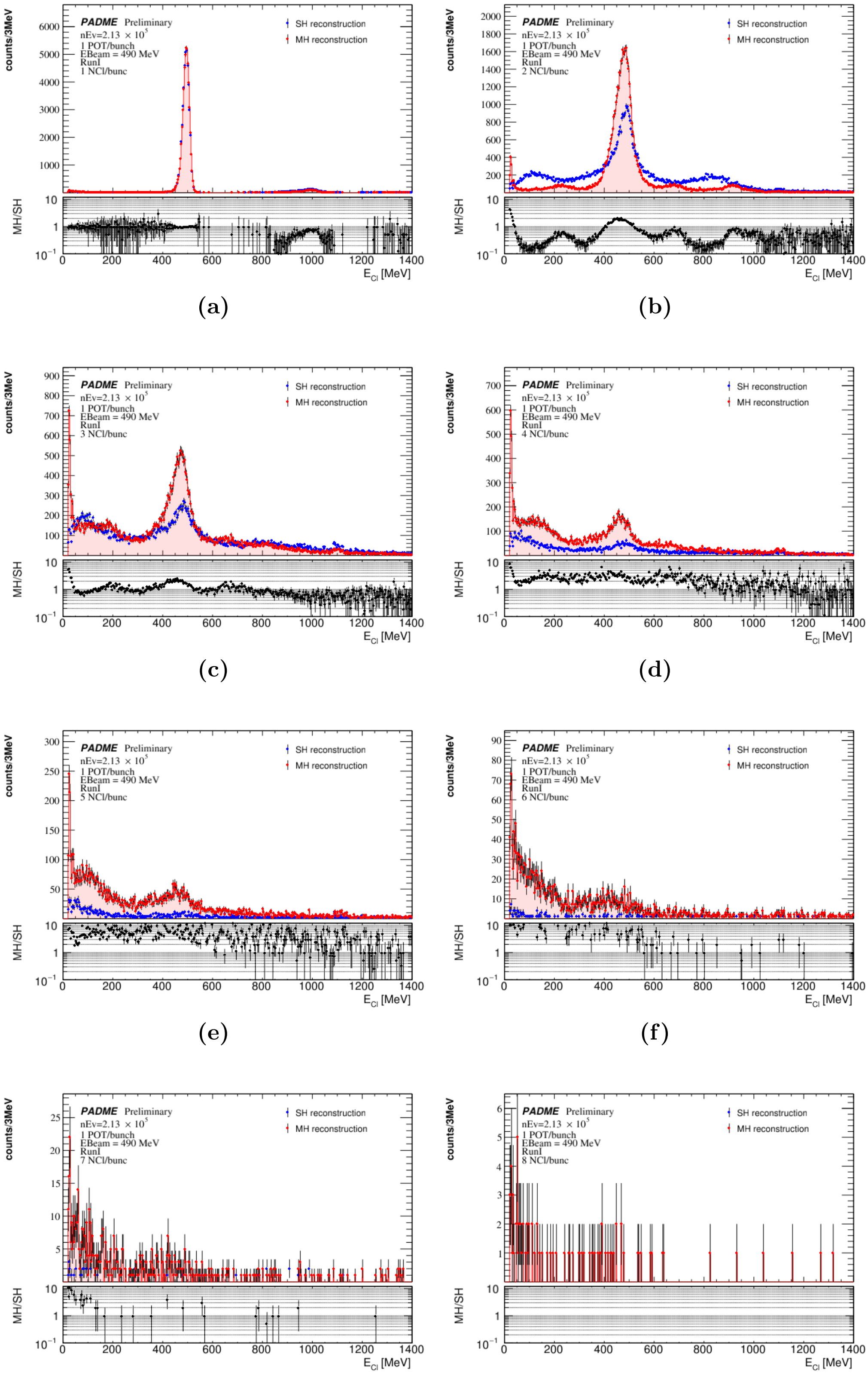

(a) (b) (c) (d) (e) (f) (g) (h)

Figure 4.21: *Cluster energy as reconstructed by the single hit and the multi-hit algorithms for events with the same number of clusters, from 1(a), up to 8(h).*

4.6 Multi-hit reconstruction performance

The performance of the multi-hit was quantified fitting the distribution of the sum of the total cluster energy in the single positron run. The fit function is built as the sum of a polynomial for the background, a Gaussian for the pedestal, two Gaussians for the single positron signal and eight Gaussian for the multi positrons signals. Each signal peak is related to the class of events with a specific number of positrons N_{e^+} hitting the calorimeter, and therefore with a mean given by $E_{N_{e^+}} = N_{e^+}E_{beam}$. Figure 4.22 shows the best fit obtained with the contribution of all single component superimposed to total cluster energy spectrum. For $E > 3.5$ GeV the low statistic doesn't allow to fit the distribution for nine positrons. The central value of the Gaussian functions of the fit are plotted versus the corresponding number of positrons in Figure 4.23. The points were fitted with a linear function ($a + bN_{e^+}$) and the parameters extracted from the fit were $a = 35.07 \pm 0.19$ MeV and $b = 458.67 \pm 0.17$ MeV. There is an offset in the energy response but a good linearity. The energy resolution of the reconstruction obtained at the different energies from the width of the Gaussian functions of the fit is reported in Figure 4.24 (a). For $E \sim E_{beam} = 490$ MeV, the energy of real single positron events, the standard deviation of both Gaussian functions is reported. In Figure (b) the relative resolution of each peak $\frac{\sigma(E)}{E_{mean}}$ as a function of the mean energy is displayed. The first Gaussian of the first peak has the smallest absolute and relative resolution $\sim 3\%$. The absolute energy resolution increases with the number of positrons and saturates above three. On the other hand, the relative energy resolution improves with increasing multiplicity after $E^{tot}_{e^+} = 490$ MeV. Most likely, the anomalous behaviour of the last points is due to the low statistics for the signal with

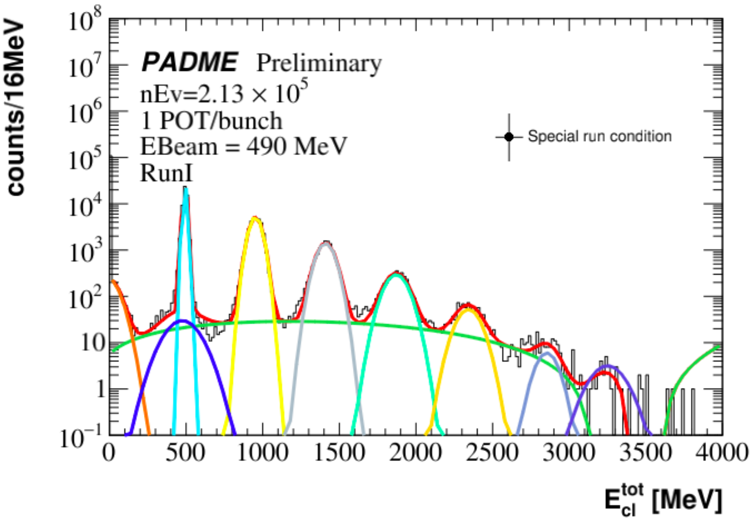

Figure 4.22: *Distribution of the total cluster energy in ECAL for the single positron run obtained with multi-hit reconstruction with a fit curve superimposed made of a polynomial function, to describe the background (green solid line), nine Gaussian functions to describe the multi positron signal and the pedestal.*

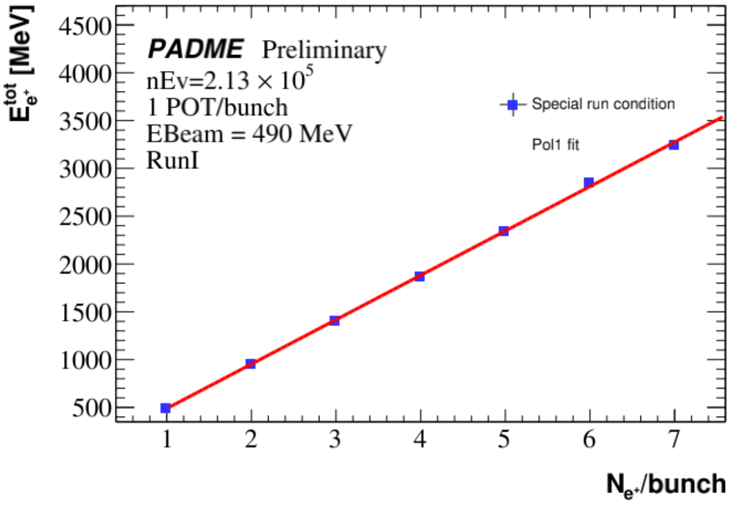

Figure 4.23: *Central energy of the n-th Gaussian function of the fit of Figure 4.22 versus N. The goodness of the fit proves the good linearity of the ECAL and the multi-hit reconstruction also with more than one positron per bunch.*

eight positrons per bunch.

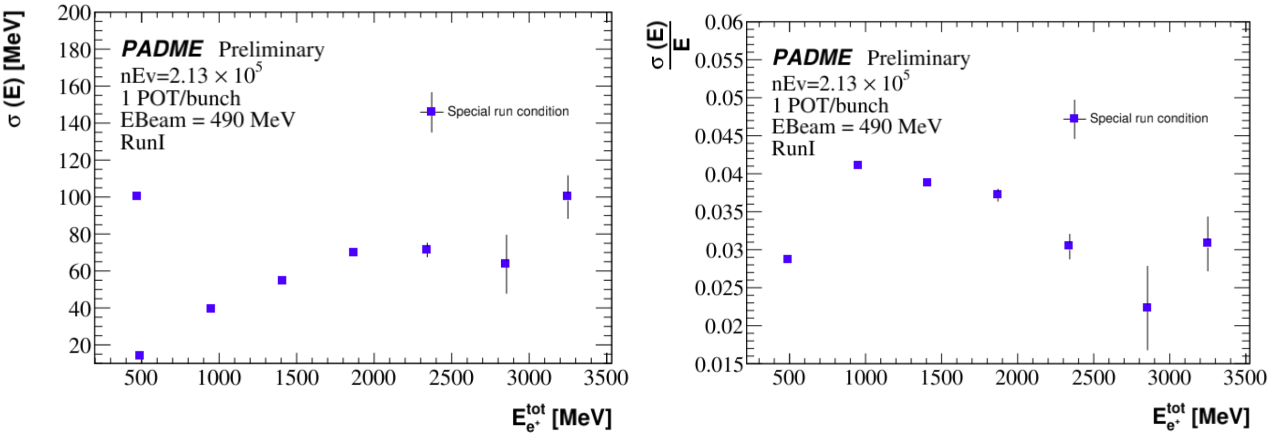

(a)

(b)

Figure 4.24: *Energy width of the n-th gaussian function of the fit of Figure 4.22 versus central energy (a) and the ratio of the two (b). These values represent the ECAL and multi-hit reconstruction energy resolution vs energy. Distribution of the $\sigma(E)$ obtained from the Gaussian fit on the total cluster energy spectrum as a function of the total cluster energy mean. (b) Relative energy resolution as a function of the total cluster energy mean.*

The total number of events for a fixed number of positrons hitting the calorimeter was measured by integrating the corresponding Gaussian functions (for single positron events, the yield is quoted as the sum of the integrals of the two Gaussian). This quantity should follow a

Poisson distribution with mean $< N_{e+} > \sim 1$. In Figure 4.25 the multi positrons signal yield is shown superimposed with the best fit Poisson function with a mean equal to $N_{e+} = 1.18 \pm 0.22$ as expected. The results are shown numerically in Table 4.4. Figure 4.25 and Table 4.4 give also

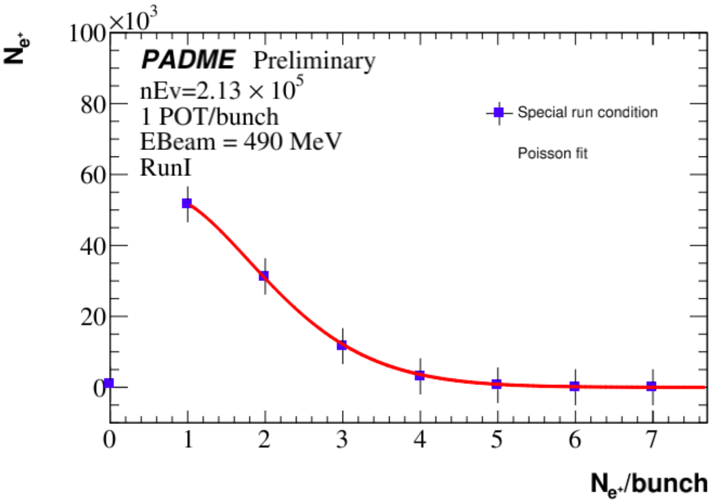

Figure 4.25: *Number of events of the n-th Gaussian function of the fit of Figure 4.22 for $N > 0$ with a Poisson fit superimposed. The mean value of the Poisson function obtained is equal to $N_{e+} = 1.2 \pm 0.2$ as expected from BTF calorimeter measurements.*

Table 4.4: *Number of events of the Gaussian and polynomial functions of the fit of the Figure 4.22 and the sums of all Gaussian functions only.*

Energy [MeV]	Yield
0	918
494	51632
953	31265
1410	11647
1870	3120
2342	566
2854	58
3250	48
Total signal yield	992657
Background	3388

the number of events in the pedestal, which clearly doesn't match the Poissonian distribution. This is due to the data suppression algorithm, applied on-line to the ECAL waveforms, strongly reduces the number of pedestal events saved on disk.

4.7 Simulation of ECAL hits

In the MC simulation the energy deposits managed by GEANT4 give rise to data structures named digi4. From them, new data structures, equal in the format to data hits, named digits are built. The process that converts hits4 in digi4 is named digitisation and the algorithm used is crucial in order to reproduce correctly the real data. For each channel, a very simple and ideal emulation of the single-hit reconstruction was made merging all the hits4 in a single digi4, with energy given by the sum of all hits4 energies and time given by the hits4 with maximum energy. A first attempt to emulate the behaviour of the multi-hit reconstruction was tried with a similar approach: the three most energetic GEANT4 hits are converted in separate digits if their relative distance is higher than 25 ns; hits closer in time are merged, summing the energy. The time of the first hit contributing to the digit is assumed as time of the digit. Eventually, in order to account for the slow decay of the BGO light signals, the energy of any digit is increased by the fraction of the energy of any previous digit overlapping in time in the same channel. Digits produced in these two ways, were directly fed to the nominal clusterization algorithm. These procedures, however, lead to a resolution in energy and time too good with respect to real data. For this reason, a new approach was developed based on the simulation of the entire waveform, which is then processed with the multi-hit algorithm based on signal template as in data. The MC reconstruction based on simulated waveforms reproduce quite well features and energy resolutions of data.

The waveform simulation is done by summing hit templates with time and integral corresponding to the time and energy of each hit4 in the channel. The conversion from hits4 energy into hits template amplitude was obtained with a toy MC. The hit template was scaled with several maximum voltage values and the energy measured from the waveform as in data: the signal was integrated in a time window of $[0, 5000]$ ns, converted in charge, as described in Equation 4.3, and then in energy. In Figure 4.26 is reported the correlation between the maximum template amplitude and energy. The linear fit on the graph gives the correlation that will be used $V_{max}[\mathrm{mV}] = \mathrm{a} + \mathrm{bE[MeV]}$, where $a = 0$ and $b = 3.21$. The function allows to converts hits4 in a time dependent voltage signal. Finally, the simulated waveform per channel was given by the sum of all hits4 signals. The waveform was then converted in a vector of ADC values and changed in sign, since the real signal has a negative amplitude.

The waveforms of the raw data have a fluctuating pedestal level, as shown in Figure 4.27. In the reconstruction the pedestal was extracted from the first 80 samples, where the signal is not yet started and subtracted to reject event by event fluctuations. Fluctuations in the determination of the pedestal are a source of energy spread. The distribution of the pedestals in data has been fit with a Gaussian function, the mean and the sigma were extracted and used to generate a random pedestal that is added to the simulated waveforms.

To simulate the saturation, all the ADC values with $W_i < 15$ was set to 15, as in data. To simulate the noise causing local fluctuation of the signal, a random contribution from a Gaussian with mean 0 and sigma $\Delta Voltage$ was added bin by bin to the waveform. In order to reproduce data, the noise was assumed to increase with energy as $\Delta Voltage = -0.17 + 0.13E - 0.0005E^2$. This relation was extracted studying the difference between many waveforms with

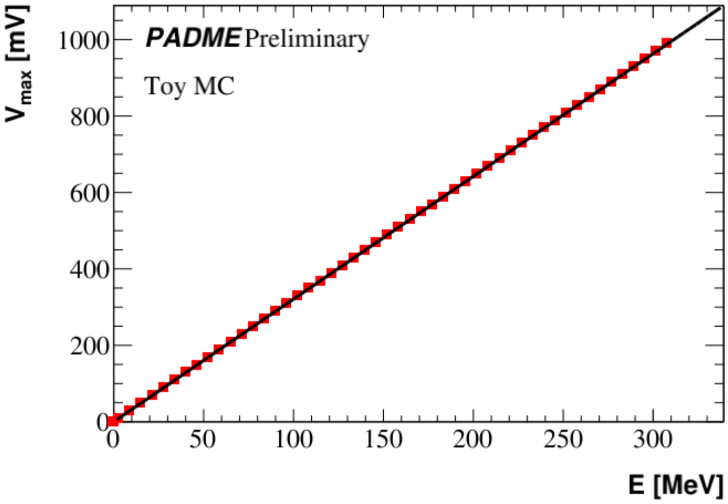

Figure 4.26: *Correlation between the hit template maximum amplitude and hit template energy extracted using a toy MC. Superimposed the liner fit* V_{max}[mV] = 3.21E[MeV] mV/MeV.

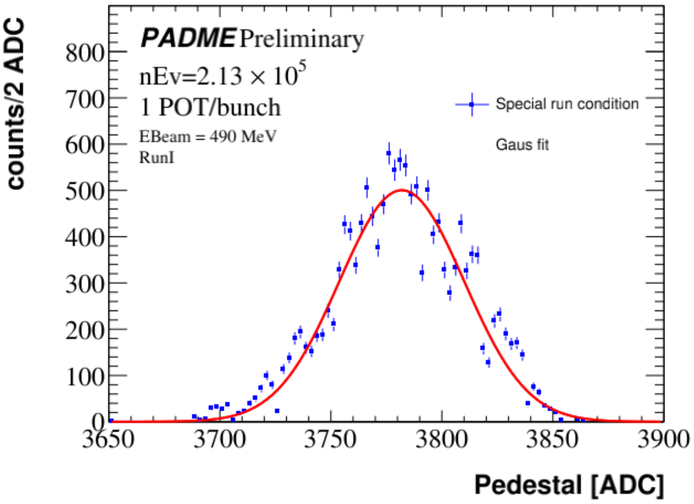

Figure 4.27: *Distribution of the pedestal in raw data extracted from the first* 80 *samples for all channels in the single positron run.*

the corresponding adjusted templates.

The simulated waveforms were generated in the reconstruction process to avoid the storage of memory-consuming waveforms for all ECAL channels. Once the waveform is simulated, it will be temporarily stored in the data format of the raw data, then reconstructed in hits and clusters as describe in the previous sections.

4.7.1 Results of single positron simulation

The MC with simulated waveforms was used to generates single positron events in the same conditions of the special single positron run. The beam background was not simulated, since the beam was generated in front of the target. The features of the single positron simulation were:

- positron energy of 490 MeV;
- positrons per bunch distributed as a Poissonian of average 1;
- beam spot size of 5 mm;
- beam energy spread of 5 MeV;
- impact point coordinates of the positrons on the ECAL front face $(x, y) = (165\,\text{mm}, 0\,\text{mm})$ obtained for $B = 0.09$T.

The single positron data and MC samples were reconstructed using the multi-hit algorithm and compared. The main features of the reconstruction are the distribution of the number of hits and the number of clusters, which are reported in Figure 4.28. The comparison shows that the number of hits reconstructed in the calorimeter for the MC sample is higher than data (Figure 4.28 (a)). However, the distributions of the physics objects, the clusters, are a good agreement (Figure 4.28 (b)).

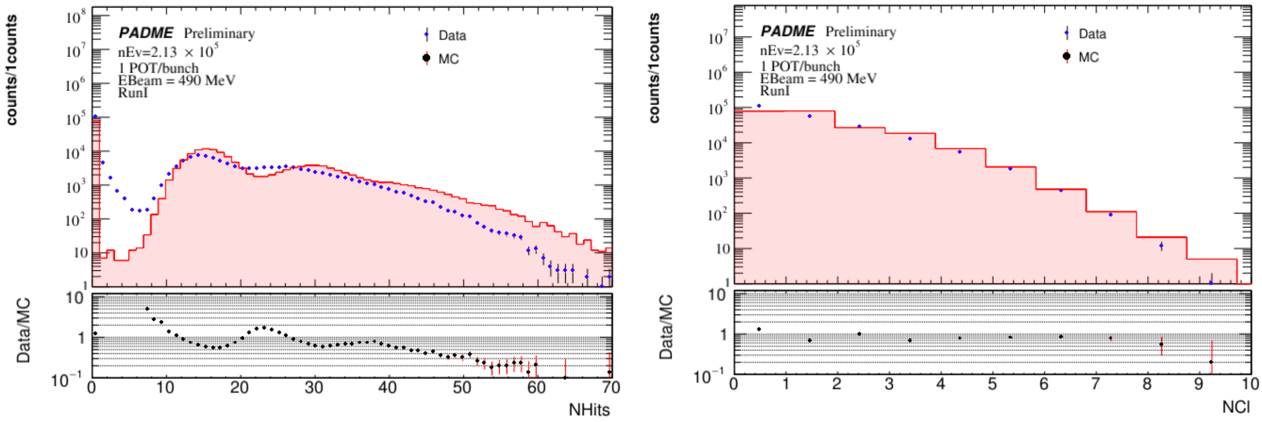

(a)

(b)

Figure 4.28: *Comparison between data (blue dots) and MC simulation (red solid line) of the distribution of number of hits and clusters per event for the single positron run.*

Figure 4.29 shows the distribution of the energy sum of all clusters. The absence in the simulation of the beamline is highlighted by the lower background level. The MC distribution has all peaks shifted at higher energy with respect to the data distribution, an effect more

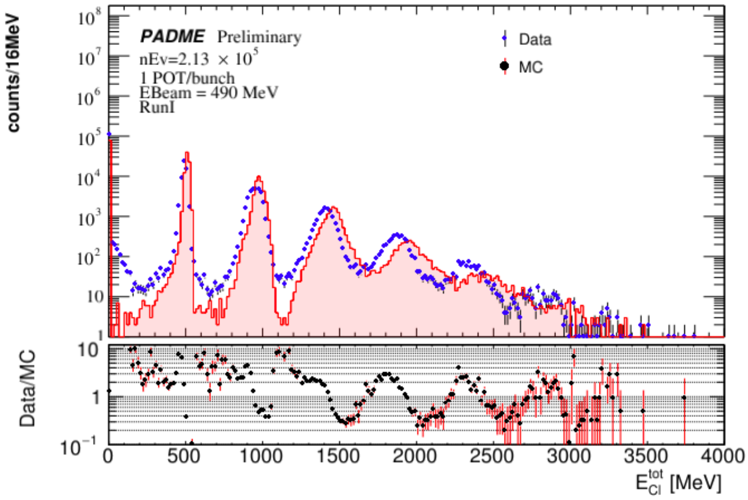

Figure 4.29: *Sum of the energy of all ECAL clusters in data (blue dots) and MC with simulated waveforms (red solid line).*

evident at high energy. It is important to notice that the energy resolution of the MC reproduces the resolution of data quite well.

The plots relevant to deduce the spatial and time resolutions are shown in Figure 4.30. In particular, in Figure 4.30 (a) the spatial resolution can be assessed from the width of the distribution of the distance in the reconstructed X coordinate between any pair of hits. A similar distribution is observed for the Y coordinate. In Figure 4.30 (b) the time resolution can be estimated from the width of the distribution of the distance in time between any pair of hits. Both distributions are indicative of a good description of the resolution, in spite of a larger number of hits in MC samples. Finally, the scatter plots of the number of hits and clusters versus hits and clusters total energy respectively are shown in Figure 4.31 for the MC with simulated waveforms. They are in nice agreement with the corresponding distributions observed in data (see Figures 4.17 (b) and 4.18 (b)).

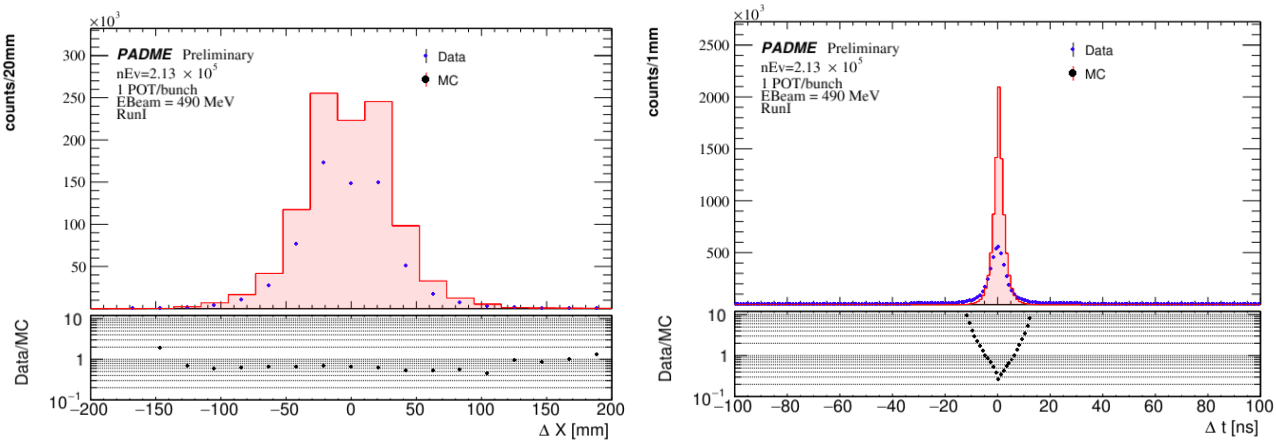

(a) (b)

Figure 4.30: *Distance in the reconstructed X coordinate (left) and in time (b) between any pair of ECAL hits in data (blue histogram points) and MC with simulated waveforms (red filled histogram).*

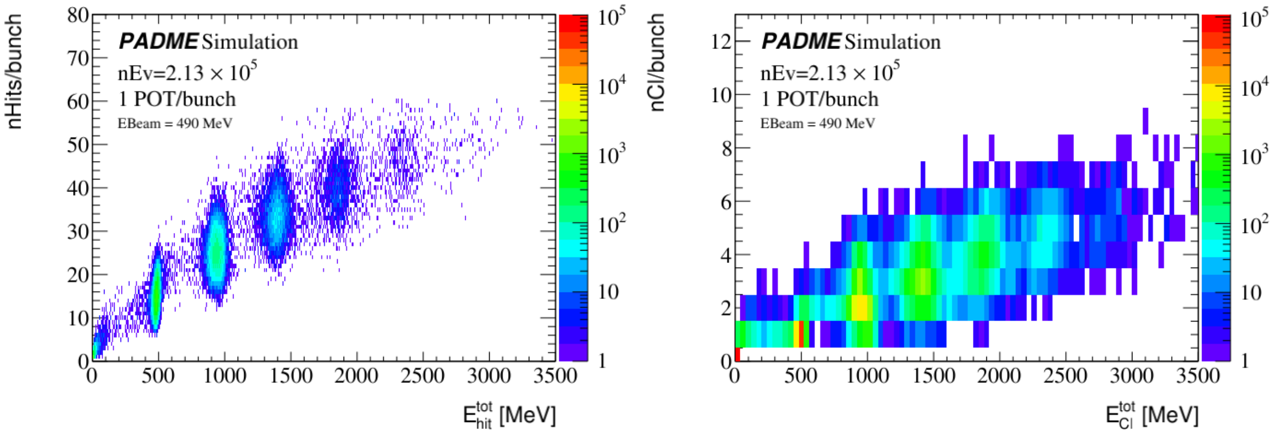

(a) (b)

Figure 4.31: *Number of hits (a) and clusters (b) as a function of the sum of the energy of all hits (a) and clusters (b) in MC with simulated waveforms. To be compared with Figures 4.17 (b) and 4.18 (b) for real data.*

5

$e^+e^- \to \gamma\gamma$ cross section measurement

The annihilation in two photons is a very important SM candle process for PADME. Gaining a good knowledge of this process allows to monitor with a physics candle the energy scale, the number of positrons hitting the target and to cross check the detector geometry. In addition, it allows to exercise on a easy test case the strategy to fight the background to the dark search. The signature of this process in the experiment consists in the presence of two photons in the electromagnetic calorimeters. Since the SAC detector is overwhelmed by Bremsstrahlung photons, only the main calorimeter, ECAL, is used to perform this analysis. The goal of this study is to measure the cross section of $e^+e^- \to \gamma\gamma$ using the data collected by the experiment during RunII. In this chapter the entire strategy is described, including a very important and challenging step that is the measurement of the efficiency. The technique adopted is first described, then validated on dedicated MC samples and applied to data. Nowadays, only a few measurements of the cross section exist at the PADME energy scale. Appendix A collects a brief review of the existing results, often affected by large uncertainties.

5.1 The cross section measurement strategy

The total cross section, σ_T, for the process $e^+e^- \to \gamma\gamma(\gamma)$ can be measured in PADME using the following relation:

$$\sigma(e^+e^- \to \gamma\gamma) = \frac{N_{sig}}{N_{POT} \times N_{\frac{e}{S}} \times A \times \epsilon} \tag{5.1}$$

where

- N_{sig} is the number of signal processes observed after a selection based on the kinematic correlations typical of annihilation events once subtracted of the background component. In this thesis work several selection procedures for the annihilation process have been considered. In addition, for searches based on the identification of a pair of photons, event selections using only one photon have been studied. The choice among the various possibilities has been taken, balancing the difficulty in estimating the background from physics process and from spurious beam interactions and the difficulty in evaluating the overall selection efficiency;

- N_{POT} is the total number of positrons hitting the target measured with the Active Diamond Target;
- $N_{\frac{e}{S}}$ is the number of atomic electrons per unit surface in the PADME target. It is estimated as $N_{\frac{e}{S}} = \frac{\rho \times N_A \times Z \times d}{M_W} = 0.0105 \pm 0.0001\ \mathrm{b}^{-1}$, where $\rho = 3.520 \pm 0.002\ \mathrm{g/cm}^3$ is the Diamond density, N_A is the Avogadro number, Z the atomic number, $d = 100 \pm 1\ \mu\mathrm{m}$ is the target thickness and M_W is the atomic weight;
- A is the acceptance of the PADME detector and of the selection criteria applied. Therefore, it results from both geometric and kinematic constraints. The determination of the acceptance will be described in Section 5.5.1. The acceptance allows to relate the total cross section σ_T to the so called fiducial cross section σ_F, corresponding to the fraction of the cross section directly visible in the experimental apparatus and lying within the kinematic selection requirements $\sigma_T = \sigma_F/A$;
- ϵ is the overall efficiency to identify signal processes. It represents the combination of the detection efficiency of the PADME calorimeter. the photon reconstruction and identification efficiency for both photons and the event selection efficiency. Therefore, when N_{sig} is measured with a selection requiring two photons in ECAL, the efficiency ϵ is the product of the identification efficiencies, $\epsilon(\gamma_1)$ and $\epsilon(\gamma_2)$ of the two photons.

Detector defects and asymmetries often prevent the performance of photon reconstruction algorithms from being uniform. Therefore, the event efficiency varies depending on the regions of the detector where the photons have been detected and, in general, the efficiency ϵ cannot be applied as a constant term in Equation 5.1, unless it is estimated as an average value over the data sample.

Several procedures can be applied to generalize Equation 5.1 taking into account these problems. An approach consists in measuring the fiducial cross section as follows:

$$\sigma_F = \sigma(\theta_0 < \theta_{\gamma_{1,2}} < \theta_1) = \frac{\sum W_i - N_{bkg}}{N_{POT} \cdot n_{\frac{e}{S}}}. \tag{5.2}$$

Each candidate contributes to the counting with a weight accounting for all the efficiency factors that determine the probability of such event to be selected. N_{bkg} is the estimated background contaminating the sample of selected events corrected for the efficiency. For the candidate annihilation event i, the weight W_i is given by the inverse probability to identify the two photons in the event:

$$W_i = P^{-1}(\theta_{\gamma_{i_1}}, \theta_{\gamma_{i_2}}) = [A_{eff}(\theta_{\gamma_{i_1}}, \theta_{\gamma_{i_2}}) \times \epsilon(\theta_{i1}, \phi_{i1}) \times \epsilon(\theta_{i2}, \phi_{i2})]^{-1} \tag{5.3}$$

where $\epsilon(\theta_{i_{1,2}}, \phi_{i_{1,2}})$ is the efficiency as a function of the position in the calorimeter for the first or second photon. The factor $A_{eff}(\theta_{\gamma_{i_1}}, \theta_{\gamma_{i_2}})$ is the visible acceptance and it represents a correction to the acceptance that takes into account resolution effects causing the migration of events from the acceptance region to the outside and vice versa. It will be discussed in more details and estimated in Section 5.5.2.

The efficiency values used in Equation 5.2 can be estimated with simulation or can be directly measured in data if a suitable sample of reference photons can be defined and used to measure the fraction of them that is successfully detected and identified. Section 5.6.1 describes a data-driven determination of the efficiency that is used in the cross section measurement, exploiting the approach of Equation 5.2. This technique was developed for the first time in this work.

Data-driven efficiency measurements may be affected by biases. Some example will be discussed in Section 5.7.2. On the other hand, simulations are often affected by residual mismodeling of the detector response and geometry and of the beam features. Another strategy, meant to address these problems, consists in estimating the reconstruction and selection efficiency in a simulation corrected for MC mismodeling. In practice, this is done by replacing ϵ in Equation 5.1 with a global efficiency factor C given by the ratio between simulated and generated events inside the fiducial region corrected for mismodelling. The corrections are expressed in terms of scale factors equal to the ratio between event efficiency measured in data $\epsilon^{data}(\theta, \phi)$ and in simulation $\epsilon^{MC}(\theta, \phi)$, the latter being obtained with exactly the same method of data. In summary,

$$\sigma_F = \frac{N_{sel}}{C_{\gamma\gamma} \cdot N_{POT} \cdot n_{\frac{e}{S}}}, \tag{5.4}$$

with

$$C_{\gamma\gamma} = \frac{N_W^{MC}(\theta_{min} < \theta_{\gamma_1,\gamma_2} < \theta_{max})}{N^{gen}(\theta_{min} < \theta_{\gamma_1,\gamma_2} < \theta_{max})}, \tag{5.5}$$

with

$$N_W^{MC}(\theta_{min} < \theta_{\gamma_1,\gamma_2} < \theta_{max}) = \sum_i f_i^{data/MC}, \tag{5.6}$$

with

$$f_i^{data/MC} = \prod_j f_{ij}^{data/MC} \tag{5.7}$$

where $f_{ij}^{data/MC}$ is the data-simulation scale factor for any efficiency contribution, for example for photon 1 in event i leads a scale factor $f_{i1} = \epsilon_{DD}^{data}(\theta_1, \phi_1)/\epsilon_{DD}^{MC}(\theta_1, \phi_1)$, where the efficiency $\epsilon_{DD}^{data}(\theta_1, \phi_1)$ is measured with a data-driven (DD) method both in data and in Monte Carlo. Therefore, the quantity N_W^{MC} represents the number of signal events selected in the simulation, but corrected for local mismodelling of data, and N^{gen} is the number of simulated signal events that at generator level fall in within the acceptance of the selection. Finally, the factor $C_{\gamma\gamma}$ would correspond to purely MC based efficiency for the selection if all scale factors were equal to 1.

In this work the cross section measurement will be derived using Equation 5.1, and Equation 5.2 as a cross check, relying on a data-driven determination of the photon selection efficiency. The possible biases of the methods are studied in dedicated simulations and found to be negligible or mitigated by compensation effects. This topic will be discussed in Section 5.7.2, where the cancellation due to compensation effects will be described, and in Section 5.7.3, where a careful implementation of the data-driven method will be shown to lead to negligible biases. The second approach based on scale factors was also investigated on MC simulating detector defects and found to be a powerful methodology. However, it was not used for the measurement due to the unavailability of a suitable simulation of the PADME beam line and the related background.

5.2 Theory predictions

The CalcHEP [88] and Babayaga [96] MC generators were used to obtain a prediction for the total annihilation cross section for a beam energy of 430 MeV. The prediction based on a Leading Order matrix element are $\sigma(e^+e^- \to \gamma\gamma)^{CalcHEP} = 1.91218$ mb and $\sigma(e^+e^- \to \gamma\gamma)^{Babayaga} = 1.91096 \pm 0.00036$ mb. They are compatible within 0.06%. Using Babayaga it is also possible to obtain the Next Leading Order prediction, which turns out to be $\sigma(e^+e^- \to \gamma\gamma(\gamma))^{Babayaga} = 1.9573 \pm 0.0005$ mb.

5.3 Data sample, simulation and reconstruction

5.3.1 Data sample

The data used for this measurement have been chosen among the sample collected during RunII, because of the smallest background level, as seen in Chapter 3. During these runs the energy of the beam was $E_{beam} = 430$ MeV and the beam density ~ 100 POT/ns. A summary of the runs used for the analysis with their main features is collected in Table 5.1. The total number of positrons on target corresponding to the full data sample is $N_{POT} = 3,97 \times 10^{11}$. In Figure 5.1 the structure in time of the bunch is shown for the different runs. As highlighted by Table 5.1 and Figure 5.1 the runs have different features not only in multiplicity per bunch but also in bunch structure. The run selection was driven by the requirement of high stability of the beam intensity and of the beam spot position on target during data taking. Indeed, the data

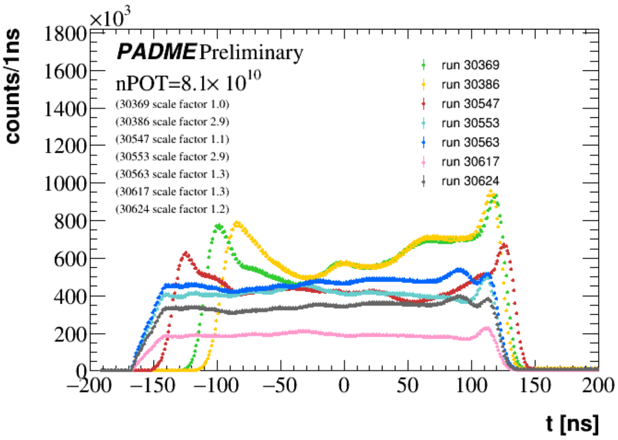

Figure 5.1: *Bunch temporal structure of the runs used in this analysis recorded with the SAC.*

quality monitor of the experiment shows that the number of positrons on target measured by the Diamond is very stable as is shown in Figure 5.2 for run 30617.

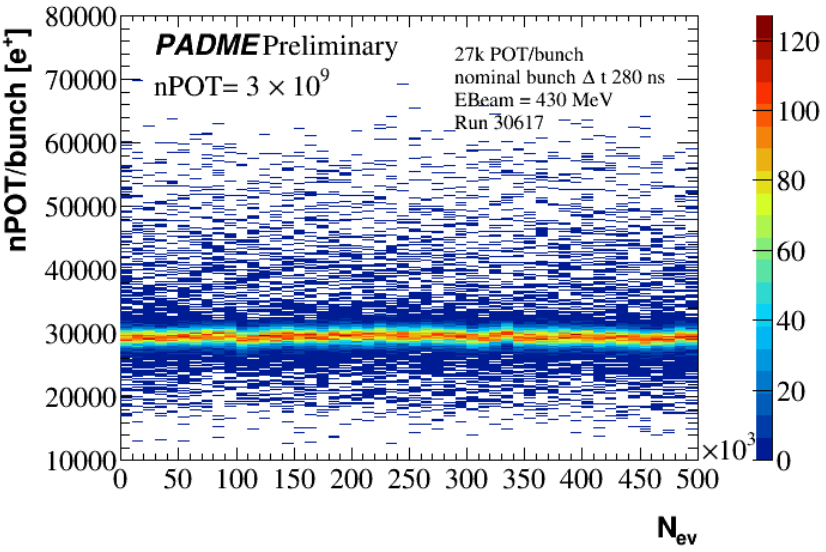

Figure 5.2: *Number of positrons per bunch as measured by the Active Diamond Target as a function of the event number for run* 30617*.*

A special data sample consisting of two runs, recorded with the target out of the beam line, has also been used. This sample allows to study the beam related background observed in PADME .

Table 5.1: *Main features of the analysed runs: run number, total N_{POT} measured by target, mean and sigma of a Gaussian fit to the peak of the N_{POT} distribution, bunch length and month of data taking.*

Run number	$N_{POT}/10^{10}$	$\mu(N_{POT})$	$\sigma(N_{POT})$	bunch length [ns]	Date	
30369	8.2	26993	1738	260	Sept	
30386	2.8	19057	1385	240	Sept	
30547	7.1	31480	1402	270	Oct.	
30553	2.8	35729	1314	260	Oct.	
30563	6.0	26785	1231	270	Oct.	
30617	6.1	27380	1496	270	Nov.	
30624	6.6	29515	2070	270	Nov.	
30654	/	~ 27000	/	~ 270	Nov.	no target
30662	/	~ 27000	/	~ 270	Nov.	no target

With a total of $N_{POT} = 4 \times 10^{11}$, assuming a product of acceptance and efficiency of the order of $\sim 5\%$ the number of detected annihilation events is about $\sim 5 \times 10^5$; if the background is negligible or compatible with the signal, the relative statistical error on the cross section measurement would be $\sim 1\%$ and even if the background rate is ten times larger than the signal, the statistical uncertainty would be $\leq 3\%$ which is unlikely to be larger than the systematic uncertainties affecting the measurement. Therefore, the sample selected is adequate in size to the measurement.

5.3.2 Simulation samples

The PADME MC is based on a GEANT4 [87] simulation of the experimental apparatus and of the beam line. Annihilation processes are simulated when the positrons of the beam cross the Active Diamond Target along with the other dominant QED processes: Bremsstrahlung in particular, Bhabha scattering, and other minor effects. However, a large number of positrons per bunch must be simulated to achieve a reasonable statistics of annihilation processes, therefore the final state from a $e^+e^- \to \gamma\gamma$ event often overlaps with other photons in the calorimeter. Moreover, the signal process, $e^+e^- \to \gamma\gamma$, is generated, together with all other processes, through the GEANT4 simulation of the propagation of the beam inside the target. However, the PADME MC does not keep a record of the kinematics of annihilation photons in MC truth. In order to study the kinematics of annihilation events either in a background free simulation, or flagging the final state particles, the CalcHEP generator was used. From the $e^+e^- \to \gamma\gamma$ generation, a text file was saved with the four-momenta of all particles involved in the process. A special functionality in PADME MC allows to plug the two photons from an event generated by CalcHEP in a point of the target where a positron from the incoming beam is killed. The photons are then propagated through the detectors like any particle managed by GEANT4.

Several MC data samples were used across the analysis:

1. CalcHEP event generator samples, used to study the MC truth and generator level properties;

2. CalcHEP samples simulated with PADME MC with a beam consisting of a single positron. In this case the final state of each event contains only two photons from e^+e^- annihilation that can fall inside or outside the detector geometrical acceptance;

3. CalcHEP samples simulated with PADME MC as in case 2. but with a beam of 25×10^3 positrons in average per bunch. This simulation allows investigating the effect of the pileup of the signal event with physics background processes originating from beam interactions in the target.

The CalcHEP generator performs all calculations in the Leading Order (LO) approximation for the final state selected by the user, that can be in our case, $\gamma\gamma$ or $\gamma\gamma\gamma$. In order to study how the kinematics of two-photon annihilation changes at Next Leading Order (NLO), the Babayaga generator was used. In particular samples of 10^6 events of photons annihilation at LO and at NLO were generated.

5.3.3 Event reconstruction

The selection of annihilation events uses only the PADME BGO electromagnetic calorimeter. Therefore, here a brief reminder of the main features of the reconstruction of clusters in ECAL is given, while an extensive description of the algorithms is given in Chapter 4.

The multi-hit reconstruction, described in Section 4.4, was used. For each waveform up to three hits can be identified, with energy and time estimated fitting with a signal template obtained from clean waveforms recorded in a single positron run. The template allows to naturally account and correct for problems related to the data acquisition like the limited acquisition time window and the saturation. For signals, where only one hit is identified in the waveform, energy and time determination follow the same logic applied in the single-hit reconstruction, described in Section 4.2.

Once the hit collection is defined, clusters are reconstructed merging hits in nearby crystals in time coincidence. The energy required for the cluster seed is at least 20 MeV, while hits contributing to the cluster must have energy above 1 MeV, a distance from the seed not exceeding three crystals and a maximum distance in time from the seed of 6 ns. The hits energies were corrected for the relative calibration factor extracted using the cosmic rays. However, an additional absolute calibration factor is needed to have the annihilation peak at the beam energy, this factor is equal to 1.11 for RunII data.

The cross section measurement requires the determination of the number of POT. This was estimated using the calibration procedure described in Section 2.2.3. This procedure rely on the absolute energy calibration of the BTF calorimeter that is verified to 4%.

5.4 Experimental signature of annihilation events

The selection of annihilation processes is based on the constrained photon-photon kinematics. In the assumption of a final state consisting of exactly two photons sharing the energy and momentum of the initial state, several relationships can be exploited between the energies E_1 and E_2, the polar angles[1] θ_1, θ_2, and the azimuthal angles[2] ϕ_1, ϕ_2 of the photons. The most relevant of them are listed in the following, adopting the convention of using the index 1 for the most energetic photon in the pair:

1. the sum of the energies E_1+E_2 is equal to the beam energy with very good approximation;
2. the transverse momenta of the photons are back to back, therefore $\phi_1 + \pi = \phi_2$
3. for each photon the polar angle θ is a function of the energy;
4. As a consequence of properties 1 and 3 the polar angles of the two photons are strictly correlated;

---

[1] The polar angle θ is defined as the angle between the photon direction and the z axis of the PADME reference frame, which is assumed to match the direction of the incoming positron beam.

[2] The azimuthal angle ϕ is the angle between the direction of a photon in the plane perpendicular to the beam and a reference axis conventionally chosen to be the x axis.

5. The previous considerations imply that knowing E_1 sets the value of the second photon polar angle θ_2; the same is true if the role of the two photons is exchanged;

6. The momentum balance implies the following relation between the coordinates of the impact point of the two photons in a transverse plane

$$x(y)_{CoG} = \frac{x(y)_1 E_1 + x(y)_2 E_2}{E_1 + E_2} \sim 0. \tag{5.8}$$

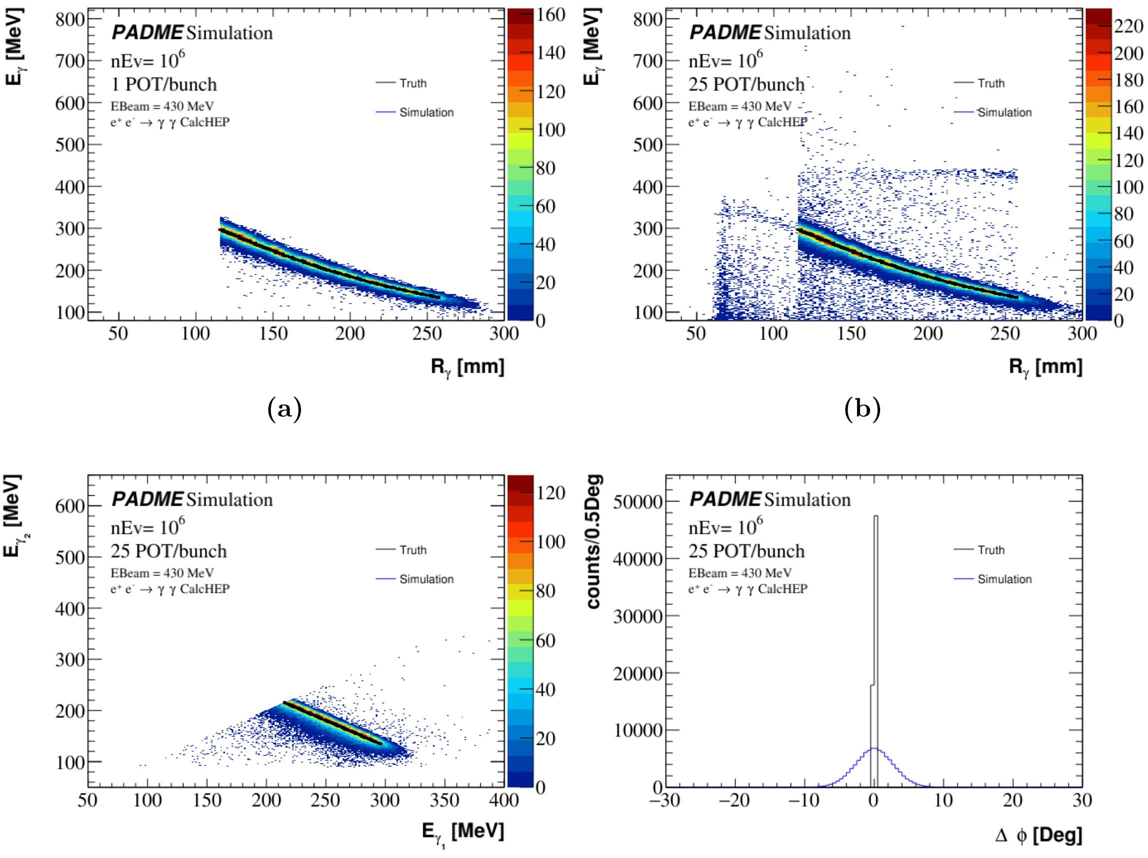

(a) (b)

(c) (d)

Figure 5.3: *Comparison of CalcHEP generation and simulation of the same events with and without pileup. Correlation between energy and radial position of the photon for annihilation events (a) and adding pileup events (b). Correlation between the energy of the first and second photon (c) and distribution of* $\Delta\phi$ *(d).*

In Figure 5.3 the correlation between the energy E_γ and the radial position R_γ (that corresponds to the polar angle θ_γ) of the two photons is reported along with the two photons energy correlation and the distance in ϕ between a photon and the other extrapolated in the backward direction. Figure 5.4 shows the X and Y center of gravity for the CalcHEP simulation.

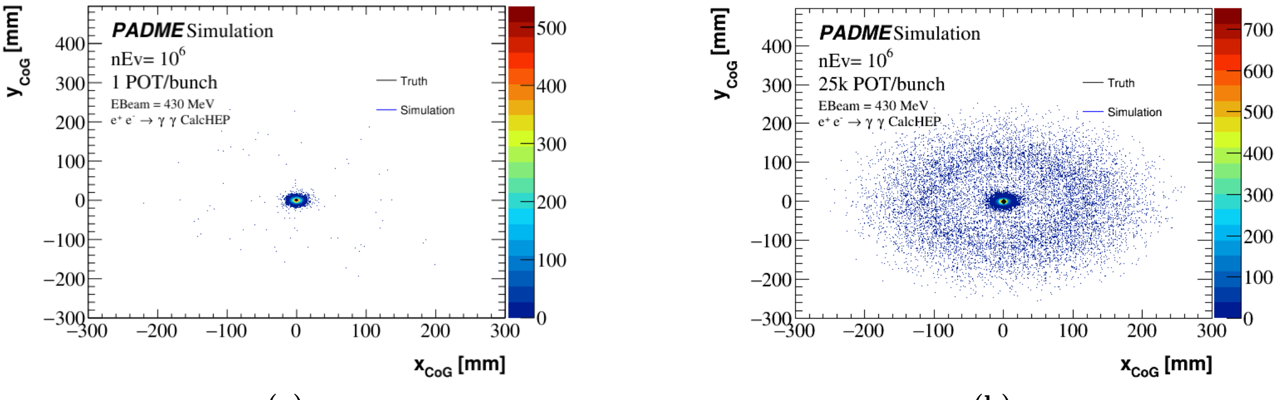

(a) (b)

Figure 5.4: *X and Y Center of Gravity map for annihilation events (a) and adding pileup events (b).*

When the beam intensity is of the order of 25000 POT/bunch, the pair of photons in time coincidence produced by an annihilation event is overlapped to energy deposits in the calorimeters and hits in the veto detectors that are produced by the physics background processes due to interactions of other positrons in the bunch with the target. The background photons, positrons and possibly electrons seen in the detectors are distributed within the $\sim$ 280 ns time width of the bunch. Therefore, the time coincidence between the two signal photons is a powerful handle to suppress the background which can be used along with the kinematic correlations. Figures 5.3 (a) and 5.4 (a) show the correlation between the energy-radial coordinate and the CoG map, respectively, for a pure annihilation process simulation. Figures 5.3 (b) and 5.4 (b), instead, show the same distributions for a sample of pure annihilation events simulated in PADME MC along with 25000 positrons.

In the PADME data the scenario is further complicated by the beam induced background, which, due to the high rate, implies a high probability of accidental two-photon coincidence, and, in general, the accidental occurrence of the kinematic correlations typical of annihilation events.

The annihilation yield, i.e. the number of annihilation processes seen in the PADME detector, can be measured starting from the distribution of the sum of the two photon energies, or of the CoG coordinates, or of the difference in the azimuthal angle $\Delta\phi = \phi_1 + 180^\circ - \phi_2$. In all these distributions a peak, corresponding to signal events, will emerge over the combinatorial background, provided the latter is small enough. The background reduction can be achieved exploiting the other variables or correlations sensitive to the signal. For example, photons from the annihilation process can be selected by requiring a minimum energy and the consistency between energy and polar angle: $|\Delta E| = |E_\gamma - E(\theta_\gamma)| < \Delta_E^{Max}$.

In the following a sequence of selection cuts, summarized in Table 5.2, will be used to show how the annihilation signal emerges in RunII data. The energy cuts reported in Table 5.2 are set studying the energy of the two photons of CalcHEP truth, see Figure 5.5.

In addition to the cuts on the kinematic variables and on the time coincidence, a geometrical

Table 5.2: *Annihilation selection cut, threshold applied on each variable and cut flow for CalcHEP simulation with pileup from* 25000 *positrons per bunch and for data (run 30563).*

Cut ID	Cut description		Threshold	Simulation	data
a	Time coincidence	$\lvert t_{\gamma_1} - t_{\gamma_2} \rvert$	< 10 ns	1.00	1.00
b	γ_1 in FR	R_{γ_1}	$\in]115.82\ \text{mm}, 258\ \text{mm}[$	0.70	0.73
c	CoG	$\lvert x_{CoG} \rvert$	< 50 mm	1.00	0.87
d	CoG	$\lvert y_{CoG} \rvert$	< 50 mm	1.00	0.96
e	γ energy	$E_{\gamma_1}, E_{\gamma_2}$	$\in [90\ \text{MeV}, 400\ \text{MeV}]$	1.00	1.00
f	sum of γ energies	$E_{\gamma_1} + E_{\gamma_2}$	$\in [300\ \text{MeV}, 600\ \text{MeV}]$	1.00	0.98
g	γ_2 in FR	R_{γ_2}	$\in]115.82\ \text{mm}, 258\ \text{mm}[$	0.96	0.96

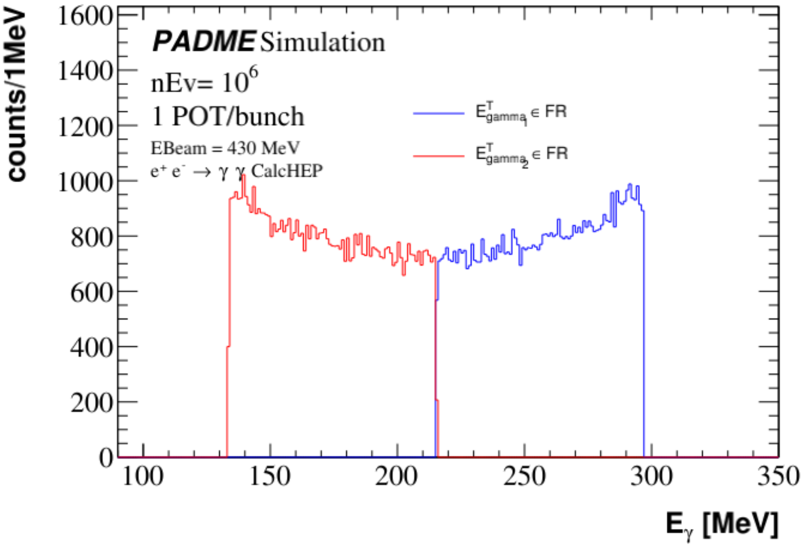

Figure 5.5: *Energy distributions in blue for the leading photon and in red for the sub-leading photon.*

requirement is introduced to ensure a reliable reconstruction of the photons. Indeed, the position of the clusters in ECAL must be at distance from the inner and from the outer border of the calorimeter equal to al least twice the width of a BGO crystal. This ensures limited transverse shower leakage and therefore a good determination of the energy and position. Applying in sequence the selection cuts improve the background rejection as demonstrated by Figure 5.7. The sum of the energy of the two selected photons $E_{\gamma_1} + E_{\gamma_2}$ corresponds to events passing the time coincidence and the fiducial region requirement for the most energetic photon γ_1. The amount of background is strongly reduced adding the CoG request. The energy cuts applied to each photon help to further reduce the background. The population of events under the peak, clearly corresponding to annihilation processes, is not significantly reduced by the cuts.

Figure 5.8 (a) shows that the additional cut of the FR on the second photon (the less energetic one) reduces (of $\sim 5\%$) the yield of the annihilation. In Figure 5.8 (b) only the most

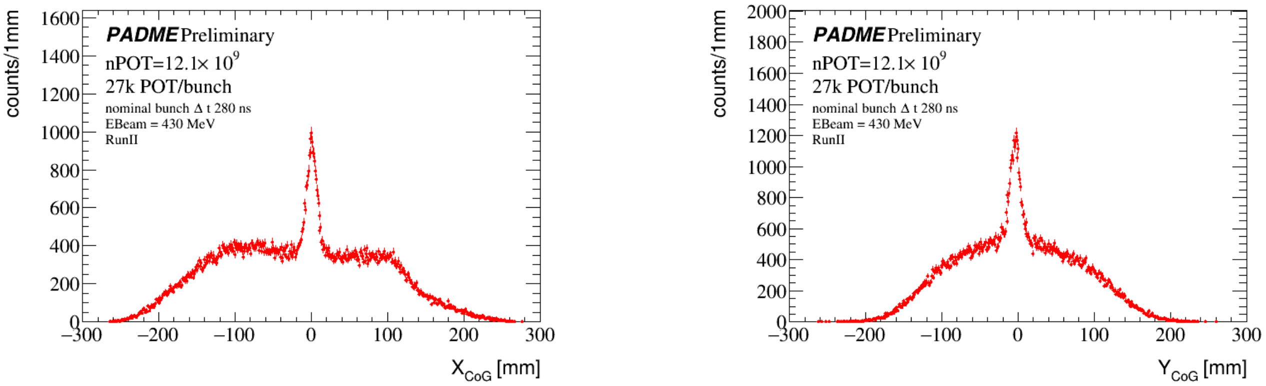

(a) **(b)**

Figure 5.6: *Distribution of the Center Of Gravity variables for events that satisfy the time coincidence cut and with the leading photon in FR (described in Table 5.2). (a) distribution of* X_{CoG}*, (b) distribution of the* Y_{CoG}*.*

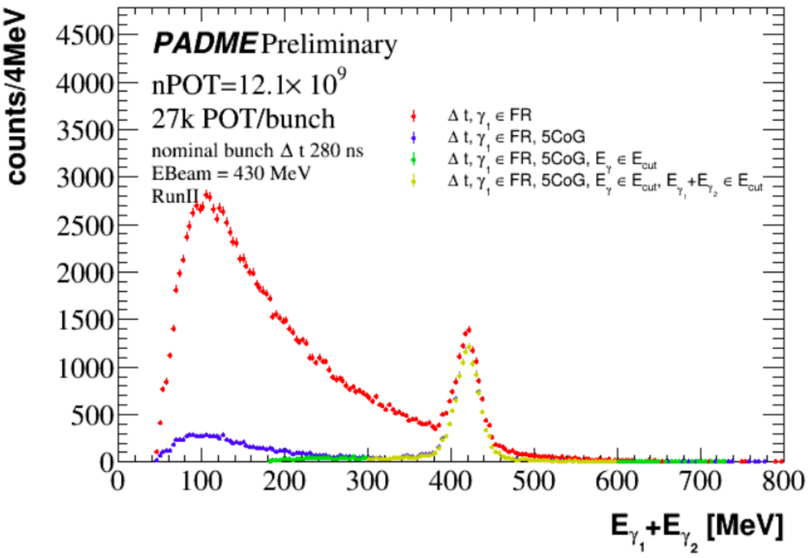

Figure 5.7: *Sum of the photon energies for pairs of photons passing various sets of cuts. In red events that pass the time coincidence request with the first photon in the FR; in blue the distribution for events passing also the CoG cut (5 cm). Finally in green (yellow) events satisfy also the energy requirements for one photon (both photons).*

energetic photon is required to be in the FR. It is interesting to notice that this requirement does not lead to a sharp cut-out of the R_{γ_2} distribution and this is the reason of the smaller acceptance of the selection requiring both photons in the FR. Most of the studies in this work are performed with both analysis variants: selecting only events with the first photon in the FR or selecting events with both photons in the FR.

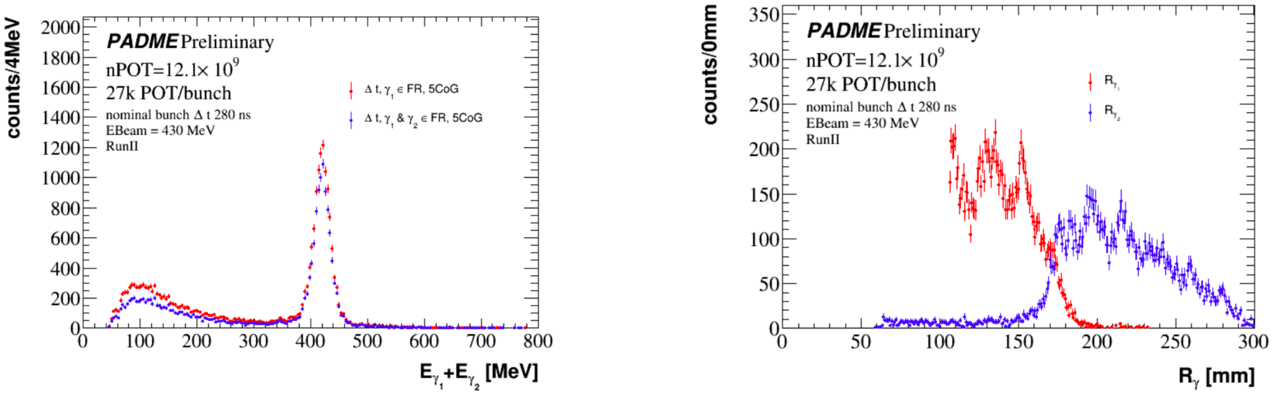

(a) (b)

Figure 5.8: *(a) Distribution of the sum of the photon energies for the events that pass the cuts of time coincidence and CoG (described in Table 5.2). In red the request of FR is applied only to the most energetic photon, while in blue on both photons. (b) Radial distribution of the most energetic photon in red and of the second most energetic photon in blue, for events passing time coincidence, FR on the most energetic photon, CoG and energy cuts.*

5.5 Acceptance

The acceptance has been introduced in Equation 5.1 as a global factor describing the fraction of events, corresponding to the process under study, that can be detected by the experimental apparatus of PADME with the kinematic requirements applied. This concept is based on the assumption of full efficiency of the PADME detectors, DAQ and data reconstruction algorithms. Indeed, in Equation 5.1 all the motivations that can lead to a loss of signal in the data of PADME related to instrumental effects are described through the efficiency term ϵ. As a consequence, the determination of the acceptance must be based on a generator-level simulation of the signal process, before any efficiency, resolution and miscalibration effect plays any role.

The selection cuts described in Table 5.2 are all applied to kinematic properties, involving energies and momenta, except for the requirement that the most energetic photon (or both photons) falls inside a fiducial region of the electromagnetic calorimeter (FR) described by an inner and an outer radial position. This cut, apparently defined as a geometrical criterion, is dictated by the ECAL geometry, but it also has an impact on the energy distribution of the two signal photons, due to the completely closed kinematics. This is also the only selection cut shaping the phase space of the annihilation process. Indeed, all other cuts are dictated by considerations related to the detector and reconstruction resolution.

These boundaries need to be set inside the geometrical boundaries of the calorimeter in order to minimize the effect of the shower leakage. In addition, the strong correlation of the two photons implies that for a given value of the beam energy, setting a constraint on the region where, for example, the most energetic photon can be found, directly defines the corresponding region where the second most energetic photon can lie. In order to choose a consistent definition of the fiducial region and estimate the corresponding acceptance, dedicated studies were done using CalcHEP and Babayaga simulations at generator level and PADME MC at detector level.

The CalcHEP generator has been used to produce a sample of 10^6 annihilation events according to the LO approximation for the process $e^+e^- \to \gamma\gamma$, with an electron momentum $\vec{P_{e^-}} \sim 0$ MeV/c and a positron energy equal to the energy of the beam $E_{e^+} = 430$ MeV. The three components of the momenta $\vec{P}$ of the two photons are saved on a text file and used directly to study the events before any detector effect. The same events simulated in PADME MC allow to assess detector and resolutions effects. The truth information can easily be compared with the simulated event.

A crucial quantity is the radial distance from the original beam direction of the cluster produced by the photon in the calorimeter. In data and in simulation this quantity is computed from the energy weighed position of the BGO crystals in the cluster (see Section 4.3 for a detailed discussion).

The measured R_γ allows to measure the polar angle of the photon through the relation

$$R_\gamma = \tan(\theta) \times \mathrm{D} = \frac{\mathrm{p_T}}{\mathrm{p_z}} \times \mathrm{D} \tag{5.9}$$

where p_T and p_z are the transverse and longitudinal components of the photon momentum and D is the distance between the target and the plane perpendicular to the z axis representing the ECAL measurement plane.

The parameter D is not trivially equal to the distance between the target and the entrance surface of the crystals in ECAL. The position of the target and of the ECAL calorimeter in the PADME reference frame are known from design and from survey measurement. The target position[3] is $z_{Target} = -1030$ mm. Concerning the z coordinate of ECAL, there are three options to consider: the ECAL front face, the plane where the shower reaches the maximum development and the one corresponding to the mean multiplicity of charged particles in the shower. In Figure 5.9 the distribution of the z coordinates of the GEANT4 hits produced by charged particles in the electromagnetic shower is shown. Thus the options for the z coordinate of the ECAL measurement plane are:

- ECAL front face = 2440 mm;
- most probable value of the shower maximum = 2483 mm, obtained from a fit of the shower longitudinal profile with a Landau function;
- mean of the shower profile = 2513 mm.

The value of the distance $D = (1030 + 2513)$ mm using the mean of the shower z profile is finally chosen. This value statistically guarantees a good match between the radial position R_γ, computed from the true photon directly with Equation 5.9, and the R_γ, corresponding to the cluster position in the simulation. The distributions of the differences between R_{truth} ($D =$

---

[3] The origin of the PADME reference frame is at the center of the PADME dipole magnet. The position of the target is defined as the position of the center of the Diamond sensor.

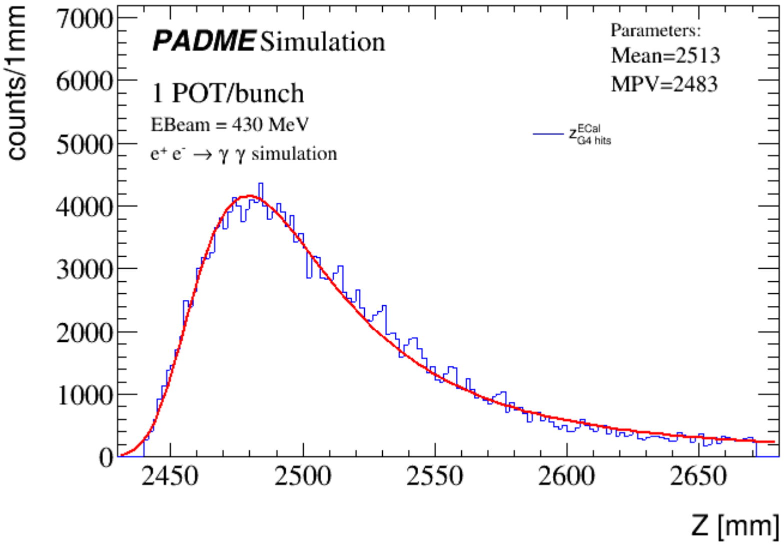

Figure 5.9: *Distribution of the z coordinate of all the hits generated in the BGO crystals of ECAL superimposed by a fit using a Landau function. The simulation used CalcHEP generated events simulated in PADME MC.*

3543 mm) and $R_{cluster}$ for the most energetic photon and the least energetic one are shown in Figure 5.10, right and left, respectively. Both distributions, for this value of D, have the mean of the Gaussian fit close to 0 and a standard deviation of $\sim$ 5 mm.

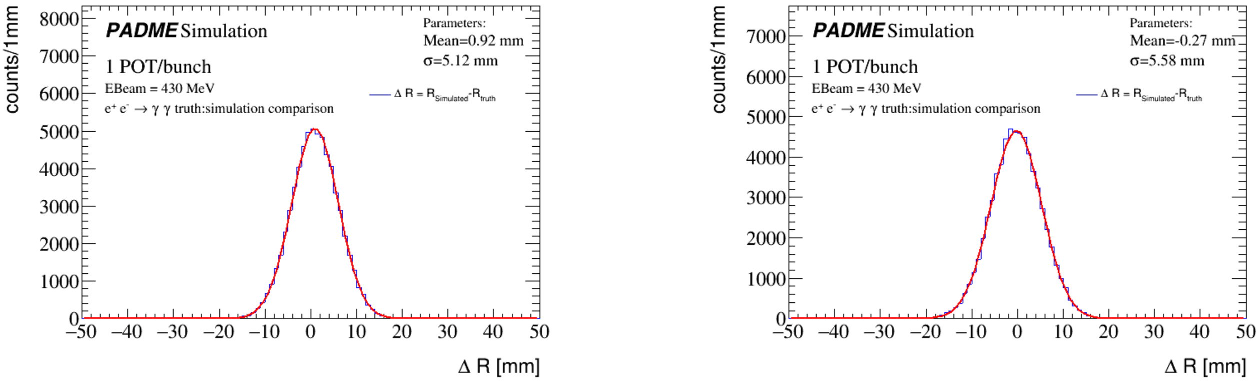

(a) **(b)**

Figure 5.10: *Distribution of the difference between the radial position of the photon simulated in PADME MC and the radial position of the truth in the transverse plane at a distance* $D = 3543$ mm *from the Active Diamond Target for the most energetic photon (a) and for the second most energetic photon (b).*

Clusters in ECAL may be used as photon candidates if the measured energy and position are reliable. For photons hitting the calorimeter in a peripheral regions, energy and positions are likely biased. The features of the clusterization algorithm implemented in the reconstruction suggest that the bias due to transversal shower leakage is small if the cluster position is reconstructed at a distance at least equal to twice the pitch of the BGO crystal matrix. Using this criterion, the maximum radial position of a reliable cluster is equal to $R_{max} = 258$ mm. Due to the fact that the first and the second photon are correlated in energy, thus in space, the corresponding minimum radial position is constrained by the kinematics. In practice, it is extracted with a scan on R_{min} studying the number of γ_1 and γ_2, with radial position inside the range, according to MC truth in a CalcHEP $e^+e^- \to \gamma\gamma$ sample. The value of R_{min} that gives a number of first photons (most energetic) equal to the number of second photons (less energetic) inside R_{max} is chosen. As a result the fiducial region for the selection of annihilation photons in the PADME calorimeter is defined as the interval $FR = [115.82, 258]$ mm. Another important parameter is the value of the radial position $R_{mid} = R_{\gamma_1}(E_{mid}) = R_{\gamma_2}(E_{mid})$ where the two photons have the same energy and therefore the same radial position. This parameter, for an energy of the beam $E_{beam} = 430$ MeV, is equal to $R_{mid} = 172.83$ mm. Table 5.3 reports the number of γ_1 and γ_2 ($N_{\gamma_{1(2)}}$) found in ECAL regions defined in terms of the parameters R_{min}, R_{max} and R_{mid}. The counters show the consistency of the definition for the three parameters, since the number of N_{γ_1} is equal to N_{γ_2}, and all most energetic photons fall in the inner ring of ECAL, while all others less energetic fall in the outer ring, as expected by kinematics. These numbers show that at each γ_1 corresponds a γ_2 in opposite ECAL regions.

Table 5.3: *Yield of the most energetic photon γ_1 and the less energetic one γ_2 in the two radial ECAL regions. The radial position range* $]115.82, 258[$ mm *is considered to be the fiducial region, the radial position* $R_{mid} = 172.83$ mm *is the radial position where the two photon has the same energy.*

Cuts	N_{γ_1}	N_{γ_2}
$\gamma \in]115.82, 258[$ mm	65320	65318
$\gamma \in]115.82, 172, 83[$ mm	65320	0
$\gamma \in [172, 83, 258[$ mm	0	65318

A confirmation that the distance target-ECAL D considered is appropriate is given by the fact that the value of R_{mid} found in CalcHEP truth is confirmed by CalcHEP sample simulated in PADME MC. Figure 5.11 shows the distribution of R_γ for the first photon (most energetic) and the second photon (less energetic). Two analysis variant are presented: one with only the first photon in the FR and one with also the second photon in FR (i.e. $R^T_{\gamma_1}$ only and also $R^R_{\gamma_2}$ in the range $[R_{min}, R_{max}]$). For the first case the distribution of $R^T_{\gamma_1}$ and $R^T_{\gamma_2}$ are shown in blue by the solid and dotted line, respectively. The two distributions do not overlap and span the entire range of the FR with the first (second) photon well contained below (above) R_{mid}. For the first selection, the distribution of $R^R_{\gamma_1}$ is sharply cut at R_{min}, but some migration above R_{mid} is induced by resolution; the $R^R_{\gamma_2}$ distribution starts before R_{mid} and ends after R_{max}. For the second selection, also the distributions of $R^T_{\gamma_2}$ also ends sharply at R_{max} (see Figure 5.11 (b)).

The same correlation between the radial position of the first and second photon predicted

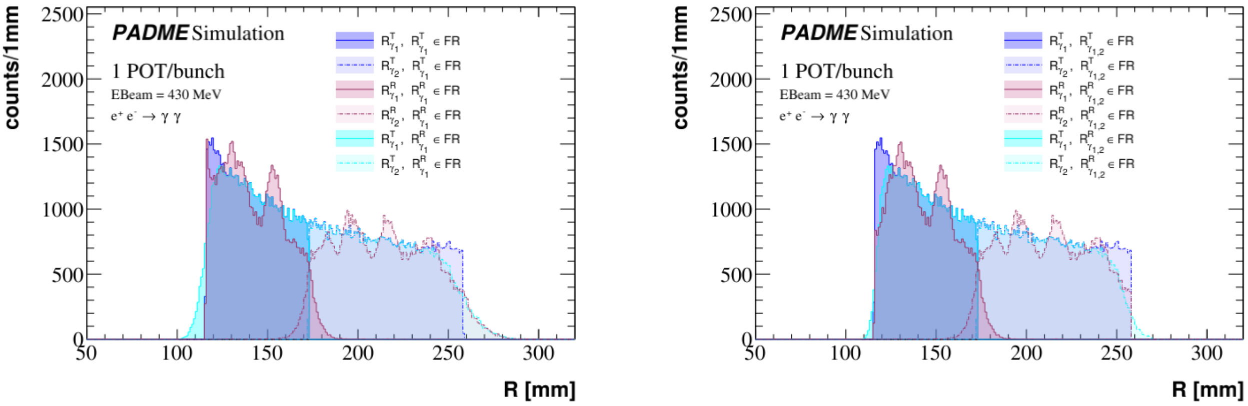

(a) (b)

Figure 5.11: *Distribution of true and reconstructed radial position of photons from annihilation events. Continuous lines refer to the most energetic photon, dotted lines to the second most energetic photon. Events are selected for the first photon only (a) and for both (b) belonging to the fiducial region at MC truth level or at reconstruction level.*

by the simulation should be observed in data, if beam energy and detector geometry are well known. In Figure 5.12 the points show R_{γ_2} as a function of R_{γ_1} in PADME annihilation events. The annihilation photon candidates are selected with the application of the cuts presented in the Section 5.4 (in particular cuts a,b,c,d,e,f of Table 5.2 are applied). The black continuous line is the correlation observed in CalcHEP sample using MC truth. The agreement is a check of the good description of the geometry.

5.5.1 Acceptance at Leading Order

The acceptance of the fiducial region is separated in a global factor, telling what fraction of the annihilation events reach ECAL in the FR, and in a factor defined as a function of the photon polar angle to take into account migration effects due to the reconstruction. This function will be estimated with simulations in the next section but later it will be used as a correction to the efficiency.

The global acceptance is given by

$$A = \frac{N^{gen}_{\gamma\gamma} \in FR}{N^{gen}_{\gamma\gamma}} \tag{5.10}$$

where $N^{gen}_{\gamma\gamma} \in FR$ is the number of the annihilation events generated by CalcHEP that fall in the FR, and $N^{gen}_{\gamma\gamma}$ is the total number of the generated events. The sample used for this study consist of 10^6 annihilation events, and the number of the annihilation events observed in the FR is $\sim 65.3 \times 10^3$, thus the global acceptance is $A = 0.0653 \pm 0.0003$ where the error comes from the statistics of the MC sample.

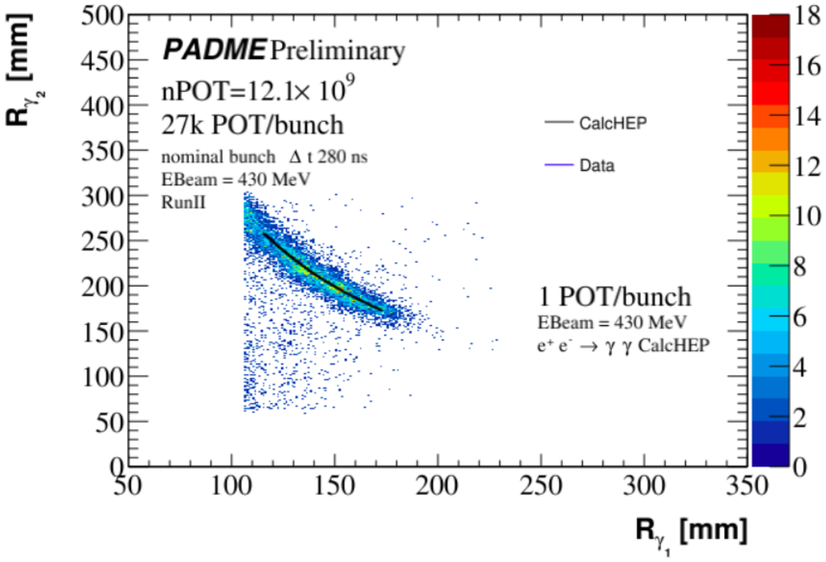

Figure 5.12: *Correlation between the radial position of the first and second most energetic photon. Points are data after a tight selection of annihilation events, corresponding to cuts a,b,c,d,e,f of Table 5.2. The black line is the same correlation according to MC truth in CalcHEP.*

5.5.2 A correction for migration effects

The CalcHEP sample can be used to understand how the number of events that are truly in the FR, $N_{\gamma\gamma}^{gen} \in FR$, relates to the number of events that are reconstructed with efficiency one and remain within the FR, $N_{\gamma\gamma}^{reco} \in FR$ despite the θ_γ smearing. The ratio,

$$A_{mig}(\theta_1, \theta_2) = \frac{N_{\gamma\gamma}^{reco} \in FR}{N_{\gamma\gamma}^{gen} \in FR} \tag{5.11}$$

will multiply the event dependent efficiency at the denominator of Equation 5.1. In this way the detector efficiency effects are disentangled from migration effects.

The correction A_{mig} has been estimated using a smearing of the polar angle of the photons from the MC truth and comparing with distributions at generator level. The Gaussian smearing was defined using the data, and looking at the width of the distribution of the reconstructed polar angle of γ_1, when the value of theta for the other photon falls in a bin 0.45 mrad wide. The width of the distribution was found to have a negligible dependence on the polar angle of the sub-leading photon and to be equal to $\sigma_\theta = 2.04$ mrad. After that, the following samples of events are considered:

1. annihilations at generator level from CalcHEP in the entire phase space;
2. annihilations at generator level from CalcHEP in the entire phase space with both photon polar angles smeared by σ_θ.

The correction is measured as a function of only one angle using all photons:

$$A_{mig}(\theta) = \frac{N_{\gamma}^{smeared}(\theta_i)}{N_{\gamma}(\theta_i)} \tag{5.12}$$

where $N_{\gamma}^{smeared}(\theta_i)$ is the number of photons with a smeared polar angle θ_i, and $N_{\gamma}(\theta_i)$ is the number of photons with a truth polar angle θ_i.

The first step is to select all the events in the samples 1 (MC truth) and 2 (MC reconstructed) that have $R_{\gamma_1} \in FR$ and corresponding to the first analysis variant. These are shown in Figure 5.13 (a). The ratio of the two distributions, as described in Equation 5.12, is represented in Figure 5.13 (b). This shows that the correction for migration effects is always compatible with one, if the event selection enforces the FR cut only to this photon[4]. Indeed, this is the most energetic photon and it never reaches a radial position so high to meet the conditions on an average value of $A_{mig}(\theta_1)$ less than one (see Figure 5.13 (b)).

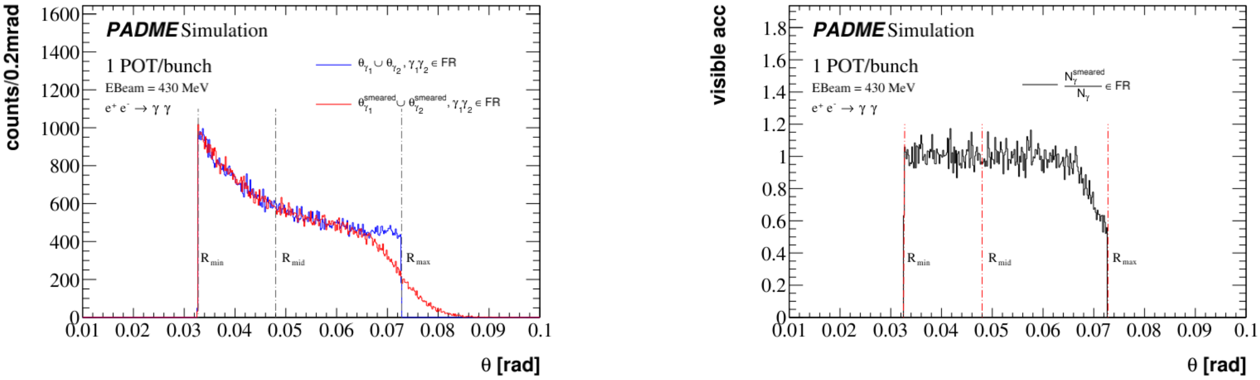

(a) **(b)**

Figure 5.13: *(a) Distribution of the polar angle of the two photons of the annihilation sample, in blue the events generated by CalcHEP, in red after the smearing. The selection for these events is for the first photon* $R_{\gamma_1} \in FR$. *(b) The visible acceptance calculated as the ratio between the number of annihilation after and before the smearing bin by bin (red line / blue line of (a)).*

On the other hand, the second analysis variant requires that both photons are reconstructed in the FR and the migration effects give a different correction which is a function of θ_{γ_1} (or θ_{γ_2}) as shown in Figure 5.14. The ratio of the two distributions, as described in Equation 5.12, is shown in Figure 5.14 (b). In this case, the correction is not identically equal to one. Indeed, the value of $A_{mig}(\theta_1)$ at low R_{γ_1} is less than one due to the occurrence of R_{γ_2} outside the FR (see Figure 5.14 (b)). In conclusion, migration effects do not reduce the acceptance for the first analysis variant, but for the second analysis variant the acceptance is reduced by the function $A_{mig}(\theta_1)$ of 5.14 (b).

---

[4] One has to remember that in terms of acceptance and generator level quantities, requiring only one photon in the FR is perfectly equivalent to requiring both photons in the FR.

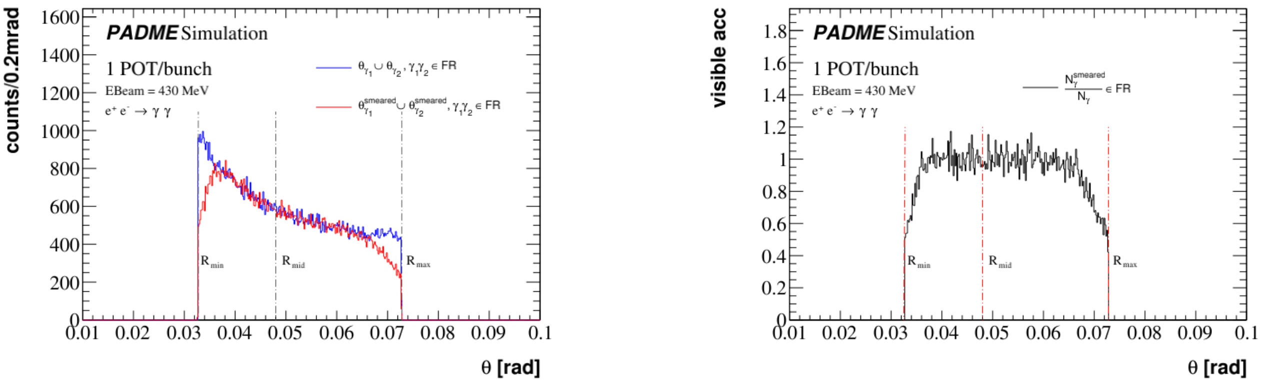

(a) **(b)**

Figure 5.14: *(a) Distribution of the polar angle of the two photons of the annihilation sample,in blue events generated by CalcHEP and in red after the polar angle smearing. The selection for these events is for both photons* $R_{\gamma 1}, R_{\gamma_2} \in FR$*. (b) Visible acceptance calculated as the ratio between the number of annihilation after and before the smearing (red line / blue line of (a)).*

5.5.3 Acceptance at Next Leading Order

The CalcHEP generator produces annihilation events at the leading order in the perturbative expansion, with exactly two photons in the final state. It can also be used to produce the process $e^+e^- \to \gamma\gamma\gamma$ at the leading order approximation. Eventually, the two samples might be combined to derive a better estimate of the inclusive cross section for the process e^+e^- to photons. On the other hand, Babayaga is a NLO event generator for the $e^+e^- \to \gamma\gamma$ process, which means that the production of two and three photons are consistently managed over the phase space. In addition, Babayaga can be configured to run in the LO approximation, therefore a check to verify the compatibility of the two LO predictions was done. A check was done to compare the kinematics measuring the global acceptance of the process. In this case the acceptance measured with Babayaga at LO is $A^{Babayaga} = 0.0651$, thus there is a relative difference of -0.4% with CalcHEP at LO. After this preliminary check, a sample was produced emulating the process $e^+e^- \to \gamma\gamma(\gamma)$ with Babayaga at NLO. Of course, in this sample events with three photons do not fullfill the kinematic constraints of two-photon final state. In this case, the ECAL granularity must be taken into account and if a soft photon falls close to another one, a single cluster may be reconstructed. For this reason, photons from Babayaga are merged if the distance in X and Y is compatible with the clusterization algorithm distance and is assigned an energy equal to the sum and a position equal to an energy weighted average of the original positions. After this procedure, the photons are requested to pass the kinematic cuts that are applied to the two-photon annihilation event selection: $E_\gamma > 90$ MeV and $|\Delta E| = |E_\gamma - E(\theta_g)| < 100$ MeV[5]. Events with at least one pair of photons passing the kinematic cuts and with the most energetic photon in the pair lying inside the FR are counted

---

[5] Notice that these conditions in a LO simulation are trivially satisfied, therefore they are not applied to estimate the acceptance in the LO approximation.

as events inside the acceptance. The ratio of the number of these events to the total number of events produced by Babayaga is used to assess the acceptance that was calculated to be: $A = 0.06424 \pm 0,00025$, which is 1.6% lower than the acceptance at the leading order. This is the acceptance value used to measure the cross section in the next sections.

The systematics that can affect the acceptance come from the perturbative approximation, from the error on the distance between the target and the ECAL detector and from the definition of the FR. For the first of them the NNLO correction is quoted be of the order of 0.1% [97], hence it can be neglected. For the second the variations of the acceptance when changing the distance between ECAL and target have been estimated and summarized in Table 5.4 . Since the systematic error of the distance measured from the PADME apparatus survey is ~ few mm, also this systematic uncertainty can be neglected.

Table 5.4: *Acceptance calculation obtained varying the distance between ECAL and target.*

Variation [mm]	$acc^{Babayaga}$	$\frac{acc^{Babayaga}}{acc_0^{Babayaga}}$
-15	0.06351	0.989
-10	0.06375	0.992
-5	0.06400	0.996
0	0.06423	1.000
5	0.06446	1.003
10	0.06468	1.007
15	0.06492	1.011

The last systematic can be due to the definition of the FR. Since the two photons have radial distances correlated, the estimation of the systematic was done varying the R^{FR}_{min} and extrapolating the acceptance, the values are summarized in Table 5.5. As clearly emerges, the systematic is not symmetric. This is due to the fact that reducing the R^{FR}_{min} (negative variation), without changing R^{FR}_{max} for the sub-leading photon, will not produce variation in the acceptance. Instead, increasing the R^{FR}_{min} will imply a reduction on R^{FR}_{max}, leading to a reduction of the total number of photon pairs falling in the region. It is reasonable to think that the error on the fiducial region is about 0.500 mm, so the systematics to be attributed to FR is 1.16%.

5.6 A method for efficiency determination in data

The photon efficiency was measured in data by developing a tag-and-probe technique exploiting the closed kinematics of annihilation events. Typically, data-driven efficiency measurements benefit from another detector, that allows to observe a sample of reference particles (probes), sometimes identified as belonging to a specific category of interest thanks to a tagging criterion. Then, the efficiency for reconstructing and identifying that category of particles with the detector and procedure under test is measured as the number of probes that are actually matched to a reconstructed particle by the detector or procedure under test. For example, in a detector

Table 5.5: *Acceptance calculation obtained varying* R^{FR}_{min}.

R^{FR}_{min} **variation [mm]**	$acc^{Babayaga}$	$\frac{acc^{Babayaga}}{acc^{Babayaga}_{0}}$
-1	0.06569	1.023
-0.500	0.06494	1.011
-0.250	0.06582	1.025
-0.100	0.06437	1.002
-0.05	0.06431	0.999
0	0.06424	1.000
0.05	0.06417	0.999
0.100	0.06409	0.998
0.250	0.06385	0.994
0.500	0.06349	0.988
1	0.06278	0.977

with a Inner Spectrometer IS, tracking all charged particles, and an Outer Spectrometer OS for muons, the OS efficiency can be measured by looking for a well reconstructed muon (tag) that combined with a track (probe), reconstructed in the IS, gives an invariant mass corresponding to theJ/Ψ mass; the OS efficiency is given by the number of probes that have a matching muon track in the OS divided by the total number of probes. In the case of annihilation events, the PADME calorimeter is a destructive detector and there is no other tagging detector to confirm the presence of a photon. Therefore, the redundancy of the kinematic constraints in the annihilation process is used to define a probe when a tag is reconstructed and to test whether the probe is matched.

5.6.1 Tag-and-probe with annihilation events in PADME

As already extensively discussed, the two photons produced in the final state of $e^+e^- \to \gamma\gamma$ are correlated in energy and in space. Figure 5.15 shows that the polar angle of an annihilation photon predicts its energy, through an analytical function $E = f(\theta)$[6]. Therefore, if a photon in ECAL comes from annihilation the following considerations are verified:

- its energy is compatible with $E_\gamma = f(\theta_\gamma)$;
- a second photon must exist back to back in phi to the first with $E_{\gamma 2} = E_{beam} - E_{\gamma 1}$;
- the energy of the second photon is also compatible with $E_{\gamma 2} = f(\theta_{\gamma 2})$.

Given these considerations, a photon with

$$\Delta E_{tag} = E_{tag} - f(\theta_{tag}) \tag{5.13}$$

---

[6] The best fit function is represented by an exponential with the constant factor equal to 6.40 and a slope of -2.05.

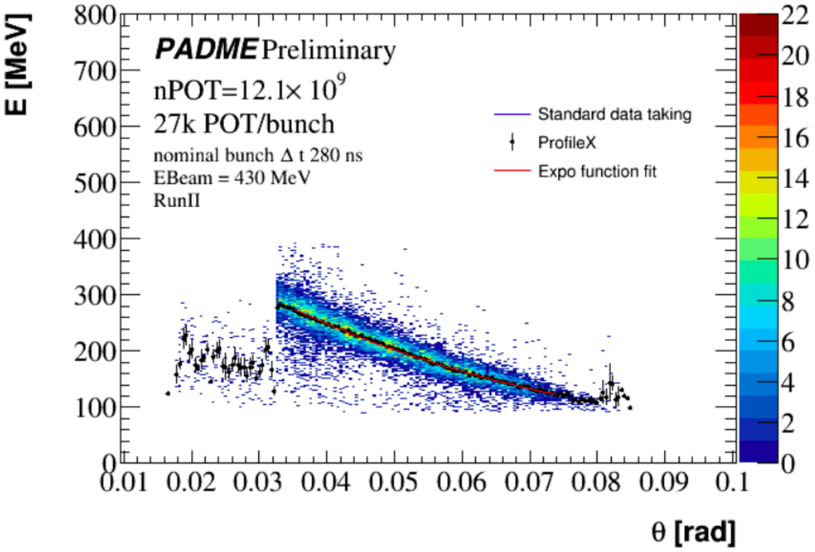

Figure 5.15: *Correlation between the energy E and the polar angle θ of annihilation photons. For the plot are used data of RunII and events that pass the selection: a,b,c,d,e, described in Section 5.4. The function $E = f(\theta_g)$ is extracted by an exponential fit to the histogram profileX in the clean region* $[0.035, 0.074]$ rad. *The function is used in this analysis to correlate polar angle to energy for photos coming from annihilation events in the target.*

close to zero can be used to "tag" the annihilation process. Indeed, all ECAL clusters in the FR with $|\Delta E_{tag}| < 100$ MeV are considered tag candidates. This is a very loose selection criterion considering that the resolution on ΔE_{tag} is of the order of ~ 15 MeV, which is meant to populate the sidebands of the distribution in order to estimate and subtract the background. The function $f(\theta)$ has been derived on a sub-set of the data sample and no attempt was made to optimise it. This function will be used only to detect a peak in the ΔE_{tag} distribution, correlated to signal annihilation photons, and to measure its integral, corresponding to the number of tags. The wide range adopted for ΔE_{tag} guarantees that no bias is induced in the counting of annihilation photons from an inaccuracy on $f(\theta)$.

When a tag candidate is found, the probe is defined as the "expected second photon" from the annihilation, therefore the number of probes is equal to the number of tags.

Finally, a matched probe candidate is defined as a cluster with features similar to the probe hypothesis; this means with $|\phi - \phi_{probe}| < 25°$ and $|\Delta E| = |E - f(\theta_{probe})| < 100$ MeV. In addition, a matched probe is requested to be in time with the tag photon within 7 ns. Matched probe candidates are used to fill a distribution of $\Delta E_{probe} = E - E_{beam} + f(\theta_{tag})$ in the range -100, $+100$ MeV, where the integral of the peak standing on top of a small background will allow to count the matched probes. If more than one cluster match the probe, a choice is made by selecting the candidate matched probe with the minimum χ^2 defined as follows:

$$\chi^2 = \frac{\Delta E^2_{probe} + \Delta E^2}{\sigma(E_{\gamma_1})^2 + \sigma(E_{\gamma_2})^2} \tag{5.14}$$

where $\sigma(E_{\gamma_i})$ for $i = 1, 2$ is the energy resolution of the calorimeter and it is considered equal to 15 MeV for all clusters.

Finally, given the sample of tag candidates, the counting of the "signal tags" N^{sig}_{tag}, i.e. the photons that are really originating from an annihilation, requires the subtraction of a large background in the ΔE_{tag} distribution; similarly, given the sample of matched probe candidates, the counting of "signal matched probes" N^{sig}_{probe} requires the subtraction of a background in the ΔE_{probe} distribution that, in this case, is very small.

Indeed, the subtraction of the background for the determination of the number of signal tags is the most critical step in the procedure and several approaches have been tried. A first approach was based on a modelling of the background in the sideband with a pure background data sample. Then a Gaussian fit was applied to the background subtracted distribution to estimate the standard deviation of the signal peak. Finally, the number of tags was computed as the integral of the background subtracted distribution in the range corresponding to $\pm 3\sigma$ around the peak. The same procedure is applied to count the number of signal probes. An assessment of the systematic error affecting the efficiency determination is obtained by estimating the number of signal tags and signal probes consistently as the integral within $\pm 1\sigma$ or $\pm 5\sigma$ around the peak after background subtraction.

Another approach, eventually adopted, is based of a fit using templates for the signal and for two components of the background: non-collision background and pileup. This second approach leads to stable results and allows to account for non Gaussian tails in the signal component of the ΔE_{tag} distribution, which is at the origin of the biases on the tag-and-probe efficiency derived with the previous method. It will be discussed in detail in Section 5.8 and 5.9.4.

Section 5.7 describes a detailed validation with MC of the tag-and-probe efficiency and of its use for the cross section measurement. Those studies played a crucial role in consolidating the measurement strategy; however, they are unessential for a reader interested in the procedure eventually applied and in the results.

5.7 Closure tests with simulation

5.7.1 Tag-and-probe and other efficiency definition

The entire methodology was tested on MC samples of different types: pure annihilation events, annihilation events overlapped to a realistic pileup of other interactions, in a calorimeter with and without local defects like dead crystals.

Efficiency from MC truth

A first study addressed the relation between true photons and reconstructed photons in a perfect ECAL for pure annihilation events. ECAL was divided in 8 azimuthal slices and each one in two radial intervals: $R_{min} - R_{mid}$ and $R_{mid} - R_{max}$. The following quantities were estimated:

- effective efficiency for each bin $\epsilon^{effective} = \frac{N^{sim}_{\gamma}}{N^{gen}_{\gamma}}$, defined as the ratio between the number of reconstructed photons N^{sim}_{γ} and the number of generated photons N^{gen}_{γ}. This is shown

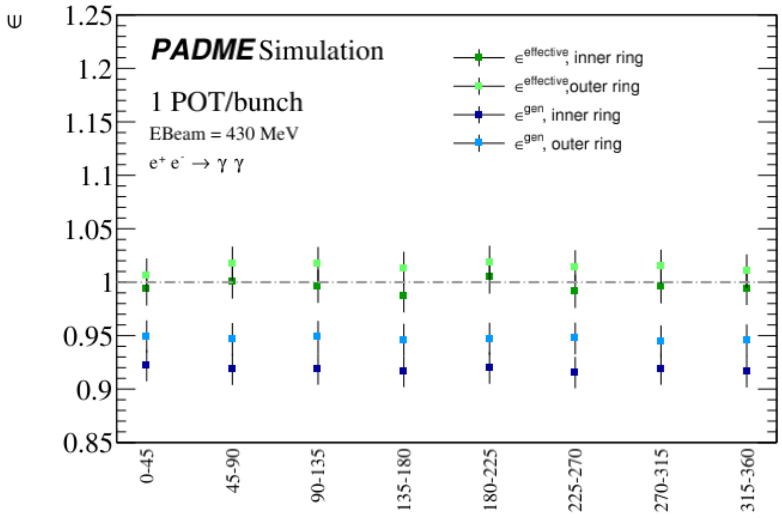

Figure 5.16: *True and effective efficiency for photons from annihilation events, in the absence of pileup and detector defects. The efficiency is quoted in 8 bins of the azimuthal angle ϕ one each divided in 2 bins of the radial position R.*

by green square in Figure 5.16 for each bin. A first observation is that in some bins the effective efficiency is higher than 1 due to migration effects. Indeed, the photon reconstructed coordinates are modified, with respect to generated coordinates, by the resolution and segmentation of the detector. This effect is observed in all bins of the outer ring;

- true efficiency for each bin $\epsilon^{gen} = \frac{N_\gamma^{sim}(\gamma^{gen})}{N_\gamma^{gen}}$, defined as the ratio between the number of photons having true and reconstructed spatial coordinates falling in that bin $N_\gamma^{sim}(\gamma^{gen})$ and the number of the generated photons falling in that bin. This is shown by blue squares in Figure 5.16 for each bin. The true efficiency in the outer ring $[R_{mid} - R_{max}]$ is systematically higher then in the inner ring $[R_{min} - R_{mid}]$ due to a stronger migration to the outer ring of photons generated in the inner region then vice versa;
- The feed-through for each bin at the inner (outer) boundary is defined as the ratio between the number of photons reconstructed in that bin but generated at $R < R(bin)_{min}$ $(R > R(bin)_{max})$ and the total number of photons generated in that bin;
- The loss for each bin at the inner (outer) boundary is defined as the ratio between the number of photons generated in that bin but reconstructed at $R < R(bin)_{min}$ $(R > R(bin)_{max})$ and the total number of photons generated in that bin;

Tables 5.6 (for the inner ECAL ring) and 5.7 (for the outer ECAL ring) report for all the azimuthal slices the true efficiency and the effective efficiency, the feed-through and loss at the inner and at the outer boundary.

Table 5.6: *True and effective efficiency, feed-through and loss at the inner boundary for photons from annihilation events, in the absence of pileup and detector defects, in 8 ϕ bins for R in $]R_{min}, R_{mid}[$.*

Angle range	true ϵ ±0.015	effective ϵ ±0.016	feed through in ±0.002	loss in ±0.002	feed through out ±0.002	loss out ±0.002
$[0, 45[$	0.923	0.994	0.046	0.044	0.030	0.034
$[45, 90[$	0.918	1.000	0.050	0.046	0.029	0.037
$[90, 135[$	0.919	0.996	0.047	0.045	0.028	0.037
$[135, 180[$	0.917	0.987	0.047	0.050	0.031	0.033
$[180, 225[$	0.920	1.005	0.047	0.044	0.029	0.036
$[225, 270[$	0.915	0.994	0.049	0.048	0.028	0.036
$[270, 315[$	0.919	0.996	0.048	0.050	0.034	0.033
$[315, 360[$	0.916	0.994	0.046	0.049	0.029	0.035

Table 5.7: *True and effective efficiency, feed-through and loss at the outer boundary for photons from annihilation events, in the absence of pileup and detector defects in 8 ϕ bins for R in $[R_{mid}, R_{max}[$.*

Angle range	true ϵ ±0.015	effective ϵ ±0.016	feed through in ±0.002	loss in ±0.002	feed through out ±0.002	loss out ±0.002
$[0, 45[$	0.949	1.020	0.035	0.030	0.027	0.021
$[45, 90[$	0.947	1.017	0.040	0.027	0.030	0.026
$[90, 135[$	0.949	1.017	0.039	0.026	0.033	0.026
$[135, 180[$	0.946	1.013	0.034	0.030	0.027	0.024
$[180, 225[$	0.947	1.018	0.036	0.029	0.027	0.024
$[225, 270[$	0.947	1.014	0.037	0.024	0.033	0.028
$[270, 315[$	0.945	1.015	0.035	0.031	0.032	0.024
$[315, 360[$	0.946	1.010	0.035	0.028	0.027	0.026

Tag-and-probe on MC

A second study addressed the estimate of the tag-and-probe efficiency in simulated pure annihilation events, ignoring pileup and defects of the calorimeter. In this simulated sample the selection of the tags and of the matched probes is free from backgrounds. The counting of tags and probes and the estimate of the systematic uncertainty are done as described in section 5.6.1. Figure 5.17 shows in blue the tag-and-probe efficiency ϵ^{TP}; in red the tag-and-probe efficiency within the fiducial region defined as the number of matched probes in the fiducial region $N_{probe_{FR}}$ divided by the number of tags N_{tag}. Error bars represent the statistical error σ while the shaded band corresponds to the total error $\sigma_{stat} \oplus \sigma_{sys}$ including the systematic uncertainty.

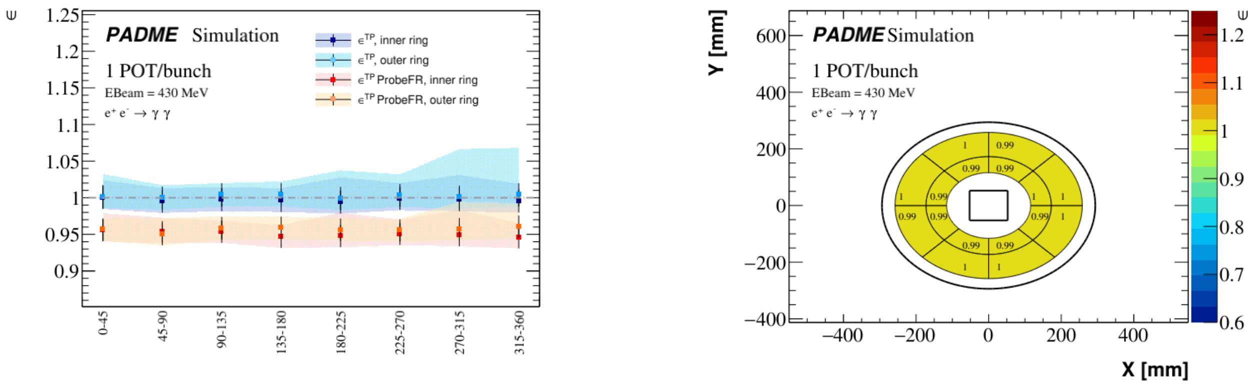

(a) **(b)**

Figure 5.17: *Tag-and-probe efficiency estimated for photons from annihilation events, in the absence of pileup and detector defects. The efficiency is quoted in 8 bins of ϕ each divided in 2 bins of R. (a) The efficiency is quoted with (red) and without (blue) the requirement that the matched probe belongs to the FR. (b) Map efficiency without any requirement on the probe photon.*

Comparing effective and tag-and-probe efficiency

The effective efficiency showed in Figure 5.16 differ from tag-and-probe efficiency represented in Figure 5.17. However, a meaningful comparison bin per bin between the effective efficiency $\epsilon_i^{effective} = \frac{N_{\gamma_i}^{sim}}{N_{\gamma_i}^{gen}}$ and the tag-and-probe efficiency $\epsilon_i^{TP} = \frac{N_{Probe_i}}{N_{Tag_j}}$ [7], without the request for the matched probe to be in the FR, can be done. As discussed in Section 5.7.1, the differences between the effective efficiency in the inner bins and in the outer bins is due to migration effects. In the tag-and-probe efficiency this effect is reduced. In addition, the tag-and-probe efficiency is never higher than 1 because the existence of a probe is constrained to the existence of a tag, so also when the number of tags is lower than the number of photons in the opposite bin, the number of matched probes cannot be higher than the number of tags. When the number of tags is higher than the number of photons in the opposite bin (case of the tag in the outer ring) the absence of an explicit radial boundary for searching a matched probe allows to find one with an efficiency still close to one. From these considerations it follows that the efficiency estimated with the tag-and-probe is more stable when moving from an inner to an outer bin and the small differences are induced by cluster reconstruction.

Table 5.8 summarizes the ratio between the effective efficiency and the tag-and-probe (TP) efficiency:

$$\alpha_i = \frac{\epsilon_i^{effective}}{\epsilon_i^{TP}} = \frac{\frac{N_{\gamma_i}^{sim}}{N_{\gamma_i}^{gen}}}{\frac{N_{Probe_i}}{N_{Tag_i}}}. \tag{5.15}$$

---

[7] The subscript i labels the bin where the ECAL efficiency is measured, while j is the bin with opposite azimuthal angle and opposite radial position bin to respect the constraints deriving from the kinematics of the annihilation.

for all phi slices in the inner and outer rings. In the inner ring the effective and TP efficiencies are equal to better than 1%, while in the outer ring the effective efficiency is higher than the TP one by $1 - 2\%$, because migration effects are bigger.

Table 5.8: *Ratio between the effective efficiency and TP efficiency derived from MC without ECAL defects.*

Angle range	α inner ring	α outer ring
$[0, 45[$	0.994	1.018
$[45, 90[$	1.004	1.018
$[90, 135[$	0.999	1.013
$[135, 180[$	0.991	1.009
$[180, 225[$	1.011	1.019
$[225, 270[$	0.995	1.011
$[270, 315[$	0.999	1.014
$[315, 360[$	0.999	1.006

5.7.2 Tag-and-probe efficiency with ECAL defects

A third study addressed the dependence of tag-and-probe efficiency on ECAL defects. The previous pure annihilation sample $e^+e^- \rightarrow \gamma\gamma$ was reconstructed emulating four dead crystals in ECAL in the bin $\phi \in [45, 90]^\circ$ as illustrated in Figure 5.18.

First, the effective efficiency for this special sample was estimated using the MC truth as defined in section 5.7.1. The dependence on the bin in ECAL is shown in Figure 5.19. As expected, the efficiency is lower only in the region where the detector response is affected by the dead crystals. Then, the ΔE_{tag} and ΔE_{probe} distributions were used to extract the tag-and-probe efficiency. The distribution of these variables in the presence of dead crystals are not Gaussian for all the bins. Figure 5.20 shows the distribution of ΔE_{tag} for tags reconstructed in a bin without defects $\phi \in [180, 225]^\circ$ and $R_{min} < R < R_{mid}$ while Figure 5.20 (b) in a bin with defects $\phi \in [45, 90]^\circ$and $R_{min} < R < R_{mid}$. In the bin with dead crystals, a long left tail appears. The matched probes have similar behaviour as indicated in Figure 5.21, where the ΔE_{Probe} distributions are reported for the same bins of Figure 5.20 and a left tail appears where there are dead crystals. The tag-and-probe efficiency for all bins is reported in Figure 5.22 (a). In the ECAL slice with four dead crystals the tag-and-probe efficiency is reduced more than expected, if compared to the effective efficiency, and an artificial increase is observed in the opposite phi slice where no dead crystals are present. This double bias in tag-and-probe efficiency is due to the long left tails of the matched probes and tags in the region with dead crystals which escape the $\pm 3\sigma$ interval around the peak. This happens because dead crystals (or in general any local inefficiency) induce an inaccurate energy and position measurement.

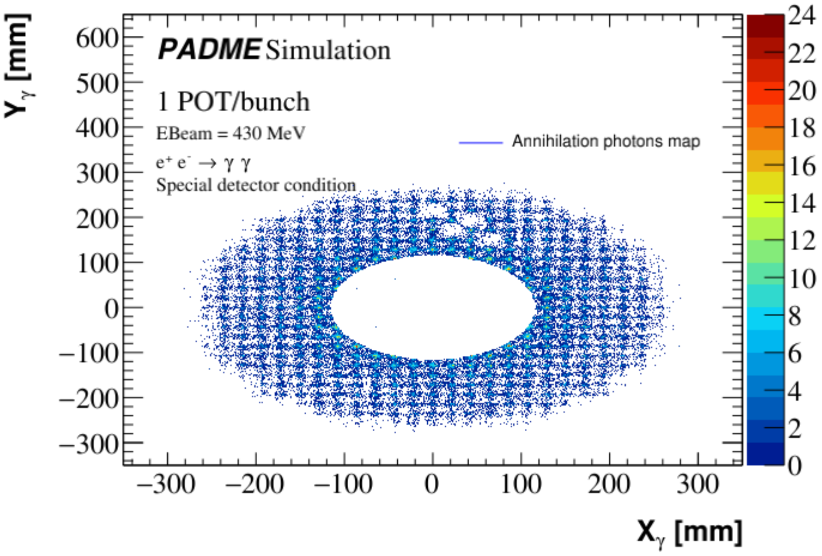

Figure 5.18: *Map of the annihilation photons selected with only the time coincidence requirement and the application of the FR to the most energetic photon with four simulated dead ECAL crystals.*

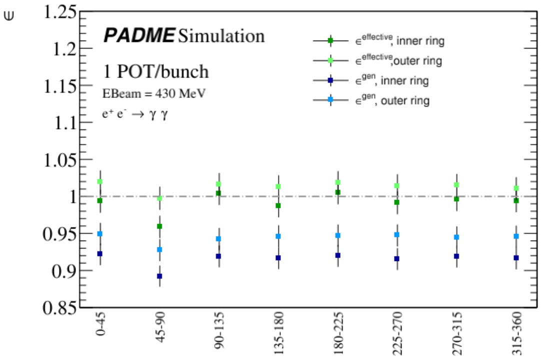

Figure 5.19: *Effective efficiencies of a simulated sample where the ECAL has dead channels.*

These biases make difficult to give an interpretation to the tag-and-probe efficiency. However, since the annihilation yield is corrected by the event efficiency $\epsilon(\gamma_1) \times \epsilon(\gamma_2)$, it turns out that the two opposite biases compensate each other. Indeed, in the problematic region the TP event efficiency is $0.86 \times 1.08 = 0.93 < 1$. Figure 5.23 (a) shows the effective and TP event efficiencies. The event efficiency from the tag-and-probe in the problematic bin is slightly lower than the effective event efficiency. This is expected because the effective efficiency is calculated without photon energy threshold cuts. A photon hitting a dead crystal or a nearby crystals produces clusters with a measured energy lower than the photon energy. The tag-and-probe selection rejects this cluster (if the energy is below the energy threshold). On the other hand, in the effective efficiency calculation this cluster counts as a photon. If an energy threshold is applied also to estimate the effective efficiency, the two event efficiencies become compatible

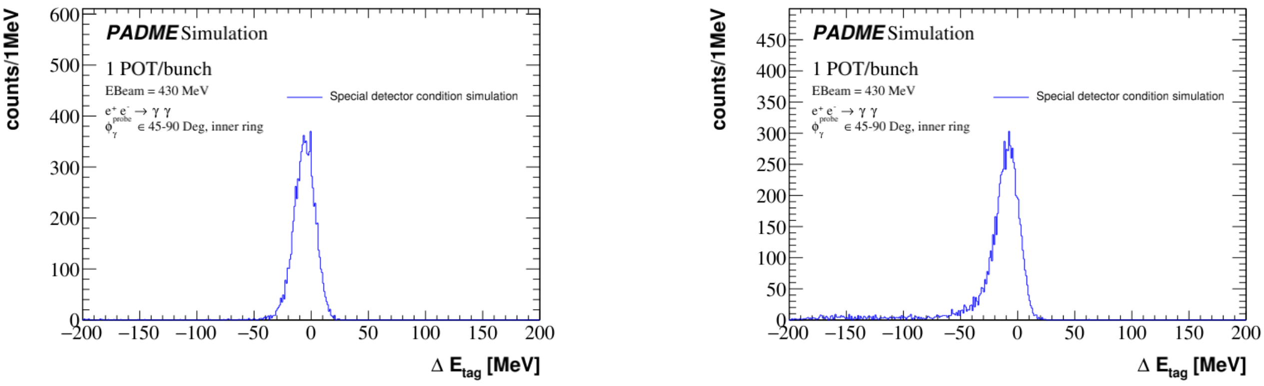

(a) **(b)**

Figure 5.20: *ΔE_{tag} distribution for the MC simulation of pure annihilation events where the detector has dead channels. On the left the distribution for a bin without dead crystals, on the right the same distribution for a bin with dead crystals.*

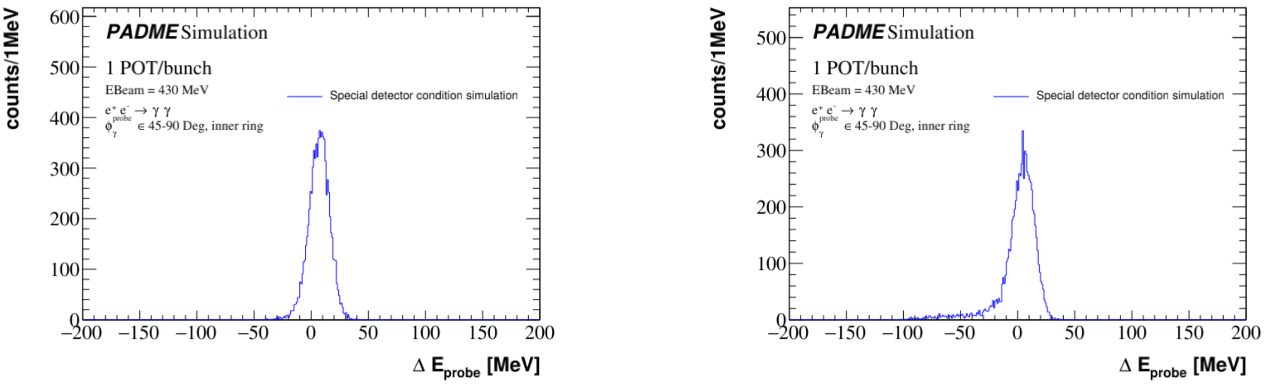

(a) **(b)**

Figure 5.21: *ΔE_{Probe} distribution for the MC simulation of pure annihilation events where the detector has dead channels. On the left the distribution for a bin without dead crystals, on the right the same distribution for a bin with dead crystals.*

within the errors, as Figure 5.23 (b) shows.

5.7.3 Measurement strategy based on tag-and-probe efficiency

The strategy to measure the cross section based on Equation 5.1 using the single photon efficiency as measured with the tag-and-probe method was validated by the simulation of annihilation events generated by CalcHEP, with four dead crystals and no pileup. This was done by verifying the consistency between the MC truth yield and the reconstructed annihilation yield, when the latter is corrected for acceptance and event efficiency as obtained with the data-driven

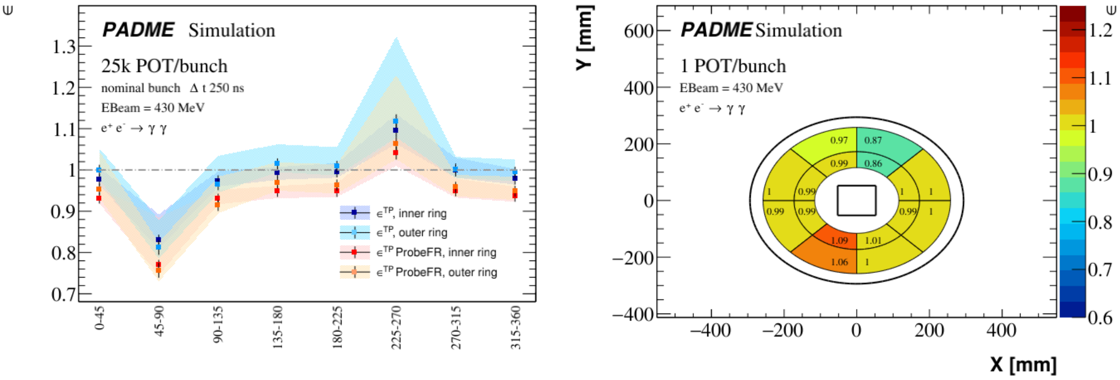

(a) **(b)**

Figure 5.22: *Efficiencies of a simulated sample where the ECAL has dead channels. (a) TP efficiency. (b) Map of the TP efficiency without any requirement on the probe photon.*

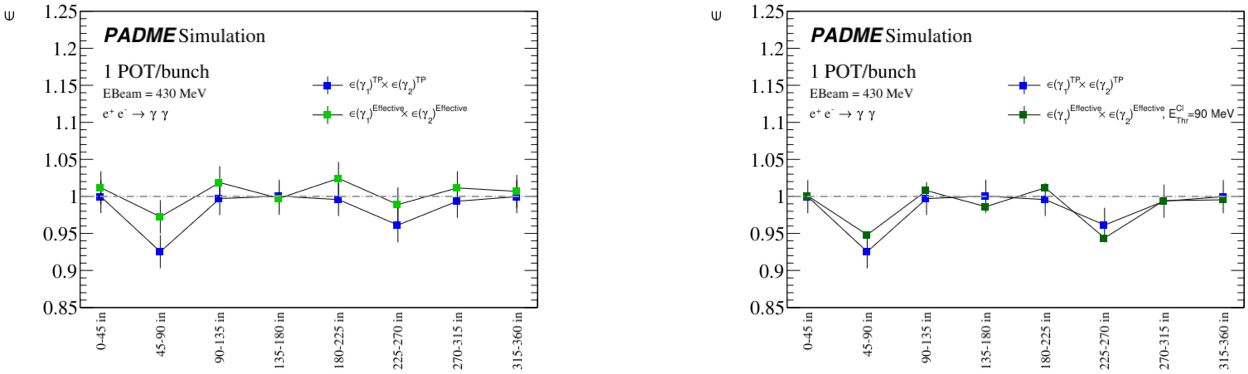

(a) **(b)**

Figure 5.23: *Effective and TP event efficiencies given by* $\epsilon(\gamma_1) \times \epsilon(\gamma_2)$ *without (a) and with (b) cluster energy threshold of* 90 MeV*.*

method. The tag-and-probe single photon efficiency used in this closure test is the one shown in Figure 5.22 (a) for the two analysis variants.

For the first analysis variant, when only the most energetic photon belongs to the fiducial region, the efficiencies assigned to both photons were the tag-and-probe efficiencies obtained without requiring that matched probe belongs to the FR. The corresponding acceptance correction A_{mig} was the one of Figure 5.13 (b).

On the other hand, for the second analysis variant when both photons belong to the FR, the efficiency assigned to the less energetic photon was the tag-and-probe efficiency obtained requiring that the matched probes belong to the FR. The corresponding acceptance correction A_{mig} was still the one of Figure 5.13 (b). This was proved to be equivalent to using the tag-and-probe efficiency obtained without requiring that the matched probes belongs to the FR also for the less energetic photon, but with the corresponding acceptance correction A_{mig} of Figure 5.14 (b).

The yields of the annihilation candidates were given by integrating the $E_{\gamma_1} + E_{\gamma_2}$ spectra in the energy range $[300, 600]$ MeV. Figure 5.24 shows the annihilation peak of all events that pass the time coincidence cut, with the first photon in the FR and the CoG coordinates within 5 cm. Reconstructed and corrected yields are reported in Table 5.9. After applying the correction for efficiency and acceptance, the corrected yield matches within an error of 0.5% the number of

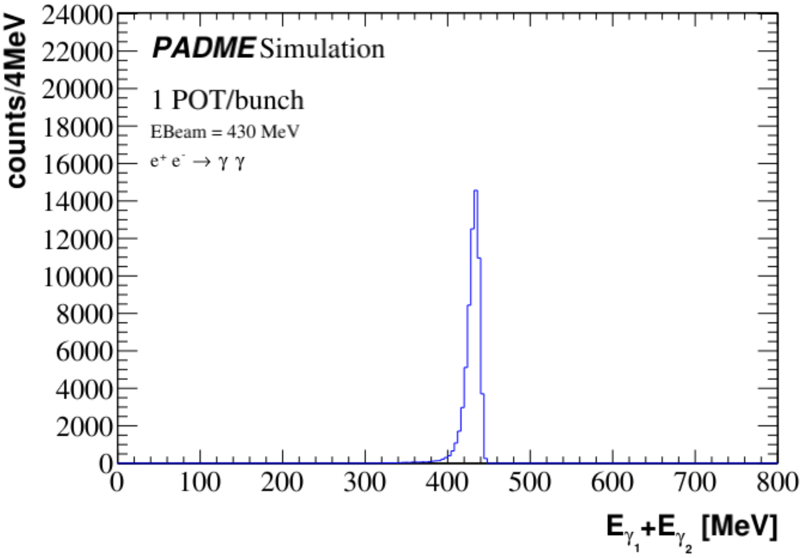

Figure 5.24: *Distribution of the sum of the two photons energy for all events that pass the time coincidence cut, with the first photon in the FR and CoG coordinates within* 5 cm *for a MC sample of pure annihilation events and with four dead crystals in ECAL .*

Table 5.9: *Reconstructed yield of annihilation events in a simulation with ECAL defects and no pileup. The yield after correction for efficiency and acceptance are reported (last two rows) and compared to the number of events in the acceptance at generator level (first row).*

Sample and cut	$\gamma_1 \in FR$	$\gamma_1, \gamma_2 \in FR$
CalcHEP **generation** (expectation)		
$\in FR$	65320	65318
CalcHEP **simulation**		
$\in FR$, $\lvert CoG\rvert < 5$ cm	64006	61041
$\in FR$, $\lvert CoG\rvert < 5$ cm, corrected for $\epsilon_{TP} \times \epsilon_{TP}$	65057	
$\in FR$, $\lvert CoG\rvert < 5$ cm, corrected for $\epsilon_{TP} \times \epsilon_{TP,probe\in FR}$		65088
$\in FR$, $\lvert CoG\rvert < 5$ cm, corrected for $\epsilon_{TP} \times \epsilon_{TP} \times A_{mig}^{\gamma_2 \in FR}(\theta_{\gamma_1})$		65649

MC truth events in the acceptance. This successful closure test validates the acceptance, the tag-and-probe efficiency and the cross section measurement strategy also in case of local defects of the calorimeter.

5.7.4 Measurement strategy based on scale factors

Also the strategy to measure the cross section based on Equation 5.2 using the "scale factors method" was validated with simulation. This was done correcting the simulated efficiency with scale factors given by the MC/Data mismodelling of the tag-and-probe efficiency due to ECAL dead crystals not considered in the simulation efficiency.

The simulation of annihilation events with the four dead crystals in the top-right quadrant of ECAL (see a hit map in Figure 5.18) has been split in two sub-samples defined as "MC" and "data":

- sub-sample "MC", shown in green in Figure 5.25, is free of ECAL defects plays the role of simulation;
- sub-sample "data", shown in yellow in Figure 5.25, with the detector defects plays the role of data.

Sub-sample "MC", can be considered as an imperfect simulation of sub-sample "data". In particular, a one-to-one relation between "MC" and "data" regions can be defined by a $\pi/2$ rotation, i.e., photons at ϕ in the "MC" region simulate photons at $\phi + \pi/2$ in the "data" region. The number of annihilation events from MC truth in the two samples are statistically compatible as reported in Table 5.10. Two simulations are considered: the first one with a single positron beam (no pileup), the second one with 25000 positrons in each event uniformly distributed in a time interval of 250 ns (with pileup).

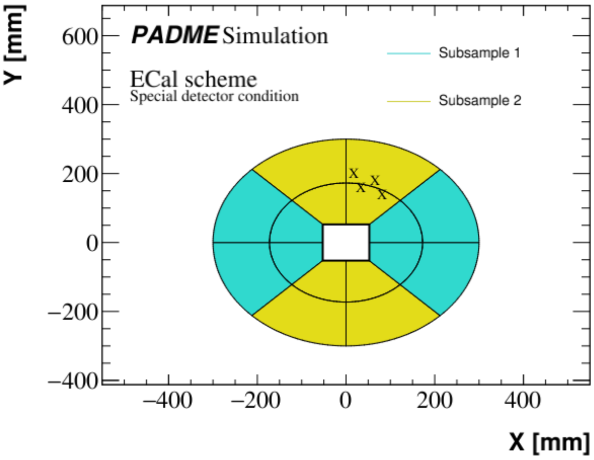

Figure 5.25: *XY map of the two sub-samples used to validate the scale factors method.*

Table 5.10: *Number of annihilation events in the sub-sample 1 ("MC") and 2 ("data"), known from MC truth.*

Sub-sample	Yield
"Data"	32649
"MC"	32671

Simulation with no pileup

In the absence of pileup, the number of annihilation candidates reconstructed in the "data" and "MC" regions are listed in Table 5.11, along with the selection criteria applied. As expected the dead crystals are responsible for a lower yield reconstructed in the "data" region with respect to "MC" region.

Table 5.11: *Number of annihilation candidates reconstructed in "data" and "MC" regions from the integration of the distribution of $E_{\gamma_1}+E_{\gamma_2}$ in the range $[300, 600]$ MeV. Two selections are considered: the first requiring that the leading photon belongs to the FR, the second requiring that both photons are in the FR. No pileup is simulated.*

Sample	**Cut**	$\gamma_1 \in FR$	$\gamma_1, \gamma_2 \in FR$
"Data"	$\lvert\Delta t\rvert < 10$ ns, $\lvert X(Y)_{CoG}\rvert < 5$ cm	31443	29940
"MC"	$\lvert\Delta t\rvert < 10$ ns, $\lvert X(Y)_{CoG}\rvert < 5$ cm	32537	31088

As a first closure test each event passing the selection of Table 5.2 is reweighed according to Equation 5.3 using the tag-and-probe efficiency measured in 16 bins and shown in Figure 5.22 (a). The corrected yields, reported in Table 5.12, are in agreement with the expected value of Table 5.10 within 1%. It is interesting to observe that in the "data" region, where there are the dead crystals, the corrected yield is in agreement with the expectation, as in the "MC" region, where there are no not ECAL defects. This is a confirmation that the bias of the efficiency, clearly visible in Figure 5.22 (a), is compensated in the product $\epsilon(\gamma_1) \times \epsilon(\gamma_2)$.

Table 5.12: *Number of annihilation candidates reconstructed in "data" and "MC" regions from the integration of the distribution of $E_{\gamma_1}+E_{\gamma_2}$ in the range $[300, 600]$ MeV. The yields were extracted integrating the $E_{\gamma_1}+E_{\gamma_2}$ spectrum in a fixed range ($[300, 600]$ MeV) from the sample simulated with four dead ECAL crystals in the top right quarter.*

Sample	**Cut**	$\gamma_1 \in FR$	$\frac{\gamma_1 \in FR}{expetation}$	$\gamma_1, \gamma_2 \in FR$	$\frac{\gamma_1,\gamma_2 \in FR}{expetation}$
"Data"	$\lvert\Delta t\rvert < 10$ ns, $\lvert CoG\rvert < 5$ cm	32429	0.993	32477	0.995
"MC"	$\lvert\Delta t\rvert < 10$ ns, $\lvert CoG\rvert < 5$ cm	32598	0.998	32594	0.998

As a second closure test, the reconstructed yields are deriving using the scale factor method. Therefore, each event in the “MC” region is weighted by the product of two scale factors corresponding to the tag-and-probe efficiency of the two photons.

The tag-and-probe efficiency scale factor is defined as follows:

$$f_i = \frac{\epsilon^{TP}(data|\phi_i, R_i)}{\epsilon^{TP}(MC|\phi_i, R_i)} = \frac{\epsilon^{TP}(\text{“}data''|\phi_i + \pi/2, R_i)}{\epsilon^{TP}(\text{“}MC''|\phi_i, R_i)} \tag{5.16}$$

where ϕ_i varies inside the “MC” region and the efficiency at the numerator, estimated in data, is the efficiency measured in “data” region at $\phi + \pi/2$ and the efficiency at denominator, estimated in MC, is the efficiency measured in “MC” region at ϕ_i. From these scale factors and the reconstructed yields, the factor $C_{\gamma\gamma}$, defined in Section 5.1 is computed and the yields corrected according to the scale factor method are obtained.

Also this test was done for the two analyses variants and all relevant results are summarized in Table 5.13. In particular, the signal yield in the “data” region, after correction by the scale factor method (last row) agree with the MC truth yield (first row) within 0.5%.

Table 5.13: *Annihilation yield re-weighted and not by scale factors for “MC” sample and yield corrected or not by the $C_{\gamma\gamma}$ factor for “data” sample from simulation without pileup. The MC truth yields and the $C_{\gamma\gamma}$ factor are also reported.*

	“data” region		“MC” region	
	$\gamma_1 \in FR$	$\gamma_1, \gamma_2 \in FR$	$\gamma_1 \in FR$	$\gamma_1, \gamma_2 \in FR$
MC truth	32649		32671	
Yield	31443	29940	32550	31095
Yield re-weighed with scale factors			31627	30065
$C_{\gamma\gamma}$ factor			0.968	0.920
Yield corrected with $C_{\gamma\gamma}$	32480	32535		

A simulation with pileup

The simulation used for this closure test is the sample of annihilation events from CalcHEP embedded on the GEANT4 simulation of 25000 positrons interacting in the target for each event. This sample contains annihilation processes also from GEANT4 which should not be taken into account in the yield determination because they are not recorded in MC truth. For this reason reconstructed annihilation candidates are considered only if the two-photon kinematics matches the CalcHEP MC truth for that event. The matching logic was established in a pure annihilation simulation without dead crystals. The variables under study were the photon energy and the azimuthal angle. The differences $\Delta E = E_\gamma - E_{cl}$ and $\Delta\phi = \phi_\gamma - \phi_{cl}$ between generated and reconstructed values for all events passing the selection cuts a,b,c,d described in Table 5.2 are shown in Figure 5.26.

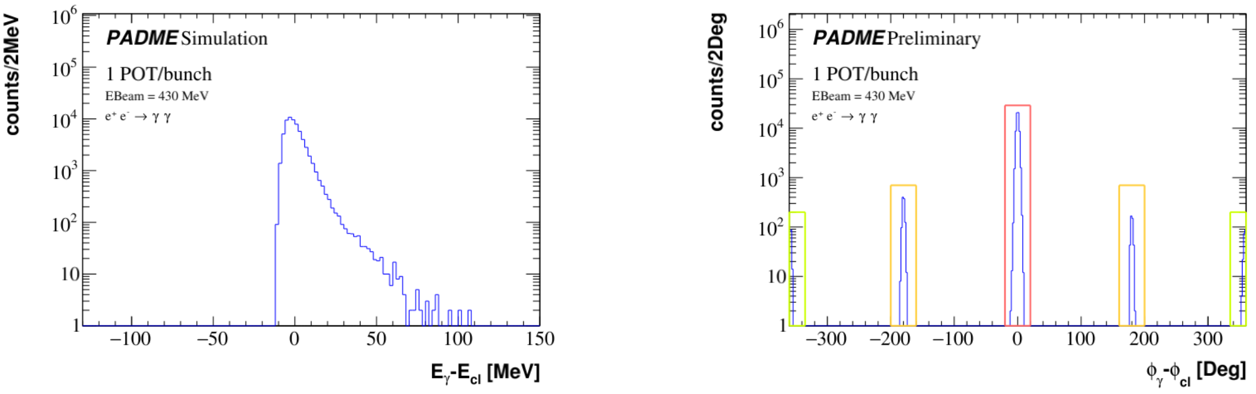

(a) (b)

Figure 5.26: *Distribution of* $\Delta E = E_\gamma - E_{cl}$ *(a) and of the* $\Delta\phi = \phi_\gamma - \phi_{cl}$ *for events passing the selection cuts a, b, c, d described in Table 5.2 for a annihilation simulation without pileup.*

based on these distributions, the matching requirements applied are $|\Delta E| < 50$ MeV and $|\Delta\phi| < 45°$ (care is taken to treat correctly the case of $\Delta\phi = 180°$, occurring when, due to reconstruction, the order of the two photons is reversed).

The efficiency of the matching logic become lower when the detector has defects; this has been verified using the simulation of ECAL with 4 dead crystals in the top right quarter. The same procedures applied to the "data" region (where defects lie) and the "MC" region (where the detector has no defects) gives the matching yields reported in Table 5.14. From these results, and from Table 5.11, where the number of annihilation events from MC truth is reported, the efficiency of the matching criterion in the "data" region is found to be $\beta = \frac{30809}{31443} \simeq \frac{29313}{29940} = 0.98$.

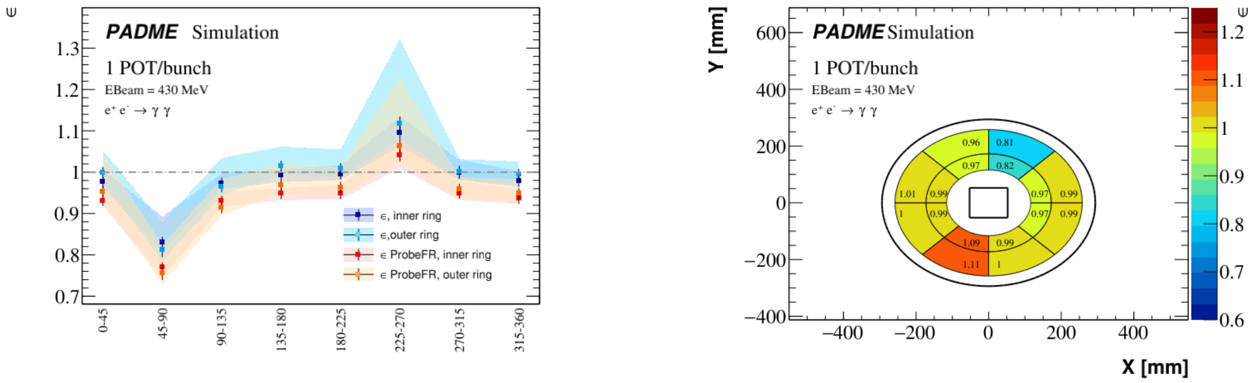

(a) (b)

Figure 5.27: *Tag-and-probe efficiency for MC simulation of CalcHEP with pileup. In (b) efficiency map measured without any requirement on the probe photon.*

Taking these matching efficiency into account, the number of annihilation candidates selected in the sample with pileup is corrected with the tag-and-probe efficiency measured in the same sample and shown in Figure 5.27. The results, reported in Table 5.15 for the "data" and the "MC" regions, show a very good match with MC truth, both for the selection with the leading photon in the FR and for the selection with both photons in the FR.

This successfully comparison relies on the assumption of low inefficiency of the matching criterion and low contamination of the annihilation sample generated with CalcHEP due to annihilation processes simulated by GEANT4. Indeed, both these effects were found to be lower than 0.3%.

Table 5.14: *Yield of reconstructed annihilation events in a simulation of* $e^+e^- \rightarrow \gamma\gamma$ *with* 25000 *positron per bunch and four dead ECAL crystals in the top right quarter ECAL region matched with MC truth.*

	$\gamma_1 \in FR$		$\gamma_1, \gamma_2 \in FR$	
Sample	All events	Matching to MC truth applied	All events	Matching to MC truth applied
"Data"	31443	30809	29940	29313
"MC"	32537	32489	31088	31042

Table 5.15: *Yield of reconstructed annihilation events in a simulation of* $e^+e^- \rightarrow \gamma\gamma$ *with* 25000 *positron per bunch and four dead ECAL crystals in the top right quarter after correction for the tag-and-probe efficiency ECAL region using the scale factor method .*

	$\gamma_1 \in FR$		$\gamma_1, \gamma_2 \in FR$	
Sample	All events	Matching to MC truth applied	All events	Matching to MC truth applied
"Data"	32429	31765	32477	32553
"MC"	32598	31784	32594	32548

Finally, the scale factor method was applied to simulation with pileup gives the results summarized in Table 5.16.

In summary, the results of the various closure tests performed in the simulation are very satisfying also in the difficult case of pileup and of detection in a detector region with some dead crystals. As a consequence, the long list of checks discussed in this section allows to gain strong confidence on the tag-and-probe technique for the efficiency measurement and on the cross section measurement strategy that will be applied for the analysis of PADME data.

Table 5.16: *Annihilation yield re-weighted and not by scale factors for "MC" sample and yield corrected and not by the* $C_{\gamma\gamma}$ *factor for "data" sample from simulation with pileup. The MC truth yields and the* $C_{\gamma\gamma}$ *factor are also reported.*

	"data" region		"MC" region	
	$\gamma_1 \in FR$	$\gamma_1, \gamma_2 \in FR$	$\gamma_1 \in FR$	$\gamma_1, \gamma_2 \in FR$
MC truth	32649		32671	
Yield	31443	29940	32553	32548
Yield re-weighed with scale factors			31583	30022
$C_{\gamma\gamma}$ yield			0.967	0.919
Yield corrected with $C_{\gamma\gamma}$	32516	32579		

5.8 Background subtraction

In Chapter 3 the background in PADME, and in ECAL in particular, has been widely discussed comparing data collected in RunI and in RunII, after the commissioning of the beam line. Despite the big improvement in the quality of data collected in RunII, the occupancy of the electromagnetic calorimeter is still dominated by beam induced background. In addition, the simulation of the beam line with all relevant materials along with the focusing and bending magnets is a very complex task. An important effort has been undertaken in the collaboration to achieve the goal of a realistic simulation of the beam line, however a tuning of such simulation suitable to describe the data of RunII has not yet been completed. This situation implies that the subtraction of the background, both in the selection of the annihilation events, and in the selection of tag (and probe) photons for the efficiency measurement, requires a data-driven approach.

Figure 5.28 shows the distributions of the sum of the energies of the two photons passing a selection for annihilation events in data. The three plots refer to different thresholds for the x and y coordinates of the CoG: 20, 50 and 80 mm. The peak at 430 MeV, corresponding to the signal events, overlaps with a shoulder related to combinatorial background whose relative importance is as bigger as looser is the cut on the center of gravity. Figure 5.29 shows the same distributions obtained by applying the same selection to a simulation of annihilation events with the pileup of physics background from the interactions of 25000 positrons per bunch in the target. In this case the background is smaller in size and different in shape with respect to the background observed in data.

Much more severe is the problem of background subtraction for the selection of tag photons. This is shown for data in Figure 5.30 (a) and in the simulation with pileup in Figure 5.32 (a). Eventually, the distribution of the photon identified as matched probes is almost free of background, therefore the shape of the distribution observed in data (Figure 5.31 (a)) is similar to the distribution in the simulation Figure 5.32 (b).

A fundamental help comes from the samples of data recorded with the Active Diamond Target removed from the beam line. In these data samples the signals recorded by the PADME

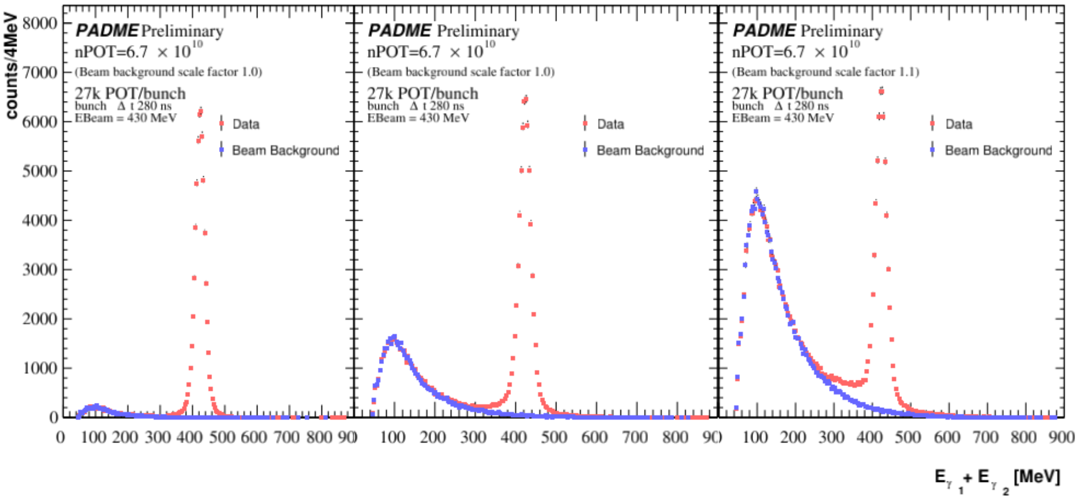

Figure 5.28: *Sum of the photon energies for the pair of candidate annihilation photons (passing cuts a and b described in Table 5.2) in a standard run (red dots) and in a background run, with the target out of the beam line (blue dots). The candidates are requested to have x and y coordinates of the CoG smaller than* 20 mm *(a),* 50 mm *(b), and* 80 mm *(c).*

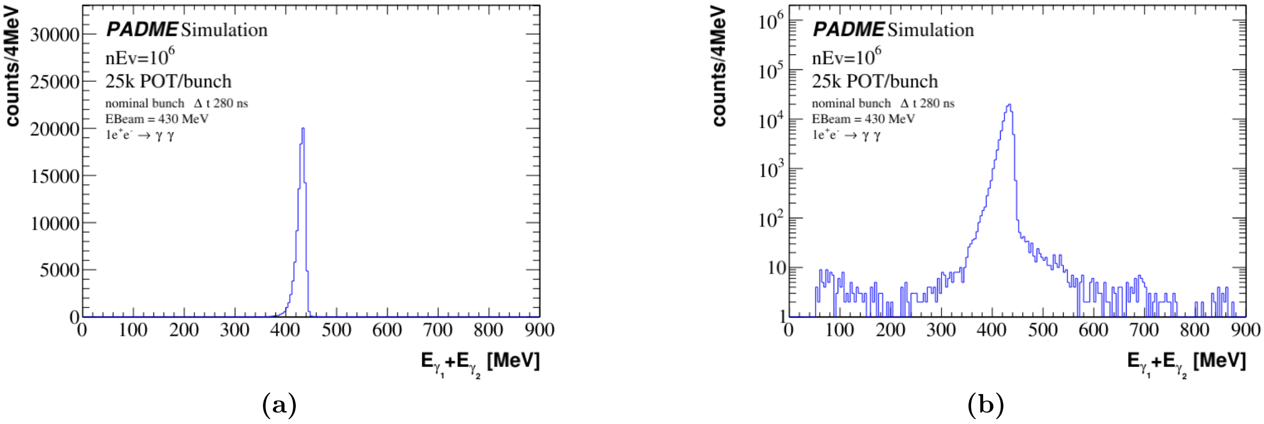

Figure 5.29: *Sum of the photon energies for the pair of candidate annihilation photons (passing cuts a, b and c described in Table 5.2) in simulation with pileup in a linear (a) and logarithmic (b) scale.*

detectors are produced only by beam related background and by positrons in the tail of the beam spot interacting in passive materials surrounding the target. In Figure 5.28 the distribution in blue superimposed to the data represents the result of the annihilation selection applied to no-target data with a normalization adjusted in order to match the amplitude of the background shoulder in the distribution observed in target data. The distribution corresponding to signal events can be obtained as the difference between the target and scaled no-target distributions. The same strategy can be applied in the case of the selection of tag photons. In Figure 5.30 (b)

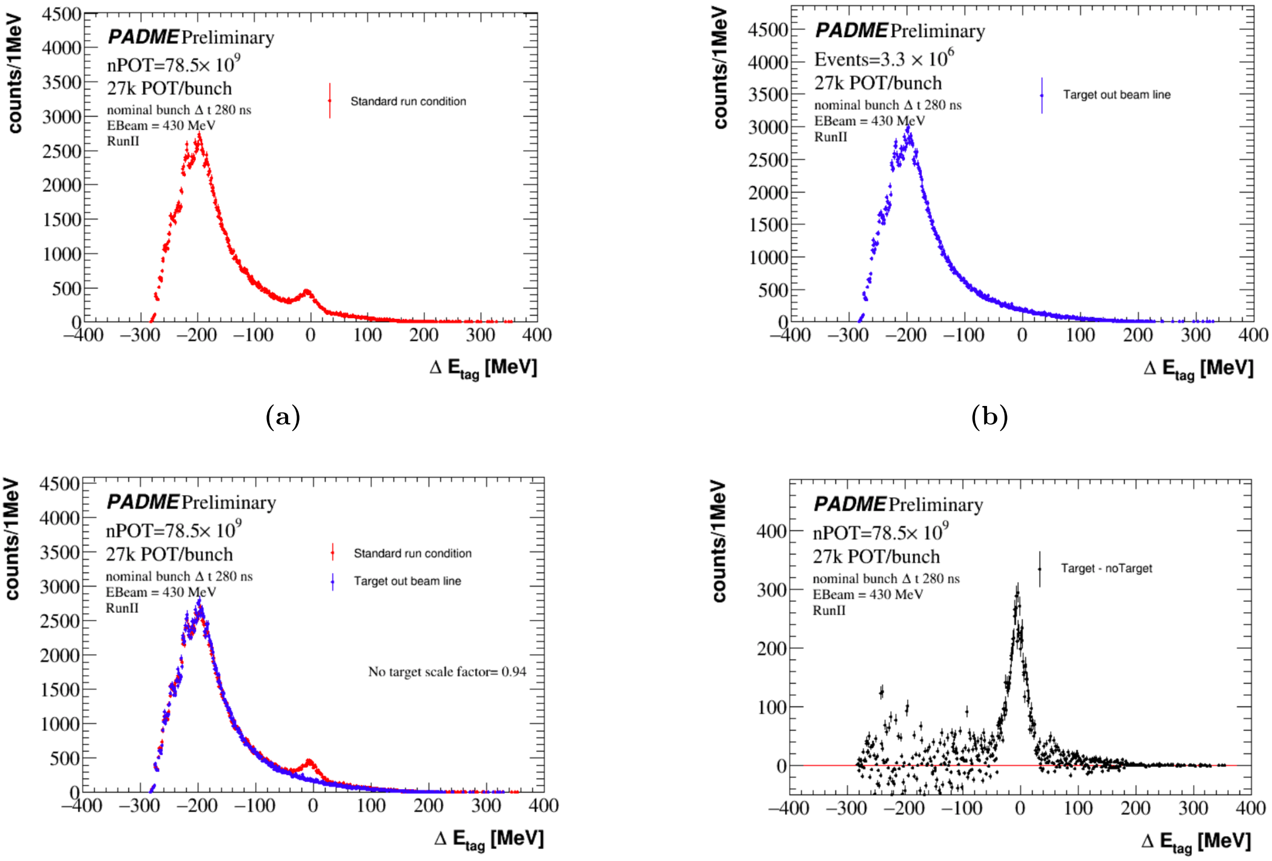

(a) (b)

(c) (d)

Figure 5.30: *Distribution of $\Delta E = E_\gamma - f(\theta)$ for tag candidates in standard run (a) and in a background run with the target out of the beam line (b). The distributions in (a) and (b) are superimposed in (c) and subtracted in (d) after scaling of the background distribution.*

the distribution of ΔE_{tag} obtained in no-target data is shown. Figure 5.30 (c) shows the overlap of this distribution to the same distribution obtained in target data. Finally, the distribution for tag candidates subtracted by the background estimated with the scaled no-target data is shown in Figure 5.30 (d).

The background is normalised equalizing the integral of the distribution of no-target and target data in the range $\Delta E_{tag} \in [-150, -90]$ MeV. For consistency the same background subtraction procedure is applied to the distribution of ΔE_{probe} for the matched probe candidates. One should observe that no-target data are suitable to describe the beam induced background, but they do not describe the sub-dominant contribution of the background arising from the pileup of interactions of the high intensity beam in the target[8]. The relative importance of

---

[8] The target data also contain primary beam positron interaction with the target Aluminium structure which is not described in the no-target data. This beam background component was not negligible in RunI [77] but it is believed to be negligible in this analysis because of the well focused primary beam reached in RunII.

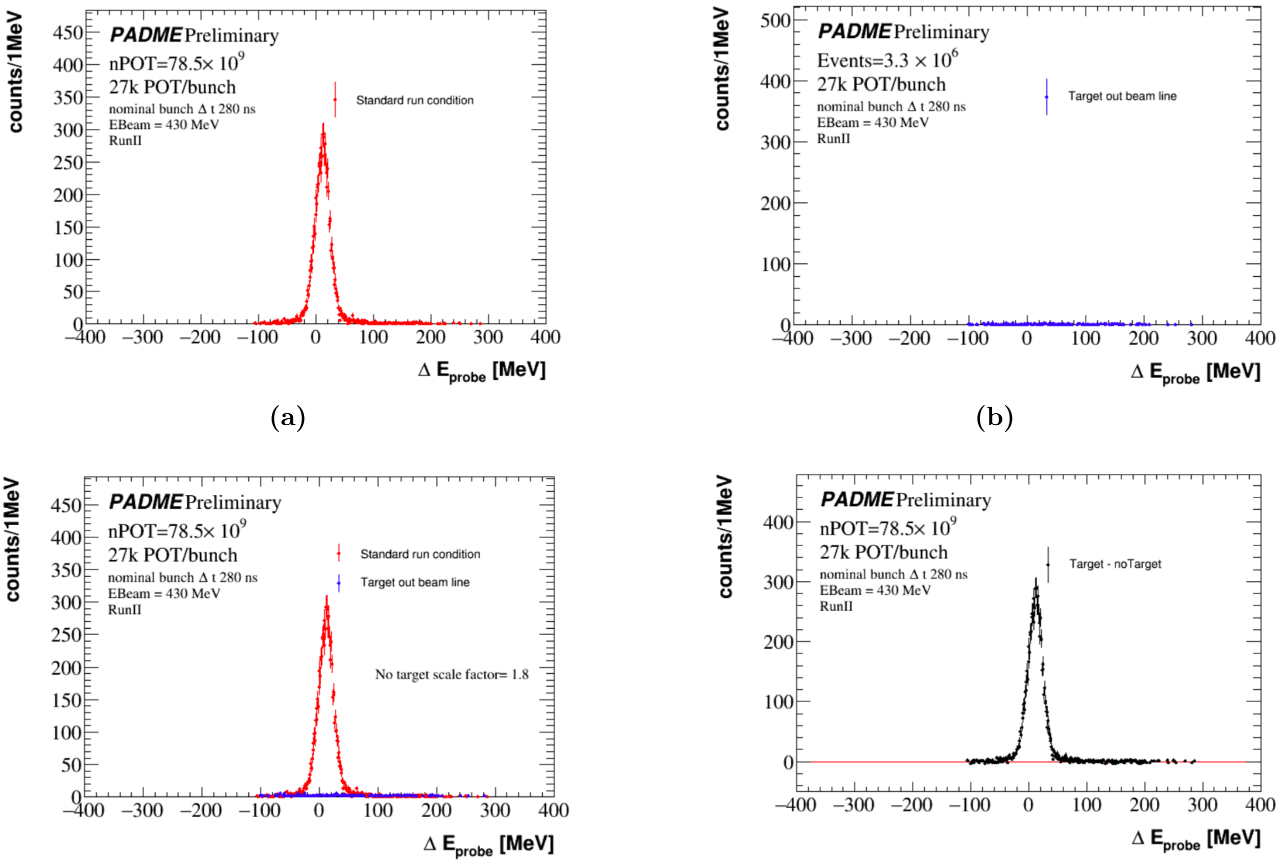

(a) (b)

(c) (d)

Figure 5.31: *Distribution of $\Delta E_{Probe} = E_\gamma - (E_{Beam} - f(\theta_{Tag}))$ for probe candidates in standard run (a) and in a background run with the target out of the beam line (b). The distributions in (a) and (b) are superimposed in (c) and subtracted in (d) after scaling of the background distribution.*

beam induced background and background from the pileup can be assessed by comparing the simulation with pileup and the data for the selection of candidate tag-photons, i.e. Figure 5.30 (a) and Figure 5.32 (a). In the assumption that the contribution of pileup can be ignored, the procedure described in Section 5.6.1 can be applied to estimate the number of tag-photons and matched probes after background subtraction using the no-target data. This allows to estimate the tag-and-probe efficiency and its systematic variations in all 16 bins of ECAL . The results are shown in Figure 5.33 for all matched probes and for matched probes requested to belong to the FR. They exhibit an unclear pattern with respect to the known features of ECAL, in addition to biases indicated by few values higher than one.

The known defects of ECAL in RunII data, that can be observed in Figure 3.7 (a) (a two-dimensional cluster map) and Figure 5.34 (a two-dimensional map of candidate photons from annihilation), are:

- 3 dead crystals: one in the external bin of slice $270 - 315°$, one in the external bin of

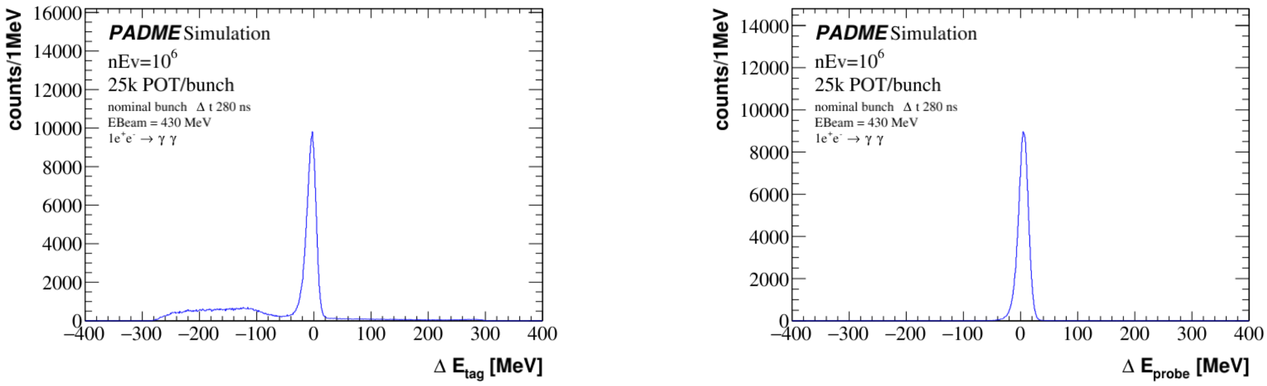

(a) (b)

Figure 5.32: *Distribution of* $\Delta E = E_\gamma - f(\theta)$ *for tag candidates (a) and of* $\Delta E_{Probe} = E_\gamma - (E_{Beam} - f(\theta_{Tag}))$ *for probe candidates (b) in the CalcHEP simulation with pileup.*

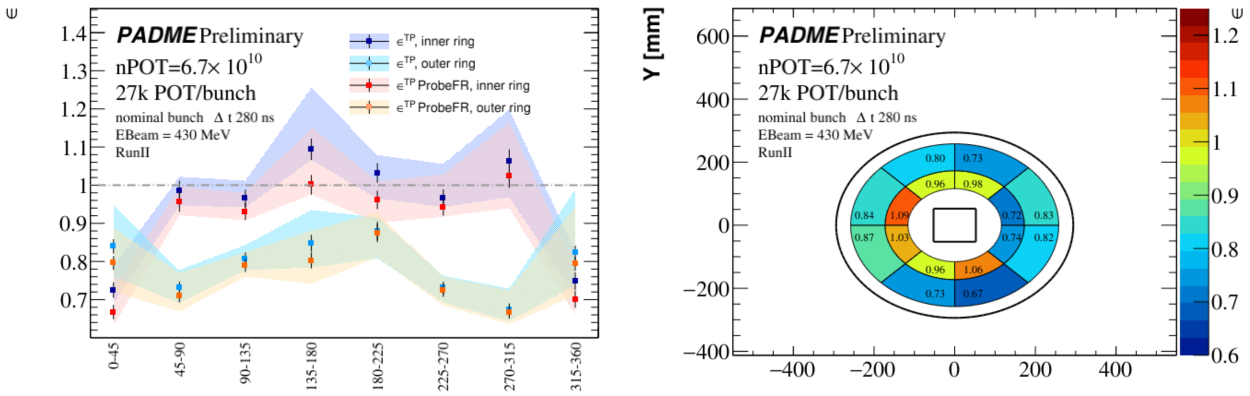

(a) (b)

Figure 5.33: *Tag-and-probe efficiency in 8* ϕ *bins of the inner and outer ring of the FR, with and without the requirement for the matched probe photon to be in the FR. The systematic uncertainty, estimated as described in Section 5.6.1 and combined with the statistical error, is shown by the coloured bands in (a). Efficiency map (b).*

slice $315 - 360°$; the third at the inner border of the FR at the boundary between slice $270 - 315°$ and slice $315 - 360°$;

- a reduction of the acceptance at the top and at the bottom of the fiducial region appearing as a shadow from inert materials (presumably the top and bottom walls of the vacuum chamber at the exit of the magnet dipole); this effect is seen also in simulation and in data it causes a slightly larger effect at the bottom of ECAL, suggesting some mismodeling of the vertical offset of ECAL with respect to the vacuum chamber;

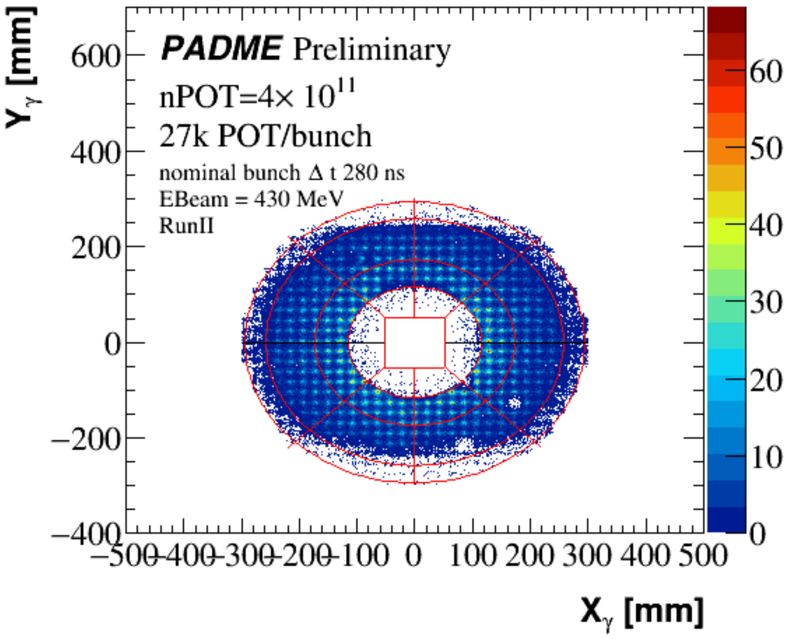

Figure 5.34: *Map of the annihilation photon candidates passing the requirements a and b described in Table 5.2.*

- in some runs a few adjacent crystals in the top-right quarter ECAL region have a low efficiency due to a DAQ problem. Some of these features can be recognised in the efficiency map of ECAL shown in Figure 5.33, but other unclear effects show up in these measurements; also they appear rather sensitive to the criteria applied to count signal tags and probes in the distributions obtained after background subtraction.

As a consequence a few improvements have been introduced in the overall data analysis process, affecting on one side the data-driven efficiency determination and on the other side the measurement of the number of annihilation candidates. They will be applied for the derivation of results in the next section. They are briefly anticipated here:

- The overall rate of background photon candidates will be reduced by applying a preselection on the cluster shape parameters;
- The distribution of ΔE_{tag} has been subtracted of the background by considering the contribution of beam related background and pileup; the shape of the beam background is inferred from no-target data while the shape of the background from pileup is predicted by simulation. The normalization of both of them will be obtained from a fit to the data;
- The yield of annihilation events will be obtained from the distribution of the difference in phi between a photon and the direction expected from the other photon; the background contamination is easily subtracted since it is flat under the signal peak which is not true for the energy sum distribution;

- a correction of the position of ECAL in the PADME reference frame, where the z axis is defined as matching the direction of the incoming beam, will be applied leading to a distribution of the annihilation candidates symmetric in the calorimeter, after correction for the local inefficiencies. This will be determined using survey measurements and further corrections derived from data.

5.9 Event selection

5.9.1 Pre-selection

A first selection of the events was done in order to choose only events where a beam bunch arrives in the experiment, this is possible by choosing event triggered by the hardware trigger of the BTF beam.

However, even when the PADME trigger board receives the BFT trigger signal, it can happen that the event is empty, typically because of a late update of the BFT trigger signal after beam loss.

In addition, another problem can be observed looking at Figure 5.35 where the N_{POT} distribution for the events triggered by the BTF signal is shown for run 30563: up to 70 kPOT/bunch were estimated in a few cases. If the target reconstructs correctly the bunch multiplicity, events out the 5σ have a different beam background level and are affected by the pileup differently with respect to a typical event. On the other hand, events where the signals readout from the

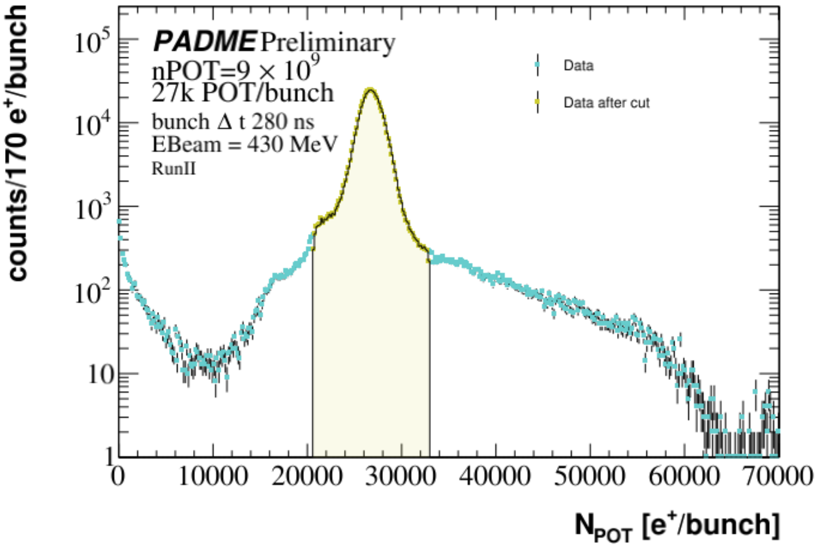

Figure 5.35: *Distribution of the Number of Positrons On Target (N_{POT}) per bunch in run* 30563 *as measured by the Active Diamond Target. The yellow area corresponds to the events passing the pre-selection requirement on the N_{POT} measurement.*

strips of the Active Diamond Target lead to an extremely low or unrealistically high measurement of the total charge lead to a wrong assessment of the number of positrons in the bunch. Although the occurrence of such events is low, they may introduce biases in the measurement of the total number of positrons on target.

To solve both these problems in each run, events with a measured number of positrons in the bunch above or below 5σ from the average bunch multiplicity have been discarded.

Table 5.17: *For each analysed run, run number, number of events triggered by the BTF trigger signal, number of events passing the N_{POT} selection, and their ratio.*

Run number	N_{ev}^{BTF}	$N_{ev}^{5\sigma}$	$\frac{N_{ev}^{5\sigma}}{N_{ev}}$
30369	2961470	2820916	0.953
30386	1437248	1307072	0.909
30547	2232745	2140028	0.958
30553	785728	746250	0.95
30563	2243220	2101791	0.937
30617	2206172	2086402	0.946
30624	2234949	2106551	0.943
All	14000000	13300000	0.95

In Table 5.17 the number of events for each analysed run before and after the luminosity selection are reported along with the fraction of events retained.

5.9.2 Photon pre-selection

In Chapter 3 it has been shown that even in RunII the PADME electromagnetic calorimeter receives a high rate of background particles, from beam related spurious interactions. Most of the times the resulting energy deposits have energy lower than 50 MeV, therefore the features of the corresponding clusters are statistically different from those of photons of energy above about 90 MeV that, as we saw, are involved with the annihilation process. Therefore, a cluster selection is applied in order to reduce the contamination of the cluster collection and improve the rejection of the background.

Cluster quality requirements

Several features of the clusters corresponding to a tight selection of annihilation events have been studied and contrasted with the same quantities observed in the overall sample of clusters. The selection of annihilation photon candidates was based on the following requirements: at least two clusters must be found in ECAL with $|t_{\gamma_1} - t_{\gamma_2}| < 10$ ns, $|\Delta\phi| = |\phi_{\gamma_1} + 180^\circ - \phi_{\gamma_2}| < 25^\circ$, $|CoG_{X(Y)}| < 5$ cm, $300 < E_{\gamma_1} + E_{\gamma_2} < 500$ MeV. In addition, the most energetic cluster in the pair was requested to be at a radial distance with respect to the direction of the incoming beam bigger than 115.82 mm.

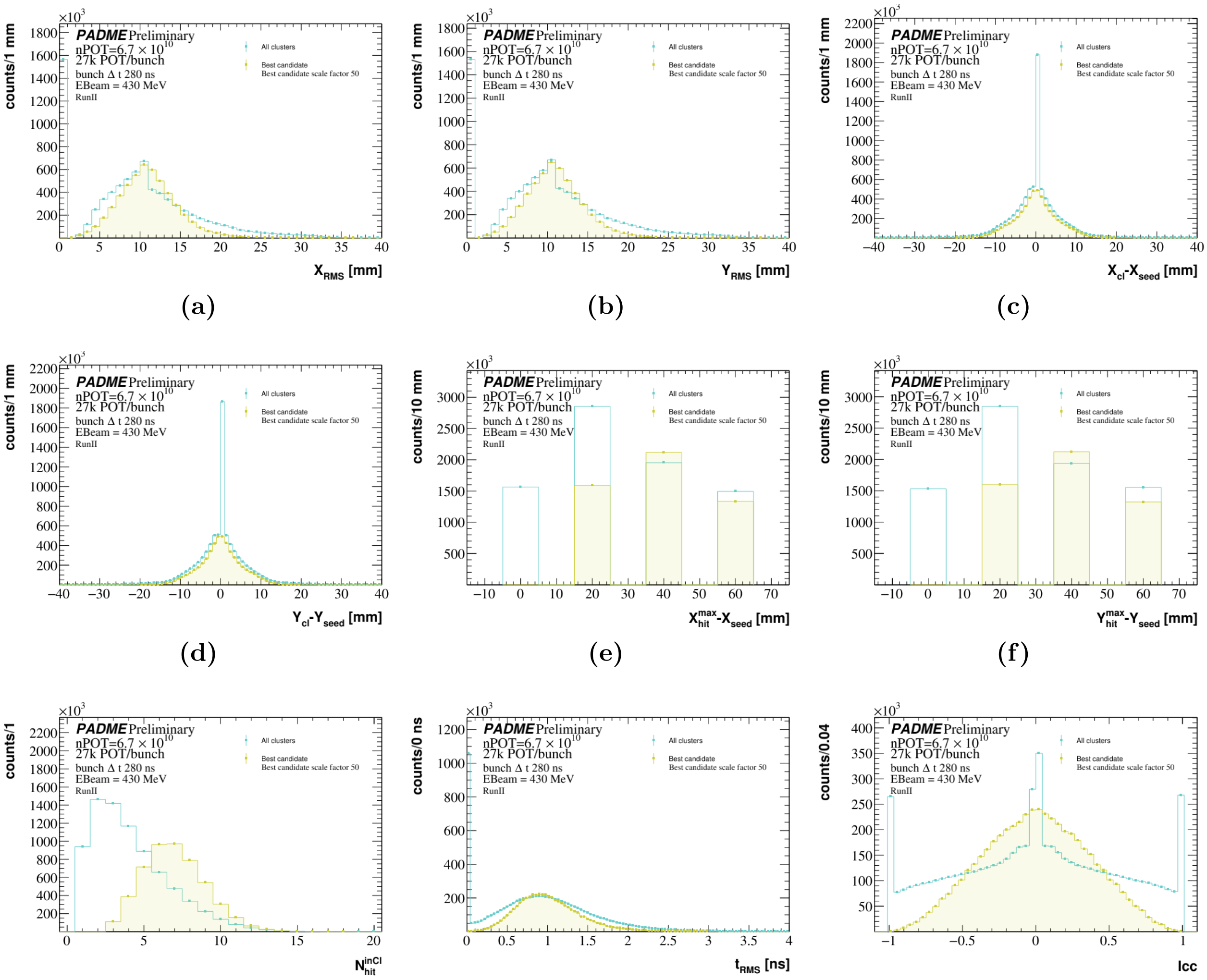

(a) (b) (c)

(d) (e) (f)

(g) (h) (i)

Figure 5.36: *Distribution of cluster variables used to improve the reconstruction quality and reduce the background contamination of the photon candidates, for all clusters (azure distributions) and annihilation candidate photons (yellow distribution): RMS of X (a) and Y (b) coordinates of hits in the cluster; distance of the cluster from its seed in the X (c) and Y (d) direction; maximum of distance between a hit in the cluster and the seed in the X (e) and Y (f) direction; cluster size (g); RMS of the hits time in the cluster (h); linear correlation coefficient of hits in the cluster (i).*

The distributions (with arbitrary relative normalization) of the variables studied are reported in Figure 5.36 for all clusters and for annihilation candidate photons. For each variable, a loose cleanup cut was defined to avoid compromising significantly the efficiency for signal photon. In the following the relevance of each variable is briefly described:

- the distance between the cluster position and its seed is peaked at zero in both the X and Y directions (see Figure 5.36 (c) and (d)), large distances may only be due to

Table 5.18: *Cluster quality requirements and fraction of clusters passing each cut with respect to those passing the previous cut.*

Quality cut	$\frac{N_i}{N_{i-1}}$
$R_{Cl-seed} < 20$ mm	0.96
$X_{RMS} \geq 1$ mm	0.79
$Y_{RMS} \geq 1$ mm	0.90
$\Delta X^{max} \geq 1$ mm	1.00
$\Delta Y^{max} \geq 1$ mm	1.00
$\lvert lcc \rvert \leq 0.99$ mm	0.92
t_{RMS}	0.996
Isolation	0.85

anomalous situations related for example by pileup; therefore only clusters with $R_{cl-seed} = (X_{Cl} - X_{seed})^2 + (Y_{Cl} - Y_{seed})^2 < 20$ mm are retained;

- X and Y RMS, defined as

$$\sqrt{\frac{\sum_{i=0}^{n_{hit \in Cl}} (X(Y)_i - X(Y)_{Cl})^2 E_i}{\sum_{i=0}^{n_{hit \in Cl}} E_i}}, \tag{5.17}$$

  are shown in Figure 5.36 (a) for X and (b) for Y RMS. A comparison between generic clusters and annihilation candidates suggests to reject clusters with $X(Y)_{RMS} \leq 1$ mm;

- the maximum distance between hits in a cluster and the cluster position along X and Y axis (Figure 5.36 (e) and (f)) is requested to be $\Delta X(Y)^{max} \geq 1$ mm in order to discard the occurrence of signals from noise in an isolated crystal;

- the cluster distribution size, reported in Figure 5.36 (g), shows that candidate photons have an average multiplicity of 7 hits per cluster, thus a threshold on the cluster multiplicity was applied $N_{hits}^{inCL} > 1$;

- the RMS of the time distribution of hits in a cluster, defined similarly to the X(Y) RMS, is shown in Figure 5.36 (h) and a value not exceeding 3 ns is requested;

- the linear correlation coefficient of hits in the cluster given by

$$lcc = \frac{\sum_{i=0}^{n_{hit}} (X_i - Xcl)(Y_i - Ycl)E_i}{\sum_{i=0}^{n_{hit}} E_i \times X_{RMS} \times Y_{RMS}} \tag{5.18}$$

  is reported in Figure 5.36 (i); only values below 0.99 are accepted;

- finally, an isolation requirement is applied: a photon is rejected if another cluster within 10 ns is found closer than 200 mm.

The sequence of cuts applied to the ECAL clusters rejects 53, 8% of them with the relative efficiency of each cut reported in Table 5.18. The loss of signal photon introduced by this cut is of about 10%.

Figure 5.37 shows how this pre-selection of ECAL clusters allows to reduce the background in the tag selection, leaving the signal almost unaffected.

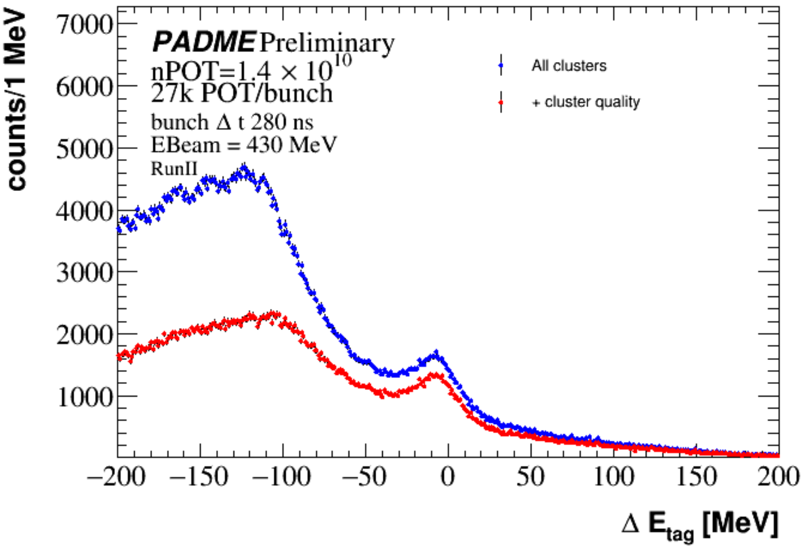

Figure 5.37: *ΔE for candidates tag photons inside the fiducial region identified in the sample of all clusters (blue) and in the sample of clusters passing the quality and selection cuts (red).*

5.9.3 Two-photon selection

The measurement of the yield of annihilation events is based on a fit of the distribution of the variable $\Delta\phi = \phi_{\gamma_1} - \phi_{\gamma_2} - 180°$. This variable has the big advantage of being affected by a background almost flat in shape. Figure 5.38 shows this variable for the entire data sample; the same distribution observed in the no-target data is superimposed for comparison, showing that the beam related background reproduces the flat behaviours of the signal side-bands in nominal data.

The two-photon annihilation yield is obtained by fitting the $\Delta\phi$ distribution with the sum of a second order polynomial and a Gaussian function. The event selection has been designed in order to be as efficient as possible for signal events, benefiting of the reduction of the background coming from the clean-up of the photon candidates. The requirements applied are summarized in Table 5.19 along with the number of PADME events in the data sample (described in Section 5.3.1) surviving each cut. The number of signal events N_{sig} is defined as the total number of candidates N_c with $|\Delta\phi| < 40°$ subtracted of the number of background events estimated by the fit:

$$N_{Sig} = N_c - N^{fit}_{Bkg} \tag{5.19}$$

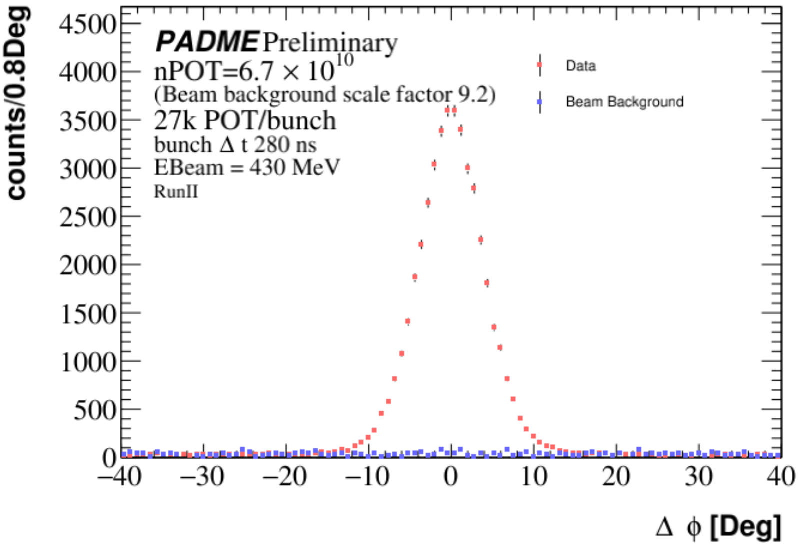

Figure 5.38: *Distribution of* $\Delta\phi = \phi_{\gamma 1} - \phi_{\gamma 2} + 180°$ *for the pair of candidate annihilation photons passing the selection cut a,b,c, described in Table 5.2 in a standard run (red dots) and in a background run with the target out of the beam line (blue dots).*

Table 5.19: *Selection cut-flow.*

Cut	
N of pre-selected events	13×10^6
N pairs of good clusters in ECAL	20×10^6
$E_{\gamma_1} > 90$ MeV	16×10^6
$E_{\gamma_2} > 90$ MeV	7×10^6
$R_{\gamma_1} \in FR$	3×10^6
$\lvert\Delta t\rvert < 10$ ns	4×10^5
$\Delta E(\theta_{\gamma_1})$	3.8×10^5
$\Delta E(\theta_{\gamma_2})$	3.2×10^5

where $N^{fit}_{Bkg} = \int_{-40}^{40} P2(x)dx$, with $P2$ the second order polynomial of the fit.

A data-driven geometry correction

In order to verify the consistency of the measured yield, the ECAL calorimeter was divided in 8 azimuthal slices and the annihilation candidates have been assigned to each slice according to the value of ϕ_{γ_1}, i.e. the azimuthal angle of the most energetic photon in the pair. The uniformity predicted by physics can be altered only by variations of the reconstruction and identification efficiency associated to detector defects. Table 5.20 summarizes the yields of the annihilation candidates in each bin for run 30563. These results are also graphically shown in

Table 5.20: *Annihilation yield from the fit of the $\Delta\phi$ distribution in 8 azimuthal slices of ECAL (absolute and normalized to the highest value) before and after the run-dependent position correction.*

			γ position correction	
ϕ Deg **range**	N_{sig}	$\frac{N_{sig}}{N_{sig}^{max}}$	N_{sig}	$\frac{N_{sig}}{N_{sig}^{max}}$
$[0, 45]$	1227	0.85	1352	1
$[45, 90]$	899	0.62	966	0.71
$[90, 135]$	866	0.60	901	0.67
$[135, 180]$	1316	0.91	1295	0.96
$[180, 225]$	1451	1	1294	0.96
$[225, 270]$	1290	0.90	1182	0.87
$[270, 315]$	1091	0.75	1089	0.81
$[315, 360]$	1334	0.92	1332	0.99

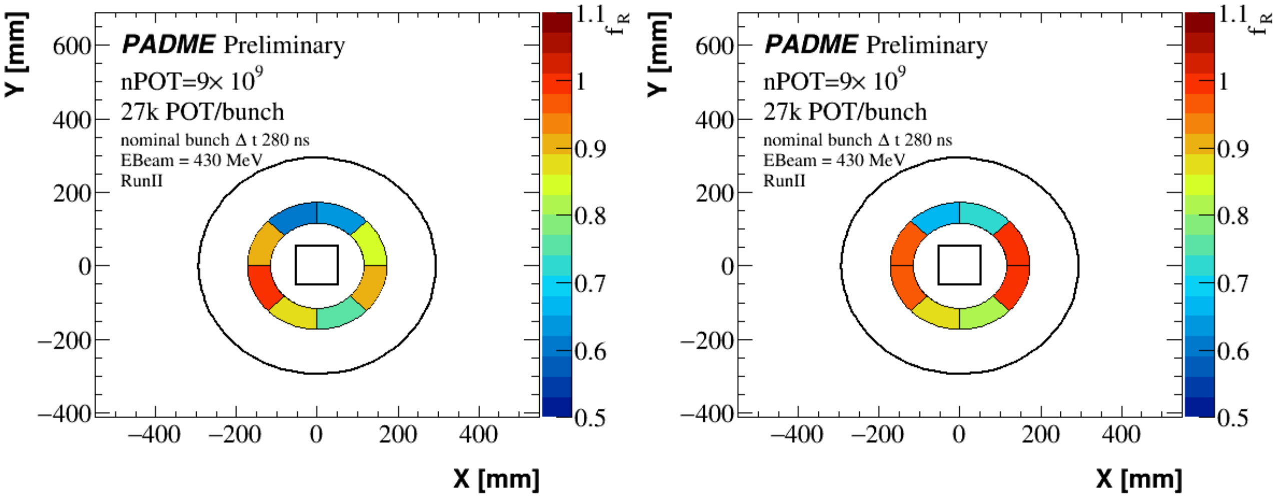

(a)

(b)

Figure 5.39: *Maps of annihilation yield from the fit to the $\Delta\phi$ distribution and normalized to the highest value, before (a) and after (b) the run-dependent position correction.*

Figure 5.39 left, where one can easily observe that the top part of ECAL seems to be depleted. A lower number of candidates in the top and bottom regions is expected due to shape of the top and bottom vacuum chamber walls shadowing the trajectories of photons with large polar angle. However, the top-bottom asymmetry is not expected and may be interpreted as an indication of a vertical offset between beam and ECAL. Indeed, a campaign of survey measurements on the experimental apparatus found a position of the center of ECAL in the PADME reference frame given by $(x_c, y_c) = (-3.13, -3.86)$ mm.

After this general correction of the PADME geometry was applied in the reconstruction software, the distribution of the x and y coordinates of the center of gravity of the two photons from annihilation candidates was studied separately for all runs. The aim of the study was to observe in data the run-dependent offset of the beam position with respect to the PADME reference frame. Indeed corrections of the order of 1 mm were derived for each run and applied to correct the geometry on a run by run basis. The distribution of the annihilation candidates after these corrections is shown in Table 5.20 and in Figure 5.39 (b). Here one can see that the left-right and top-bottom symmetry of the yield is improved. The remaining differences can be ascribed to a vertical offset of the beam with respect to the magnet dipole. The effect will be corrected through the data-driven efficiency measurement. For example, when an annihilation photon is found in the inner ring of the third phi slice, a second photon is expected in the outer ring of the seventh slice. Here the presence of one dead crystal, in addition to the reduction of efficiency due to the vacuum chamber floor at the exit of the dipole, can invalidate the measure. In summary, the pattern of the yield is now matching the known features of the detector.

The corrections described here were studied and applied before the implementation of the cluster pre-selection, therefore the numbers of candidates reported in Table 5.20 are given here just to describe the effect of the run dependent geometry correction, while the final number of candidates obtained at the end of the entire chain of selection on data corrected for these effects, are discussed in Section 5.9.4.

5.9.4 Yield of annihilation candidates

The number of annihilation candidates finally obtained from the entire data set and divided in the 8 slides of ECAL are reported in Table 5.21. The distributions of the $\Delta\phi$ coordinates used to derive them are shown in Figure C.2, with the distribution for the entire data set shown in 5.40. For these events, the distribution of the sum of the two photon energies is shown in Figure 5.41, while the $E_{\gamma_1} + E_{\gamma_2}$ for each phi slice is shown in Figure C.1. From Figure 5.41 it is possible to observe a residual energy scale offset, since the peak of the distribution,

Table 5.21: *Annihilation yield obtained separately in 8 ϕ slices of ECAL inside the radial ECAL fiducial region.*

ϕ [Deg]	$N_{\Delta\phi}$	$N_{\Delta E_{In}}$	$N_{MM^2_{In}}$	$N_{\Delta E_{Out}}$	$N_{MM^2_{Out}}$
$[0, 45]$	38780 ± 200	46950 ± 760	46920 ± 900	57000 ± 1300	57600 ± 670
$[45, 90]$	28610 ± 170	46730 ± 520	48720 ± 350	45300 ± 470	46100 ± 550
$[90, 135]$	26520 ± 160	53700 ± 1400	50040 ± 930	46320 ± 800	46800 ± 420
$[135, 180]$	37440 ± 190	45770 ± 440	48340 ± 350	51590 ± 820	52900 ± 440
$[180, 225]$	38780 ± 200	44850 ± 870	47350 ± 400	52000 ± 1100	50000 ± 860
$[225, 270]$	36290 ± 190	47470 ± 730	47000 ± 1300	38320 ± 580	39300 ± 410
$[270, 315]$	35330 ± 190	45300 ± 780	44010 ± 430	32430 ± 370	32800 ± 290
$[315, 360]$	36070 ± 190	45690 ± 840	46400 ± 1700	50400 ± 1700	46000 ± 710
All FR	276700 ± 530	375600 ± 3000	369400 ± 1100	365700 ± 3000	365200 ± 8500

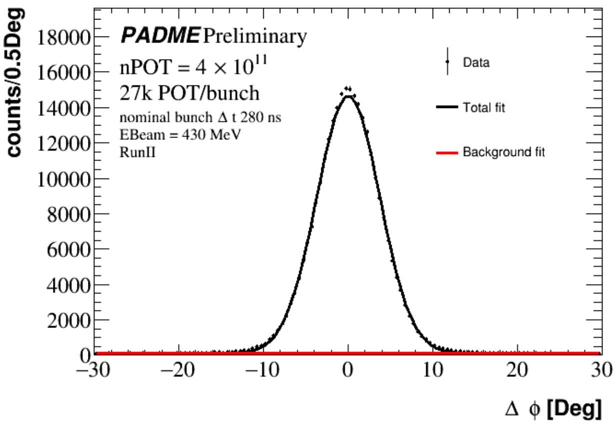

Figure 5.40: *$\Delta\phi$ distribution for the entire detector FR (data points) and its fit function (black line). The background component of the fit function (second order polynomial) is superimposed (red line).*

which should match the beam energy, is found instead at about 423 MeV. In the following it will be clear that the cross section measurement strategy does not rely on any critical energy measurement. Therefore, this residual offset has not been corrected.

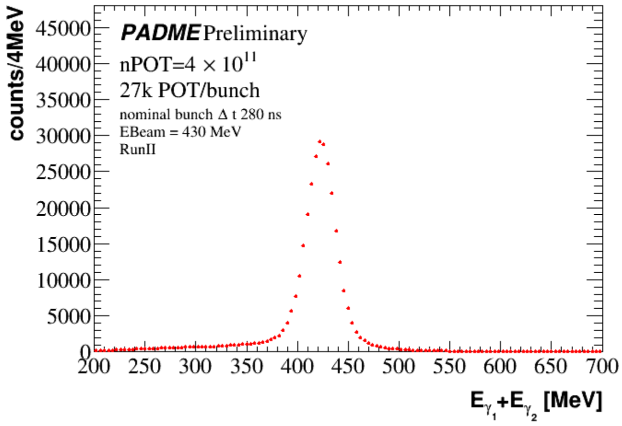

Figure 5.41: *Sum of the candidate photon energies inside the radial ECAL fiducial region.*

In addition, the selection has been applied separately in the different runs and the corresponding results and plots are shown in Table 5.22 and Figure C.9. The errors are statistical only.

The constrained kinematics of annihilation events is such that candidate events can be identified also through a search for a single photon with energy and polar angle related to each other, as expected for a photon produced in the process $e^+e^- \to \gamma\gamma$. Of course, one should count photons either in the inner ring of the FR or in the outer ring, in order to avoid a double counting of events. Therefore, two single photon selections have been designed to search for annihilation events. They are defined by the requirements summarised in Table 5.23. These

Table 5.22: *Annihilation yield obtained separately in each run.*

ϕ [Deg]	$N_{POT/10^{10}}$	$N_{\Delta\phi}$	$N_{\Delta E_{In}}$	$N_{\Delta E_{Out}}$
30369	8.2	54570 ± 230	74900 ± 1100	71100 ± 1700
30386	2.8	21440 ± 150	27900 ± 1000	26000 ± 440
30547	7.1	51470 ± 230	67100 ± 1800	66500 ± 930
30553	2.8	19040 ± 140	26340 ± 880	25100 ± 2000
30563	6.0	42200 ± 210	56500 ± 1400	55500 ± 3500
30617	6.1	43320 ± 210	58000 ± 1800	56700 ± 4400
30624	6.6	45700 ± 210	63700 ± 1400	61300 ± 3000

Table 5.23: *Single photon annihilation selection criteria.*

	$\|\Delta E\| = \|E_\gamma - f(\theta_g)\| < 100$ MeV
γ inner ring	$R_{min} < R_\gamma < R_{mid}$
γ outer ring	$R_{mid} \leq R_\gamma < R_{max}$

selections are strongly contaminated by background. This can be subtracted statistically from a fit of the signal region and of the sidebands of the distributions of the following variables: $\Delta E = E_\gamma - f(\theta_g)$, with $f(\theta)$ given by $E = exp(c + s\theta)$ where $c = 6.4$ and $s = -20.6$ (true for $E_{beam} = 430$ MeV) and, alternatively the squared missing mass:

$$M^2_{miss} = 2m_e[E_{beam} - E_\gamma(1 + \frac{E_{beam}}{2m_e}\theta^2_\gamma)]. \tag{5.20}$$

Both quantities are zero for a photon produced in a two-photon annihilation event. The background, instead, is smooth under the peak at zero, but it exhibits a different shape for the two variables. Figure 5.42 shows the distribution of ΔE and M^2_{miss} for the inner (a) and outer (b) ring of a specific slice; from the plot one can appreciate how the background shape differs not only from bin to bin of the same variable, but also when moving from one variable to the other. Therefore, even if the events used in the fit are exactly the same, the systematic uncertainty coming from the background modelling may be different. The annihilation yield obtained from both single photon searches, looking at the inner or outer ring of ECAL and from both the ΔE and M^2_{miss} distributions, are reported in Table 5.21, along with the results obtained from the two-photon selection described earlier in this section.

The subtraction of the background takes into account for beam induced background and also for background from pileup. The distributions of ΔE and M^2_{miss} have been fit with a linear combination, with free coefficients, of a template for the signal component, a template for the beam background and a template for the pileup. The beam background is obtained by applying the same single photon selection to the no-target PADME data set, while the template of the pileup is obtained from the simulated sample of annihilation events embedded in the interactions of 25000 positrons per bunch. In this kind of simulation the single photon selection clearly

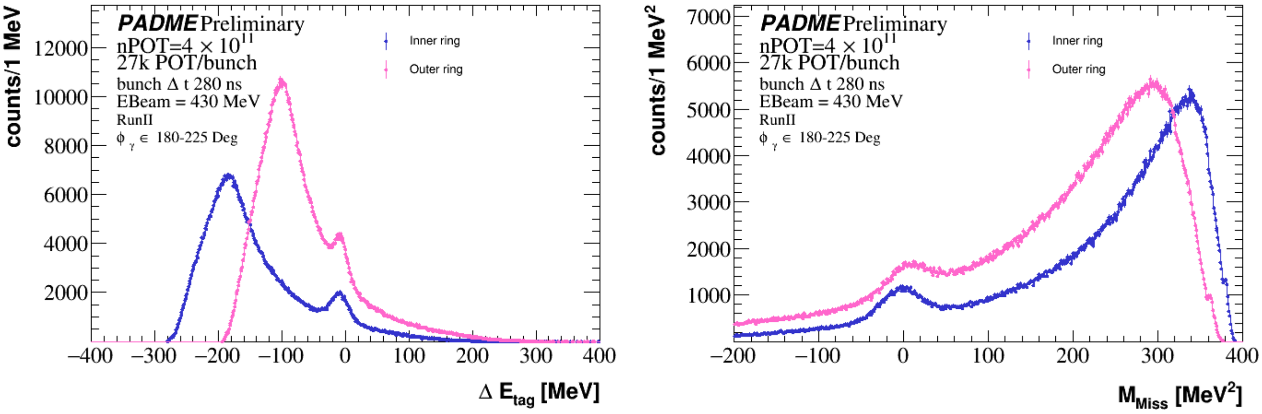

(a) (b)

Figure 5.42: ΔE_{tag} *(a) and* M^2_{miss} *(b) in a specific* ϕ *slice* $(180, 225)^\circ$ *of the inner (blue) and outer (pink) ring of FR.*

exhibits a signal component in addition to the background component. In order to obtain a signal free distribution, the signal region (i.e. the interval [-70,100] MeV) is blinded and the sidebands are simultaneously fit with a smooth function in the range $[-100\text{ MeV}, 250\text{ MeV}]$ for ΔE and $[-200\text{ MeV}, 300\text{ MeV}]$ for M^2_{miss}. This is shown in Figure B.2, where the red line, representing the function fitting and connecting the sidebands, is used as template of the background from pileup.

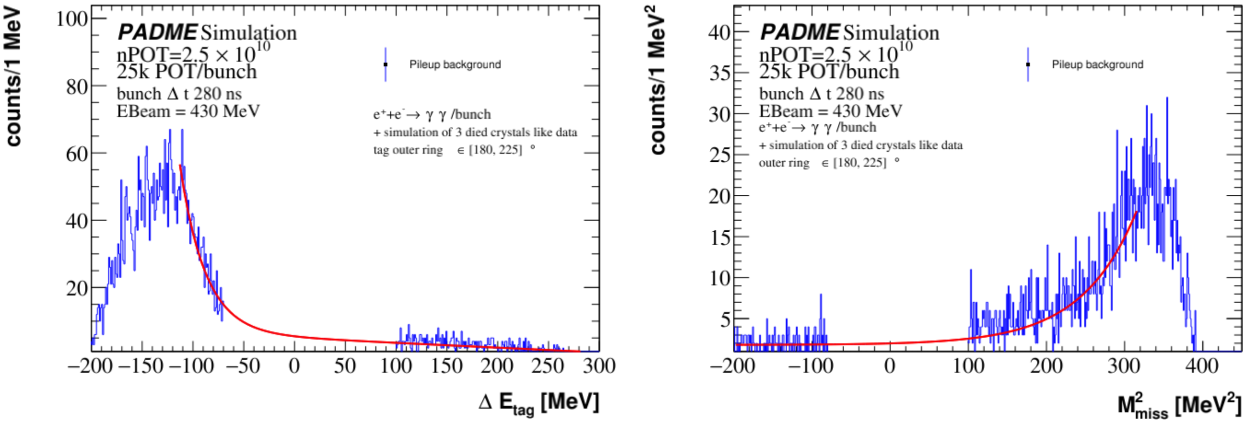

(a) (b)

Figure 5.43: ΔE_{tag} *(a) and* M^2_{miss} *(b) distributions from background originated by pileup interactions in target, predicted by MC simulation with one annihilation event generated by CalcHEP and* 25000 *positron on target generated by GEANT4. The signal region is replaced by the analytic interpolation given by a fit of the sidebands with the sum of an exponential and a first order polynomial.*

To extract the single photon signal, the fit is done with the Roofit [98] toolkit. The signal is described as the sum of two Gaussian contributions G_{lr}, G_{hr}; this allows to account for a component of the signal reconstructed with an error larger than the core resolution. The model fit to the data has the free parameters listed in Table 5.24. The best fit is achieved by minimizing the Negative LogLikelihood. Examples of the fit results are shown in Figure 5.44 for ΔE distributions and in Figure 5.45 for M^2_{miss} for the squared missing mass.

Table 5.24: *Parameters of the combined template fit of the ΔE and M^2_{miss} distributions used to measure the annihilation yield with the single photon annihilation selection of Table 5.23. The same fit is used to count the number of tags for the efficiency measurement.*

Description	parameter
Signal fraction	f_s
Mean of the first Gaussian	μ_1
Sigma of the first Gaussian	σ_1
Mean of the second Gaussian	μ_2
Sigma of the second Gaussian	σ_2
Fraction of the second Gaussian integral over the total signal	f_g
Fraction of the pileup integral over the total background	f_p

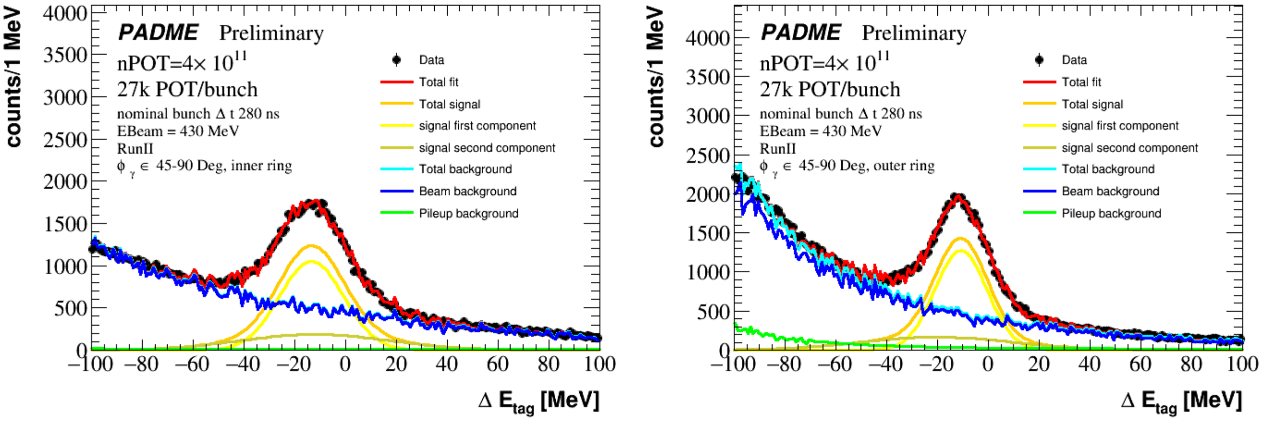

(a) (b)

Figure 5.44: *Fit of the ΔE_{Tag} distribution for photons in the ϕ slice $[45, 90]^\circ$ and in the inner (a) or outer (b) ring of the FR. The components of the total fit function (red) are shown separately: a total signal component in orange (sum of two Gaussian functions in light and acid yellow) and a total background component in cyan (sum of the pileup component in green and the beam related background in blue).*

The number of signal events is estimated as follows: $N_{sig} = f_s N_c$, where f_s is the fraction of the signal component in the best fit combination of the templates and N_c is the total number of

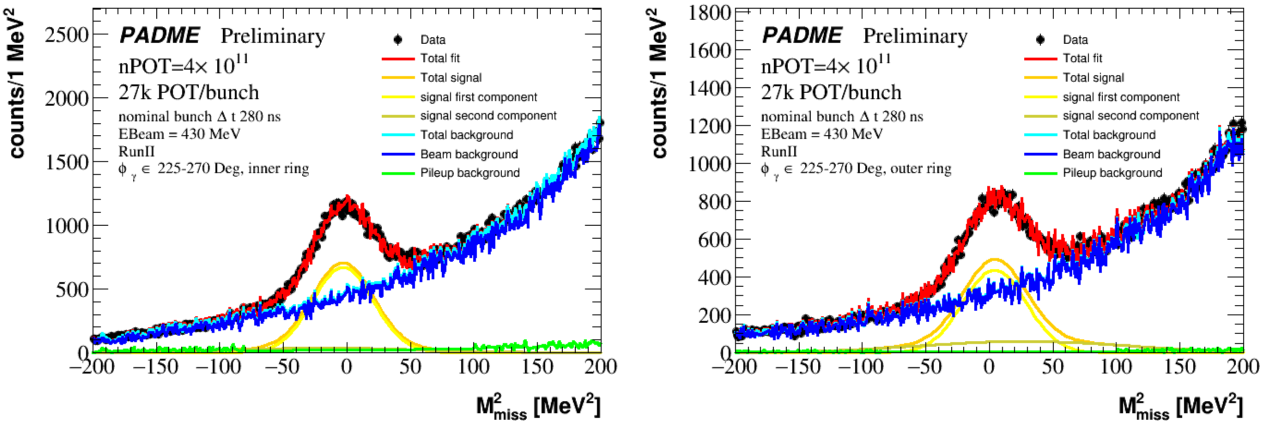

(a) **(b)**

Figure 5.45: *Fit of the squared missing mass distribution for photons in the ϕ slice $[225, 270]^\circ$ and in the inner (a) or outer (b) ring of the FR. All fit components are shown as described in Figure 5.44.*

candidates. The statistical errors quoted in Table 5.21 are estimated by propagating the errors of the number of candidates and of f_s from the fit.

5.9.5 Annihilation photon efficiency in data

The tag-and-probe technique has been applied as described in Section 5.6.1 to the data preselected, clean-up and corrected for beam-ECAL offsets. The measurement is performed in the overall data sample, and also separately in the 16 bins of ECAL. Tags are selected with the single photon selection described in Table 5.23. Then, for each tag with an energy higher than 90 MeV a search for a cluster matching the probe on the other side is performed using the following criteria:

- $|\Delta t| = |t_{tag} - t_{probe}| < 7$ ns;
- $E_{probe} > 90$ MeV
- $|\Delta\phi| < 25^\circ$;
- $|E_{probe} - f(\theta_{probe})| < 100$ MeV;

The results are shown in Table 5.25 and Figure 5.46 for the individual phi slices. The tag-and-probe distributions for the entire statistics in the inner and outer ring are reported in Figure 5.47. The individual fits are collected in Figures C.3, C.4, C.5 and C.6 in appendix C. These efficiencies represent the probability to detect, reconstruct and select an annihilation photon after all the clean-up and selection criteria, except for the FR. They are lower than the values anticipated in Section 5.8 due to the more stringent selection requirements; however the trend as a function of phi and R matches the naive expectations deriving from the knowledge of a few hardware problems affecting ECAL.

Table 5.25: *Number of tags N_{Tag}, probes N_{Probe} and TP efficiency ϵ with the error resulting from the statistical uncertainty on the tag and probe yield in each separate ECAL ϕ slice.*

ϕ [Deg]	N_{Tag}	N_{Probe}	ϵ
		Inner ring	
$[0, 45]$	52000 ± 1100	37460 ± 190	0.721 ± 0.015
$[45, 90]$	38310 ± 580	28420 ± 170	0.742 ± 0.012
$[90, 135]$	32430 ± 370	26630 ± 160	0.821 ± 0.011
$[135, 180]$	50400 ± 1700	36390 ± 190	0.723 ± 0.024
$[180, 225]$	57000 ± 1300	38890 ± 200	0.682 ± 0.016
$[225, 270]$	45300 ± 470	35560 ± 190	0.785 ± 0.009
$[270, 315]$	46320 ± 800	33610 ± 180	0.726 ± 0.013
$[315, 360]$	51590 ± 820	35280 ± 190	0.684 ± 0.011
All slices	365700 ± 4300	267370 ± 520	0.731 ± 0.009
		Outer ring	
$[0, 45]$	44850 ± 870	37870 ± 200	0.844 ± 0.017
$[45, 90]$	47470 ± 730	35520 ± 190	0.748 ± 0.012
$[90, 135]$	45300 ± 780	33980 ± 180	0.75 ± 0.014
$[135, 180]$	45690 ± 840	35610 ± 190	0.779 ± 0.015
$[180, 225]$	46950 ± 760	38160 ± 200	0.813 ± 0.014
$[225, 270]$	46730 ± 520	29430 ± 170	0.63 ± 0.008
$[270, 315]$	53700 ± 1400	27660 ± 170	0.515 ± 0.014
$[315, 360]$	45770 ± 440	36690 ± 190	0.801 ± 0.009
All slices	375620 ± 3000	268100 ± 520	0.714 ± 0.006

In Table 5.26 the annihilation yields are reported after the efficiency correction for each phi slice. In Figure 5.48 the schematic view of the relative annihilation yield is also shown before (a) and after the efficiency correction (b). As is shown, the annihilation yield distribution become more uniform after the efficiency correction.

5.10 Cross section measurement

The annihilation yield obtained in Subsection 5.9.4 and the efficiency for annihilation photons measured in data, reported in Section 5.9.5, are combined to derive a cross section measurement for the annihilation of a 430 MeV positron with an atomic electron. Using the measurement of the number of signal events obtained from the two-photon selection or the single photon selections, the average efficiency measured on the entire data set and the other parameters are summarized in Table 5.27, instead, the cross sections obtained are reported in Table 5.28. The annihilation cross section obtained by fitting the squared missing mass distribution for all runs

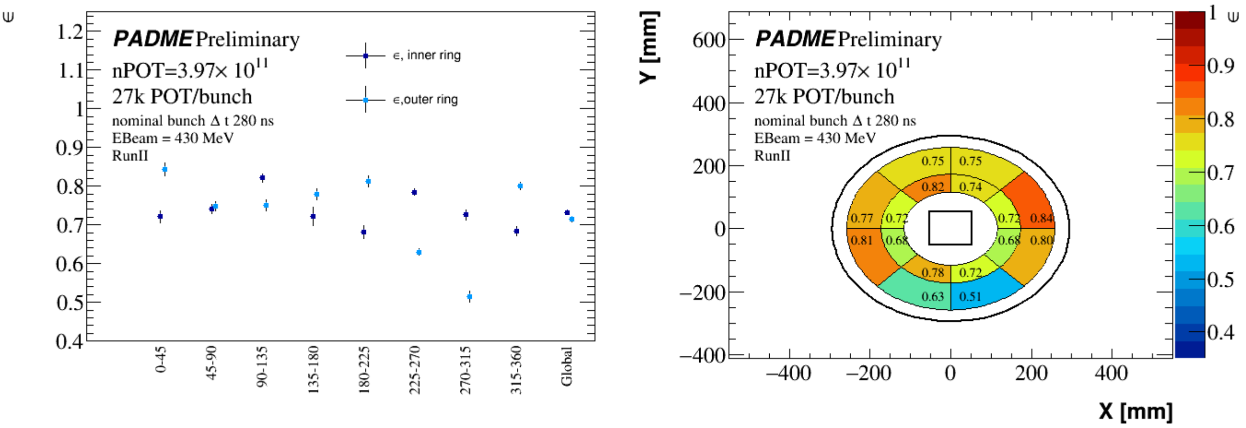

(a) (b)

Figure 5.46: *Tag-and-probe efficiency in data derived for the cross section measurement. Results are reported as obtained separately for the 8 ϕ slices and for all slices together (global) of the inner and outer ring of the FR (a). Events and clusters are preselected as described in the text and the matched probe photon is not required to be in the FR. Only statistical errors are shown. Efficiency map (b).*

Table 5.26: *Annihilation yield obtained separately in 8 ϕ slices of ECAL.*

ϕ [Deg]	$N^W_{\Delta\phi}$	$N^W_{\Delta E_{In}}$	$N^W_{M^2_{miss,\ in}}$	$N^W_{\Delta E_{Out}}$	$N^W_{M^2_{miss,\ out}}$
$[0, 45]$	66200 ± 1800	65100 ± 1700	65100 ± 1800	67500 ± 2000	68200 ± 1600
$[45, 90]$	61300 ± 1400	63000 ± 1200	65700 ± 1200	60600 ± 1200	61600 ± 1300
$[90, 135]$	62700 ± 2000	65500 ± 1900	61000 ± 1400	61800 ± 1600	62400 ± 1300
$[135, 180]$	64700 ± 2300	63300 ± 2200	66900 ± 2300	66200 ± 1700	67900 ± 1400
$[180, 225]$	67300 ± 2100	65800 ± 2000	69400 ± 1700	63900 ± 1700	61500 ± 1500
$[225, 270]$	61800 ± 1300	60500 ± 1200	59900 ± 1700	60800 ± 1200	62500 ± 1000
$[270, 315]$	64800 ± 1700	62400 ± 1500	60600 ± 1200	63000 ± 1900	63600 ± 1800
$[315, 360]$	67700 ± 1700	66800 ± 1600	67900 ± 2800	62900 ± 2200	57500 ± 1100

Table 5.27: *TP efficiency, acceptance, total number of beam positrons collected on target, and number of target electrons per unit surface used for cross section measurement.*

Variable	Value
inner ring efficiency	0.731 ± 0.009
outer ring efficiency	0.714 ± 0.006
acceptance	0.06424 ± 0.00025
N_{POT}	4×10^{11}
$N_{e/S}$	$0.0105 b^{-1}$

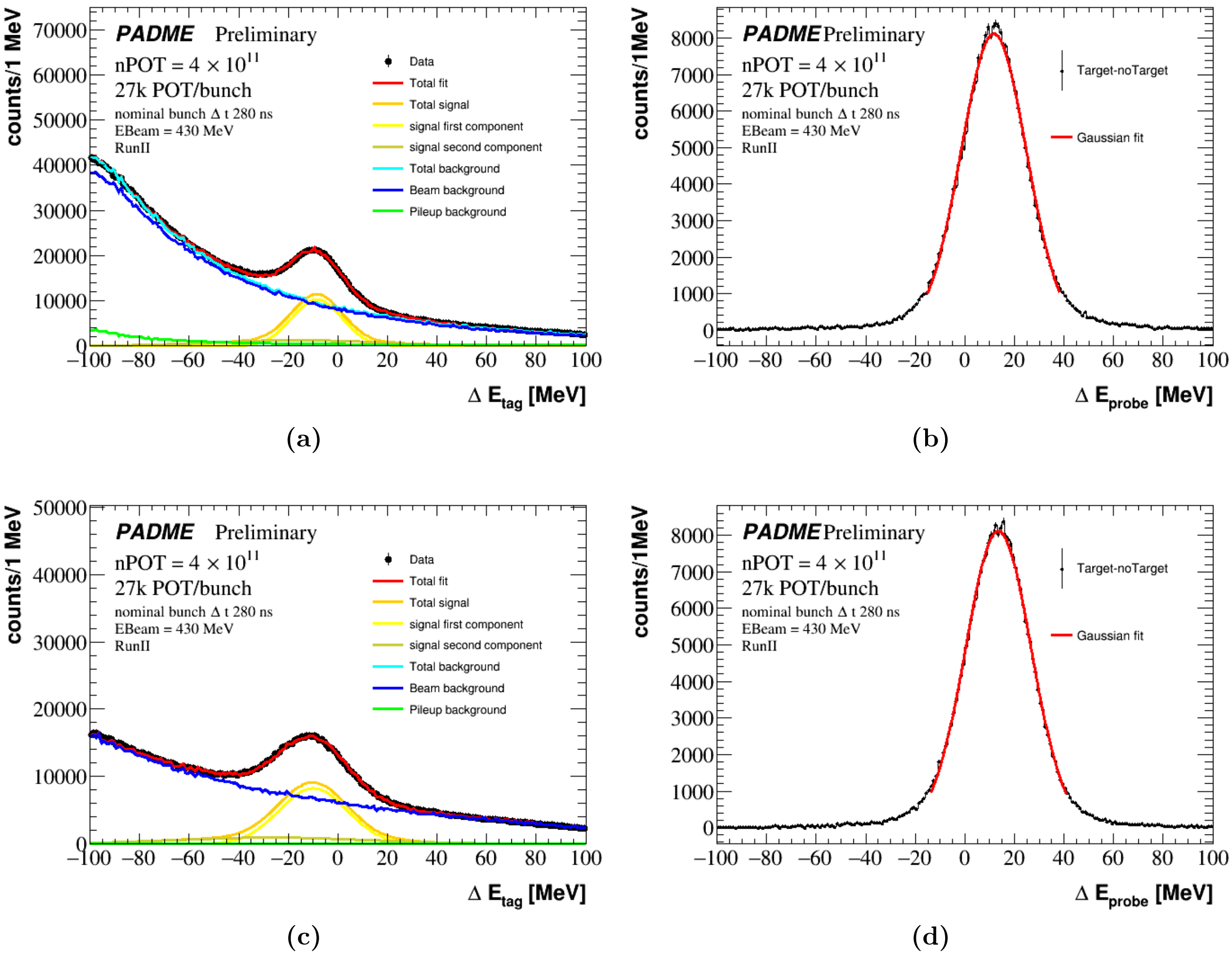

(a) (b)

(c) (d)

Figure 5.47: *ΔE Distribution of tag photons (a) and (c), and the matched probe photons, (b) and (d) in the inner ring, (a) and (b), and in the outer ring, (c) and (d).*

Table 5.28: *Yield efficiency corrected and cross section, estimated with the global TP efficiency, for the process $e^+e^- \to \gamma\gamma(\gamma)$ measured with the five methods on all detector FR and analysed runs.*

Method	Yield	cross section [mb]
$\Delta\phi$	276700 ± 530	1.981 ± 0.031
ΔE_{in}	375600 ± 3000	1.921 ± 0.028
ΔE_{out}	365700 ± 4300	1.914 ± 0.028
$M^2_{miss,\ in}$	369400 ± 1100	1.889 ± 0.027
$M^2_{miss,\ out}$	365200 ± 8500	1.912 ± 0.048

is shown in Figure 5.49.

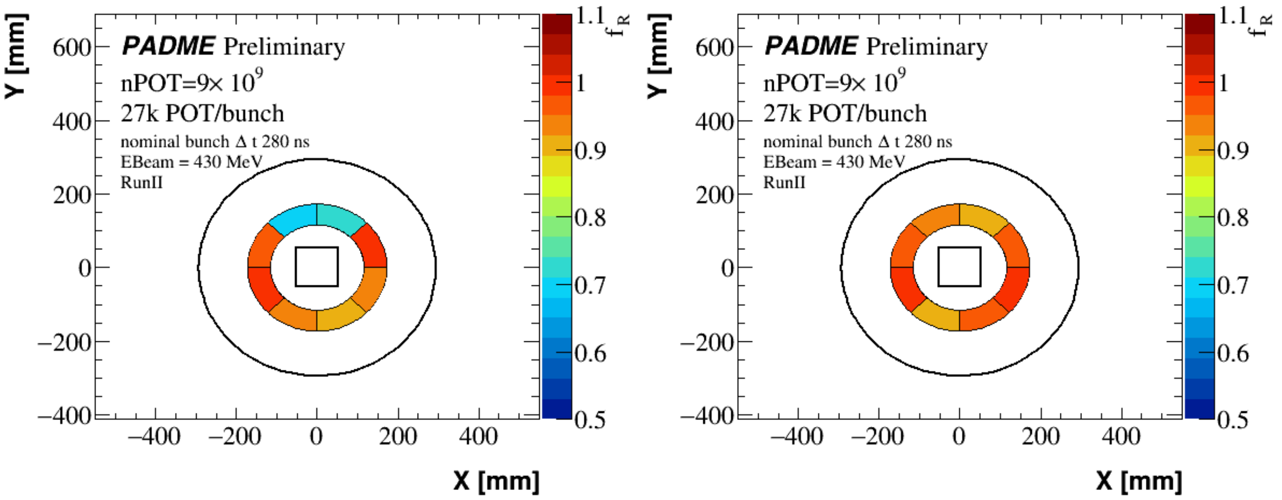

(a) (b)

Figure 5.48: *Yield maps of annihilation candidates in the 8 slices of ECAL normalised to the highest value observed before (a) and after (b) the efficiency correction. Each annihilation candidate is assigned to the slice of the the most energetic photon.*

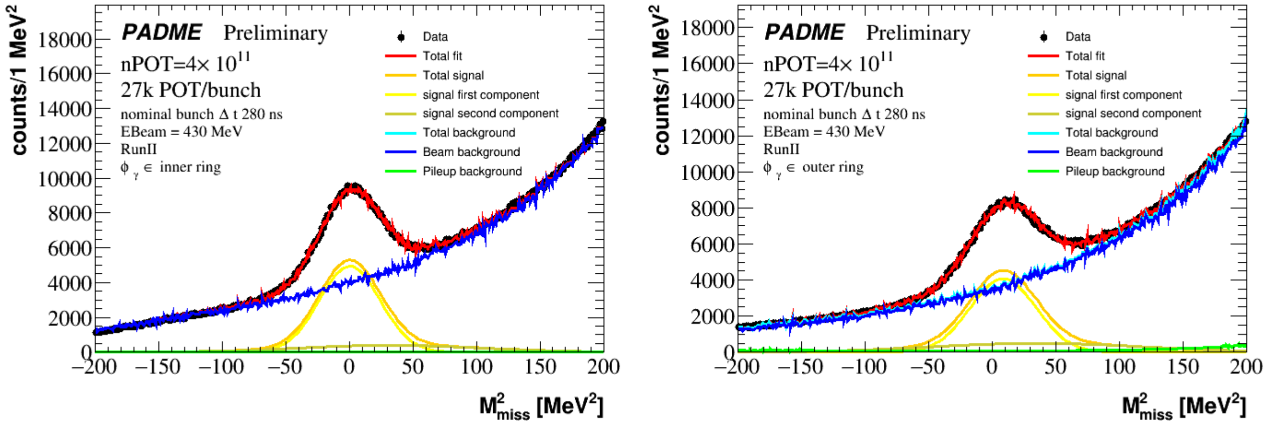

(a) (b)

Figure 5.49: *Squared missing mass distribution for annihilation photons selected in the inner (a) and outer (b) ring of the FR.*

The measurements derived from the fit to the $\Delta\phi$, ΔE_{in} and $M^2_{miss,\ in}$ distributions can be considered equivalent, since they are based on the same sample of annihilation events. Therefore, the differences will be taken into account in the assessment of the systematic uncertainty and their combination, through a simple average, gives the final cross section measurement:

$$\sigma(e^+e^- \to \gamma\gamma) = 1.930 \pm 0.029\ (\text{stat}) \pm 0.057\ (\text{syst}) \pm 0.020\ (\text{target}) \pm 0.079\ (\text{lumi})\ \text{mb}. \quad (5.21)$$

The systematic errors on the measurement are related to the yield extraction and to the efficiency determination; they will be discussed in Section 5.10.3. The error coming from the uncertainty on the total number of positrons hitting the target is quoted separately.

The measurement is compatible with the prediction from Babayaga at NLO

$$\sigma = 1.9573 \pm 0.0005 \text{ (stat)} \pm 0.0020 \text{ (syst) mb} \tag{5.22}$$

where the statistical error comes from the statistic of the generation and the systematic error is a conservative estimate of the missing perturbative contributions. Figure 5.50 shows the agreement of the two-photon annihilation measured by PADME with the NLO approximation and with the other measurements done at an energy scale close to the PADME one (a deeper description of the measurements reported is on Appendix A).

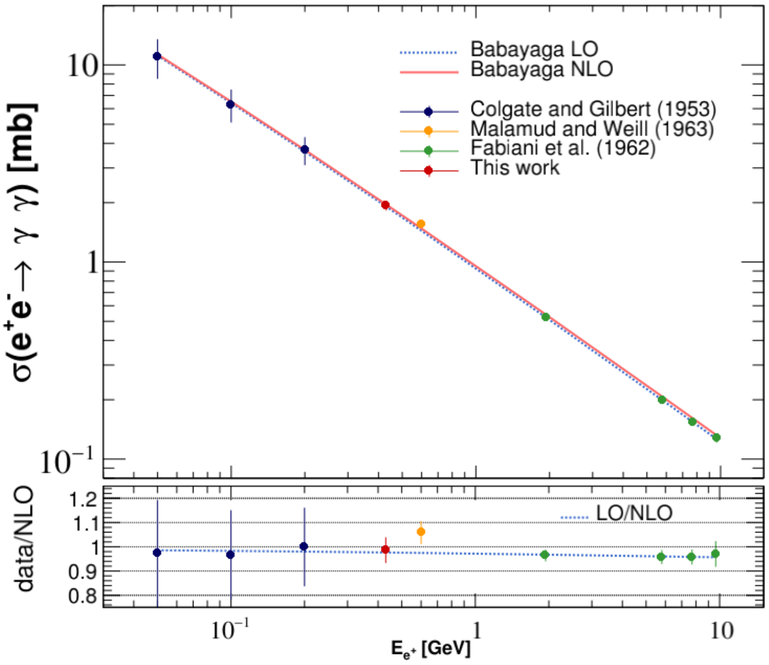

Figure 5.50: *Two-photon annihilation cross section trend. Each measurement described in Appendix A is compared with the cross section obtained in this thesis work. In addition the theory predictions are shown for the LO (azure solid line) and for the NLO (red solid line). On the bottom the ratio between the two theory approximations is illustrated compared to the ratio between the measurements and the NLO approximation.*

5.10.1 Phi dependence

In Table 5.29 the cross section measurement derived with the two-photon selection and with the fit either to ΔE or M^2_{miss} are collected. They appear fully consistent with the measurement in Equation 5.21.

Table 5.29: *Cross section for the process* $e^+e^- \to \gamma\gamma(\gamma)$ *measured with the five methods (two-photon* $\Delta\phi$ *fit and single photon* ΔE *and* M^2_{miss} *fits in the inner and outer ring measured in each* ϕ *slice of ECAL.*

ϕ [Deg]	$\sigma_{\Delta\phi}$ [mb]	$\sigma_{\Delta E_{In}}$ [mb]	$\sigma_{M^2_{miss,\ in}}$ [mb]	$\sigma_{\Delta E_{Out}}$ [mb]	$\sigma_{M^2_{miss,\ out}}$ [mb]
$[0, 45]$	1.979 ± 0.055	1.947 ± 0.051	1.946 ± 0.055	2.019 ± 0.06	2.040 ± 0.048
$[45, 90]$	1.832 ± 0.041	1.883 ± 0.037	1.964 ± 0.035	1.811 ± 0.03	1.841 ± 0.037
$[90, 135]$	1.875 ± 0.059	1.958 ± 0.058	1.823 ± 0.042	1.847 ± 0.04	1.865 ± 0.039
$[135, 180]$	1.933 ± 0.068	1.893 ± 0.065	1.999 ± 0.068	1.980 ± 0.04	2.030 ± 0.043
$[180, 225]$	2.013 ± 0.064	1.966 ± 0.060	2.076 ± 0.052	1.912 ± 0.05	1.838 ± 0.045
$[225, 270]$	1.849 ± 0.039	1.808 ± 0.035	1.791 ± 0.052	1.819 ± 0.03	1.868 ± 0.031
$[270, 315]$	1.938 ± 0.051	1.866 ± 0.046	1.813 ± 0.037	1.883 ± 0.05	1.902 ± 0.054
$[315, 360]$	2.024 ± 0.051	1.997 ± 0.049	2.030 ± 0.083	1.880 ± 0.06	1.719 ± 0.033

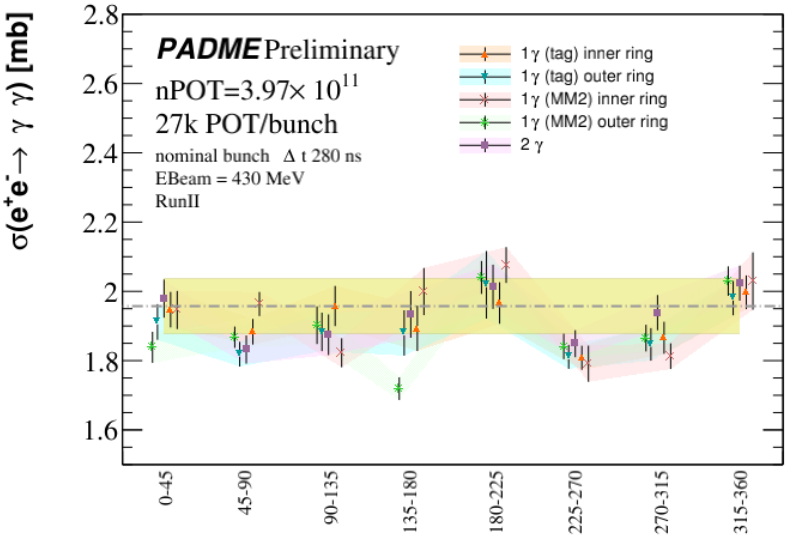

Figure 5.51: *Cross section for the process* $e^+e^- \to \gamma\gamma(\gamma)$ *measured with the five methods (two-photon* $\Delta\phi$ *fit and single photon* ΔE *and* M^2_{Miss} *fits in the inner and outer ring measured in each* ϕ *slice of ECAL. The yellow band , around the theory prediction, represents the 4% uncertainty related to the number of* N_{POT}*, while the dark yellow the luminosity added to target atomic electron systematic.*

Figure 5.51 and Table 5.29 show the cross section measured in the 8 independent slices of ECAL, with the five methods. Despite the differences in performance of the various slices, the most relevant caused by local inefficiencies, the cross section measurement appear pretty stable and in agreement with the SM prediction within the measurement errors.

5.10.2 Run dependence

To study the stability of the result as a function of the pileup, beam background and time structure of the beam bunch, the cross section was measured separately in each run: for each sub-sample the average efficiency in the inner ring, the average efficiency in the outer ring and the yield of signal annihilation events were measured. The results on the efficiency measurements are reported in Table 5.30 and in Figure 5.52.

Table 5.30: *Number of tags N_{Tag}, number of probes N_{Probe} and TP efficiency ϵ with the error resulting from the statistical uncertainty on the tag and probe yield for each run analysed and for all statistic.*

Run number	N_{Tag}	N_{Probe}	ϵ
		Inner ring	
30369	71100 ± 1700	52340 ± 230	0.736 ± 0.018
30386	26010 ± 440	20540 ± 140	0.790 ± 0.014
30547	66490 ± 930	49150 ± 220	0.739 ± 0.011
30553	25100 ± 2000	18110 ± 140	0.720 ± 0.057
30563	55500 ± 3500	40370 ± 200	0.728 ± 0.046
30617	56700 ± 4400	41910 ± 210	0.740 ± 0.058
30624	61300 ± 3000	44040 ± 210	0.719 ± 0.035
All runs	365700 ± 4300	267370 ± 520	0.731 ± 0.009
		Outer ring	
30369	74900 ± 1100	52680 ± 230	0.703 ± 0.011
30386	27900 ± 1000	20630 ± 140	0.741 ± 0.028
30547	67100 ± 1800	49480 ± 220	0.737 ± 0.02
30553	26340 ± 880	18170 ± 140	0.690 ± 0.024
30563	56500 ± 1400	40590 ± 200	0.718 ± 0.018
30617	58000 ± 1800	41800 ± 200	0.721 ± 0.023
30624	63700 ± 1400	44360 ± 210	0.696 ± 0.016
All runs	375620 ± 3000	268100 ± 520	0.714 ± 0.006

The yield of annihilation events is obtained both with the usual two-photon selection, fitting the $\Delta\phi$ distribution, and with the single photon selection fitting the ΔE distribution. The annihilation yield corrected for the efficiency are reported in Table 5.31.

The so obtained cross section measurements are summarised in Table 5.32 and represented in Figure 5.53.

5.10.3 Systematics

The cross section measurement is heavily relying on the data-driven efficiency measurement. The latter exhibits a non trivial dependence on the sector of ECAL that can be ascribed to local defects but also to the uneven distribution of background in the detector. The systematic

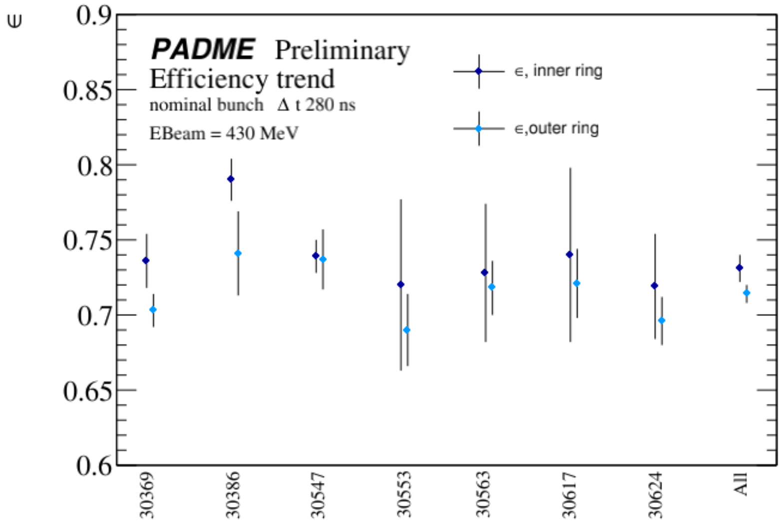

Figure 5.52: *Tag-and-probe efficiency for each analysed run and splitted in inner and outer FR ring. Only statistical errors are shown.*

Table 5.31: *Annihilation yield obtained for each analysed run and for all analysed runs.*

ϕ [Deg]	$N_{POT/10^{10}}$	$N^W_{\Delta\phi}$	$N^W_{\Delta E_{In}}$	$N^W_{\Delta E_{Out}}$
30369	8.2	105500 ± 3100	101800 ± 2900	101200 ± 2900
30386	2.8	36700 ± 1500	35300 ± 1500	35100 ± 1500
30547	7.1	94400 ± 3000	90800 ± 2800	90200 ± 2800
30553	2.8	38300 ± 3300	36600 ± 3100	36400 ± 3100
30563	6.0	80700 ± 5600	77600 ± 5200	77200 ± 5200
30617	6.1	81100 ± 6800	78300 ± 6600	78600 ± 6600
30624	6.6	91400 ± 5000	88600 ± 4700	88000 ± 4800
All	39.7	530100 ± 8200	513800 ± 7500	512100 ± 7300

uncertainty deriving from an imperfect accounting of these effects can be assessed looking at the differences in the annihilation yield corrected for the efficiency obtained in the different slices and summarised in Table 5.29. Each sector is independent from the others and the statistics of events in each slice is approximately the same, therefore one can look at how the eight measurements deviates from their average and establish whether there is any fluctuation in excess of the expected statistical contribution. Indeed, the cross sections estimated with all five methods fluctuate more than the statistical error on their average, leading to the indication of a systematic error. This has been quantitatively assessed with the following procedure. For the cross section based on the $\Delta\phi$ fit in two photon selection, the statistical error on the weighted average of the measurement obtained in the eight sectors, has been subtracted in quadrature from their root squared mean [99]. The result of this calculation is interpreted as

Table 5.32: *Cross section for the process $e^+e^- \to \gamma\gamma(\gamma)$ measured with the three methods (two-photon $\Delta\phi$ fit and single photon ΔE fit in the inner and outer ring measured in each analysed run. and all analysed runs.*

Run number	$\sigma_{\Delta\phi}$ [mb]	$\sigma_{\Delta E_{In}}$ [mb]	$\sigma_{\Delta E_{Out}}$ [mb]
30369	1.917 ± 0.056	1.848 ± 0.05	1.837 ± 0.052
30386	1.954 ± 0.081	1.880 ± 0.07	1.871 ± 0.077
30547	1.963 ± 0.062	1.887 ± 0.05	1.875 ± 0.057
30553	2.025 ± 0.176	1.934 ± 0.16	1.925 ± 0.165
30563	1.987 ± 0.137	1.911 ± 0.12	1.902 ± 0.129
30617	1.963 ± 0.166	1.896 ± 0.16	1.902 ± 0.160
30624	2.043 ± 0.111	1.980 ± 0.10	1.968 ± 0.107

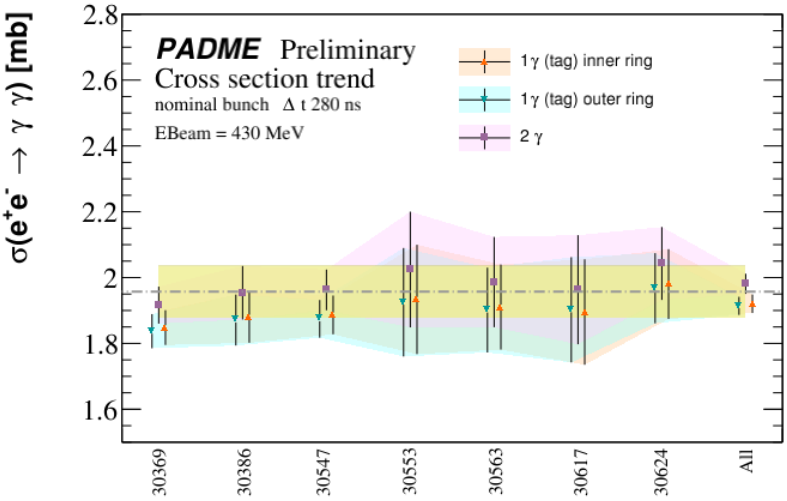

Figure 5.53: *Cross section for the process $e^+e^- \to \gamma\gamma(\gamma)$ measured with the three methods (two-photon $\Delta\phi$ fit and single photon ΔE fit in the inner and outer ring measured in each analysed run. The yellow band, around the theory prediction, represents the 4% uncertainty related to the number of N_{POT}, while the dark yellow the luminosity added to target atomic electron systematic.*

systematic error from the dis-uniformity in the efficiency for identifying annihilation photons. The procedure repeated for the cross sections $\sigma(\Delta\phi)$, $\sigma(\Delta E_{in})$, $\sigma(MM_{in})$ give consistent errors: 0.020 mb, 0.017 mb and 0.020 mb respectively. Therefore, the systematic error coming from detector and efficiency dis-uniformities is conservatively set to 0.021 mb.

Statistically independent samples can also be obtained by dividing the entire statistics by the run number. As discussed in Section 5.3.1 the runs used for this measurement have an average number of positrons per bunch that varies from 19000 to 36000; in addition, the time profile of the positron current in the bunch is not completely uniform. Since the amount of background impacts on the performance of the photon reconstruction and identification, the assumption of an efficiency averaged over the different runs may be incorrect. However, the fluctuations of the cross sections measured in each run are fully consistent with the statistical expectation, therefore no systematic error is assigned.

The background modelling, though the choice of the interpolating template, is another source of systematic uncertainty. It can be assessed comparing the results from the fit of the $\Delta\phi$ distribution, in the two-photon selection, with the result of the ΔE and M^2_{miss} distributions in the single photon selection applied to the inner ring of ECAL. In this case the measurements are obtained from the same sample. This is strictly true for the fit of the ΔE and M^2_{Miss} distributions, that are just different representations of the relationship between photon energy and polar angle. However, in the two photon selection used for the $\Delta\phi$ fit, the set of the most energetic photon in the pair is almost in complete overlap with the set of photons of the inner ring used for the ΔE and M^2_{Miss} fits. Therefore, the differences among all these measurements have only a systematic origin [99], to be ascribed, as anticipated, to the background modelling. Since there is no argument to prefer one of the three measurements, the central value is set to a simple average of the three. The systematic error is estimated as the root mean square of the three values multiplied by $\sqrt{3}$ in order to avoid the suppression factor that correctly describes the combination of measurements only in case of statistical independence. The procedure gives the error of 0.047 mb.

In addition, the difference between the cross section obtained in the single photon selection applied in the inner and outer rings must be considered. The two measurements are based on consistent, but experimentally different, definitions of the fiducial region, the first using the range $[R_{min}, R_{mid}]$ for the photon radial position, the second using the range $[R_{mid}, R_{max}]$. Therefore, the difference between the two measurements obtained from ΔE_{in} and ΔE_{out} can be considered as an indication of a systematic uncertainty on the acceptance. This has been assessed, again in the assumption of largely overlapping statistics, as the root mean square of the two values multiplied by $\sqrt{2}$. The same procedure applied to the comparison of $M^2_{Miss_{in}}$ and $M^2_{Miss_{out}}$ leads to a different result. A simple average of the two is assumed as a contribution to the systematic error on the acceptance. The result is $\sigma(\text{sys}_{\text{acc}_{\text{var}}}) = 0.011$ mb. In general, the acceptance is also affected by a theoretical error due to the missing NNLO contributions in Babayaga and to the uncertainty coming from the procedure matching the theory prediction at generator level to the experimental reconstruction and selection requirements. These errors are estimated to be negligible. The contribution that should be added to the acceptance systematics comes from the definition of the FR and fund to be equal to 1.16% (see also Section 5.5.1 and 5.5.2 and Table 5.5).

A separate source of error comes from the estimate of the number of positrons collected on target. A careful calibration of the Active Diamond Target response relative to the BGO calorimeter of the BTF and a study of the stability of the measurement of over the data set used for this analysis lead to an estimate of a relative error on N_{POT} equal to 4%. Finally the uncertainty on the thickness of the Active Diamond Target, estimated to be of the order of 1 μm, and on its density (0.6%) lead to a further contribution of the order of 0.020 mb.

Table 5.33 summarizes all the sources of systematic errors combined in quadrature in the measurement in Equation 5.21.

Table 5.33: *Systematic uncertainties of the measured annihilation cross section.*

Detector defects	0.020 mb
Background modelling	0.047 mb
Acceptance	0.025 mb
Luminosity	0.079 mb
Target atomic electron	0.020 mb

6 Dark photon search

The main role of the ECAL calorimeter is the detection of the ordinary photon produced in association with the dark photon A'. As described in Chapter 2, the technique used by PADME is based on the study of the missing mass distribution $M^2_{A'} = M^2_{miss} = (p_{e^+} + p_{e^-} - p_\gamma)^2$, which requires, in addition to a good knowledge of the beam energy, a reliable measurement of the energy and angle of the photon.

The signal search strategy may be a simple counting experiment, if candidate events are selected in a narrow window on M^2_{miss}, around the value corresponding to the A' mass hypothesis under test. The expected number of background events is large, therefore the Gaussian statistic can be used. As a consequence, following the approach adopted in the first PADME sensitivity study [75], to be able to constrain the effective coupling of the A' with a 68% confidence level the number of events observed in such M^2_{miss} interval must not exceed the expected background by an amount Δ, such that $\Delta/\sqrt{N_{bkg}} > 0.47$.

As discussed in Chapter 2.4, the number of signal events $e^+e^- \to \gamma A'$ can be expressed as:

$$N_{sig} = \epsilon^2 \delta \sigma(e^+e^- \to \gamma\gamma) N_{POT} \epsilon_{sig} N_{e/S} \tag{6.1}$$

where

- ϵ is the effective coupling of A' to the photon;
- δ (see Table 2.3) is the kinematic factor defined as the ratio of the signal cross section to the SM cross section of the annihilation in two photons $\sigma(e^+e^- \to \gamma\gamma)$;
- $\sigma(e^+e^- \to \gamma\gamma)$ is the two-photon annihilation cross section (1.96 mb for a beam energy of 430 MeV at NLO, according to Babayaga);
- N_{POT} is the number of positrons collected on target;
- ϵ_{sig} is the efficiency for the A' signal, which can be decomposed in several terms: acceptance, photon efficiency, efficiency of the selection cuts and efficiency for the signal of the veto cuts
$$\epsilon_{sig} = \epsilon^{sel}_\gamma \times A \times \epsilon_\gamma \times \epsilon^{veto}_{sig}; \tag{6.2}$$
- and $N_{e/S} = 0.0105$ b^{-1} is the number of electrons of the target per unit surface.

Hence, if no excess is observed in data with respect to the SM prediction, for any given A' mass hypothesis, values of the coupling ϵ^2 such that

$$\epsilon^2 > 0.47\sqrt{N_{Bkg}}/(\delta\sigma(e^+e^- \to \gamma\gamma)N_{POT}\epsilon_{sig}N_{e/S}) \tag{6.3}$$

can be excluded at the confidence level of 68%. With this formula, the physics reach of PADME with the RunII data is assessed.

6.0.1 Data sample, simulation, reconstruction and pre-selection

The data set used for the dark photon analysis is composed by the seven runs analysed for the annihilation cross section measurement, described in Section 5.3.1.

A simulation of the new physics process allows to estimate the acceptance and efficiency of the PADME detector and of the selection cuts. This is done in the PADME MC as described in Section 2.2.5. Several MC samples of 10^6 pure $e^+e^- \to \gamma A'$ events were simulated with different values of the dark photon mass in the range $[2.5\ \text{MeV}, 17.5\ \text{MeV}]$ with a step of 2.5 MeV. In Table 6.1 the statistic of the simulated A' samples for different masses is reported.

Table 6.1: *Simulated dark photon samples.*

$M_{A'}$ MeV	$N_{ev}/10^6$	$N_{POT}/10^{15}$ ($\epsilon = 10^{-3}$)
2.5	1	3.07
5	1	3.07
7.5	1	2.80
10	1	2.57
12.5	1	2.03
15	1	1.54
17.5	1	1.05

Photons are reconstructed in ECAL with the same algorithms described in the previous chapters; in particular the multi-hit reconstruction of hits in ECAL is adopted.

The other detectors involved are PVeto and SAC where the multi-hit reconstruction is based on ROOT tools (TSpectrum Peak Finder [100]) and requires a minimum peak amplitude, 20 mV for PVeto and 40 mV for the SAC. The clusterization algorithm, used to merge hits and build clusters, is analogous to the one described for the ECAL detector in Section 4.3. A few differences exist in the clusterization parameters:

- for the PVeto an energy higher than 0.1 MeV is required for seed and hits. The hits are merged to the seed if they are close in time within 4 ns and in space ΔChannelID ≤ 2;
- for the SAC, the cluster seed is required to have energy higher than 3 MeV while the other hits must have energy above 2 MeV. Hits are merged to the seed if they are close in time within 1 ns and in space $\Delta Cell \leq 2$.

Also for this analysis, event pre-selection cuts and ECAL cluster quality cuts were applied. The cuts are described in Section 5.9.2. In addition, ECAL clusters are considered candidate partners of an A' produced in e^+e^- annihilation if they have energy higher than 90 MeV and a radial position in the range $[115.82\text{ mm}, 258\text{ mm}]$. These are the same kinematic features of photons used for the annihilation cross section measurement and, therefore, the efficiency estimated with the tag-and-probe technique for annihilation photons may be considered a reasonable approximation for the identification efficiency of signal photons. As a consequence of this pre-selection, the A' mass range reach is limited. In Figure 6.1 the squared missing mass M^2_{miss} is reported for all ECAL photons, for ECAL photons passing the FR cut, and for ECAL photons passing also the energy threshold cut. Since $M^2_{miss} \leq 300$ MeV, the maximum mass that can be probed in this analysis is 15 MeV.

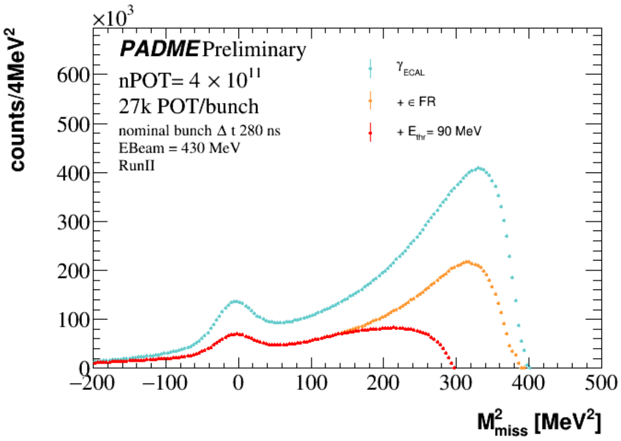

Figure 6.1: *Squared missing mass from RunII data for all clusters recorded in ECAL in azure, for clusters that pass the FR request in orange and for those that pass also the energy threshold cut in red.*

6.0.2 Rejection of the physical background processes

In an experiment with negligible non-collision background, as assumed in the PADME proposal, the main sources of background are the Bremsstrahlung and the annihilation in two and three photons, as described in Section 2.3.2. In the following, this scenario was assumed and a rejection strategy for the electromagnetic background processes was described. However, it will be shown that, since the beam induced background is not at all negligible, the only cut useful to reject the physical background is the veto of two-photon annihilation events.

Annihilation in two photons

The two-photon signature was deeply discussed in the previous sections. The rejection of this background was done requiring that no other photon with energy higher than 90 MeV and in time coincidence within 4 ns (~ 3 times the ECAL time resolution observed in the two-photon time correlation) exist in ECAL.

Bremsstrahlung rejection

A photon revealed in ECAL might be originated from a Bremsstrahlung interaction. In this case, a low energy positron in time coincidence should be detected in the PVeto and the sum of the energies of photon and positron should be compatible with the beam energy.

The distribution of the difference in time between a candidate signal photon and any cluster observed in the PVeto is shown in Figure 6.2. A peak with a Gaussian width of 2.2 ns emerges over a triangular background, due to uncorrelated particles uniformly distributed within the time window of the beam bunch. Based on the width of this Gaussian distribution, the time coincidence cut was set to $2 \times \sigma \sim 5$ ns. For a signal photon candidate in ECAL and a positron in time coincidence, Figure 6.3 shows the energy of the photon and the number of the PVeto channel ID where the positron is detected. This number increases with the kinetic energy of the positron, therefore, for bremsstrahlung processes, a low photon energy corresponds to a high PVeto channel and vice versa. In the plot, it is possible to observe the correlation typical of Bremsstrahlung events on top of a large background. The positron energy can be obtained from the calibration curve of the PVeto as explained in Section 2.2.3. After that, the quantity $\Delta E_{brem-veto} = E_{\gamma}^{ECAL} + E_{e^+}^{PVeto} - E_{beam}$, that is expected to be zero in Bremsstrahlung interactions, can be used to identify and veto the fraction of candidates with an in time positron compatible with the Bremsstrahlung process. To define a cut on this variable, the correlation between the energy of the photons (with $E_\gamma > 90$ MeV) and positrons (reconstructed as a PVeto cluster with seed in the range [20, 70] of the PVeto channel ID) that pass the time coincidence of 1 ns is shown in Figure 6.4. The red line corresponds to the condition $E_\gamma + E_{e^+} = E_{beam}$ MeV and, since it overlaps the signal from Bremsstrahlung events, the requirement $|\Delta E_{brem-veto}| < 50$ MeV can be used, thus tagging as Bremsstrahlung events those in between the two dotted lines in Figure 6.4.

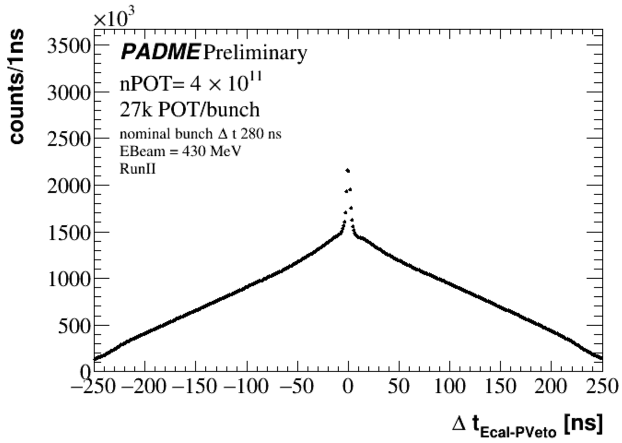

Figure 6.2: *Difference in time between the ECAL clusters and PVeto clusters from RunII data for ECAL cluster energy higher than* 90 MeV*, inside the FR and passing the two-photon annihilation veto.*

However, Figure 6.3 shows a huge background component, which is due to signals in accidental coincidence but also to a large component of photon-positron in time background. The

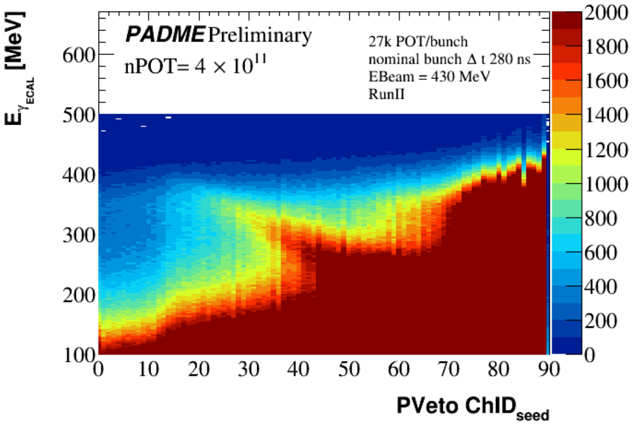

Figure 6.3: *Energy of signal photon candidates in ECAL as a function of the PVeto cluster seed channel ID in time coincidence within* 5 ns.

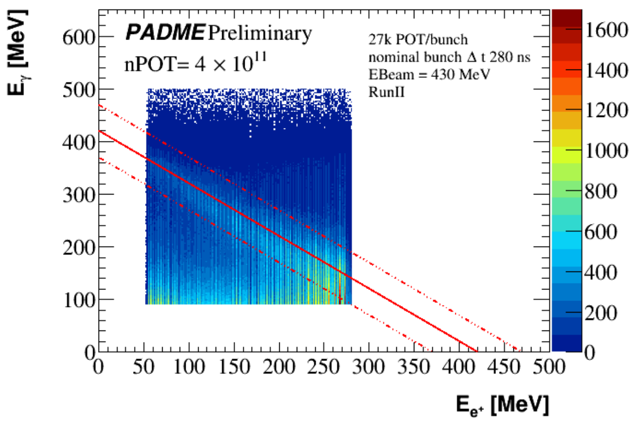

Figure 6.4: *Correlation between the energy of an ECAL photon with* $E_\gamma > 90$ MeV *and the energy of a positron detected as a PVeto cluster with seed in the channel ID range* $[20, 70]$*. Photon and positron are in time coincidence within* 1 ns*. The red solid line corresponds to* $E_\gamma + E_{e^+} = E_{beam}$*, while the dotted lines represent an interval of* ±50 MeV *around the solid line corresponding to the Bremsstrahlung veto cut.*

latter can be confirmed looking at no-target data. In Figure 6.5 the difference in time between a photon and a positron (reconstructed as a PVeto cluster with seed in the channel ID range [20, 70]) is shown before and after applying a shift to the photon time. Figure (a) shows the variable for a standard run and (b) refers to data collected with the target out of the beam line. As anticipated, in time positrons and photons are observed also in a pure background data set. Therefore, the cut designed to veto Bremsstrahlung will reduce also this kind of background, as well as photons in accidental coincidence with clusters in the PVeto.

Figure 6.6 shows the energy correlation between positrons in the PVeto and ECAL candidate signal photons falling in the FR in time coincidence. It is possible to notice how the

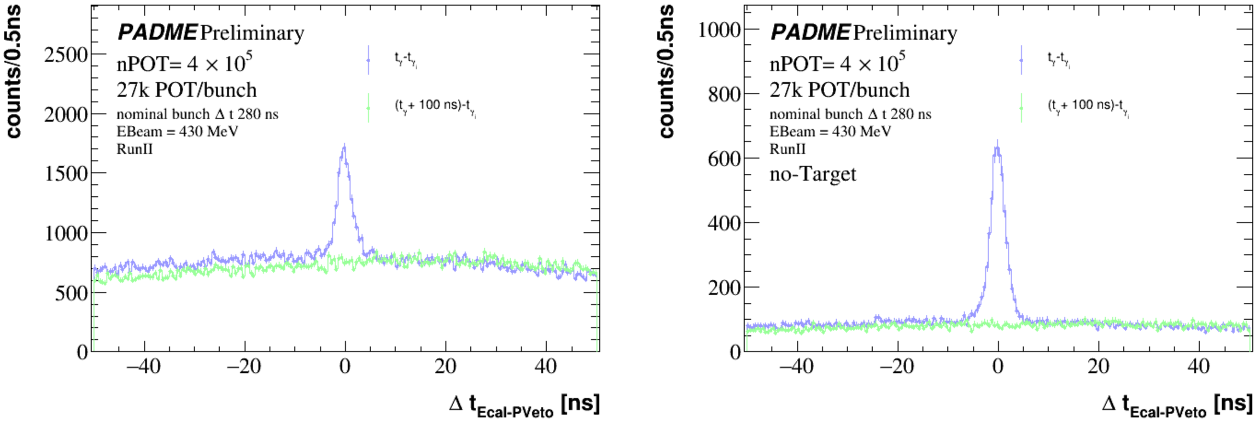

(a) (b)

Figure 6.5: *Difference in time between an ECAL photon and a PVeto positron with cluster seed in the channel ID range* [20, 70]*. The distribution in green represents the same distribution after shifting the photon time by* 100 ns*. The distributions are reported both for (a) data with the target in the beam line and (b) data with the target out of the beam line.*

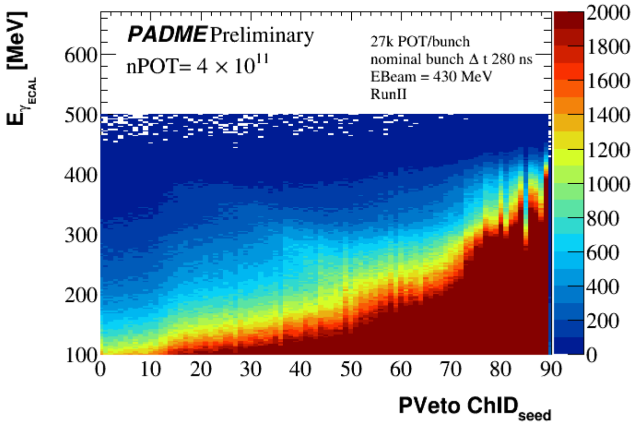

Figure 6.6: *Energy of signal photon candidates in ECAL as a function of the PVeto positron cluster seed channel ID in time coincidence within* 5 ns*.*

Bremsstrahlung signature is basically masked by the large beam induced background.

$\gamma\gamma\gamma$ rejection

The last kind of physical background is the annihilation in three photons. If all the three photons fall in ECAL, this background is rejected by the two-photon annihilation veto by releasing the energy thresholds on the second photon. However, this process may also lead to a final state with only one photon in ECAL. This configuration might be identified looking for an in time energy release in SAC, related to one or more photons. To reject this background a time coincidence is required between the ECAL photon and a cluster in the SAC. Since the SAC has an energy resolution of 50 MeV, only SAC clusters with energy above 50 MeV are considered.

To estimate the frequency of these kind of events, the sample of $e^+e^- \to \gamma\gamma(\gamma)$ events generated with Babayaga was fed to the PADME simulation without pileup (see Section 5.3.2). The N' number of reconstructed events that satisfy the following requests: one photon in the ECAL FR with $E_\gamma > 90$ MeV and at least one photon in the SAC with $E_\gamma > 50^{SAC}$ MeV was estimated to be equal to 0.2% of the total number of annihilation events. Therefore, this turns out to be a tiny source of background.

To define the time coincidence window the difference in time between the photon recorded in ECAL and in the SAC is shown in Figure 6.7 (a). A peak with a Gaussian width of ~ 7 ns can be observed on top of a triangular background distribution; therefore, a time coincidence of $2\sigma \sim 14$ ns is chosen. However, for events that pass the $\gamma\gamma$ and Bremsstrahlung veto cut, the peak disappears, as shown in Figure 6.7 (b). This effect is due to the frequent coincidence PVeto - SAC induced by very forward Bremsstrahlung positrons. Figure 6.8 shows the correlation between $\Delta t_{ECAL-PVeto}$ and $\Delta t_{ECAL-SAC}$. Events clustering around $\Delta t_{ECAL-PVeto} \simeq 0$ ns include Bremsstrahlung processes with the photon in ECAL, events clustering on the line at $\Delta t_{ECAL-SAC} \simeq 0$ ns are compatible with annihilation in three photons. Finally, a strong diagonal correlation is observed, that can be ascribed to Bremsstrahlung processes with the photon in the SAC. From the plot it is clear that the cut designed to veto Bremsstrahlung in ECAL depletes the distribution of Δt between ECAL and SAC photons around zero.

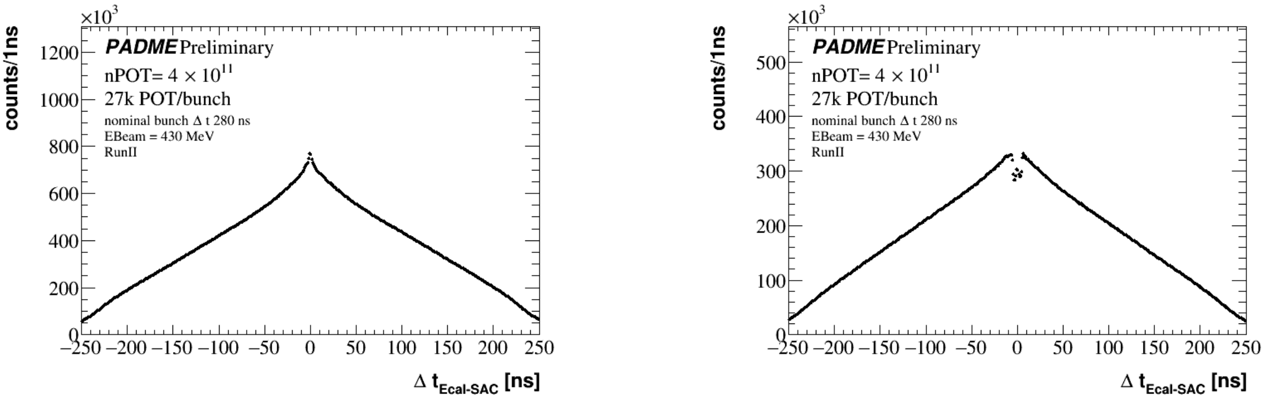

(a) **(b)**

Figure 6.7: *Difference in time between ECAL photons and SAC photons with energy higher than* 50 MeV *that pass the* $\gamma\gamma$ *veto only (a) and also the Bremsstrahlung veto (b).*

Since the Bremsstrahlung veto masks any physical correlation between ECAL and SAC, removing any evidence for three photon events, no veto will be applied against this physical background.

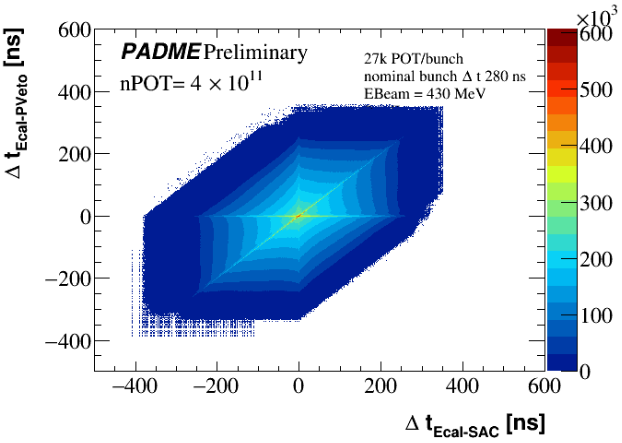

Figure 6.8: *Scatter plot of the difference in time between photons in ECAL and positrons in PVeto and the difference in time between photons in ECAL and photons in SAC with energy higher than* 50 MeV*.*

6.0.3 A' kinematic cuts

Others considerations can be done studying the kinematics of the photon produced along with the dark photon. In particular, the allowed photon energy range for each mass and the correlation between the energy and the photon radial position are distinctive features of the signal.

For each A' mass hypothesis, the distribution of the photon energy in ECAL, as reconstructed in simulation, is shown in Figure 6.9 (a). A minimum and maximum value for the energy can be identify for each A' mass. Figure 6.9 (b) shows the correlation between the energy of the photon and its radial position for three A' mass hypotheses observed in MC.

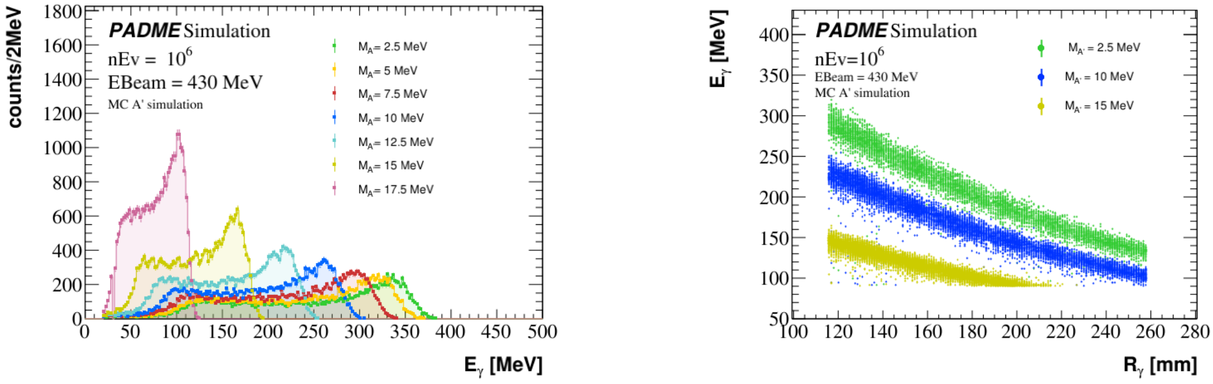

(a) **(b)**

Figure 6.9: *(a) Simulated photon energy distribution for A' mass hypothesis from* 2.5 MeV *to* 17.5 MeV*. (b) Simulated correlation between the energy of the photon and its radial position for A' mass hypotheses $M_{A'} = 2.5$ MeV in green, $M_{A'} = 10$ MeV in blue and $M_{A'} = 15$ MeV in orange. In (b) the photons are required to pass the energy threshold of* 90 MeV *and to be inside the ECAL.*

From these distributions the function $E(R_\gamma, M_{A'})$ is extracted in order to consider the cut $|\Delta E| = |ECAL_\gamma - E(R_\gamma, M_{A'})| < 30$ MeV, where 30 MeV is about 3σ of the ΔE distribution evaluated from A' simulations. In Figure 6.10 the M^2_{miss} spectrum is shown for photons passing the two-photon annihilation veto, the energy range requirement for the mass hypothesis of 10 MeV and the energy-position correlation requirement for the same mass hypothesis. These cuts are not helpful to reject background, since they just reduce the sidebands of the squared missing mass distribution.

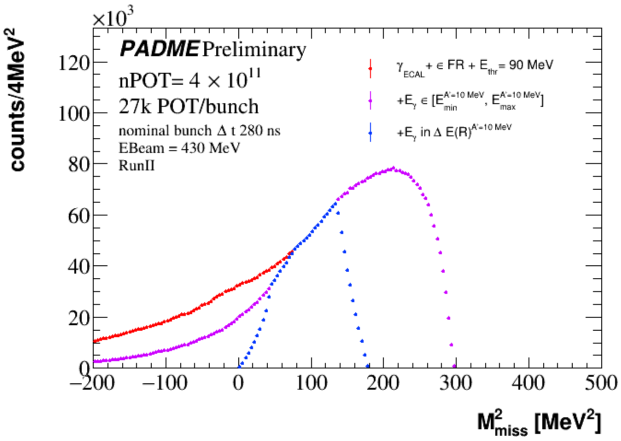

Figure 6.10: *Squared missing mass distribution from RunII data for events that pass the* $\gamma\gamma$ *veto in red, the energy range requirement for* $M_{A'} = 10$ MeV *in pink and the correlation between the energy and the radial position for the same mass hypothesis.*

6.0.4 Selection cut flow

The distributions of the squared missing mass in the selected RunII data set are shown in Figure 6.11 (a) applying sequentially the previously described selection cuts: starting with photons with energy higher than 90 MeV inside the FR, later applying the two-photon veto, the Bremsstrahlung veto and, eventually, the three-photon annihilation veto.

The Bremsstrahlung veto rejects candidate events more than the expectation. This is a consequence of the beam background contaminating the selection of Bremsstrahlung events.

In Figure 6.11 (b) the M^2_{miss} distributions are shown for A' simulated without pileup for several mass hypotheses after the same selection applied in data.

In Table 6.2 the corresponding cut-flows for data and simulation ($M_{A'} = 10$ MeV) are reported.

6.0.5 Background determination

To estimate the background the number of photons falling in the signal region for each mass hypothesis were counted. The boundaries of the signal region are defined using A' simulated

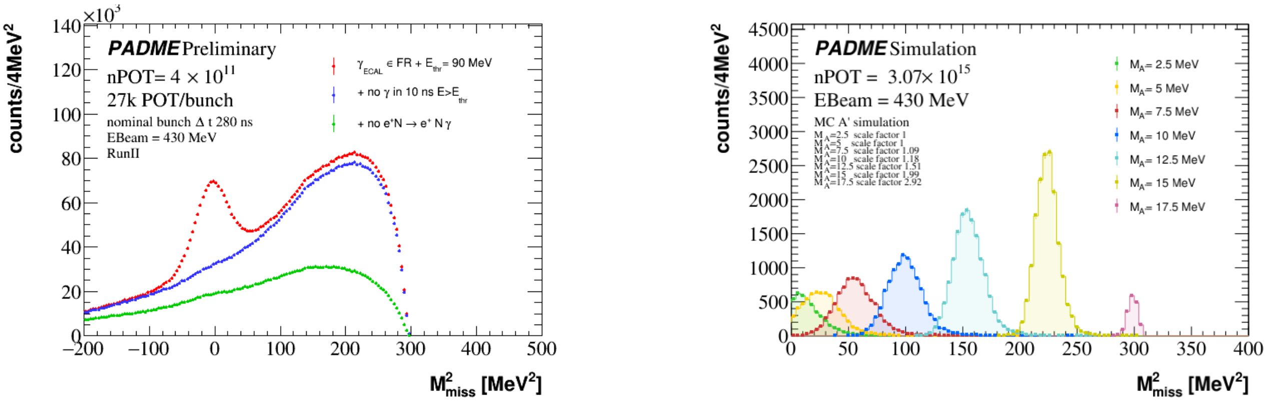

(a) **(b)**

Figure 6.11: *Squared missing mass of photons that pass the veto cuts for RunII data (a) and for signal simulated at different A' masses without pileup (b).*

Table 6.2: *Selection criteria and number of photons passing the cuts in 10^6 simulated dark photon events with $M_{A'} = 10$ MeV and in RunII data.*

		N_γ	
		simulation $M_{A'} = 10$ MeV	data
Selection	N_{POT}	2.6×10^{15}	4×10^{11}
	All photons	19631	2.4×10^7
	Photons in FR	9245	1.2×10^7
	$E_g > 90$ MeV	9213	6.4×10^6
Veto	no other photons with $E > 90$ MeV in 4 ns	9213	5.5×10^6
	no e^+ in $\|\Delta t\| < 5$ ns and $\|\Delta E\| < 50$ MeV	9213	2.6×10^6

samples according to a Gaussian fit to the squared missing mass distribution allowing to define a two sigma interval around the peak: $[M^2_{miss} - 2\sigma_{M^2_{miss}}, M^2_{miss} + 2\sigma_{M^2_{miss}}]$.

The squared missing mass distribution in data does not hint to any localised excess with respect to the smooth background therefore, the number of signal events in the signal region are assumed to be negligible and constraints on the signal can be derived. The distribution was then fit with a polynomial. From this fit the number of background events in the signal region was counted. In Figure 6.12 an example of the procedure for $M_{A'} = 10$ MeV is shown.

The procedure was applied to each mass hypothesis and for each veto cut. The number of background events estimated with this procedure in the signal region for each mass points is shown in Figure 6.13.

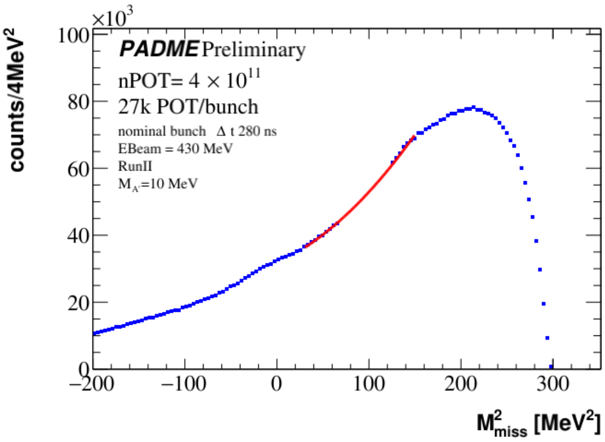

Figure 6.12: *Interpolation (red line) to estimate the background from the squared missing mass distribution in RunII data for a dark photon search of* $M_{A'} = 10$ MeV*.*

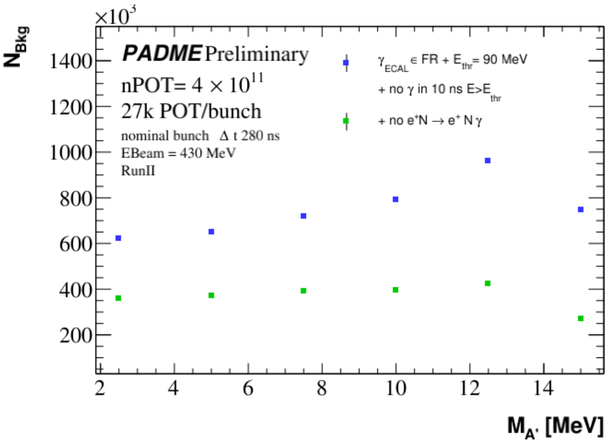

Figure 6.13: *Number of background photons passing the signal selection and the two-photon annihilation veto in blue and the number of background photons passing also the Bremsstrahlung veto in green.*

6.0.6 Acceptance and selection efficiency

To measure the A' acceptance and efficiency the factor $A \times \epsilon_\gamma^{sel} = \frac{N_s}{N_g}$ was measured on dark photon simulated samples. N_s corresponds to the number of photons that pass the selection and N_g is the number of $e^+e^- \to \gamma A'$ generated. In Figure 6.14 the signal acceptance times efficiency is reported for each A' mass hypothesis. Of course this kind of simulation, without pileup and other sources of background, cannot be used to estimate how many signal photons are rejected by the veto cuts. A different strategy, discussed in next section, must be adopted to assess the impact of the veto requirements on signal events.

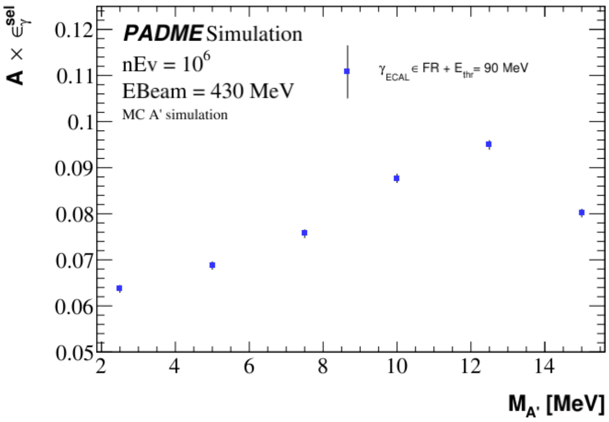

Figure 6.14: *Acceptance times selection efficiency, $A \times \epsilon_\gamma^{sel}$, as a function of the A' mass from a signal simulation with no pileup and background.*

6.0.7 Signal efficiency of the veto conditions

The requirements designed to veto the background processes induce an inefficiency for the signal. This would be a negligible effect in the absence of pileup of interactions occurring in the same bunch. However, this is clearly not the case in PADME, due to the high number of positrons per bunch, leading to the expectation of a few interactions (Bremsstrahlung, Bhabha scattering, annihilation in photons) taking place in the same bunch and possibly happening in time coincidence. In addition, as already discussed, PADME suffers from a not negligible level of background related to particles in the beam halo interacting with the materials of the beam line and of the experiment. For this reason, there is a high probability that veto cuts reject signal photons. To estimate the accidental coincidence of a candidate signal photon with a second photon, mimicking an annihilation process that satisfies the veto condition, or with a positron, mimicking a Bremsstrahlung process, the following procedure was applied. The time of the candidate signal photon was shifted of 100 ns (and subtracted of the bunch length when exceeding the upper boundary of the bunch time interval) before applying the veto cut. This is equivalent to decorrelate in time the photon with respect to the other particles. Thus the efficiency for the signal of the veto cut was evaluated as:

$$\epsilon_{sig}^{veto} = 1 - \frac{N'}{N} \tag{6.4}$$

where N is the number of photons passing all previous selection (and veto) requirements and N' is the number of photons that pass the veto requirement after being shifted in time. For example, in the case of the two-photon annihilation veto, N represents the number of photons that are inside the FR with an energy higher than 90 MeV and N' corresponds to the number of those which, after being shifted in time, happen to be in coincidence within 4 ns with another ECAL cluster in the FR with$E > 90$ MeV. Figure 6.15 shows the difference in time between a candidate signal photon and any other photon satisfying the energy and position requirements, before and after shifting the time of the candidate. From the plot, one can see that the veto cut

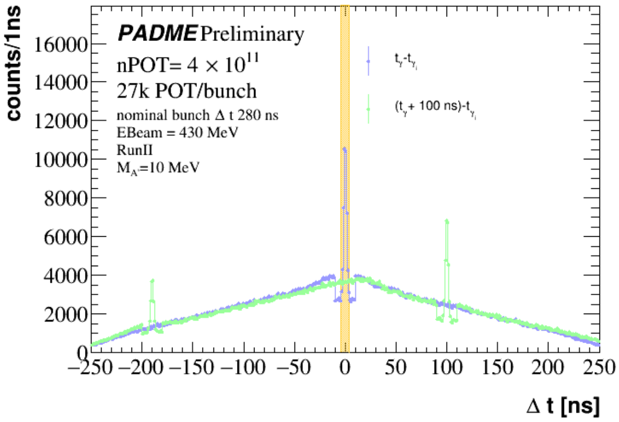

Figure 6.15: *Distribution of the time difference between two clusters in ECAL from RunII data when the first photon passes the energy and radial FR requests in azure. In green the same distribution is shown when to the first photon is applied a* 100 ns *time shift. The yellow vertical band represents the time coincidence window.*

applied when the time is shifted rejects signal candidate photons in accidental coincidence with uncorrelated ECAL photons, from other physics processes or, most likely, from beam induced background.

The same procedure was applied to measure the veto efficiency for the Bremsstrahlung veto cut. In Figure 6.16 the efficiencies of the two veto conditions for signal photons are reported as a function of the A' mass hypothesis. While the annihilation veto reduces the number of signal photons only by a few percent, the Bremsstrahlung veto leads to a large inefficiency due to the very high occupancy of the PVeto detector.

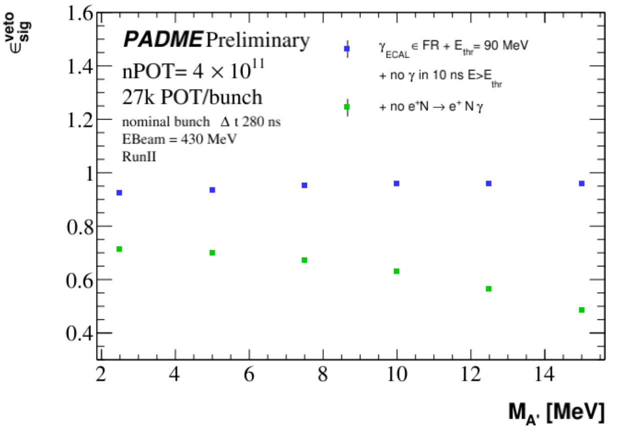

Figure 6.16: *Efficiency of the veto conditions for signal photons as a function of the A' mass hypothesis: in blue the annihilation veto and in green the Bremsstrahlung veto.*

6.0.8 Results and prospectives

Since no evidence for any localized excess is seen in the data, a first assessment of the limits, at the confidence level of 68%, on the ϵ parameter has been derived for different values of the A' mass using Equation 6.3. The result is shown in Figure 6.17 for two analysis strategies: the first vetoing only the process of annihilation in two photons, the second one vetoing also Bremsstrahlung interactions. Despite a large reduction of the background observed when the Bremsstrahlung is applied (see Figure 6.1 (a)), the limits become worse. This is due to signal inefficiency introduced by the veto. Indeed background and signal are reduced at the same rate by this veto requirement, hence the limit on ϵ^2 becomes worse for a factor $1/\sqrt{\epsilon_{veto}}$.

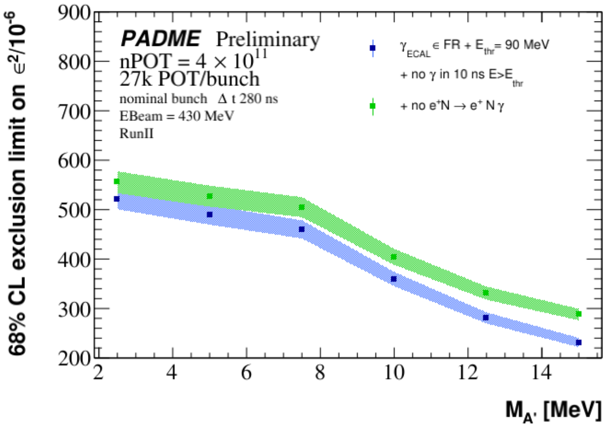

Figure 6.17: *Limits at 68% C.L. on ϵ^2 as a function of the A' mass hypothesis and for different vetoes conditions, obtained counting events in $\pm 2\sigma$ around the peak position of M^2_{miss}: limits in blue are obtained after applying the two-photon veto while the band of limits in green is obtained after applying both two-photon and Bremsstrahlung veto.*

For this reason the preliminary assessment of the limits was done by applying only the veto for annihilation in two photons and neglecting systematic uncertainties.

Figure 6.18 shows the limits derived with the data analysed so far and the projection to the full RunII data set of $N_{POT} = 5 \times 10^{12}$, under the assumption that the remaining data feature the same quality of the seven runs analysed in this thesis. In addition, in Figure 6.18 the projection to the statistics of $N_{POT} = 4 \times 10^{13}$, assumed in the PADME proposal, is reported. The limits are a factor $\sim$ 20 worse than the limits anticipated (see Figure 1.11 (b)). This result is a consequence of the unexpected huge beam background. With the current quality of data calibration and reconstruction, the beam related background cannot be rejected and, in addition, it is responsible for a strong contamination of the selections of physical backgrounds other than two-photon annihilation events. Therefore, any veto condition designed to reject Bremsstrahlung or $e^+e^- \to \gamma\gamma\gamma$ introduces a sizeable inefficiency for signal photons leading to a degradation of the sensitivity.

This first study allows to identify the main difficulties that must be faced in order to approach the design sensitivity of the experiment. Work is ongoing in the collaboration to

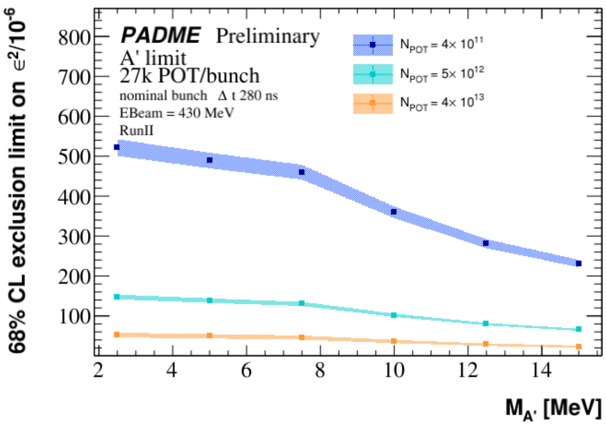

Figure 6.18: *Limits at 68% C.L. on ϵ^2 as a function of the A' hypothesis mass obtained counting events in $\pm 2\sigma$ around the expected peak position of M^2_{miss}. In blue the limits obtained with the analysed RunII runs ($N_{POT} = 4 \times 10^{11}$). In azure the limits extrapolated to the full RunII statistics ($N_{POT} = 5 \times 10^{12}$) and in orange the limits extrapolated to the statistics of $N_{POT} = 4 \times 10^{13}$ anticipated in the PADME proposal [75].*

improve the reconstruction of positrons in the PVeto and to achieve a precise calibration in time and in energy of all detectors. These actions will allow to reduce the inefficiency for the signal of background veto conditions. Further dedicated studies of background data collected with the target out of the beam line may lead to define a strategy for the suppression of the beam background in data.

Conclusions

During my Ph.D. I worked actively for the PADME experiment, I participated in the construction of the main calorimeter, which is the key detector for the dark photon search, I developed the software to simulate, reconstruct and analyse the data of PADME and I participated in person and remotely at all the data taking periods of the experiment. The active participation in all aspects of PADME makes me deeply understand the experimental and data analysis implications of the dark photon search at accelerators.

My analysis of the data collected in RunI and of the simulation allowed to understand the main sources of background. The data collected with the secondary positron beam, which was initially used, were shown to be heavily contaminated by a diffuse background. While the situation is much improved with a primary positron beam, still an important residual background arises from interactions of positrons in the tail of the beam hitting materials of the beam line and from the resulting secondary particles. A major source of this beam related background was the Beryllium window separating the LINAC vacuum from the PADME vacuum. In order to reduce the background level in the experiment, the Beryllium window was replaced with a Mylar window and further shielding was achieved with new collimators. A study was conducted to understand the impact of pileup on the calorimeter reconstruction. The rate of annihilation in two photons events was measured as a function of the bunch density, showing that a density of positron in the bunch exceeding 100 e^+/ns leads to a reconstruction efficiency loss. All this work guided the choice of the beam conditions of RunII, producing an improvement in the detection of the two main SM physics processes: Bremsstrahlung and annihilation in two photons.

The unexpected background level was faced by this thesis work improving the ECAL reconstruction going from single-hit to multi-hit per event. An innovative idea was developed using a template fit of the signal waveforms to identify up to three hits per channel. The algorithm is stable and robust against problems like the limited acquisition time window and signal saturation. The reconstruction was tested on a special run collected with a single positron per bunch that I required for this purpose during RunI. The results show that this new technique is able to reconstruct up to eight positrons per bunch (the single-hit reconstruction identifies at most four), and the frequency of the various multiplicity is nicely described by a Poisson distribution with mean close to one as expected. The features of the multi-hit reconstruction logic need to be taken into account in the simulation. Therefore, I implemented a digitisation of the Geant 4 hits in the ECAL crystals which emulates the resolution of the reconstruction and I also introduced a complete emulation of digital waveforms to be processed with exactly the same software used for data.

The main achievement of this thesis is the measurement of the cross section for the QED process $e^+e^- \to \gamma\gamma(\gamma)$. This is a crucial step toward the dark photon search using the main calorimeter. To do this the annihilation in two photons was deeply studied using CalcHEP and Babayaga generators before using data. I used them to extract the acceptance and to define the radial photon Fiducial Region (FR). I obtained the annihilation yield with a two photons selection and also with one photon selection. Both were applied on data preselected with a careful check of the topological features of the clusters in ECAL. I designed and implemented an original method to determine the photon efficiency from data. Since there are no photon tagging detectors other than ECAL, the measurement of the efficiency was performed using the constrained kinematics of the annihilation in an ad-hoc variation of the tag and probe method. This strategy was tested on several MC samples simulated in different detector conditions, then applied to data obtaining a data driven efficiency measurement as a function of the radius and of the azimuthal angle. This was achieved through a fit of the data, with signal and background templates, the latter obtained from simulation and also from special background data, collected after removing the target from the beam line. I finally measured the cross section efficiency and considered several contributions to the systematic error. The final measurement of the e^+e^- annihilation cross section in two gammas at center of mass energy of 20.7 MeV is $\sigma(e^+e^- \to \gamma\gamma) = 1.955 \pm 0.028$ (stat) $\pm\, 0.054$ (syst) $\pm\, 0.020$ (target) $\pm\, 0.079$ (lumi) mb compatible with the NLO Babayaga prediction of 1.957 ± 0.005 mb.

I concluded this work, which is the first rigorous data analysis of PADME data, discussing the implications of the current data quality and understanding for the dark photon search. This is used to figure out the possible achievements of PADME in RunII and prepare the future plans. A critical step, both for the yield assessment and for the efficiency measurement, is the background subtraction.

Appendices

A Previous in-flight $e^+e^- \to \gamma\gamma$ cross section measurements

Several $e^+e^- \to \gamma\gamma$ cross section measurements in flight, at PADME energy scale with fixed target, were done in the second half of the 1950s. All the measurements were done only with disappearance techniques, counting the positron tracks disappearing in the target.

Only three measurements at low energies (from 100 MeV to 10 GeV incident positron energy) were done so far. The first ones were performed by Colgate and Gilbert in 1953 by attenuation measurements for 50, 100 and 200 MeV positron energies with a precision of 20% [101]. The second ones were performed by Malamud and Weill in 1963 by a bubble chamber for 600 MeV positron energy with a precision of about 4% [102].

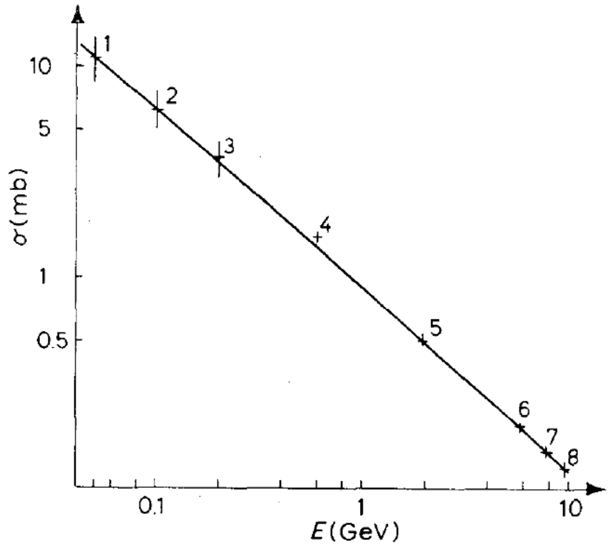

Figure A.1: *Positron-electron annihilation cross section as a function of positron energy. The solid line shows the theoretical predictions, the data points are measurements from Colgate and Gilbert [101], Malamud and Weill [102], Fabiani et al. [103]. For comparison the measurement of this thesis work is also shown with the big ref cross.*

Table A.1: *Positron-electron annihilation in two-photon cross section measurements.*

Positron energy [MeV]	Cross section [mb]	Reference
50	11.0 ± 2.5	[101]
100	6.3 ± 1.2	[101]
200	3.7 ± 0.6	[101]
600	$1.563 \pm 4.5\%$	[102]
1.94×10^3	0.520 ± 0.013	[103]
5.80×10^3	0.198 ± 0.006	[103]
7.71×10^3	0.154 ± 0.005	[103]
9.64×10^3	0.128 ± 0.007	[103]

The last low energy measurements were done by Fabiani et al. [103] in 1962 at CERN for energies of the positrons equal to 1.94, 5.80, 7.71, 9.64 GeV with an uncertainty better than 5%. All measurements are reported in Table A.1 and plotted in Figure A.1 together with the theoretical prediction at leading order.

A.0.1 $e^+e^- \to \gamma\gamma$ for E_{e^+} between 50 and 200 MeV

Colgate and Gilbert led their experiment in 1953 at the Radiation Laboratory at Berkeley. The main purpose of the experiment was to understand the electron and positron disappearance in flight. The main backgrounds of the positron annihilation were the ionisation loss, the Bremsstrahlung, multiple scattering and single large angle scattering. The backgrounds processes listed are common to positron and electron beams. For this reason runs with electron beams were planned to predict the background, while the annihilation cross section measurement were performed by positron beams.

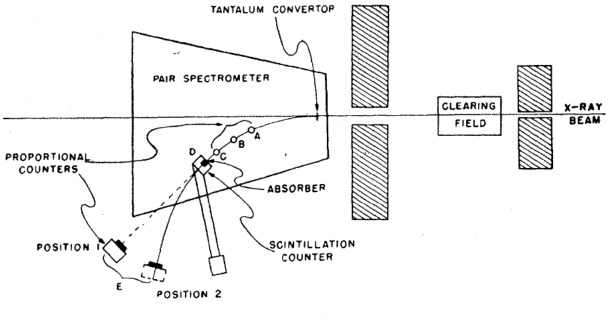

Figure A.2: *Experimental apparatus of Colgate and Gilbert for positron annihilation in-flight [101].*

In Figure A.2 is reported the experimental arrangement used. A gamma ray beam collided on a conversion target, then several proportional counters (A,B,C,D,E) were placed along the track that a particle of a specific charge would follow inside the magnetic field. The alignment of the proportional chambers was done optimising the rate of each one and maximising the coincidence rate between them. Inside the counter D an absorber can be inserted. A coincidence ABC defined the presence of a particle, while its disappearance was defined by an anti-coincidence in D. The particle loss rate is evaluated subtracting to ABC coincidence rates the ABCD coincidence rates.

A confirmation of the presence of a photon annihilation was done using the proportional counter E. The same counter placed in position 1 allowed to measure the efficiency of the D counter.

A.0.2 $e^+e^- \to \gamma\gamma$ measurement for $E_{e^+} = 600$ MeV

The measurement of the positron-electron annihilation in photons at 600 MeV is made at the Laboratoire de Recherches Nucleaires at Luisanne in 1963. The annihilation in two photons occurred in a propane-filled bubble chamber, placed inside a magnetic field of 7350 G. The positron beam entered in 15.24 cm diameter bubble chamber through a thin window consisting of $0.079X_0$ of duraluminium. A total of 50000 pictures were recorded and 575 positron-electron annihilation in photons events were founded in the fiducial region. The main background for the experiment is the Bremsstrahlung with photon taking a huge part of the primary energy.

A.0.3 $e^+e^- \to \gamma\gamma$ measurement for E_{e^+} between 2 and 10 GeV

These latest measurements were made at CERN in 1962 measuring the relative number of positrons of well-defined momentum, which disappear, in a thin beryllium target, under emission of photons of the appropriate energy. In Figure A.3 is reported a scheme of the experiment. The positron beam, after entering into the experimental area, pass through two scintillation counters 1 and 3 and a gas Cerenkov threshold counter 2, counting only positrons. In a volume

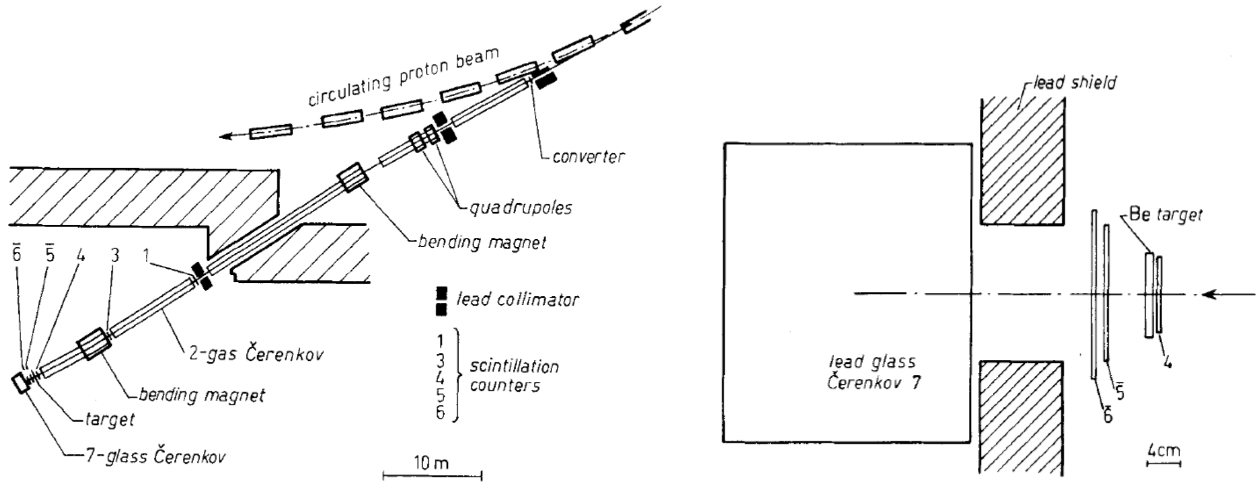

(a) (b)

Figure A.3: *(a) Beam line and experiment layout and (b) layout of the target region for in-flight annihilation measurement at CERN [103].*

of $9 \times 9 \times 0.2$ cm^3, a magnetic field was superimposed to bend the charged particles in the apparatus at point 4 followed by

- two anticoincidence counters 5 and 6, operating in parallel;
- lead-glass Cerenkov counter 7. The pulse-height from this counter is proportional to the total energy of all positrons, electrons and photons that arrive simultaneously.

Between 4 and 5 a target of low z could be inserted and a lead shield, 10 cm thick, was added to reduce the background related to the beam.

A beam particle was defined by 12347*, where 7* indicates that the output of counter 7 was required to be higher than a given threshold value. A positron-electron annihilation candidate was defined as $12347^*\bar{5}\bar{6}$ and the ratio $\frac{D}{B} = \frac{12347^*\bar{5}\bar{6}}{12347^*}$ was measured for runs with the target in the beam line and for the target out of the beam line. The measurements were repeated for an electron beam of the same energy and using Aluminium and Beryllium targets. The annihilation rate was extracted by:

$$R = \left[\left(\frac{D}{B}\right)^{+}_{in} - \left(\frac{D}{B}\right)^{+}_{out}\right] - \left[\left(\frac{D}{B}\right)^{-}_{in} - \left(\frac{D}{B}\right)^{-}_{out}\right] \tag{A.1}$$

where

- $\left(\frac{D}{B}\right)^{+}_{in}$ is measured with a positron beam and the target inside the beam line and it corresponds to the relative rate of two photons annihilations occurred in the target, in counter 4, in material between counter 4 and 5, and in counter 5 with a residual contamination of Bremsstrahlung;
- $\left(\frac{D}{B}\right)^{+}_{out}$ is measured with a positron beam and the target outside the beam line and it corresponds to the relative rate of two photons annihilations occurred in counter 4, in material between counter 4 and 5, and in counter 5 with a residual contamination of Bremsstrahlung;
- $\left(\frac{D}{B}\right)^{-}_{in}$ is measured using an electron beam and the target inside the beam line and it corresponds to the relative rate of the residual contamination of Bremsstrahlung;
- $\left(\frac{D}{B}\right)^{-}_{out}$ is measured using an electron beam and the target outside the beam line and it corresponds to the relative rate due to the anti-coincidence efficiency.

B

$e^+e^- \to \gamma\gamma$ measurement without cluster quality cuts

This appendix collects tables and plots showing the yield, the efficiency and the cross section derived by the same procedure described in Section 5.10 without applying quality cuts to the ECAL clusters.

The results appear consistent with those in section 5.10 but they are affected by much larger systematic offsets. The comparison with the baseline analysis demonstrates the benefit arising from the cluster selection discussed in 5.9.2.

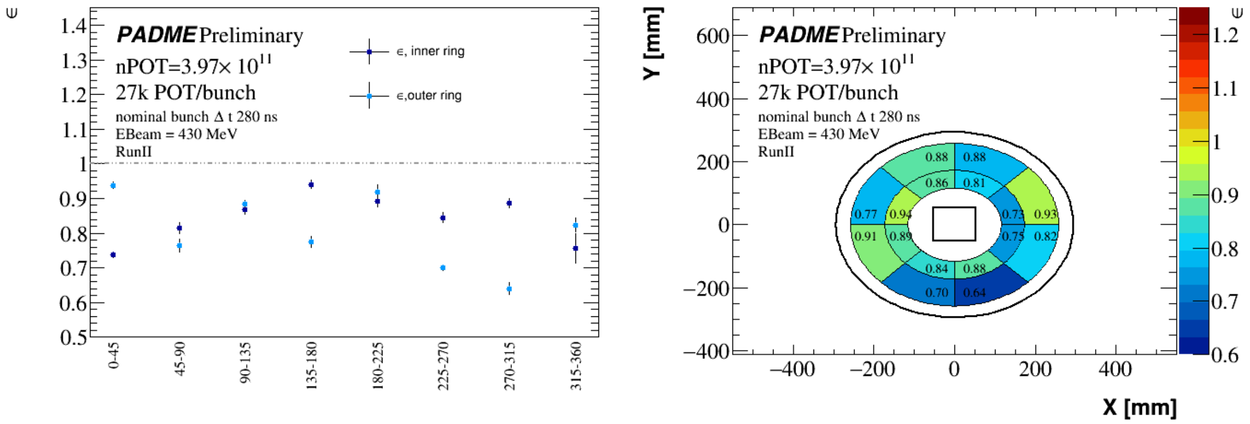

(a) (b)

Figure B.1: *(a): ECAL photon efficiency for 8 ϕ slices in the inner ring (blue) and outer ring (light blue) after beam multiplicity cuts; (b) ECAL photon efficiency map.*

Table B.1: *Number of tag N_{Tag} and its error ΔN_{Tag}, number of probe N_{Probe} and its error ΔN_{Probe} and the efficiency ϵ measured form the ratio of the probe over the tag yield with the error $\Delta\epsilon$ obtained applying the error propagation formula. The yields correspond to $N_{POT} = 4 \times 10^{11}$.*

ϕ [Deg]	N_{Tag}	ΔN_{Tag}	N_{Probe}	ΔN_{Probe}	ϵ	$\Delta\epsilon$
			Inner ring			
$[0, 45]$	62318	648	45968	214	0.738	0.008
$[45, 90]$	42433	816	34575	186	0.815	0.016
$[90, 135]$	37141	545	32266	180	0.869	0.014
$[135, 180]$	47867	580	45034	212	0.941	0.012
$[180, 225]$	53620	910	47780	219	0.891	0.016
$[225, 270]$	50830	813	42960	207	0.845	0.014
$[270, 315]$	46465	617	41207	203	0.887	0.013
$[315, 360]$	57955	337	43815	209	0.756	0.006
			Outer ring			
$[0, 45]$	48803	481	45787	214	0.938	0.01
$[45, 90]$	56531	1400	43167	208	0.764	0.019
$[90, 135]$	46797	457	41402	203	0.885	0.01
$[135, 180]$	57192	1084	44342	211	0.775	0.015
$[180, 225]$	51248	1078	47112	217	0.919	0.02
$[225, 270]$	51337	530	35982	190	0.701	0.008
$[270, 315]$	53048	1416	33954	184	0.640	0.017
$[315, 360]$	55798	1253	45976	214	0.824	0.019

Table B.2: *Cross sections measured with the yields of one tag in the inner ring, one tag in the outer ring and two photons as a function of the azimuthal angles. The cross sections are obtained with events that pass the beam multiplicity cut.*

ϕ [Deg]	$\sigma_{\Delta\phi}$ [mb]	σ_{TagIn} [mb]	σ_{TagOut} [mb]
$[0, 45]$	2.127 ± 0.051	2.104 ± 0.05	1.732 ± 0.035
$[45, 90]$	1.843 ± 0.043	1.908 ± 0.042	2.015 ± 0.06
$[90, 135]$	1.76 ± 0.055	1.849 ± 0.058	1.59 ± 0.028
$[135, 180]$	1.73 ± 0.045	1.796 ± 0.046	2.265 ± 0.046
$[180, 225]$	1.707 ± 0.036	1.659 ± 0.034	2.054 ± 0.05
$[225, 270]$	2.051 ± 0.061	2.027 ± 0.06	1.834 ± 0.041
$[270, 315]$	1.65 ± 0.033	1.598 ± 0.028	1.758 ± 0.053
$[315, 360]$	2.3 ± 0.048	2.292 ± 0.047	1.76 ± 0.046

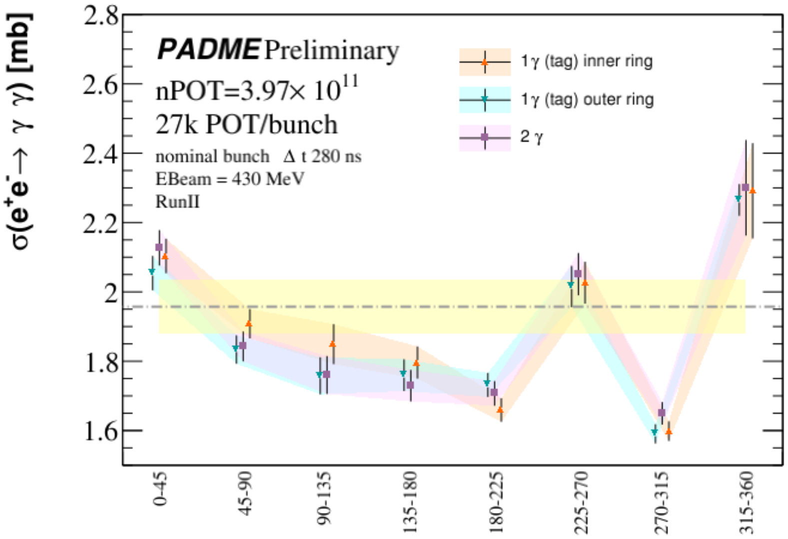

Figure B.2: *Measured cross section as a function of the 8 ϕ slices. The yellow band represents the uncertainty of* 4% *on the beam multiplicity measurement. The orange dots are measurements done with a tag in the inner ring, the azure dots with a tag in the outer ring, the violet dots with the two-photon analysis.*

C

Compendium of $e^+e^- \to \gamma\gamma$ analysis fits

In this appendix, the main variables for the two-photon annihilation process are shown. In particular, Figure C.1 shows the sum of the photon energies for all analysed runs and for each ϕ slice.

Afterwards, the fit used to extract efficiency and annihilation yield for all analysed runs and for each ϕ slice (Figures C.2, C.3, C.4, C.5, C.6) and for each analysed run (Figures C.9, C.10, C.11, C.12, C.13) are reported. Figures C.2 and C.9 show the polynomial plus Gaussian fit on $\Delta\phi$ variable. Figures C.3, C.5, C.10 and C.12 show the tag yield extraction fits for inner (Figures C.3, C.10) and outer (Figures C.5,C.12)radial range. The corresponding probe distributions, with the Gaussian fit superimposed, are shown in Figures C.4, C.6, C.11 and C.13. In addition, the fit squared missing mass distributions are reported for inner (Figure C.7) and outer (FigureC.8) ECAL ring.

Figure C.1: *Sum of the photon energies from annihilation event candidate for each ϕ slice.*

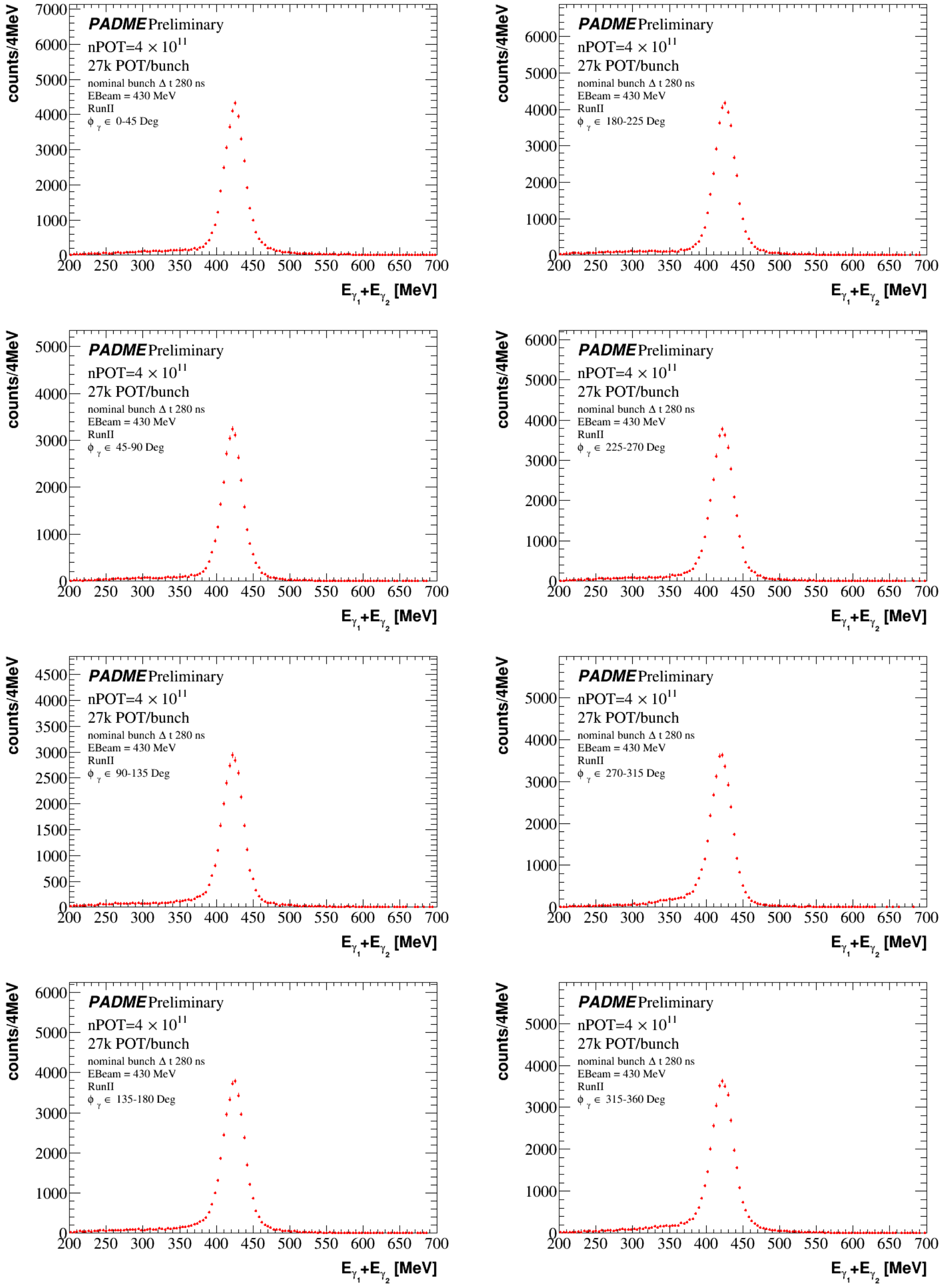

Figure C.2: *Azimuthal angle difference of two photons from annihilation event candidates for each ϕ slice whit the total fit superimposed (black line). The red line is the background component of the fit. The yields extracted from the fits are reported in Table 5.21.*

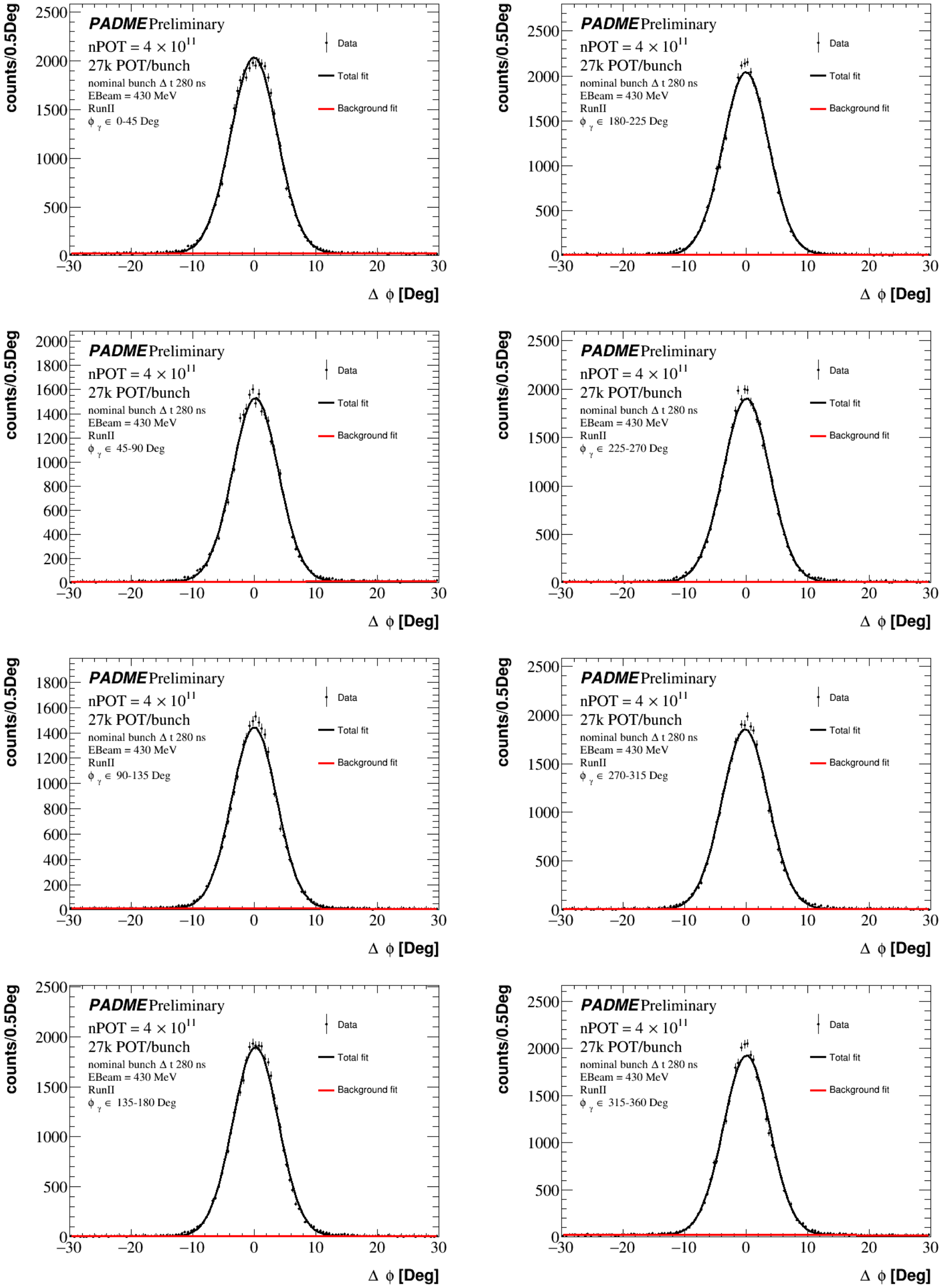

Figure C.3: *Photon tag energy residual for each inner ϕ slice with total and partial fits superimposed. The yields extracted from the fits are reported in Table 5.21.*

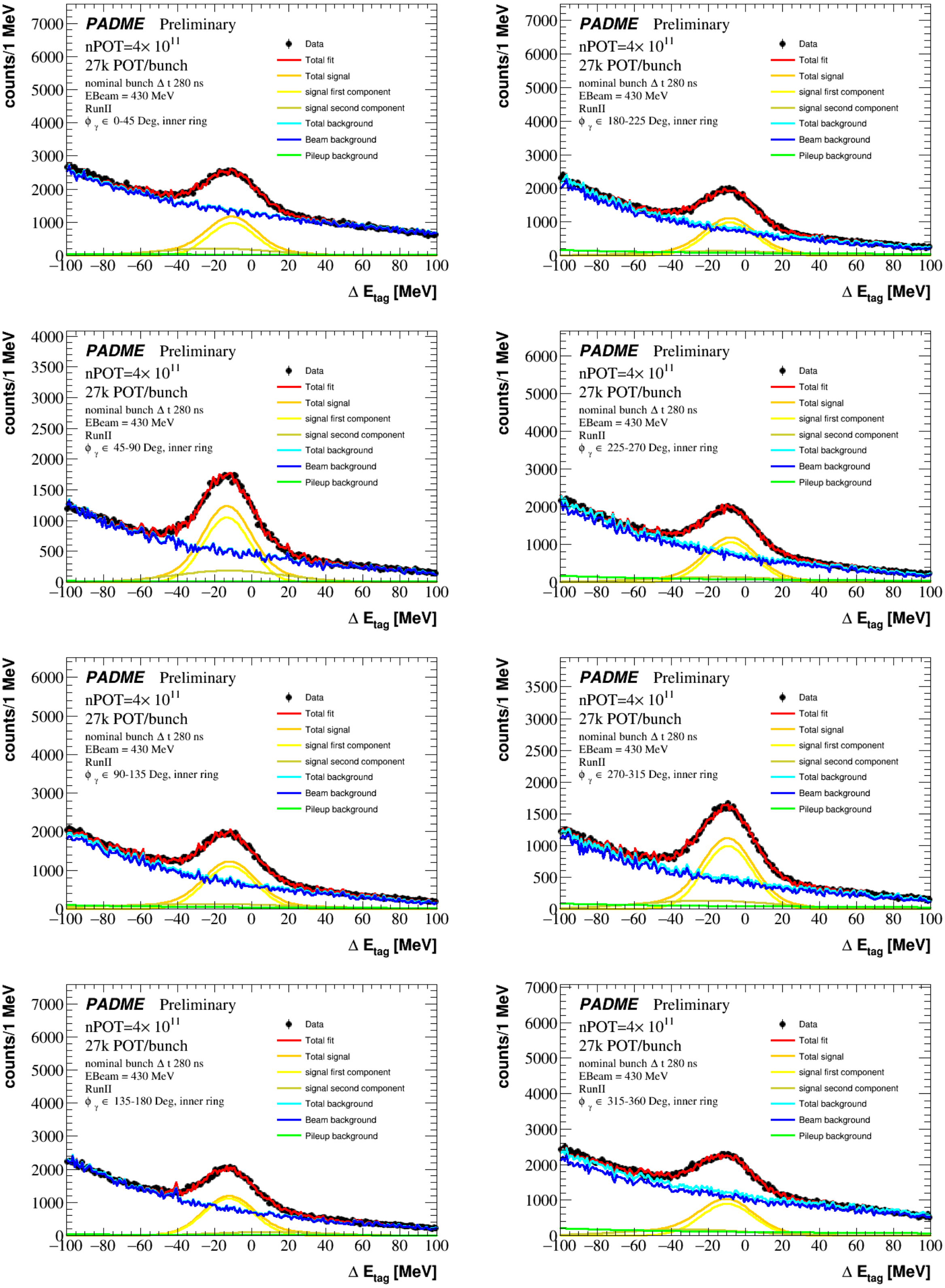

Figure C.4: *Photon probe energy residual for each inner ϕ slice fit superimposed. The yields extracted from the fits are reported in Table 5.25.*

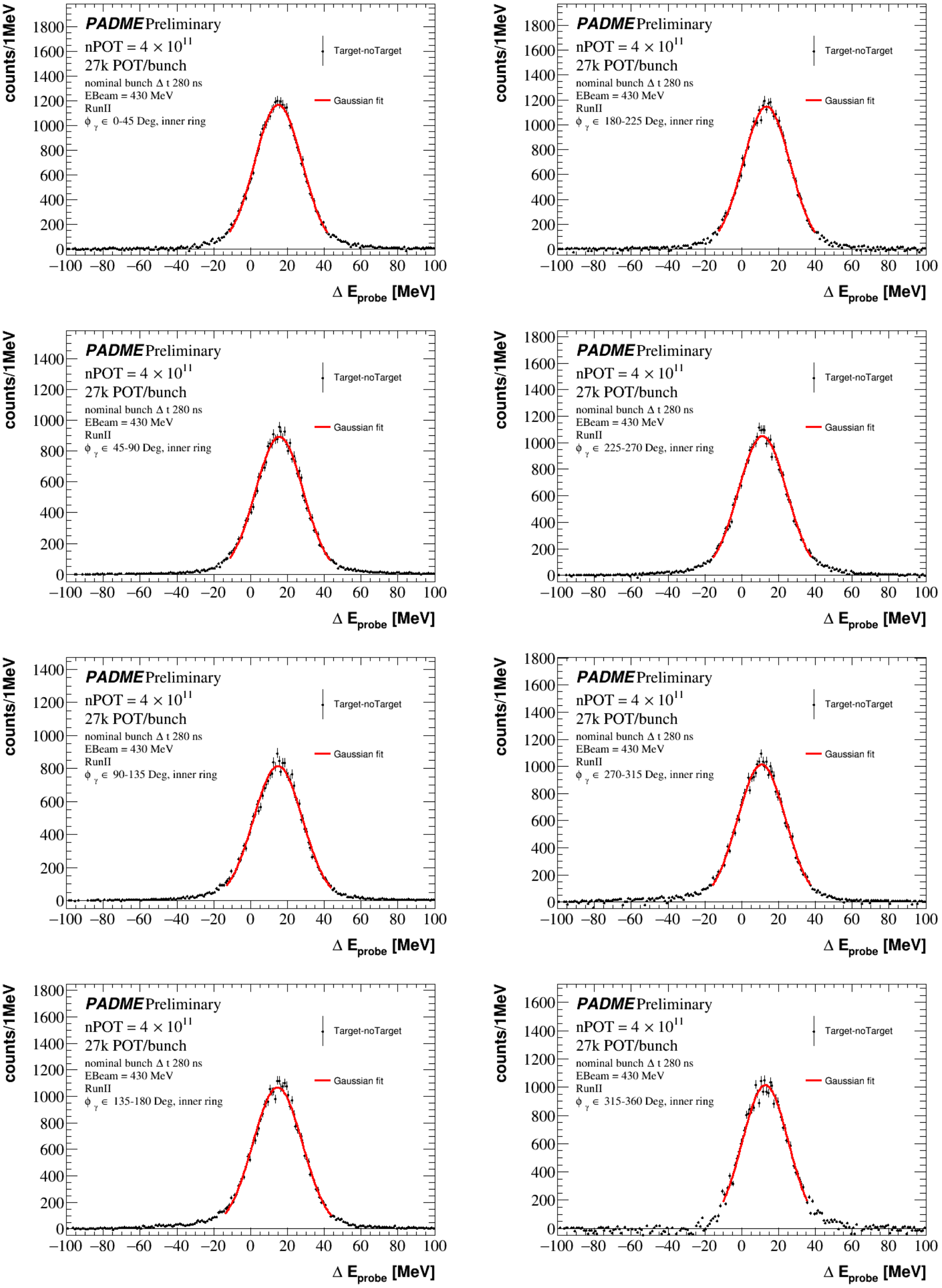

Figure C.5: *Photon tag energy residual for each outer ϕ slice with total and partial fits superimposed. The yields extracted from the fits are reported in Table 5.21.*

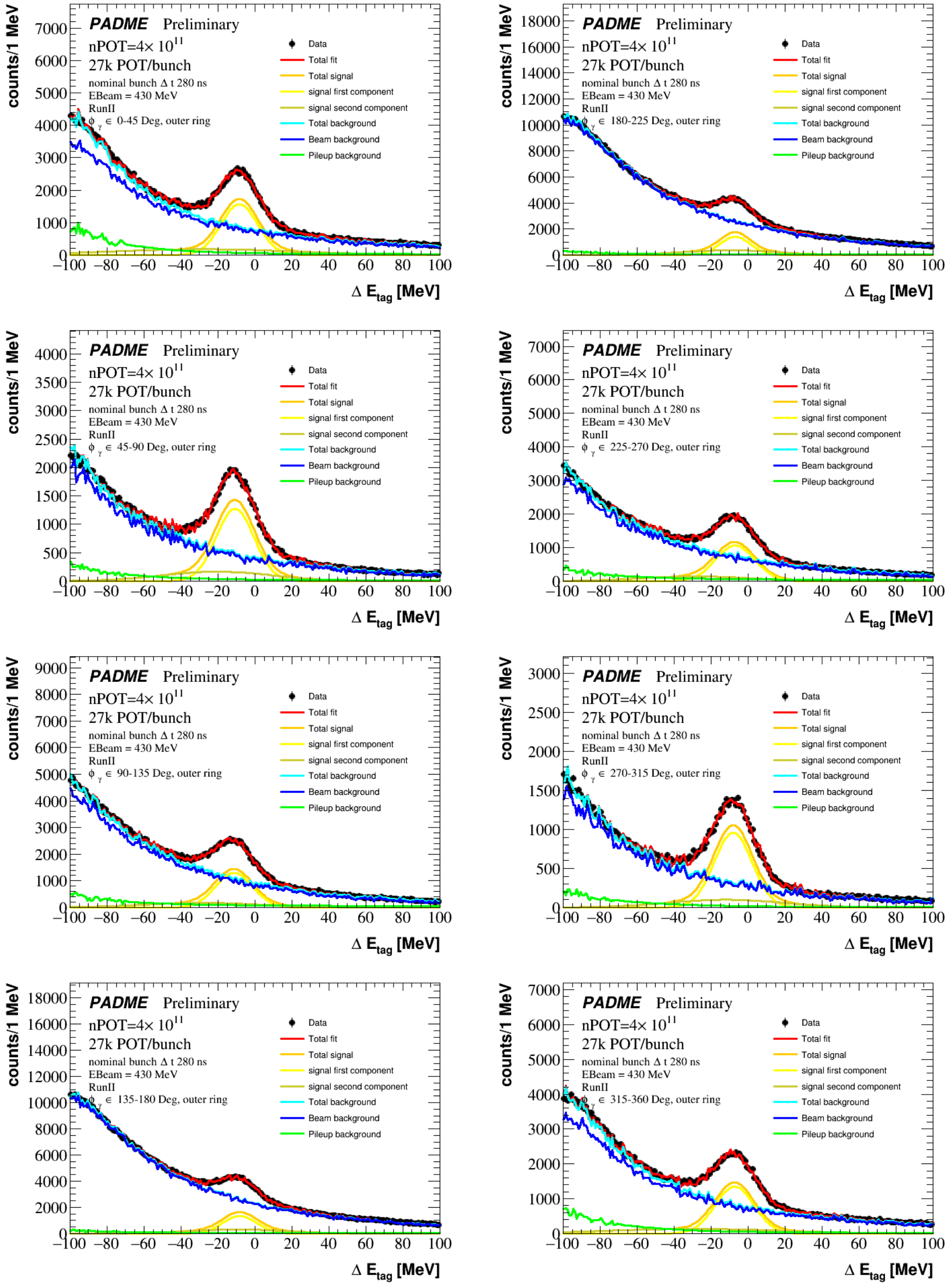

Figure C.6: *Photon probe energy residual for each outer ϕ slice with fit superimposed. The yields extracted from the fits are reported in Table 5.25.*

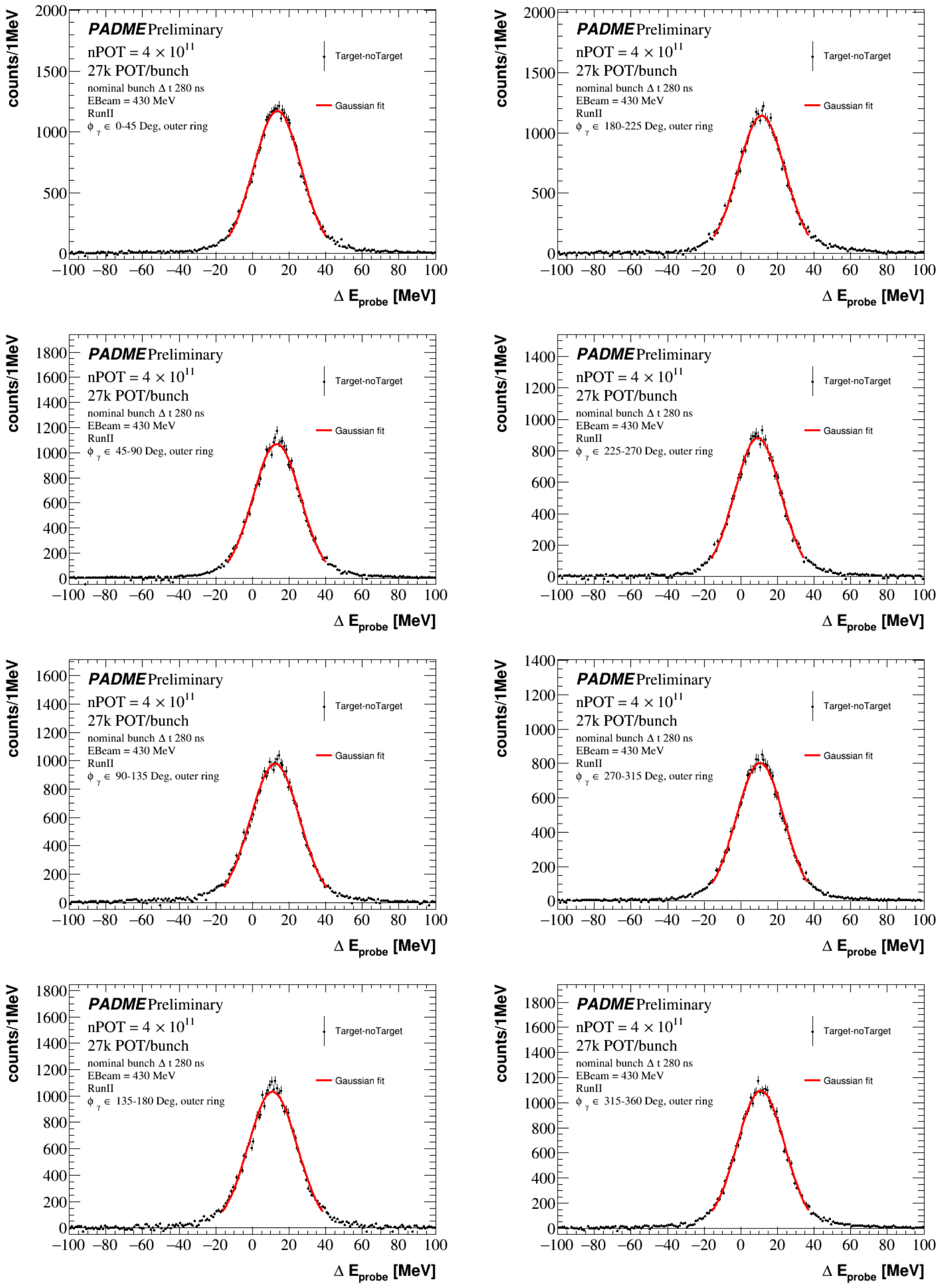

Figure C.7: *Photon squared missing mass for each inner ϕ slice with total and partial fits superimposed. The yields extracted from the fits are reported in Table 5.21.*

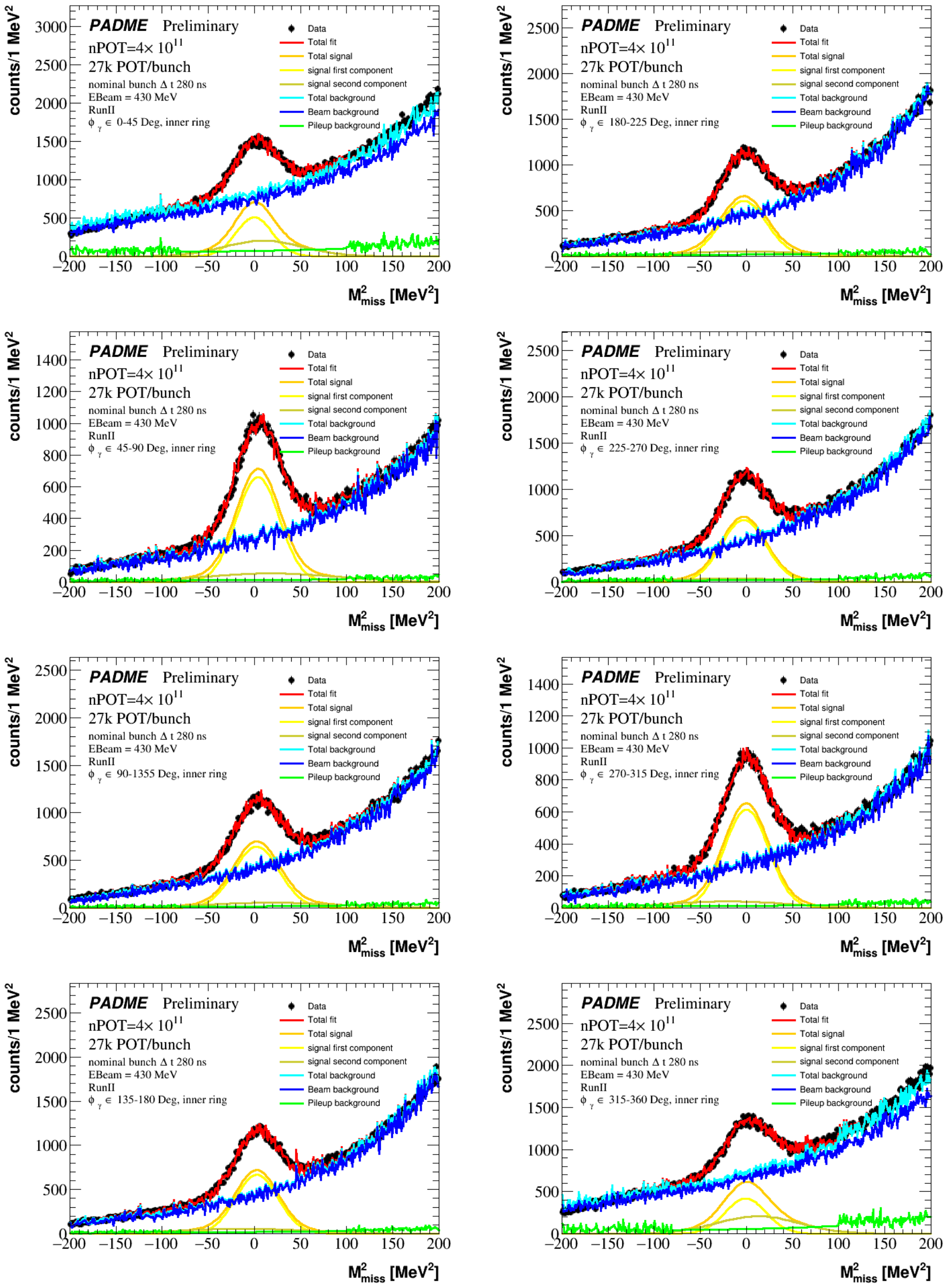

Figure C.8: *Photon squared missing mass for each outer ϕ slice with total and partial fits superimposed. The yields extracted from the fits are reported in Table 5.21.*

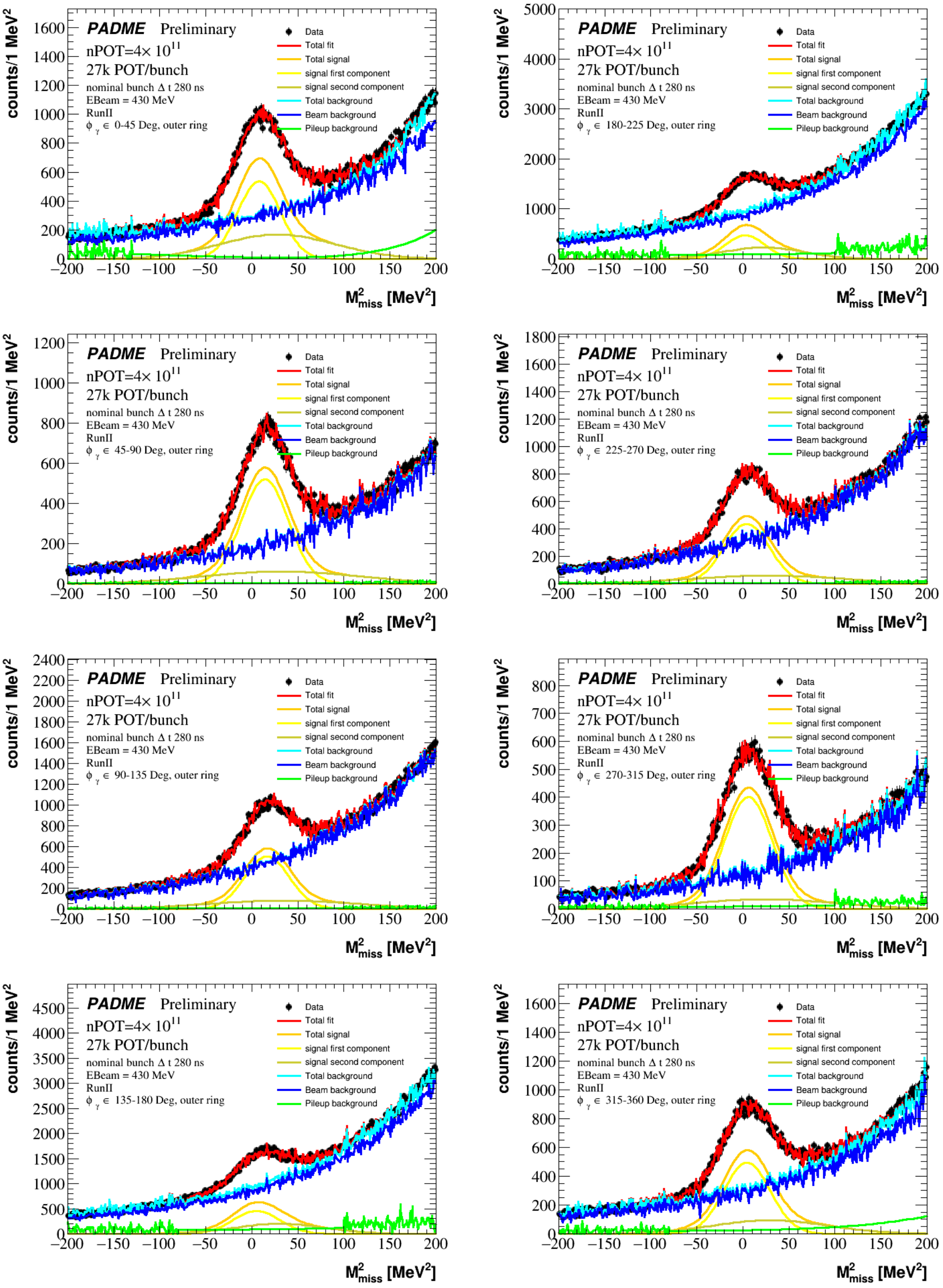

Figure C.9: *Azimuthal angle difference of two photons from annihilation event candidates for each analysed run whit the total fit superimposed (black line). The red line is the background component of the fit. The yields extracted from the fits are reported in Table 5.22.*

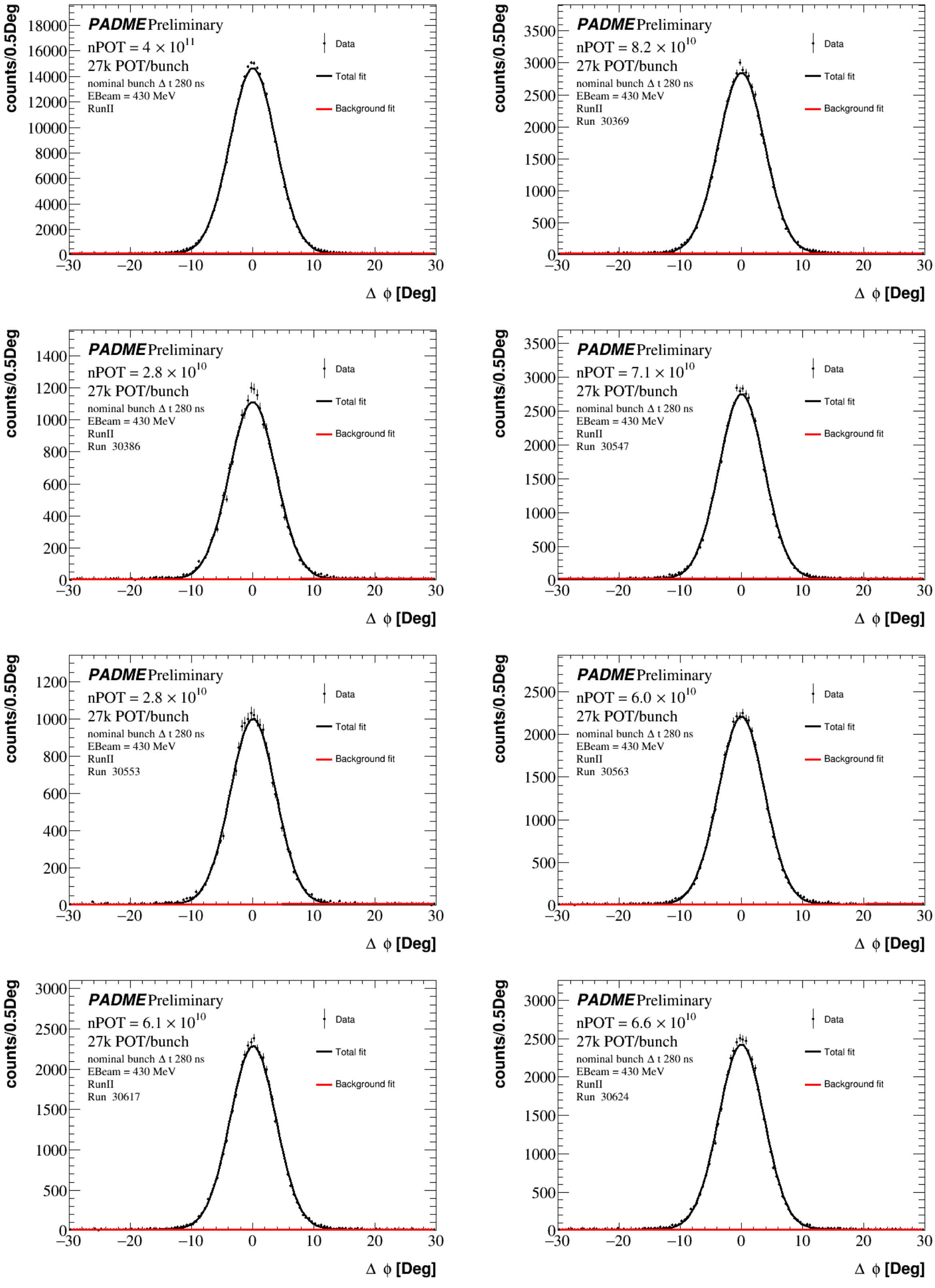

Figure C.10: *Inner photon tag energy residual for each analysed run with total and partial fits superimposed. The yields extracted from the fits are reported in Table 5.22.*

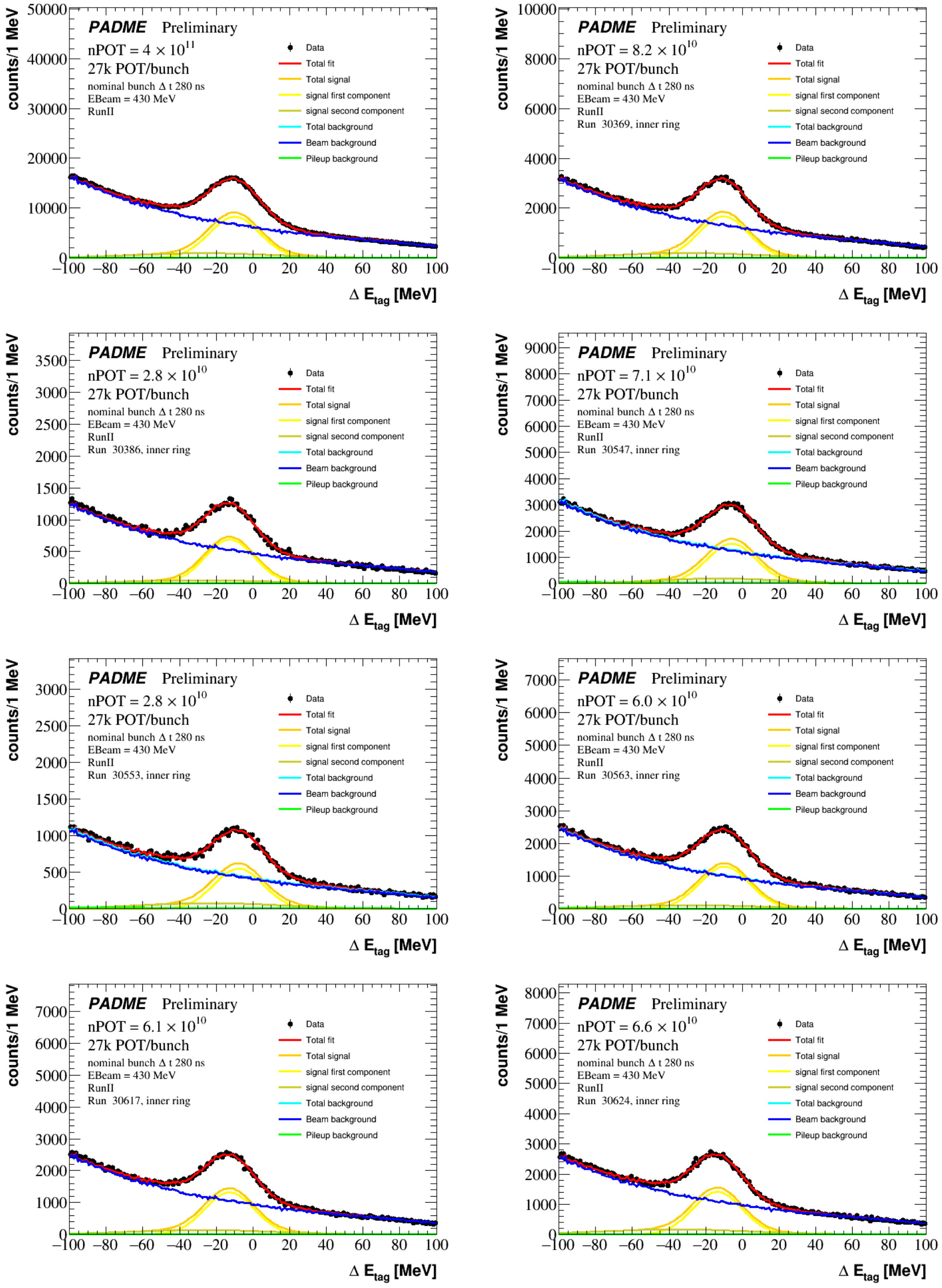

Figure C.11: *Inner photon probe energy residual for each analysed run with fit superimposed. The yields extracted from the fits are reported in Table 5.30.*

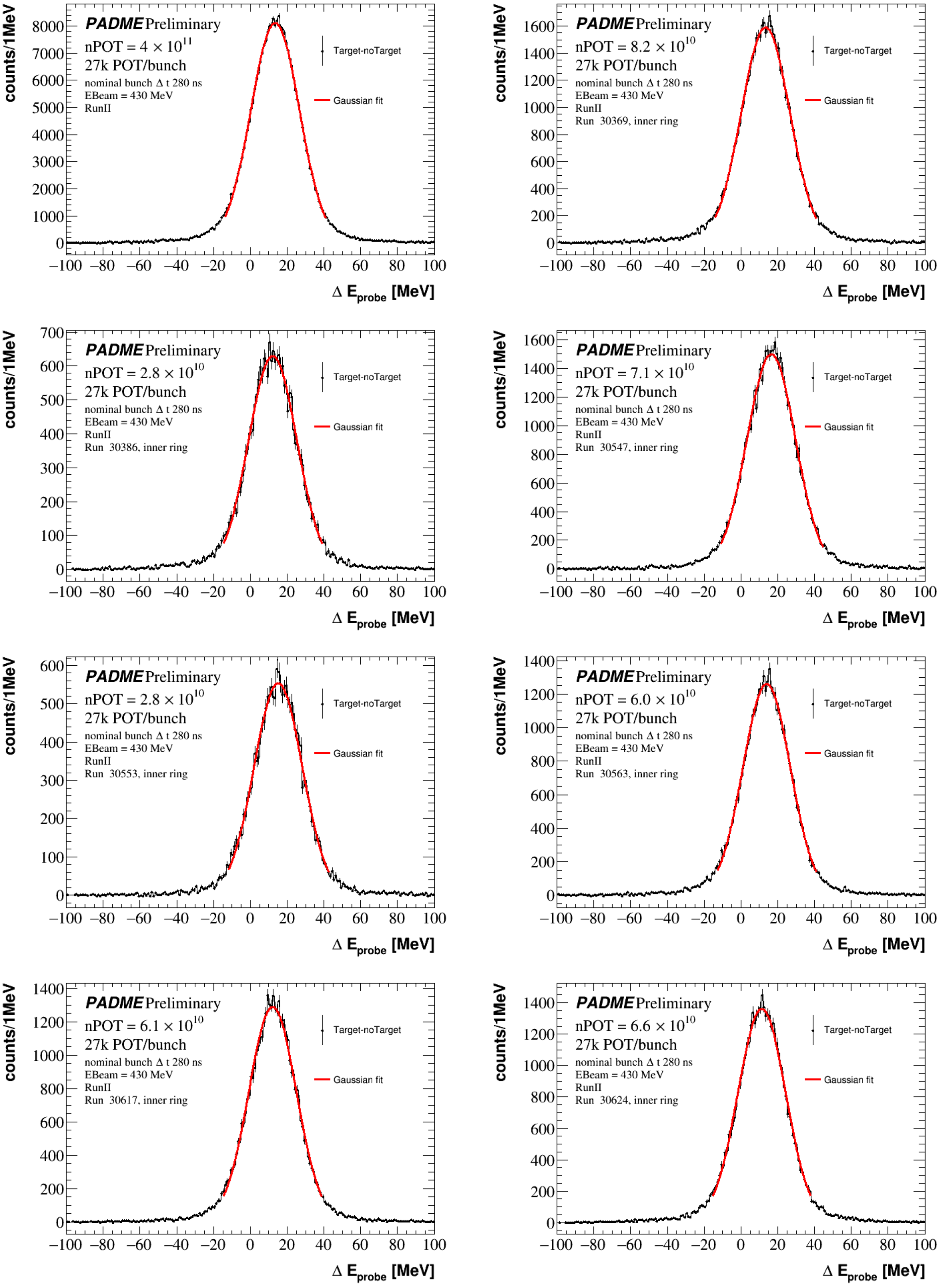

Figure C.12: *Outer photon tag energy residual for each analysed run with total and partial fits superimposed. The yields extracted from the fits are reported in Table 5.22.*

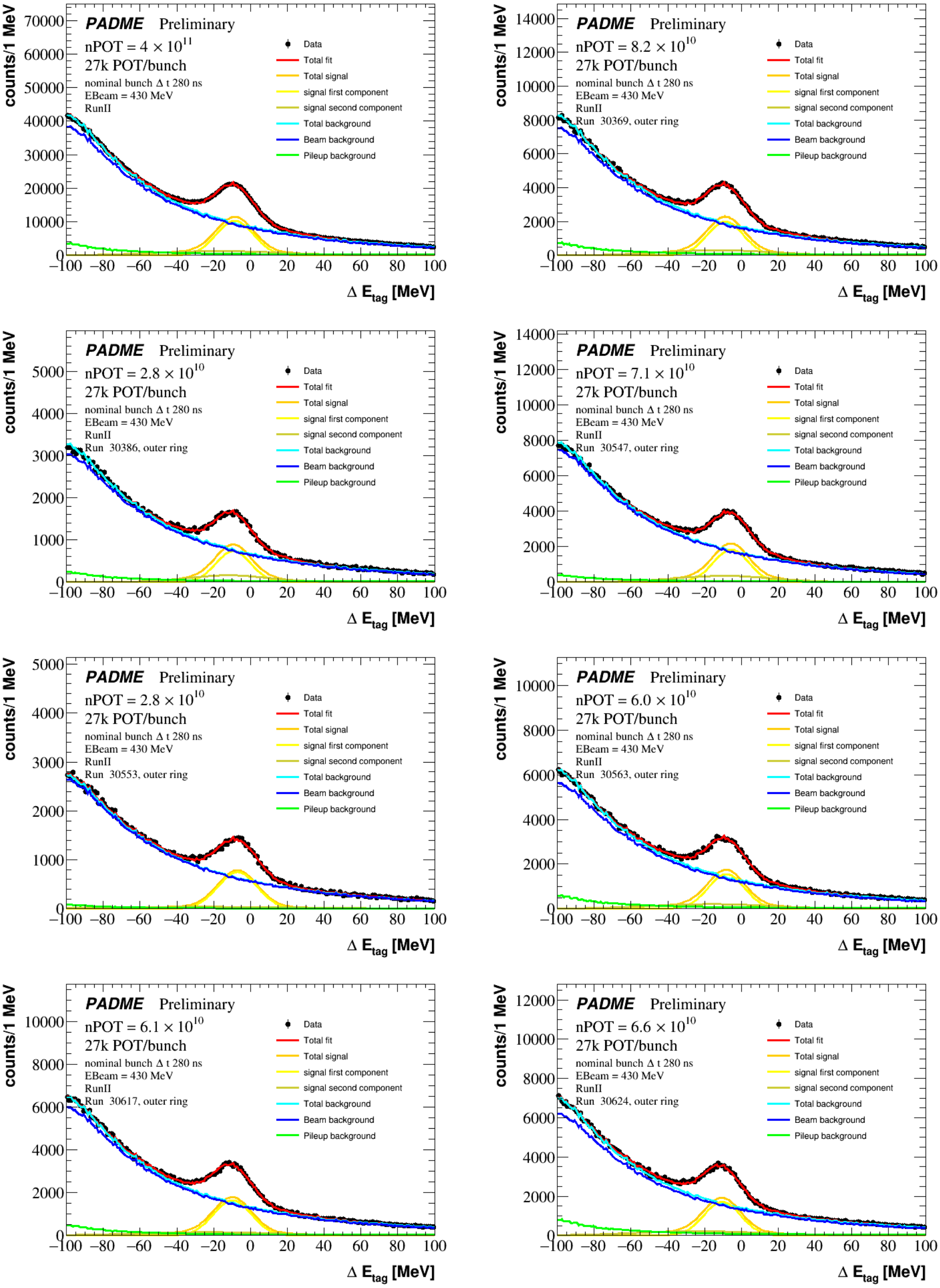

Figure C.13: *Outer photon probe energy residual for each analysed run with total and partial fits superimposed. The yields extracted from the fits are reported in Table 5.30.*

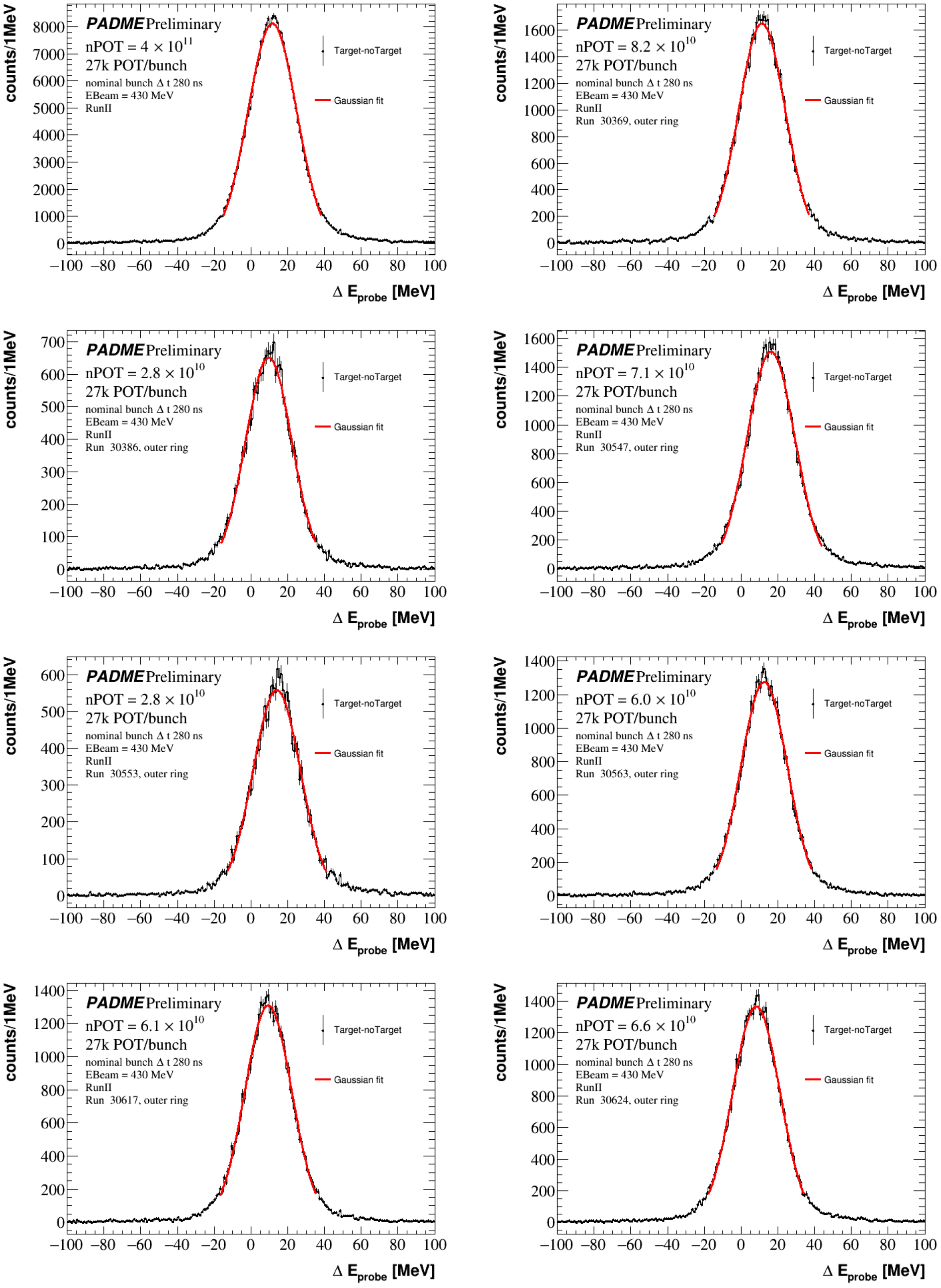

Bibliography

[1] G. Gamow, Expanding universe and the origin of elements, Phys. Rev. 70 (1946) 572–573. `doi:10.1103/PhysRev.70.572.2`.
URL `https://link.aps.org/doi/10.1103/PhysRev.70.572.2`

[2] R. A. Alpher, H. Bethe, G. Gamow, The origin of chemical elements, Phys. Rev. 73 (1948) 803–804. `doi:10.1103/PhysRev.73.803`.
URL `https://link.aps.org/doi/10.1103/PhysRev.73.803`

[3] R. A. Alpher, R. C. Herman, On the relative abundance of the elements, Phys. Rev. 74 (1948) 1737–1742. `doi:10.1103/PhysRev.74.1737`.
URL `https://link.aps.org/doi/10.1103/PhysRev.74.1737`

[4] R. A. Alpher, R. C. Herman, Remarks on the evolution of the expanding universe, Phys. Rev. 75 (1949) 1089–1095. `doi:10.1103/PhysRev.75.1089`.
URL `https://link.aps.org/doi/10.1103/PhysRev.75.1089`

[5] R. W. Penzias, A. A. ; Wilson, A measurement of excess antenna temperature at 4080 mc/s., Astrophysical Journal 142. `doi:10.1086/148307`.
URL `https://link.aps.org/doi/10.1103/PhysRev.75.1089`

[6] N. Aghanim, Y. Akrami, M. Ashdown, J. Aumont, C. Baccigalupi, M. Ballardini, A. J. Banday, R. B. Barreiro, N. Bartolo, et al., Planck 2018 results, Astronomy and Astrophysics 641 (2020) A6. `doi:10.1051/0004-6361/201833910`.
URL `http://dx.doi.org/10.1051/0004-6361/201833910`

[7] F. Zwicky, Die Rotverschiebung von extragalaktischen Nebeln, Helv. Phys. Acta 6 (1933) 110–127. `doi:10.1007/s10714-008-0707-4`.

[8] V. C. Rubin, W. K. Ford, Jr, Rotation of the andromeda nebula from a spectroscopic survey of emission regions., Astrophys. J. 159: 379-403(Feb 1970).`doi:10.1086/150317`.
URL `https://www.osti.gov/biblio/4148861`

[9] K. G. Begeman, A. H. Broeils, R. H. Sanders, Extended rotation curves of spiral galaxies: Dark haloes and modified dynamics, Mon. Not. Roy. Astron. Soc. 249 (1991) 523.

[10] M. Markevitch, A. Vikhlinin, W. R. Forman, C. L. Sarazin, Mass profiles of the typical relaxed galaxy clusters a2199 and a496, The Astrophysical Journal 527 (2) (1999) 545–553. `doi:10.1086/308124`.
URL `http://dx.doi.org/10.1086/308124`

[11] T. Treu, Strong lensing by galaxies, Annu. Rev. Astron. Astrophys. (2010) 87–126`doi:10.1146/annurev-astro-081309-130924`.

[12] D. Clowe, M. Bradač, A. H. Gonzalez, M. Markevitch, S. W. Randall, C. Jones, D. Zaritsky, A direct empirical proof of the existence of dark matter, The Astrophysical Journal 648 (2) (2006) L109–L113. `doi:10.1086/508162`.
URL `http://dx.doi.org/10.1086/508162`

[13] M. T. et al., Review of particle physics (2020). `arXiv:Phys.Rev.D`, `doi:98:030001`.

[14] P. A. R. Ade, N. Aghanim, C. Armitage-Caplan, M. Arnaud, M. Ashdown, F. Atrio-Barandela, J. Aumont, C. Baccigalupi, A. J. Banday, et al., Planck2013 results. xv. cmb power spectra and likelihood, Astronomy and Astrophysics 571 (2014) A15. `doi:10.1051/0004-6361/201321573`.
URL `http://dx.doi.org/10.1051/0004-6361/201321573`

[15] S. Das, T. Louis, M. R. Nolta, G. E. Addison, E. S. Battistelli, J. R. Bond, E. Calabrese, D. Crichton, M. J. Devlin, S. Dicker, et al., The atacama cosmology telescope: temperature and gravitational lensing power spectrum measurements from three seasons of data, Journal of Cosmology and Astroparticle Physics 2014 (04) (2014) 014–014. `doi:10.1088/1475-7516/2014/04/014`.
URL `http://dx.doi.org/10.1088/1475-7516/2014/04/014`

[16] K. T. Story, C. L. Reichardt, Z. Hou, R. Keisler, K. A. Aird, B. A. Benson, L. E. Bleem, J. E. Carlstrom, C. L. Chang, H.-M. Cho, et al., A measurement of the cosmic microwave background damping tail from the 2500-square-degree spt-sz survey, The Astrophysical Journal 779 (1) (2013) 86. `doi:10.1088/0004-637x/779/1/86`.
URL `http://dx.doi.org/10.1088/0004-637X/779/1/86`

[17] G. Hinshaw, D. Larson, E. Komatsu, D. N. Spergel, C. L. Bennett, J. Dunkley, M. R. Nolta, M. Halpern, R. S. Hill, N. Odegard, et al., Nine-year wilkinson microwave anisotropy probe (wmap) observations: Cosmological parameter results, The Astrophysical Journal Supplement Series 208 (2) (2013) 19. `doi:10.1088/0067-0049/208/2/19`.
URL `http://dx.doi.org/10.1088/0067-0049/208/2/19`

[18] E. Komatsu, J. Dunkley, M. R. Nolta, C. L. Bennett, B. Gold, G. Hinshaw, N. Jarosik, D. Larson, M. Limon, L. Page, et al., Five-year wilkinson microwave anisotropy probe observations: Cosmological interpretation, The Astrophysical Journal Supplement Series 180 (2) (2009) 330–376. `doi:10.1088/0067-0049/180/2/330`.
URL `http://dx.doi.org/10.1088/0067-0049/180/2/330`

[19] W. J. Percival, S. Cole, D. J. Eisenstein, R. C. Nichol, J. A. Peacock, A. C. Pope, A. S. Szalay, Measuring the baryon acoustic oscillation scale using the sloan digital sky survey and 2df galaxy redshift survey, Monthly Notices of the Royal Astronomical Society 381 (3) (2007) 1053–1066. `doi:10.1111/j.1365-2966.2007.12268.x`.
URL `http://dx.doi.org/10.1111/j.1365-2966.2007.12268.x`

[20] R. V. Wagoner, W. A. Fowler, F. Hoyle, On the synthesis of elements at very high temperatures, Astrophysical Journal 148. `doi:10.1086/149126`.

[21] L. Forestell, D. E. Morrissey, G. White, Limits from bbn on light electromagnetic decays, Journal of High Energy Physics 2019 (1). `doi:10.1007/jhep01(2019)074`.
URL `http://dx.doi.org/10.1007/JHEP01(2019)074`

[22] B. D. Fields, The primordial lithium problem, Annual Review of Nuclear and Particle Science 61 (1) (2011) 47–68. `doi:10.1146/annurev-nucl-102010-130445`.
URL `http://dx.doi.org/10.1146/annurev-nucl-102010-130445`

[23] V. Springel, J. Wang, M. Vogelsberger, A. Ludlow, A. Jenkins, A. Helmi, J. F. Navarro, C. S. Frenk, S. D. M. White, The aquarius project: the subhaloes of galactic haloes, Monthly Notices of the Royal Astronomical Society 391 (4) (2008) 1685–1711. `doi:10.1111/j.1365-2966.2008.14066.x`.
URL `http://dx.doi.org/10.1111/j.1365-2966.2008.14066.x`

[24] B. Abi, T. Albahri, S. Al-Kilani, D. Allspach, L. Alonzi, A. Anastasi, A. Anisenkov, F. Azfar, K. Badgley, S. Baeßler, et al., Measurement of the positive muon anomalous magnetic moment to 0.46 ppm, Physical Review Letters 126 (14). `doi:10.1103/physrevlett.126.141801`.
URL `http://dx.doi.org/10.1103/PhysRevLett.126.141801`

[25] A. Krasznahorkay, M. Csatlós, L. Csige, Z. Gácsi, J. Gulyás, M. Hunyadi, I. Kuti, B. Nyakó, L. Stuhl, J. Timár, et al., Observation of anomalous internal pair creation inbe8: A possible indication of a light, neutral boson, Physical Review Letters 116 (4). `doi:10.1103/physrevlett.116.042501`.
URL `http://dx.doi.org/10.1103/PhysRevLett.116.042501`

[26] A. J. Krasznahorkay, M. Csatlos, L. Csige, J. Gulyas, M. Koszta, B. Szihalmi, J. Timar, D. S. Firak, A. Nagy, N. J. Sas, A. Krasznahorkay, New evidence supporting the existence of the hypothetic x17 particle (2019). `arXiv:1910.10459`.

[27] S. D. McDermott, H.-B. Yu, K. M. Zurek, Turning off the lights: How dark is dark matter?, Physical Review D 83 (6). `doi:10.1103/physrevd.83.063509`.
URL `http://dx.doi.org/10.1103/PhysRevD.83.063509`

[28] S. W. Randall, M. Markevitch, D. Clowe, A. H. Gonzalez, M. Bradac, Constraints on the self-interaction cross section of dark matter from numerical simulations of the merging

galaxy cluster 1e 0657-56, The Astrophysical Journal 679 (2) (2008) 1173–1180. `doi:10.1086/587859`.
URL `http://dx.doi.org/10.1086/587859`

[29] D. A. Buote, T. E. Jeltema, C. R. Canizares, G. P. Garmire, Chandraevidence of a flattened, triaxial dark matter halo in the elliptical galaxy ngc 720, The Astrophysical Journal 577 (1) (2002) 183–196. `doi:10.1086/342158`.
URL `http://dx.doi.org/10.1086/342158`

[30] D. Harvey, R. Massey, T. Kitching, A. Taylor, E. Tittley, The nongravitational interactions of dark matter in colliding galaxy clusters, Science 347 (6229) (2015) 1462–1465. `doi:10.1126/science.1261381`.
URL `http://dx.doi.org/10.1126/science.1261381`

[31] J. Madsen, Generalized Tremaine-Gunn limits for bosons and fermions, Phys. Rev. D 44 (1991) 999–1006. `doi:10.1103/PhysRevD.44.999`.

[32] L. Randall, J. Scholtz, J. Unwin, Cores in dwarf galaxies from fermi repulsion, Monthly Notices of the Royal Astronomical Society (2017) stx161`doi:10.1093/mnras/stx161`.
URL `http://dx.doi.org/10.1093/mnras/stx161`

[33] R. Hlozek, D. Grin, D. J. Marsh, P. G. Ferreira, A search for ultralight axions using precision cosmological data, Physical Review D 91 (10). `doi:10.1103/physrevd.91.103512`.
URL `http://dx.doi.org/10.1103/PhysRevD.91.103512`

[34] E. Armengaud, N. Palanque-Delabrouille, C. Yeche, D. J. E. Marsh, J. Baur, Constraining the mass of light bosonic dark matter using sdss lyman-α forest, Monthly Notices of the Royal Astronomical Society 471 (4) (2017) 4606–4614. `doi:10.1093/mnras/stx1870`.
URL `http://dx.doi.org/10.1093/mnras/stx1870`

[35] M. Nori, R. Murgia, V. Irsic, M. Baldi, M. Viel, Lyman α forest and non-linear structure characterization in fuzzy dark matter cosmologies, Monthly Notices of the Royal Astronomical Society 482 (3) (2018) 3227–3243. `doi:10.1093/mnras/sty2888`.
URL `http://dx.doi.org/10.1093/mnras/sty2888`

[36] B. Bozek, D. J. E. Marsh, J. Silk, R. F. G. Wyse, Galaxy uv-luminosity function and reionization constraints on axion dark matter, Monthly Notices of the Royal Astronomical Society 450 (1) (2015) 209–222. `doi:10.1093/mnras/stv624`.
URL `http://dx.doi.org/10.1093/mnras/stv624`

[37] E. O. Nadler, V. Gluscevic, K. K. Boddy, R. H. Wechsler, Constraints on dark matter microphysics from the milky way satellite population, The Astrophysical Journal 878 (2) (2019) L32. `doi:10.3847/2041-8213/ab1eb2`.
URL `http://dx.doi.org/10.3847/2041-8213/ab1eb2`

[38] M. A. Monroy-Rodríguez, C. Allen, The end of the macho era, revisited: New limits on macho masses from halo wide binaries, The Astrophysical Journal 790 (2) (2014) 159. `doi:10.1088/0004-637x/790/2/159`.
URL `http://dx.doi.org/10.1088/0004-637X/790/2/159`

[39] T. D. Brandt, Constraints on macho dark matter from compact stellar systems in ultra-faint dwarf galaxies, The Astrophysical Journal 824 (2) (2016) L31. `doi:10.3847/2041-8205/824/2/l31`.
URL `http://dx.doi.org/10.3847/2041-8205/824/2/L31`

[40] B. Audren, J. Lesgourgues, G. Mangano, P. D. Serpico, T. Tram, Strongest model-independent bound on the lifetime of dark matter, Journal of Cosmology and Astroparticle Physics 2014 (12) (2014) 028–028. `doi:10.1088/1475-7516/2014/12/028`.
URL `http://dx.doi.org/10.1088/1475-7516/2014/12/028`

[41] Y. Bai, A. J. Long, S. Lu, Tests of dark machos: lensing, accretion, and glow, Journal of Cosmology and Astroparticle Physics 2020 (09) (2020) 044–044. `doi:10.1088/1475-7516/2020/09/044`.
URL `http://dx.doi.org/10.1088/1475-7516/2020/09/044`

[42] P. Cushman, C. Galbiati, D. N. McKinsey, H. Robertson, T. M. P. Tait, D. Bauer, A. Borgland, B. Cabrera, F. Calaprice, J. Cooley, T. Empl, R. Essig, E. Figueroa-Feliciano, R. Gaitskell, S. Golwala, J. Hall, R. Hill, A. Hime, E. Hoppe, L. Hsu, E. Hungerford, R. Jacobsen, M. Kelsey, R. F. Lang, W. H. Lippincott, B. Loer, S. Luitz, V. Mandic, J. Mardon, J. Maricic, R. Maruyama, R. Mahapatra, H. Nelson, J. Orrell, K. Palladino, E. Pantic, R. Partridge, A. Ryd, T. Saab, B. Sadoulet, R. Schnee, W. Shepherd, A. Sonnenschein, P. Sorensen, M. Szydagis, T. Volansky, M. Witherell, D. Wright, K. Zurek, Snowmass cf1 summary: Wimp dark matter direct detection (2013). `arXiv:1310.8327`.

[43] C. Mondino, M. Pospelov, J. T. Ruderman, O. Slone, Dark higgs dark matter, Physical Review D 103 (3). `doi:10.1103/physrevd.103.035027`.
URL `http://dx.doi.org/10.1103/PhysRevD.103.035027`

[44] A. Ringwald, K. Saikawa, Axion dark matter in the post-inflationary peccei-quinn symmetry breaking scenario, Physical Review D 93 (8). `doi:10.1103/physrevd.93.085031`.
URL `http://dx.doi.org/10.1103/PhysRevD.93.085031`

[45] T. Mannel, Theory and Phenomenology of CP Violation, Nuclear Physics B Proceedings Supplements 167 (2007) 170–174. `doi:10.1016/j.nuclphysbps.2006.12.083`.

[46] Y.-L. Tang, S.-h. Zhu, Dark matter relic abundance and light sterile neutrinos, Journal of High Energy Physics 2017 (1). `doi:10.1007/jhep01(2017)025`.
URL `http://dx.doi.org/10.1007/JHEP01(2017)025`

[47] J. Liu, N. Weiner, W. Xue, Signals of a light dark force in the galactic center, Journal of High Energy Physics 2015 (8). `doi:10.1007/jhep08(2015)050`.
URL `http://dx.doi.org/10.1007/JHEP08(2015)050`

[48] H. An, M. Pospelov, J. Pradler, Observing dark photon with dark matter detectors (2014). `arXiv:1401.8287`.

[49] S. Biswas, E. Gabrielli, M. Heikinheimo, B. Mele, Higgs-boson production in association with a dark photon in e^+e^- collisions (2016). `arXiv:1503.05836`.

[50] A. Konaka, et al., Search for Neutral Particles in Electron Beam Dump Experiment, Phys. Rev. Lett. 57 (1986) 659. `doi:10.1103/PhysRevLett.57.659`.

[51] E. M. Riordan, et al., A Search for Short Lived Axions in an Electron Beam Dump Experiment, Phys. Rev. Lett. 59 (1987) 755. `doi:10.1103/PhysRevLett.59.755`.

[52] J. D. Bjorken, S. Ecklund, W. R. Nelson, A. Abashian, C. Church, B. Lu, L. W. Mo, T. A. Nunamaker, P. Rassmann, Search for Neutral Metastable Penetrating Particles Produced in the SLAC Beam Dump, Phys. Rev. D 38 (1988) 3375. `doi:10.1103/PhysRevD.38.3375`.

[53] A. Bross, M. Crisler, S. H. Pordes, J. Volk, S. Errede, J. Wrbanek, A Search for Shortlived Particles Produced in an Electron Beam Dump, Phys. Rev. Lett. 67 (1991) 2942–2945. `doi:10.1103/PhysRevLett.67.2942`.

[54] M. Davier, H. Nguyen Ngoc, An Unambiguous Search for a Light Higgs Boson, Phys. Lett. B 229 (1989) 150–155. `doi:10.1016/0370-2693(89)90174-3`.

[55] H. Merkel, P. Achenbach, C. Ayerbe Gayoso, J. C. Bernauer, R. Böhm, D. Bosnar, L. Debenjak, A. Denig, M. O. Distler, A. Esser, et al., Search for light gauge bosons of the dark sector at the mainz microtron, Physical Review Letters 106 (25). `doi:10.1103/physrevlett.106.251802`.
URL `http://dx.doi.org/10.1103/PhysRevLett.106.251802`

[56] S. Abrahamyan, et al., Search for a New Gauge Boson in Electron-Nucleus Fixed-Target Scattering by the APEX Experiment, Phys. Rev. Lett. 107 (2011) 191804. `arXiv:1108.2750`, `doi:10.1103/PhysRevLett.107.191804`.

[57] C. Bravo, The heavy photon search experiment (2019). `arXiv:1910.04886`.

[58] S. N. Gninenko, N. V. Krasnikov, V. A. Matveev, Search for dark sector physics with na64, Physics of Particles and Nuclei 51 (5) (2020) 829–858. `doi:10.1134/s1063779620050044`.
URL `http://dx.doi.org/10.1134/S1063779620050044`

[59] G. Mandaglio, Kloe/kloe-2 results and perspectives on dark force search (2017). `doi:10.22323/1.314.0073`.

[60] J. Lees, V. Poireau, V. Tisserand, E. Grauges, A. Palano, G. Eigen, D. Brown, M. Derdzinski, A. Giuffrida, Y. Kolomensky, et al., Search for invisible decays of a dark photon produced in e^+e^- collisions at babar, Physical Review Letters 119 (13). `doi:10.1103/physrevlett.119.131804`.
URL `http://dx.doi.org/10.1103/PhysRevLett.119.131804`

[61] J. R. Batley, et al., Search for the dark photon in π^0 decays, Phys. Lett. B 746 (2015) 178–185. `arXiv:1504.00607`, `doi:10.1016/j.physletb.2015.04.068`.

[62] G. Agakishiev, et al., Searching a Dark Photon with HADES, Phys. Lett. B 731 (2014) 265–271. `arXiv:1311.0216`, `doi:10.1016/j.physletb.2014.02.035`.

[63] A. Adare, et al., Search for dark photons from neutral meson decays in p+p and d+au collisions at $\sqrt{s_{_{NN}}}$=200 gev (2015). `arXiv:1409.0851`.

[64] M. Fabbrichesi, E. Gabrielli, G. Lanfranchi, The physics of the dark photon, SpringerBriefs in Physics`doi:10.1007/978-3-030-62519-1`.
URL `http://dx.doi.org/10.1007/978-3-030-62519-1`

[65] J. Beacham, et al., Physics Beyond Colliders at CERN: Beyond the Standard Model Working Group Report, J. Phys. G 47 (1) (2020) 010501. `arXiv:1901.09966`, `doi:10.1088/1361-6471/ab4cd2`.

[66] F. Bossi, Dark photon searches using displaced vertices at low energy e+e- colliders (2014). `arXiv:1310.8181`.

[67] S. Adler, et al., Further evidence for the decay $K^+ \to \nu\bar{\nu}$, Phys. Rev. Lett. 88 (2002) 041803. `arXiv:hep-ex/0111091`, `doi:10.1103/PhysRevLett.88.041803`.

[68] B. Aubert, et al., Search for Invisible Decays of a Light Scalar in Radiative Transitions $\upsilon_{3S} \to \gamma$ A0 (7 2008). `arXiv:0808.0017`.

[69] B. Wojtsekhowski, D. Nikolenko, I. Rachek, Searching for a new force at vepp-3 (2012). `arXiv:1207.5089`.

[70] B. Wojtsekhowski, D. Nikolenko, I. Rachek, Status of the experiment for the search of a dark photon at vepp–3 (2017). `arXiv:142:01025`.

[71] J. Alexander, MMAPS: Missing-Mass A-Prime Search, EPJ Web Conf. 142 (2017) 01001. `doi:10.1051/epjconf/201714201001`.

[72] T. Akesson, A. Berlin, N. Blinov, O. Colegrove, G. Collura, V. Dutta, B. Echenard, J. Hiltbrand, D. G. Hitlin, J. Incandela, J. Jaros, R. Johnson, G. Krnjaic, J. Mans, T. Maruyama, J. McCormick, O. Moreno, T. Nelson, G. Niendorf, R. Petersen, R. Pöttgen, P. Schuster, N. Toro, N. Tran, A. Whitbeck, Light dark matter experiment (ldmx) (2018). `arXiv:1808.05219`.

[73] W. Altmannshofer, et al., The Belle II Physics Book, PTEP 2019 (12) (2019) 123C01, [Erratum: PTEP 2020, 029201 (2020)]. `arXiv:1808.10567`, `doi:10.1093/ptep/ptz106`.

[74] P. Valente, All., Linear accelerator test facility at lnf conceptual design report (2016). `arXiv:1603.05651`.

[75] M.Raggi, V. Kozhuharov, Proposal to search for a dark photon in positron on target collisions at daϕne linac, Advances in High Energy Physics (2014) 1–14`doi:10.1155/2014/959802`.

[76] V. Kozhuharov, M. Raggi, P. Valente, New projects on dark photon search (2016). `arXiv:1610.04389`.

[77] F. Oliva, The padme active diamond target and positron bremsstrahlung analysis (2021).

[78] I. Oceano, on behalf of PADME collaboration, The performance of the diamond active target of the padme experiment (2020). `doi:15C04045`.

[79] F. Ferrarotto, L. Foggetta, G. Georgiev, P. Gianotti, V. Kozhuharov, E. Leonardi, G. Piperno, M. Raggi, C. Taruggi, L. Tsankov, P. Valente, Performance of the prototype of the charged-particle veto system of the padme experiment, IEEE Transactions on Nuclear Science 65 (8) (2018) 2029–2035. `doi:10.1109/TNS.2018.2822724`.

[80] H. Z. P. Technology, Co. [link].
URL `http://www.hzcphotonics.com/en_introduction%20of%20products.html`

[81] P. Albicocco, et al., Characterisation and performance of the padme electromagnetic calorimeter, Journal of Instrumentation 15 (10) (2020) T10003–T10003. `doi:10.1088/1748-0221/15/10/t10003`.
URL `http://dx.doi.org/10.1088/1748-0221/15/10/T10003`

[82] M.Raggi, et al., Performance of the padme calorimeter prototype at the daϕne btf, Nuclear Instruments and Methods in Physics Research A (862) (2017) 31–35.

[83] A. Frankenthal, et al., Characterization and performance of padme's cherenkov-based small-angle calorimeter, Nuclear Instruments and Methods in Physics Research Section A: Accelerators, Spectrometers, Detectors and Associated Equipment 919 (2019) 89–97. `doi:10.1016/j.nima.2018.12.035`.
URL `http://dx.doi.org/10.1016/j.nima.2018.12.035`

[84] I. Valin, C. Hu-Guo, J. Baudot, G. Bertolone, A. Besson, C. Colledani, G. Claus, A. Dorokhov, G. Dozière, W. Dulinski, M. Gelin, M. Goffe, A. Himmi, K. Jaaskelainen, F. Morel, H. Pham, C. Santos, S. Senyukov, M. Specht, G. Voutsinas, J. Wang, M. Winter, A reticle size CMOS pixel sensor dedicated to the STAR HFT, Journal of Instrumentation 7 (01) (2012) C01102–C01102. `doi:10.1088/1748-0221/7/01/c01102`.
URL `https://doi.org/10.1088/1748-0221/7/01/c01102`

[85] T. Poikela, J. Plosila, T. Westerlund, M. Campbell, M. De Gaspari, X. Llopart, V. Gromov, R. Kluit, M. van Beuzekom, F. Zappon, V. Zivkovic, C. Brezina, K. Desch, Y. Fu, A. Kruth, Timepix3: a 65K channel hybrid pixel readout chip with simultaneous ToA/ToT and sparse readout, Journal of Instrumentation 9 (5) (2014) C05013. `doi:10.1088/1748-0221/9/05/C05013`.

[86] D. analysis framework. [link].
URL `https://root.cern.ch`

[87] S. Agostinelli, et all., Geant4—a simulation toolkit, Nuclear Instruments and Methods in Physics Research Section A: Accelerators, Spectrometers, Detectors and Associated Equipment 506 (3) (2003) 250–303. `doi:https://doi.org/10.1016/S0168-9002(03)01368-8`.
URL `https://www.sciencedirect.com/science/article/pii/S0168900203013688`

[88] A. Belyaev, N. D. Christensen, A. Pukhov, Calchep 3.4 for collider physics within and beyond the standard model, Computer Physics Communications 184 (7) (2013) 1729–1769. `doi:10.1016/j.cpc.2013.01.014`.
URL `http://dx.doi.org/10.1016/j.cpc.2013.01.014`

[89] I. Oceano, Studio della strategia di analisi dei dati dell'esperimento padme per la ricerca del fotone oscuro (2018).

[90] P. Ciafaloni, G. Martelli, M. Raggi, Searching for dark sectors in multi lepton final state in e+ e- collisions`arXiv:2012.04754`.

[91] A. Krasznahorkay, et al., New evidence supporting the existence of the hypothetic X17 particle`arXiv:1910.10459`.

[92] L. Darmé, F. Giacchino, E. Nardi, M. Raggi, Invisible decays of axion-like particles: constraints and prospects, Journal of High Energy Physics 2021 (6). `doi:10.1007/jhep06(2021)009`.
URL `http://dx.doi.org/10.1007/JHEP06(2021)009`

[93] M. Moszyński, C. Gresset, J. Vacher, R. Odru, Timing properties of bgo scintillator, Nuclear Instruments and Methods in Physics Research 188 (2) (1981) 403–409. `doi:https://doi.org/10.1016/0029-554X(81)90521-8`.
URL `https://www.sciencedirect.com/science/article/pii/0029554X81905218`

[94] B.Rossi, High energy particles, Prentice Hall (1952) Chapter 5.

[95] CAEN. [link].
URL `https://www.caen.it/products/v1742/`

[96] C. M. Carloni Calame, G. Montagna, O. Nicrosini, F. Piccinini, The BABAYAGA event generator, Nucl. Phys. B Proc. Suppl. 131 (2004) 48–55. `arXiv:hep-ph/0312014`, `doi:10.1016/j.nuclphysbps.2004.02.008`.

[97] G. Balossini, C. Bignamini, C. M. C. Calame, G. Montagna, O. Nicrosini, F. Piccinini, Photon pair production at flavour factories with per mille accuracy, Phys. Lett. B 663 (2008) 209–213. `arXiv:0801.3360`, `doi:10.1016/j.physletb.2008.04.007`.

[98] ROOT. [link].
URL `https://root.cern/manual/roofit/`

[99] e. a. J.M. Link, Study of the cabibbo-suppressed decay modes $d^0 \to \pi^-\pi^+$ and $d^0 \to k^-k^+$, Physics Letters B 555 (3) (2003) 167–173. `doi:https://doi.org/10.1016/S0370-2693(03)00053-4`.
URL `https://www.sciencedirect.com/science/article/pii/S0370269303000534`

[100] ROOT. [link].
URL `https://root.cern.ch/doc/master/classTSpectrum.html`

[101] S. A. Colgate, F. C. Gilbert, Electron-positron annihilation in flight, Phys. Rev. 89 (1953) 790–792. `doi:10.1103/PhysRev.89.790`.
URL `https://link.aps.org/doi/10.1103/PhysRev.89.790`

[102] E. Malamud, R. Weill, Electron-positron annihilation in flight at 600 MeV, Il Nuovo Cimento 27 (1953) 418–424. `doi:https://doi.org/10.1007/BF02785552`.

[103] F. Fabiani, M. Fidecaro, G. Finocchiaro, G. Giacomelli, D. Harting, N. H. Lipman, G. Torelli, Positron-electron annihilation in flight between 2 and 10-GeV, Nuovo Cim. 25 (1962) 655. `doi:10.1007/BF02733703`.